



Bimolecular reaction dynamics and spectroscopy of weakly bound complexes

Voute, Alexandre Paolo

Publication date:
2021

Document Version
Publisher's PDF, also known as Version of record

[Link back to DTU Orbit](#)

Citation (APA):
Voute, A. P. (2021). *Bimolecular reaction dynamics and spectroscopy of weakly bound complexes*. DTU Chemistry.

General rights

Copyright and moral rights for the publications made accessible in the public portal are retained by the authors and/or other copyright owners and it is a condition of accessing publications that users recognise and abide by the legal requirements associated with these rights.

- Users may download and print one copy of any publication from the public portal for the purpose of private study or research.
- You may not further distribute the material or use it for any profit-making activity or commercial gain
- You may freely distribute the URL identifying the publication in the public portal

If you believe that this document breaches copyright please contact us providing details, and we will remove access to the work immediately and investigate your claim.

Bimolecular reaction dynamics and spectroscopy of weakly bound complexes

Ph.D. thesis

Written by:

Alexandre Voute

Supervisors:

Niels Engholm Henriksen

René Wugt Larsen

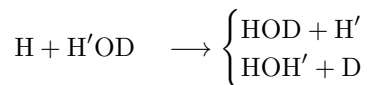
Klaus Braagaard Møller

Technical University of Denmark
Department of Chemistry
Kemitorvet, building 207
2800 Kongens Lyngby, Denmark
www.kemi.dtu.dk

Summary

A large number of experimental studies revealing the dynamics of unimolecular reactions at femtosecond time resolution have been carried out in the last thirty to forty years and are supported by a substantial amount of theoretical work. However, the study of time-resolved bimolecular reactions is limited to a few studies from the late 1980's and early 1990's and, in this context, no theoretical study using a full quantum mechanical approach exists to date. Here, bimolecular reactions are initiated by performing a weakly bound complex $(A-B)\cdots C$ of two molecules $A-B$ and C and then dissociating the $A-B$ bond with a ultrashort laser pulse, so as to have the B fragment colliding against the C moiety. The reaction starting time and the relative orientations of the reactants are thus well-defined.

The work presented in this thesis aims at reviving the interest in this type of studies. In particular, we explore the dynamics of the exchange reactions

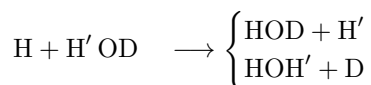


initiated by vertical photoexcitation and subsequent dissociation of HCl in the $(HCl)\cdots(HOD)$ hydrogen-bound complex. This reaction is studied using quantum mechanical wavepacket propagations with the MCTDH method on state-of-the-art potential energy surfaces. When initiated in these conditions, the collision of H with HOD does not give rise to new products most of the time, i.e. it mostly leads to the scattering of the hydrogen atom against the HOD molecule. The cause lies in the fact that the photodissociation of HCl yields a large collision energy (about 3 eV) between H and HOD . This makes the collision too fast to allow a redistribution of the relative kinetic energy of the reactants over the bonds of HOD . However, to a minor extent, some exchange products are obtained, whereas abstraction products (i.e. $HD + OH$ or $H_2 + OD$) are not. Overall, the typical reaction time in these exchange processes is of the order of 10 fs. Moreover, the natural selectivity of the reaction, i.e. the preference in producing $HOD + H'$ over $HOH' + D$, can be tuned by vibrational pre-excitation of the HOD molecule within the complex. The presence of the chlorine atom is not expected to be more than a negligible perturbation to the reaction and thus acts as a spectator atom.

On the other hand, this Ph.D. project features an experimental component aiming at characterizing weakly bound complexes via Fourier Transform Infrared spectroscopy. To this end, we describe a new design which has been constructed in our laboratory for the realization of matrix isolation spectroscopy of these complexes. In particular, this setup has been used to deposit HCl, H₂O and deuterated isotopologues in solid neon matrices and measure their mid-infrared spectrum. This led to the observation of spectral bands associated to the (HCl) ··· (H₂O) complex and its analogous isotopologues. In view of carrying out matrix isolation spectroscopy experiments in the challenging far-infrared spectral region, the development of a new para-hydrogen enrichment setup is also presented. The designed instrumentation and software allow for routine production of this matrix host material with purity larger than 99.95%. In the future, this will be applied for a number of studies, including that of the (HCl) ··· (H₂O) complex.

Et stort antal eksperimentelle undersøgelser, der afslører dynamikken i unimolekylære reaktioner ved femtosekund tidsopløsning, er blevet udført i de sidste tredive til fyre år og understøttes af en betydelig mængde teoretisk arbejde. Undersøgelsen af tidsopløste bimolekylære reaktioner er dog begrænset til nogle få undersøgelser i slutningen af 1980'erne og begyndelsen af 1990'erne og, i denne sammenhæng, ingen teoretisk undersøgelse med en fuld kvantemekanisk tilgang eksisterer. Her, initieres bimolekylære reaktioner ved at præformere et svagt bundet kompleks $(A-B) \cdots C$ af to molekyler $A-B$ og C og derefter dissociere $A-B$ -binding med en ultrakort laserpuls for at få B fragmentet til at kolliderer mod C -delen. Reaktionens starttid og de relative orienteringer af reaktanterne er således veldefineret.

Arbejdet præsenteret i denne afhandling sigter mod at genoplive interessen for denne type studier. Især undersøger vi dynamikken i udvekslingsreaktionerne



initieret af vertikal fotoexcitation og efterfølgende dissociation af HCl i $(HCl) \cdots (HOD)$ hydrogenbundet kompleks. Denne reaktion undersøges ved hjælp af kvantemekanisk tidsudvikling af bølgepakker med MCTDH-metoden på state-of-the-art potentielle energiflader. Når den initieres under disse forhold, giver kollisionen mellem H med HOD ikke nye produkter det meste af tiden, dvs. det fører for det meste til, at hydrogenatomet spredes fra HOD -molekylet. Årsagen ligger i det faktum, at fotodissociationen af HCl giver en stor kollisionsenergi (ca. 3 eV) mellem H og HOD . Dette gør kollisionen for hurtig til at muliggøre en omfordeling af reaktanternes relative kinetiske energi over bindingerne af HOD . Imidlertid opnås der i mindre grad nogle udvekslingsprodukter, mens abstraktionsprodukter (dvs. $HD + OH$ eller $H_2 + OD$) ikke observeres. Samlet set er den typiske reaktionstid i disse udvekslingsprocesser i størrelsesordenen 10 fs . Desuden kan reaktionens naturlige selektivitet, dvs. præferencen i at producere $HOD + H'$ frem for $HOH' + D$, påvirkes ved vibrationel præ-excitation af HOD molekylet i komplekset. Chloratomet forventes ikke at være mere end en ubetydelig forstyrrelse af reaktionen.

Den anden del af denne Ph.D.-afhandling er dedikeret eksperimentel karakterisering af svagt bundne molekulære komplekser ved hjælp af infrarød spektroskopi. Til

dette formål beskriver vi et nyt eksperimentelt design, der er konstrueret i vores laboratorium til realisering af matrixisolationsspektroskopi af molekyllkomplekser. Især er denne opstilling blevet benyttet til at deponere HCl, H₂O og deutererede isotopologer i inerte neonmatricer til detektion af deres midt-infrarøde spektre. Dette har ført til observationen af spektralovergange associeret med komplekser mellem HCl og H₂O og analoge isotopologer. Til udførelse af disse spektroskopiske eksperimenter i det udfordrende fjern-infrarøde spektralområde præsenteres også opbygningen af et nyt synteseapparat til berigede prøver af para-hydrogen. Den designede instrumentering og software muliggør rutineproduktion af dette inerte materiale med berigelser højere end 99.95%. I fremtiden vil dette blive anvendt på en række fjern-infrarøde undersøgelser, herunder for komplekset mellem HCl og H₂O.

Preface

This thesis has been submitted to the Department of Chemistry, Technical University of Denmark, in partial fulfilment of the requirements for the Ph.D. degree in the subject of chemistry. The work presented herein was carried out from November 2017 to March 2021, under the supervision of Associate Professor Niels E. Henriksen, Associate Professor René W. Larsen, and Professor Klaus B. Møller. In addition, part of the work was carried out during a four-months period from February 2020 to May 2020 at the Institut des Sciences Moléculaires d'Orsay (ISMO) in Orsay, France, under the supervision of Fabien Gatti, Ph.D.

Kongens Lyngby, March 2021



Alexandre Voute

Acknowledgements

Many people contributed to make this thesis possible and I am forever grateful for the help and support that I have received in this adventure.

First, I would like to thank my supervisor Prof. Niels E. Henriksen. Thank you for introducing me to femtochemistry, being my guide in this Ph.D. project, for always being willing to give advice and for the many fruitful scientific discussions. I have definitely learned a lot from you. I would also like to express my gratitude to my co-supervisor Prof. René W. Larsen. Thank you for accompanying me through the world of weakly bound complexes since my early times in Denmark when I was only a M.Sc. student and for always being so encouraging. Our friendly discussions and shared excitement about various scientific (and non-scientific) topics over these years were a great pleasure. I want to thank my co-supervisor Prof. Klaus B. Møller for the attentive and constructive remarks in our discussions throughout the project. Your feedback and sharp observations are always useful. Special thanks to Dr. Fabien Gatti for welcoming me in his department during my stay in France. Thank you for all the invaluable help that you gave me in the (HCl)(HOD) project.

Many thanks to Dr. Dmytro Mihrin for the constructive discussions we had during the development of the instrumentation described in this work as well as for all the help in carrying out the matrix isolation experiments. I thank Dr. Peter W. Jacobsen for the preparatory work on the matrix isolation setup. I want to thank the staff of the AILES beamline at Synchrotron SOLEIL and, in particular, beamline scientist Dr. Laurent Manceron for his guidance in using his cryogenic long path absorption cell. It always feels good to come back to the beamline.

An experimental setup under preparation always looks nice on a computer screen. But if you want it to work in real life you need skilled craftsmen which have the ability to make properly the parts that you need. I am deeply thankful to the staff of the machine shop of the department of Chemistry, in particular to Ishaq Khaliqdad and Andreas Pedersen, who made a wonderful job at producing the mechanical parts we needed. Without them, our labs would severely suffer and the instrumentation described in this thesis would have merely stayed on paper.

I want to thank the DTU Computing Center for the allocation of computational resources at the DTU High Performance Computer which I made extensive use of. I would also like to thank the students who took the courses in Physical Chemistry 3

and Applied Computational Chemistry in 2018 and 2019 for making my time as a teaching assistant an enjoyable experience.

I have been lucky to be surrounded, over these years, by talented graduate students and post-docs, members of the family of theoretical chemists. I want to thank Gianluca Levi, Mats Simmermacher, Jinfang Li, Esben Thomas, Mostafa Abedi, Diptesh Dey, Rasmus Faber, Mátyás Pápai, Shota Tsuru, Marta López Vidal, Torsha Moitra, Daniil Fedotov, Josephine Andersen, Anna-Kristina Schnack-Petersen and Bruno Cabral Tenorio. I admire your work and I did learn a lot from the friendly and engaging scientific discussions.

There are also many friends, inside and outside the department of Chemistry, who I wish to thank for accompanying me along this way. Maxime, Simon, Nicolas, Jérôme, Aurore, Laura, Quentin, Margherita, Alexandra, Svetoslava, Christin, Alina, Yara, Irene, Giorgia, Vanessa, Cecilia, Fabio, Marta (again), Luca L., Luca P., Lilja, Simone, Emilie, Fabrizio, Jakob, Michal, Ulf, Tine, Line, Mikkel and Sofie, thank you for your friendship, support and the good memories of the nice times spent together. I want to thank the Hostachy family for hosting me and supporting me while I was writing parts of this thesis.

I am immensely grateful to my family, for being always extremely supportive in what I do, and for being there when things go wrong. To my mother Cristina, my father Bertrand and my brother Fabio, thank you.

My warmest gratitude goes to you, Suzanne. Even though we have been living far from each other since we met, you have always felt close to me with your unconditional support. From the deep of my heart, thank you.

Scientific contributions

The theoretical work presented in chapter 3 is based on the following manuscript:

A. Voute, F. Gatti, K. B. Møller, and N. E. Henriksen, *Femtochemistry of bimolecular reactions from weakly bound complexes: computational study of the $H + H'OD \longrightarrow H'OH + D/HOD + H'$ exchange reactions*, J. Chem. Phys., in preparation (2021).

The following published manuscripts, related to campaigns at the SOLEIL Synchrotron in the AILES infrared beamline, are not discussed in this thesis:

D. Mihrin, P. W. Jakobsen, **A. Voute**, L. Manceron, and R. W. Larsen, *High-resolution synchrotron terahertz investigation of the large-amplitude hydrogen bond librational band of $(HCN)_2$* , PCCP **20**, 8241–8246, (2018)

D. Mihrin, P. W. Jakobsen, **A. Voute**, L. Manceron, and R. W. Larsen, *High-Resolution Infrared Synchrotron Investigation of $(HCN)_2$ and a Semi-Experimental Determination of the Dissociation Energy D_0* , Chem. Phys. Chem. **20**, 3238–3244, (2019)

Contents

1	Introduction	1
1.1	Femtochemistry	1
1.2	Bimolecular reactions initiated from weakly bound complexes	2
1.3	Intermolecular interactions and weakly bound complexes	3
1.4	Outline of the thesis	4
2	Tools for quantum molecular dynamics	7
2.1	Quantum mechanics: fundamental definitions	7
2.2	The TDSE for the nuclei in a molecule	11
2.3	Description of nuclear configurations in terms of orthogonal vectors	14
2.3.1	Jacobi vectors	19
2.3.2	Radau vectors	20
2.3.3	Combinations of orthogonal vectors	21
2.3.4	Separation of the center of mass motion: the space-fixed frame of reference	21
2.4	Polyspherical coordinates	23
2.4.1	Separation of overall rotation: the body-fixed frame of reference	23
2.4.2	Specification of the angles	25
2.4.3	Summary	27
2.4.4	Separation into subsystems	28
2.5	Molecular vibrations and normal modes	28
2.6	Numerical solution of the TDSE: the MCTDH method	31
3	Study of the $\text{H} + \text{HOD} \rightarrow \text{HOD} + \text{H} / \text{HOH} + \text{D}$ exchange reactions from the $(\text{HCl})(\text{HOD})$ complex	33
3.1	Summary of the manuscript in appendix A	34
3.2	Supplementary information	36
3.2.1	The geometry of the $(\text{HCl})(\text{HOD})$ complex and the definition of the initial state	36
3.2.2	HCl dissociation	39
3.2.3	Derivation of the kinetic energy operator	41

3.2.4	From polyspherical to Cartesian coordinates: evaluation of the potential energy	46
3.3	Additional unreported results	46
3.3.1	Wavepacket propagation at low collision energy	46
3.3.2	Propagation along the angular coordinates	48
3.4	Discussion: the presence of the Cl atom	50
3.4.1	The acceleration of H_a	50
3.4.2	Backscattering of H_a	51
3.5	Conclusion and outlook	52
4	Design of a matrix isolation setup and application to the IR spectroscopy of (HCl)(H₂O) complexes	53
4.1	General concepts	53
4.1.1	Infrared spectroscopy of weakly bound complexes	53
4.1.2	The matrix isolation technique	55
4.2	Design of a matrix deposition setup for FTIR spectroscopy	56
4.2.1	Description of the starting available equipment	57
4.2.2	General requirements and constraints	58
4.2.3	Gate valve	59
4.2.4	Inlet system	61
4.2.5	Complete setup	64
4.3	Application to the FTIR matrix isolation spectroscopy of (HCl)(H ₂ O) in neon	66
4.3.1	Introduction	66
4.3.2	Experimental details	67
4.3.3	Preliminary results	68
4.4	Conclusion and outlook	79
5	Para-hydrogen enrichment setup	81
5.1	Nuclear spin isomers of molecular hydrogen: para-hydrogen and ortho-hydrogen	81
5.2	Para-hydrogen as a host matrix	84
5.3	Catalytic ortho-para hydrogen conversion	85
5.4	Enrichment quality assessment	90
5.5	Outlook	92
6	Conclusion and perspectives	93
A	Manuscript submitted to JCP	95
B	Cartesian coordinates of H + HOD from polyspherical coordinates	117
C	Technical drawings	123

D Spectroscopy of HCl/water complexes: complementary quantum chemical calculations	149
E The bimolecular reaction $\text{Br} + \text{I}_2$ from the complex $(\text{HBr})(\text{I}_2)$	151
Bibliography	153

1

Introduction

1.1 Femtochemistry

In 1999, Ahmed Zewail received his Nobel prize for his works on time-resolved pump-probe spectroscopy of elementary chemical reactions [1], a field that Zewail himself coined *femtochemistry* [2]. With his work, the nuclear motion in molecules could be detected with sub-picosecond ($< 10^{-12}$ s) time resolution. From the early studies in the 1980's on small molecules, the field has continuously expanded and there is still, at the time of writing, active research being carried out, both theoretically and experimentally. The interest in ultrafast phenomena keeps motivating the construction of specialized large-scale facilities like the European X-Ray Free Electron Laser in Hamburg, Germany, in operation since 2017.

The technique of time-resolved pump-probe spectroscopy consists in using pairs of ultra-short laser pulses in order to follow the different stages of the fast transformation of a molecule over time. The first so-called “pump” pulse perturbs it and initiates the process under investigation. The response of the molecule to a second “probe” pulse, delayed with respect to the pump, is measured. By repeating the experiment several times at different delay times between the pump and the probe, one obtains a trace of the time evolution of that response, and thus reveal how the molecule transforms from start to finish.

Elementary chemical reactions are usually categorized into two types. On the one hand, *unimolecular reactions* are those where a single molecule absorbs light and undergoes a transformation because of the resulting gained energy. This type of reactions is the essence of photochemistry. On the other hand, *bimolecular reactions* are those occurring upon collision between two molecules. These are the most common elementary processes in chemical reactions, since they happen simply because the paths of two reactants meet and because they mostly do so in their electronic ground state.

Most works in femtochemistry have focused on unimolecular reactions, whereas

bimolecular reactions have received minor attention [3]. This is mostly due to practical difficulties in applying the pump-probe scheme in the latter which do not arise in the former. Indeed, a unimolecular reaction is initiated by the absorption of a photon and, in femtochemistry experiments, that photon is simply provided by the pump pulse. Thus the “zero of time” in the time-resolved study of such a reaction is well-defined. That is not the case for a bimolecular reactions, since any definition of an “initial distance” at which the collision between two molecules starts would be purely arbitrary. Moreover, the relative orientations and collision energy would also need to be controlled for a clear definition of initial conditions.

1.2 Bimolecular reactions initiated from weakly bound complexes

The difficulties in restricting the geometrical conditions in a bimolecular reaction are not limited to femtochemistry. In fact, this problem was debated even in the context of earlier molecular crossed-beam scattering experiments [4]. A possible solution was suggested by Jouvet & Soep [5, 6] and later by Wittig and coworkers [7–12]. Their idea is to study bimolecular reactions by taking two molecules, noted A–B and C, and forming a so-called *weakly bound complex* of these, A–B···C. The two molecules are brought together through weak intermolecular interactions, ranging from van der Waals forces to the stronger hydrogen-bonds (see below). It is then by irradiating the complex with light that a reaction involving the two moieties is triggered, namely by breaking the A–B covalent bond of the first. As a result, the fragment A is ejected away from the whole system and B is thrown against C. In other words, the bimolecular reaction between B and C is initiated from photodissociation of A–B in the preformed weakly bound complex A–B···C. The advantage obtained from this procedure is that the initial positions and relative orientations of the colliding reactants are defined by the geometry of the starting complex. In addition, the collisional process takes place in the electronic ground state of the system {B + C}, provided that the fragment A is far enough from the two others and that B is released in its electronic ground state.

Zewail and coworkers reused these ideas in their time-resolved spectroscopy experiments, in particular with the complex (HI)···(CO₂) [13, 14]. Using the pump pulse to photodissociate the HI molecule, they could follow the time evolution of the collision between H and CO₂. It is uncertain, though, how the heavy spectator iodine atom – which slowly leaves the rest of the complex – would influence the outcome. Later, similar experiments were carried out with the complex (HBr)···(I₂) [15, 16]. Here, the starting complex is supposed to have the bromine atom pointing towards the iodine molecule. The dissociation of HBr thus leads to the collision between Br and I₂ which proceeds undisturbed by the light hydrogen atom which is, instead, rapidly ejected far away. Note that in both cases, the same pump-probe scheme is used as in unimolecular reactions: the complex can be considered as a “supermolecule”, the pump pulse is a perturbation leading to the dissociation of one of its parts and the

probed phenomenon is the subsequent collision unfolding internally.

Since then, other experiments of this kind were performed by this and other groups [17–22]. Further similar studies relied on a different procedure consisting in inducing the collision via charge transfer between the moieties of the complex upon photoexcitation by the pump pulse [23–28]. To our knowledge, there has not been more experimental investigation on ultrafast dynamics of bimolecular reactions after those referenced here. Albeit substantial, this list of contributions is outnumbered by the studies on unimolecular reactions. In addition, theoretical studies supporting the observations and interpretations is somewhat scarce, in particular from a quantum mechanical point of view. The work presented in this thesis aims at reviving the interest in this type of experiments from a theoretical perspective.

1.3 Intermolecular interactions and weakly bound complexes

In spite of the fact that they take a central place in the time-resolved experiments of bimolecular reactions discussed above, weakly bound complexes are of great importance on their own.

Covalent bonds are essential for the existence of molecules and are the result of electrons sharing between atoms. However, an immense variety of systems existing in Nature rely on other weaker types of interactions between molecules. The secondary structures of proteins, the action of enzymes on specific substrates, the double-stranded helicoid shape of DNA and the way molecules pack with respect to one another in condensed matter are a few examples witnessing the existence of intermolecular forces. The latter are generally categorized into electrostatic, induction and dispersion [29–31].

- *Electrostatic interactions* refer to those between two polar molecules. These are also called “permanent dipole-permanent dipole” interactions. Similar interactions involving higher order permanent electric multipoles belong to this class. When averaged over all molecules in a system at a given temperature, these are called *orientation* or *Keesom interactions*.
- *Induction interactions* involve a polar molecule and a non-polar one. The local electric field cast over the non-polar one provokes a displacement of charges within the latter, thus creating an induced dipole moment. This type of interaction is also named “permanent dipole-induced dipole” interactions or *Debye interaction*.
- Finally, *dispersion interactions* concern all molecules, polar and non-polar. These are purely quantum mechanical but can be interpreted in a classical picture as the mutual interaction between the instantaneous dipole moments within each molecule. Typically these are referred to as “induced dipole-induced dipole” interactions or more frequently *London interactions*.

Keesom, Debye and London interactions form the class of so-called *van der Waals*

interactions [31]. These are all attractive and are proportional to the sixth inverse power of the intermolecular distance, so that they can be qualified as long-range interactions. On the other hand, these are compensated by short-range *exchange repulsion* due to the fermionic nature of the electron [29]. Their superposition gives rise to an equilibrium point, hence establishing a weak bond whose dissociation energy is of the order of 1 to $10 \text{ kJ} \cdot \text{mol}^{-1}$. For comparison, the dissociation energy for a covalent bond ranges between about 200 to $800 \text{ kJ} \cdot \text{mol}^{-1}$ [31].

A special type of weak bond, stronger than the previous ones, is the so-called *hydrogen bond*. Such a bond forms from a molecule containing a hydrogen atom covalently bound to an electronegative one and another molecule with an electronegative atom surrounded by non-bonding electrons. It is noted $\text{X}-\text{H} \cdots \text{Y}$, where X and Y are the electronegative atoms. Hydrogen bonds are of electrostatic nature, where the non-bonding electrons on Y are attracted by the partially positively charged H [30]. As a result, the hydrogen atom is, to some extent, shared between the two electronegative atoms. The dissociation energy of a hydrogen-bond lies in the range between 10 and $40 \text{ kJ} \cdot \text{mol}^{-1}$ [31].

Weakly bound complexes are the smallest units of matter manifesting the weak interactions listed above. They are the result of the encounter between molecules eventually caught by each other via these interactions. Binary complexes are the simplest of these, where only a pair of molecules is bound together. For their small size, they are ideal systems for the characterization of the single weak bond that holds the two moieties together. The study of these is critical for an understanding of macroscopic phenomena stemming from the collective action of weak interactions at the molecular length-scale. Vibrational spectroscopy is a powerful tool which has been long used for the characterization of weakly bound complexes.

In this thesis, we will show the work that has been carried out in the infrared spectroscopy laboratory in our department, namely concerning the development of new experimental setups for the study of these complexes. In addition, we will show an application to the characterization of the complex used in the theoretical study of time-resolved bimolecular reactions.

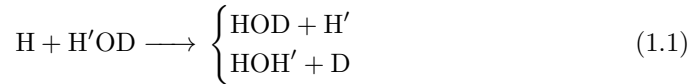
1.4 Outline of the thesis

The present thesis has two components, one theoretical and the other experimental. The former consists in the study of a hypothetical time-resolved spectroscopy experiment where a bimolecular reaction is initiated from a chosen preformed weakly bound complex. The latter focuses on the study of that complex, together with the experimental developments which have led to its characterization. The whole work is summarized in the following four chapters.

Chapter 2 introduces the fundamental concepts of quantum mechanics and molecular quantum dynamics. The problem of describing arbitrary relative positions of N nuclei in a molecule is discussed in detail. In particular, the description in terms of orthogonal vectors and their parametrization in polyspherical coordinates is pre-

sented. A brief overview of the MCTDH method used for the numerical solution of the dynamical equations of motion is given.

Chapter 3 deals with the theoretical study of the exchange reactions:



initiated from the weakly bound complex $(\text{HCl}) \cdots (\text{HOD})$ and by the photodissociation of HCl moiety. The chapter is written in relation to the manuscript submitted to The Journal of Chemical Physics, given in its original form in appendix A. On the one hand, we give here a summary of the main results and some details on points only briefly discussed in the manuscript. On the other hand, additional previously unreported results from this work are given, in particular those that will be included in a further resubmission of the manuscript.

Chapter 4 consists in the description of the design of a new matrix isolation setup that has been constructed for the study of weakly bound complexes via Fourier Transform Infrared spectroscopy. Dimensional drawings of the produced parts of this setup are given in appendix C. Next, we show an application to the characterization of the complex $(\text{HCl}) \cdots (\text{H}_2\text{O})$ and its deuterated isotopologues, thus realizing the connection between the two components of this thesis.

Finally, chapter 5 describes the development of another setup for the enrichment of parahydrogen, a compound which can be used for the study of complexes in the challenging far-infrared region. Dimensional drawings of the produced parts of this setup are also given in appendix C.

Tools for quantum molecular dynamics

2.1 Quantum mechanics: fundamental definitions

The quantum mechanical description of a dynamical phenomenon occurring in a system of mass m living in a one-dimensional space is given by the solution of the *time-dependent Schrödinger equation* (TDSE):

$$i\hbar \frac{\partial \Psi}{\partial t} = \hat{H} \Psi \quad (2.1)$$

This is a partial differential equation where the solution Ψ is a complex-valued function of time t and of the position coordinate x . In quantum mechanics, this is called the *wavefunction* or *state* of the system. In eq. (2.1), i is the imaginary number ($i^2 = -1$) and $\hbar = h/2\pi$ is the *reduced Plank's constant* ($h = 6.62 \cdot 10^{-34}$ J·s is *Plank's constant*). $\partial/\partial t$ denotes the partial derivative with respect to t . More importantly, \hat{H} is the so-called *Hamiltonian operator* (or simply *Hamiltonian*), which is proper to each system to be studied. It is a combination of the *position operator* \hat{q} and the *momentum operator* \hat{p} . These are defined by:

$$\hat{q}\Psi(x, t) = x\Psi(x, t) \quad (2.2)$$

$$\hat{p}\Psi(x, t) = \frac{\hbar}{i} \frac{\partial \Psi}{\partial x}(x, t) \quad (2.3)$$

The Hamiltonian operator is the quantum-mechanical counterpart of the classical Hamiltonian function H which is the total energy of the system. It is the sum of the kinetic energy T (a function of momentum) and the potential energy V (a function of position), i.e. $H(p, q) = T(p) + V(q)$. The Hamiltonian operator \hat{H} is obtained by replacing, in H , the momentum coordinate p and the position coordinates q by the respective operators \hat{p} and \hat{q} . This procedure is known as *quantization*:

$$\begin{aligned} q &\rightarrow \hat{q} \\ p &\rightarrow \hat{p} \end{aligned} \quad (2.4)$$

Concerning the Hamiltonian, we write:

$$\hat{H} = \hat{T} + \hat{V} \quad (2.5)$$

where \hat{T} is the *kinetic energy operator* (KEO) and \hat{V} is the *potential energy operator* (or simply *potential*). These are defined by:

$$\hat{T}\Psi(x, t) = \frac{\hat{p}^2}{2m}\Psi(x, t) = -\frac{\hbar^2}{2m}\frac{\partial^2\Psi}{\partial x^2}(x, t) \quad (2.6)$$

$$\hat{V}\Psi(x, t) = V(x)\Psi(x, t) \quad (2.7)$$

In eq. (2.6), \hat{p}^2 is to be intended as $\hat{p} \circ \hat{p}$ (the binary operation \circ denotes *composition*), which means that the momentum operator is applied twice to the wavefunction. In eq. (2.7), the function $V : x \mapsto V(x)$ is the classical potential function which is specific to the system.

In virtue of their definitions, the position and momentum operators follow the commutation relation:

$$[\hat{q}, \hat{p}] = i\hbar \quad (2.8)$$

where the term on the left-hand side denotes the commutator of \hat{q} and \hat{p} : for any two operators \hat{A} and \hat{B} , their commutator is defined by $[\hat{A}, \hat{B}] := \hat{A}\hat{B} - \hat{B}\hat{A}$.

The wavefunction, solution of eq. (2.1), does not itself have a physical meaning. It is rather the square of its modulus $|\Psi(x, t)|^2$ which can be seen as a *probability density*. More precisely, at a given time t , the probability of finding the system in an infinitesimally small region of space between x and $x + dx$ is:

$$dP(x, t) = |\Psi(x, t)|^2 dx \quad (2.9)$$

This is the so-named *Born interpretation*. This is, among other, one aspect unique to quantum mechanics: the result of a measurement on a quantum system cannot be predicted in a deterministic way but is instead subject to probabilistic uncertainties.

By integrating the probability density over a region between two points a and b , one obtains the probability of finding the system in that region:

$$P_{[a,b]}(t) = \int_a^b |\Psi(x, t)|^2 dx \quad (2.10)$$

In particular, the certainty that the system is *somewhere* is written as:

$$\int_{-\infty}^{\infty} |\Psi(x, t)|^2 dx = 1 \quad (2.11)$$

If the wavefunction fulfils eq. (2.11) at any given time t , it is easy to prove that it will at any other time too.¹ The existence of the improper integral on the left-hand side of eq. (2.11) requires that the wavefunction Ψ must be *square-integrable*.

¹This follows from taking the derivative of the left-hand-side of eq. (2.11) with respect to time and eq. (2.1). For this reason, the TDSE is said to be *unitary*.

Mathematically, this means that the solution to eq. (2.1) must be found within the set of square-integrable functions $L_2(\mathbb{R})$:

$$L_2(\mathbb{R}) = \left\{ f : \mathbb{R} \rightarrow \mathbb{C} \left| \int_{-\infty}^{\infty} |f(x)|^2 dx < \infty \right. \right\} \quad (2.12)$$

Here \mathbb{R} is the set of real numbers which is here the range of definition of the wavefunction.² We associate to the space of functions $L_2(\mathbb{R})$ the following *scalar* or *dot product*:

$$\forall (f, g) \in (L_2(\mathbb{R}))^2, \quad \langle f, g \rangle = \int_{-\infty}^{\infty} \overline{f(x)} g(x) dx \quad (2.13)$$

where the overline denotes complex conjugation. From the dot product we can define a *norm*:

$$\forall f \in (L_2(\mathbb{R})), \quad \|f\| = \sqrt{\langle f, f \rangle} = \sqrt{\int_{-\infty}^{\infty} |f(x)|^2 dx} \quad (2.14)$$

Thus, eq. (2.11) can be written $\|\Psi\| = 1$. Since its norm is 1, why we say that Ψ is *normalized*. Unless otherwise specified, a wavefunction will always be assumed to be so. The space $L_2(\mathbb{R})$ equipped with the dot product in eq. (2.13) is known as a *Hilbert space*.

With the definition of dot product eq. (2.13), we can define what connects operators with their corresponding physically observable quantities. Let \hat{A} be an operator acting on the Hilbert space of wavefunctions. We call *expectation value* of \hat{A} for the system in the state Ψ the quantity:

$$\langle \hat{A} \rangle = \langle \Psi, \hat{A}\Psi \rangle \quad (2.15)$$

We say that the operator \hat{B} is the *adjoint* or *Hermitian conjugate* operator of \hat{A} if and only if, for any pair of wavefunctions (ψ, ϕ) :

$$\langle \psi, \hat{A}\phi \rangle = \langle \hat{B}\psi, \phi \rangle \quad (2.16)$$

we write $\hat{B} = \hat{A}^\dagger$. The operator \hat{A} is said to be *self-adjoint* or *Hermitian* if and only if $\hat{A} = \hat{A}^\dagger$. In quantum mechanics, it is required that operators associated to measurable physical quantities (like position, momentum or energy) are Hermitian. In this way, the expectation value of one such operator is a real number (and can therefore represent the measurement of the physical quantity). The operators \hat{q} , \hat{p} , \hat{T} , \hat{V} and \hat{H} shown above are examples of Hermitian operators.

It is useful at this point to discuss a particular set of solutions of the TDSE called *stationary states*. One such state is written as:

$$\Psi(x, t) = \psi(x)\chi(t) \quad (2.17)$$

²In eqs. (2.11) and (2.12), we have explicitly wrote the bounds of the integral for clarity. However, in the following, we may omit them so as to avoid overcrowding the notation. The underlying meaning is that the integration is carried over the whole range of definition of the integrand.

By plugging eq. (2.17) into the TDSE, one can show that the functions ψ and χ fulfil:

$$\hat{H}\psi = E\psi \quad (2.18)$$

$$\chi(t) = Ce^{-iEt/\hbar} \quad (2.19)$$

where C is an arbitrary complex constant which, for simplicity, can be chosen to be of unit modulus.

Equation (2.18) is the famous *time-independent Schrödinger equation* (TISE). It is an eigenvalue equation, where a solution ψ is an eigenfunction (or *eigenstate*) and E its corresponding eigenvalue (or *eigenenergy*). Equation (2.18), eq. (2.19) and $|C| = 1$ imply that $|\Psi(x, t)| = |\psi(x)|$, i.e. the probability density of a stationary state is constant over time, hence the name. Since Ψ is normalized, ψ is so too.

The solutions (E, ψ) of eq. (2.18) depend on the form of the Hamiltonian \hat{H} . Finding all these is called *diagonalizing* the Hamiltonian. The set of all possible eigenenergies E_n is called the *spectrum* of the Hamiltonian, which we denote $\text{Sp}(\hat{H})$. It is important to note that, since \hat{H} is Hermitian, all its eigenvalues are real, as a consequence of the expectation values of \hat{H} in any eigenstate being real. For most standard textbook problems (particle-in-a-box, harmonic oscillator...) the spectrum $\text{Sp}(\hat{H})$ is a discrete (possibly infinite) set of numbers. We say that the energy of the system is *quantized*: it can only take values listed in $\text{Sp}(\hat{H})$. For discrete spectra we will generally write pairs of eigenvalue-eigenfunction solutions of eq. (2.18) as (E_n, ψ_n) , with $n \in \mathbb{N} = \{0, 1, 2, \dots\}$ and the energies ordered with increasing n . The state corresponding to the lowest eigenenergy is called the *ground state* and the others are the *excited states*.

Another consequence of the Hermiticity of \hat{H} is that pairs of eigenstates associated to different eigenvalues are orthogonal for the dot product eq. (2.13), i.e. for ψ_1 and ψ_2 such that $\hat{H}\psi_1 = E_1\psi_1$, $\hat{H}\psi_2 = E_2\psi_2$ and $E_1 \neq E_2$ we have $\langle \psi_1, \psi_2 \rangle = 0$. In other words, the set of eigenstates of \hat{H} forms an *orthonormal* set of functions:

$$\langle \psi_m, \psi_n \rangle = \delta_{mn} \quad (2.20)$$

where δ_{mn} is the Kronecker delta symbol, which equals 1 if $m = n$ and 0 otherwise.

Thus, any function of the form $\Psi(x, t) = \psi(x)\chi(t)$ such that eqs. (2.18) and (2.19) are fulfilled is a solution of the TDSE. Since that equation is linear (i.e. if Ψ_1 and Ψ_2 are two solutions, then any linear combination of the two is also a solution), then the general solution of the TDSE can be written as:

$$\Psi(x, t) = \sum_{n=0}^{+\infty} c_n \psi_n(x) e^{-iE_n t/\hbar} \quad (2.21)$$

With the expansion coefficients c_n being constant complex numbers determined by the initial conditions (i.e. the form of $\Psi(x, 0)$, the *initial state*). These are given by:

$$c_n = \int \overline{\psi_n(x)} \Psi(x, 0) dx \quad (2.22)$$

Because Ψ and the eigenstates ψ_n are normalized, then necessarily $\sum_{n=0}^{\infty} |c_n|^2 = 1$.

Any solution of the time-dependent Schrödinger equation can therefore be written in the form eq. (2.21). For this reason, a state which is a linear combination (or superposition) of at least two of these stationary states is also called *wavepacket*. Note that it is not a solution of the TISE. However, it is a solution of the TDSE whose probability density curve will change shape over time. The origin of this variation stems from the interferences between the stationary states composing Ψ . This is well illustrated by taking a superposition of only two stationary states. By calculating the corresponding probability density, a non-vanishing time-dependent term appears.

2.2 The time-dependent Schrödinger equation for the nuclei in a molecule

When the object of study is an isolated molecule, made of N nuclei and n_e electrons placed in the three-dimensional space, the wavefunction that describes it is a function $\Phi(\mathbf{r}, \mathbf{R}, t)$ of the $3n_e$ electronic position coordinates \mathbf{r} and the $3N$ nuclear position coordinates \mathbf{R} .

Its Hamiltonian reads:

$$\hat{H} = \hat{T}_{\text{nu}} + \hat{T}_{\text{e}} + \hat{V}_{\text{nu-nu}} + \hat{V}_{\text{nu-e}} + \hat{V}_{\text{e-e}} \quad (2.23)$$

The terms on the right-hand-side of eq. (2.23) are, from left to right: the kinetic energy of the nuclei, the kinetic energy of the electrons, the Coulomb repulsion potential between nuclei, the Coulomb attraction potential between nuclei and electrons and finally the Coulomb repulsion potential between electrons. More specifically, these are defined by:

$$\hat{T}_{\text{nu}} = \sum_{\alpha=1}^N \frac{\hat{\mathbf{P}}_{\alpha}^2}{2M_{\alpha}} \quad (2.24)$$

$$\hat{T}_{\text{e}} = \sum_{j=1}^{n_e} \frac{\hat{\mathbf{p}}_j^2}{2m_e} \quad (2.25)$$

$$\hat{V}_{\text{nu-nu}} = \sum_{\alpha=1}^N \sum_{\beta=\alpha+1}^N \frac{Z_{\alpha} Z_{\beta} e^2}{4\pi\epsilon_0 \|\hat{\mathbf{R}}_{\alpha} - \hat{\mathbf{R}}_{\beta}\|} \quad (2.26)$$

$$\hat{V}_{\text{nu-e}} = - \sum_{\alpha=1}^N \sum_{j=1}^{n_e} \frac{Z_{\alpha} e^2}{4\pi\epsilon_0 \|\hat{\mathbf{R}}_{\alpha} - \hat{\mathbf{r}}_j\|} \quad (2.27)$$

$$\hat{V}_{\text{e-e}} = \sum_{j=1}^{n_e} \sum_{j'=j+1}^{n_e} \frac{e^2}{4\pi\epsilon_0 \|\hat{\mathbf{r}}_j - \hat{\mathbf{r}}_{j'}\|} \quad (2.28)$$

and:

- M_α is the mass of nucleus α
- $\hat{\mathbf{P}}_\alpha = (\hat{P}_{\alpha,x}, \hat{P}_{\alpha,y}, \hat{P}_{\alpha,z})$ is the linear momentum operator of nucleus α , with $\hat{\mathbf{P}}_\alpha^2 = \hat{P}_{\alpha,x}^2 + \hat{P}_{\alpha,y}^2 + \hat{P}_{\alpha,z}^2$
- $m_e = 9.11 \cdot 10^{-31}$ kg is the mass of the electron
- $\hat{\mathbf{p}}_j = (\hat{p}_{j,x}, \hat{p}_{j,y}, \hat{p}_{j,z})$ is the linear momentum operator of electron j , with $\hat{\mathbf{p}}_j^2 = \hat{p}_{j,x}^2 + \hat{p}_{j,y}^2 + \hat{p}_{j,z}^2$
- $\hat{\mathbf{R}}_\alpha = (\hat{R}_{\alpha,x}, \hat{R}_{\alpha,y}, \hat{R}_{\alpha,z})$ denotes the triplet of Cartesian coordinate position operators of nucleus α
- $\hat{\mathbf{r}}_j = (\hat{r}_{j,x}, \hat{r}_{j,y}, \hat{r}_{j,z})$ denotes the triplet of Cartesian coordinate position operators of electron j
- $e = 1.60 \cdot 10^{-19}$ C is the elementary charge
- Z_α is the nuclear charge of nucleus α in multiples of e
- $\varepsilon_0 = 8.85 \cdot 10^{-12}$ F \cdot m⁻¹ is the electrical permittivity of vacuum.
- $\|\cdot\|$ denotes here the length of its argument

Solving the TDSE with such Hamiltonian is a hard task and no analytical solution can be found for the full nuclear and electronic wavefunction Φ . Owing to the fact that electrons are much heavier than the nuclei, the first approximation that is usually made is to separate the motion of the two groups of particles. One considers first the nuclei as fixed in one configuration \mathbf{R} from the perspective of the electrons and solves the time-independent Schrödinger equation for these:

$$\hat{H}_e(\mathbf{R})\psi(\mathbf{r}; \mathbf{R}) = E(\mathbf{R})\psi(\mathbf{r}; \mathbf{R}) \quad (2.29)$$

where $\hat{H}_e(\mathbf{R})$ is the *electronic Hamiltonian* which groups the four terms in eqs. (2.25) to (2.28):

$$\hat{H}_e(\mathbf{R}) := \hat{T}_e + \hat{V}_{\text{nu-nu}}(\mathbf{R}) + \hat{V}_{\text{nu-e}}(\mathbf{R}) + \hat{V}_{e-e} \quad (2.30)$$

and $\psi(\mathbf{r}; \mathbf{R})$ is an *electronic eigenstate* with corresponding eigenenergy $E(\mathbf{R})$. As indicated, the electronic Hamiltonian, eigenstates and eigenenergies depend *parametrically* on the nuclear configuration. Solving eq. (2.29) does not have solutions in closed form (except for hydrogenoid atoms and H_2^+) but methods belonging to the field of *electronic structure quantum chemistry* have been widely developed for this task.

We assume the existence of a set of orthonormal solutions $\psi_n(\mathbf{r}; \mathbf{R})$, each with a corresponding eigenvalue $E_n(\mathbf{R})$, for any value of the nuclear coordinates \mathbf{R} . We look now to the nuclear part of the problem. The total wavefunction is written in the following form, known as *Born-Huang expansion* [32, 33]:

$$\Phi(\mathbf{r}, \mathbf{R}, t) = \sum_{n=0}^{\infty} \psi_n(\mathbf{r}; \mathbf{R}) \Psi_n(\mathbf{R}, t) \quad (2.31)$$

This expansion can be seen as a particular case of eq. (2.21), where the functions $\Psi_n(\mathbf{R}, t)$ play the role of expansion coefficients c_n times the imaginary exponential, yet parametrically dependent on the nuclear configuration. By plugging eq. (2.31) into the full TDSE and using eq. (2.30), one has:

$$i\hbar \sum_{n=0}^{\infty} \psi_n(\mathbf{r}; \mathbf{R}) \frac{\partial \Psi_n}{\partial t}(\mathbf{R}, t) = \sum_{n=0}^{\infty} \hat{T}_{\text{nu}} [\psi_n(\mathbf{r}; \mathbf{R}) \Psi_n(\mathbf{R}, t)] + \sum_{n=0}^{\infty} \hat{H}_e(\mathbf{R}) [\psi_n(\mathbf{r}; \mathbf{R}) \Psi_n(\mathbf{R}, t)] \quad (2.32)$$

The terms in the first sum on the right-hand side are:

$$\begin{aligned} \hat{T}_{\text{nu}} [\psi_n(\mathbf{r}; \mathbf{R}) \Psi_n(\mathbf{R}, t)] &= -\frac{\hbar^2}{2} \sum_{\alpha=1}^N \frac{1}{M_\alpha} \nabla_\alpha^2 [\psi_n(\mathbf{r}; \mathbf{R}) \Psi_n(\mathbf{R}, t)] \\ &= -\frac{\hbar^2}{2} \sum_{\alpha=1}^N \frac{1}{M_\alpha} \left(\psi_n(\mathbf{r}; \mathbf{R}) \nabla_\alpha^2 \Psi_n(\mathbf{R}, t) \right. \\ &\quad \left. + 2 \nabla_\alpha \psi_n(\mathbf{r}; \mathbf{R}) \cdot \nabla_\alpha \Psi_n(\mathbf{R}, t) \right. \\ &\quad \left. + \Psi_n(\mathbf{R}, t) \nabla_\alpha^2 \psi_n(\mathbf{r}; \mathbf{R}) \right) \\ &= \psi_n(\mathbf{r}; \mathbf{R}) \hat{T}_{\text{nu}} \Psi_n(\mathbf{R}, t) + \Psi_n(\mathbf{R}, t) \hat{T}_{\text{nu}} \psi_n(\mathbf{r}; \mathbf{R}) \\ &\quad - \hbar^2 \sum_{\alpha=1}^N \frac{1}{M_\alpha} \nabla_\alpha \psi_n(\mathbf{r}; \mathbf{R}) \cdot \nabla_\alpha \Psi_n(\mathbf{R}, t) \end{aligned} \quad (2.33)$$

where ∇_α denotes the gradient with respect to $(R_{\alpha,x}, R_{\alpha,y}, R_{\alpha,z})$ and \cdot the canonical dot product in \mathbb{R}^3 . The terms in the second sum on the right-hand side of eq. (2.32) simply are:

$$\hat{H}_e(\mathbf{R}) [\psi_n(\mathbf{r}; \mathbf{R}) \Psi_n(\mathbf{R}, t)] = E_n(\mathbf{R}) \psi_n(\mathbf{r}; \mathbf{R}) \Psi_n(\mathbf{R}, t) \quad (2.34)$$

Thus, by projecting eq. (2.32) along any eigenstate ψ_k (the integration is carried over the electronic coordinates \mathbf{r}), one obtains:

$$i\hbar \frac{\partial \Psi_k}{\partial t}(\mathbf{R}, t) = \left(\hat{T}_{\text{nu}} + E_k(\mathbf{R}) \right) \Psi_k(\mathbf{R}, t) + \sum_{n=0}^{\infty} \left(\hat{A}_{kn}(\mathbf{R}) + \hat{B}_{kn}(\mathbf{R}) \right) \Psi_n(\mathbf{R}, t) \quad (2.35)$$

where $\hat{A}_{kn}(\mathbf{R})$ is a multiplicative operator:

$$\hat{A}_{kn}(\mathbf{R}) = \int \overline{\psi_k(\mathbf{r}; \mathbf{R})} \hat{T}_{\text{nu}} \psi_n(\mathbf{r}; \mathbf{R}) d\mathbf{r} \quad (2.36)$$

and $\hat{B}_{kn}(\mathbf{R})$ is a differential operator:

$$\hat{B}_{kn}(\mathbf{R}) \Psi_n(\mathbf{R}, t) = -\hbar^2 \sum_{\alpha=1}^N \frac{1}{M_\alpha} \int \overline{\psi_k(\mathbf{r}; \mathbf{R})} (\nabla_\alpha \psi_n(\mathbf{r}; \mathbf{R}) \cdot \nabla_\alpha \Psi_n(\mathbf{R}, t)) d\mathbf{r} \quad (2.37)$$

Neglecting the last sum in eq. (2.35) is the so-called *Born-Oppenheimer approximation*, which yields:

$$i\hbar \frac{\partial \Psi_k}{\partial t}(\mathbf{R}, t) = \left(\hat{T}_{\text{nu}} + E_k(\mathbf{R}) \right) \Psi_k(\mathbf{R}, t) \quad (2.38)$$

This equation appears to be the TDSE, where $E_k(\mathbf{R})$ plays the role of the potential operator and is thus called *potential energy surface* (PES) of the k^{th} electronic state. Its solution Ψ_k is interpreted as the *nuclear wavefunction* describing the motion of the nuclei under the influence of the PES of the state k .

We will briefly mention that the neglected terms in the sum in eq. (2.35) are so-called *non-adiabatic couplings* between electronic states. Depending on their magnitude, these allow the nuclear wavefunction to transit from an electronic state PES to the other. Generally, these quantities can be discarded when dealing with processes occurring in regions where the PES's are well separated. Conversely, they become crucial if PES's come close in energy. The latter scenario will not be considered in the present thesis.

2.3 Description of nuclear configurations in terms of orthogonal vectors

In classical mechanics, the most primitive specification of the state of a system of N points of masses m_i in a one-dimensional space³ is given by the knowledge of Cartesian position coordinates x_i in a laboratory-fixed frame of reference (LF) and the corresponding momenta $p_i = m_i \dot{x}_i$, where the dot over a coordinate denotes its derivative with respect to time. The kinetic energy is given by $T = \sum_i p_i^2 / 2m_i = \sum_i m_i \dot{x}_i^2 / 2$ and the potential V is simply a real-valued function of the x_i .

However, Cartesian coordinates with respect to LF are usually not the most convenient to use when dealing with an *isolated* system. One reason is that, in this case, the potential is invariant upon translation of the system as a whole, i.e. if we displace all the points by a constant amount a , we obtain:

$$V(x_1 + a, \dots, x_N + a) = V(x_1, \dots, x_N) \quad (2.39)$$

Therefore, the potential depends only on the *relative* position of each point with respect to the others, regardless of the position of the system of points as a whole.

We may then want to specify, instead of the primitive positions x_i and momenta p_i , another set of coordinates R_i and associated momenta P_i such that:

- R_N is associated to a point describing the motion of the system as a whole, so that the potential is independent of it,
- The other R_i 's, with $i \in \{1, \dots, N - 1\}$, describe the relative positions of the N points.

³The generalization to three dimensions is easy, as we will see.

The usual choice for R_N is the center of mass of the whole system. On the other hand, an intuitive choice for the other R_i 's would be a set of pairwise distances between the single points. However, this choice suffers from bringing complications concerning the kinetic energy. For example, if $N = 3$, we may choose:

$$\begin{aligned} R_1 &= x_2 - x_1 \\ R_2 &= x_3 - x_2 \\ R_3 &= m_1 x_1 + m_2 x_2 + m_3 x_3 \end{aligned} \tag{2.40}$$

With this choice, the kinetic energy in terms of velocities reads:

$$T = \frac{1}{2}\mu_{1-23}\dot{R}_1^2 + \frac{1}{2}\mu_{3-12}\dot{R}_2^2 + \frac{m_1 m_3}{M}\dot{R}_1 \dot{R}_2 + \frac{1}{2}M\dot{R}_3^2 \tag{2.41}$$

with $M = m_1 + m_2 + m_3$, $\mu_{1-23}^{-1} = m_1^{-1} + (m_2 + m_3)^{-1}$ and $\mu_{3-12}^{-1} = m_3^{-1} + (m_1 + m_2)^{-1}$.

The new expression of the kinetic energy is therefore somewhat similar to the original one, i.e. half of the sum of masses times squared velocities. The kinetic energy of the center of mass is the last term in eq. (2.41) and is the only one in the total energy concerning this point. The other three terms deserve a more attentive analysis. The first two look simple: they can be interpreted as the kinetic energies of two point particles with masses μ_{1-23} and μ_{3-12} , respectively. However, the third term is, up to a mass factor, a product of the velocities of these two particles. Their kinetic energies are thus coupled.

In view of quantization, it is desirable to have the expression in terms of momenta. For a given coordinate R_i we define a conjugate momentum P_i which is obtained by taking the derivative of the kinetic energy with respect to the i^{th} velocity:⁴

$$P_i = \frac{\partial T}{\partial \dot{R}_i} \tag{2.42}$$

However, the resulting momenta are ‘‘polluted’’ by the coupling term. After tedious algebra, one arrives at the expression:

$$T = \frac{P_1^2}{2\mu_{12}} + \frac{P_2^2}{2\mu_{23}} - \frac{P_1 P_2}{m_2} + \frac{P_3^2}{2M} \tag{2.43}$$

where $\mu_{12}^{-1} = m_1^{-1} + m_2^{-1}$ and $\mu_{23}^{-1} = m_2^{-1} + m_3^{-1}$. Notice that the masses at the denominators in eq. (2.43) are not the same as in the factors in eq. (2.41), in particular for in the coupling term. The algebraic manipulations necessary to obtain eq. (2.43) from eq. (2.41) are non-trivial because of that term. Moreover, the expression in the momenta looks as if it concerned different fictitious point particles than in eq. (2.41), with respective masses μ_{12} and μ_{23} .

⁴More generally, these should be the derivatives of the Lagrangian $\mathcal{L} = T - V$, but here the potential does not depend on the \dot{R}_i 's.

In the most general way, the definition of the $N - 1$ relative position coordinates R_i , whichever it may be,⁵ will lead to the appearance of at most $N(N - 1)/2$ of these coupling terms. These may become problematic in solving dynamical equations of motion (classical or quantum) because of their growing number and their form. In addition, they may not be readily interpretable from a physical point of view.

It is however possible to carefully choose a definition of the relative configuration coordinates such that the kinetic energy does not contain these coupling terms. Such a kinetic energy is then said to be *diagonal* in the velocities (or, equivalently, linear momenta), i.e. a linear combination of the square of these. As we will see, the key of such a definition of the new coordinates is an orthogonal transformation [34]. The resulting coordinates are called, somewhat misleadingly,⁶ *orthogonal coordinates*. What we seek is a linear transformation \tilde{A} :

$$(R_1, \dots, R_N) = \tilde{A}(x_1, \dots, x_N)$$

$$\forall i \in \{1, \dots, N\}, \quad R_i = \sum_{j=1}^N \tilde{A}_{ij} x_j \quad (2.44)$$

and coefficients μ_i , with $i \in \{1, \dots, N\}$, such that:

$$T = \sum_{i=1}^N \frac{1}{2} m_i \dot{x}_i^2 = \sum_{i=1}^N \frac{1}{2} \mu_i \dot{R}_i^2 \quad (2.45)$$

Thanks to this transformation, the kinetic energy of the system of N original particles with masses m_i can also be seen as that of N *fictitious particles* with masses μ_i .

The first step is to scale the coordinates x_i and R_i by the square-root of the mass of each particle, respectively m_i and μ_i (to obtain so-called *mass-weighted coordinates*):

$$x'_i = \sqrt{m_i} x_i \quad (2.46)$$

$$R'_i = \sqrt{\mu_i} R_i \quad (2.47)$$

As a consequence:

$$T = \frac{1}{2} \sum_{i=1}^N \dot{x}'_i{}^2 = \frac{1}{2} \sum_{i=1}^N \dot{R}'_i{}^2 \quad (2.48)$$

and, in relation to eq. (2.44):

$$\forall i \in \{1, \dots, N\}, \quad R'_i = \sum_{j=1}^N \frac{\sqrt{\mu_i}}{\sqrt{m_j}} \tilde{A}_{ij} x'_j = \sum_{j=1}^N A_{ij} x'_j \quad (2.49)$$

⁵The minimal requirement here is that it must be a linear transformation of the x_i and that the resulting R_i are linearly independent.

⁶They have nothing to do with geometrical perpendicularity or orthogonal coordinates in tensorial calculus. . .

Equation (2.49) defines the linear transformation A between the two sets of mass-weighted coordinates.

Now we focus on the sums in eq. (2.48). In doing this, we recall the definition of the canonical dot product in \mathbb{R}^N , the space of N -tuples. For any two members $\mathbf{x} = (x_1, \dots, x_N)$ and $\mathbf{y} = (y_1, \dots, y_N)$ of \mathbb{R}^N , this is given by:

$$\langle \mathbf{x}, \mathbf{y} \rangle = \sum_{i=1}^n x_i y_i \quad (2.50)$$

The induced norm is:

$$\|\mathbf{x}\| = \sqrt{\langle \mathbf{x}, \mathbf{x} \rangle} \quad (2.51)$$

Now, if we consider $\mathbf{x}' = (x'_1, \dots, x'_N)$ and $\mathbf{R}' = (R'_1, \dots, R'_N)$ as elements of \mathbb{R}^N , the sums in eq. (2.48) can be seen as the squares of the norms of $\dot{\mathbf{x}}'$ and $\dot{\mathbf{R}}'$ respectively, that is:

$$2T = \|\dot{\mathbf{x}}'\|^2 = \|\dot{\mathbf{R}}'\|^2 \quad (2.52)$$

and in particular using eq. (2.49), since A does not depend on time:

$$\|\dot{\mathbf{x}}'\| = \|A(\dot{\mathbf{x}}')\| \quad (2.53)$$

Equation (2.53) is valid for any arbitrary values of the \dot{x}'_i 's. Hence, it shows that the linear transformation A that we are looking for must have the special property of *preserving the norm* $\|\cdot\|$. It can be shown that such a linear transformation equivalently preserves the dot product:

$$\langle A(\mathbf{x}), A(\mathbf{y}) \rangle = \langle \mathbf{x}, \mathbf{y} \rangle \quad (2.54)$$

for any arbitrary \mathbf{x} and \mathbf{y} in \mathbb{R}^N .

A linear transformation that preserves the dot product is, by definition, an *orthogonal transformation*. Note that such a transformation is not unique. More specifically, orthogonal transformations in \mathbb{R}^2 and \mathbb{R}^3 are better known as *rotation matrices*. This is why, in the context of orthogonal coordinates, the possible N -dimensional orthogonal transformations as in eq. (2.49) verifying eq. (2.53) are called *kinematic rotations* [34]. In other words, the orthogonal coordinates R_i are obtained by a kinematic rotation of the x_i .

All of the discussion carried out in this section seamlessly extends to systems of N points in the three-dimensional space, where the position of each is specified by a vector \vec{X}_i with coordinates (x_i, y_i, z_i) in the frame LF. From these, we apply the same procedure (mass-weighting of the coordinates and application of the chosen kinematic rotation) to each of the three N -tuples (x_1, \dots, x_N) , (y_1, \dots, y_N) and (z_1, \dots, z_N) to obtain the new N -tuples (R_{x1}, \dots, R_{xN}) , (R_{y1}, \dots, R_{yN}) and (R_{z1}, \dots, R_{zN}) . Each triplet (R_{xi}, R_{yi}, R_{zi}) gives therefore the Cartesian coordinates of a vector \vec{R}_i . The vectors \vec{R}_i are called, reusing the previous appellation, *orthogonal vectors*.⁷ We then

⁷Again, this does not mean that they are mutually perpendicular. The name “orthogonal”, as we have seen, stems from the definition via an orthogonal transformation.

have:

$$T = \sum_{i=1}^N \frac{1}{2} m_i \dot{\vec{X}}_i \cdot \dot{\vec{X}}_i = \sum_{i=1}^N \frac{1}{2} \mu_i \dot{\vec{R}}_i \cdot \dot{\vec{R}}_i \quad (2.55)$$

where here the dot binary operator \cdot denotes the dot product in the physical three-dimensional space, so that we have e.g. $\dot{\vec{X}}_i \cdot \dot{\vec{X}}_i = \dot{x}_i^2 + \dot{y}_i^2 + \dot{z}_i^2$.

In view of the application of these concepts in quantum mechanics, we will rewrite the kinetic energy in terms of momenta. The diagonal form of the kinetic energy in the velocities saves us a lot of work: from eq. (2.42) and eq. (2.55), we readily obtain $\vec{p}_i = m_i \dot{\vec{X}}_i$ and $\vec{P}_i = \mu_i \dot{\vec{R}}_i$. Thus, the kinetic energy simply translates into:

$$T = \sum_{i=1}^N \frac{\vec{p}_i \cdot \vec{p}_i}{2m_i} = \sum_{i=1}^N \frac{\vec{P}_i \cdot \vec{P}_i}{2\mu_i} \quad (2.56)$$

Although presented from the perspective of classical mechanics, the concept of orthogonal vectors diagonalizing the kinetic energy are equally applicable to the quantum mechanical formulation of the kinetic energy operator. One can safely use the quantization rule as in eq. (2.4) [35]:

$$\vec{P}_i \rightarrow \hat{P}_i = \frac{\hbar}{i} \nabla_{\mathbf{R}_i} \quad (2.57)$$

where $\nabla_{\mathbf{R}_i}$ is the usual gradient in the Cartesian coordinates of the vector \vec{R}_i . The quantization rule holds since orthogonal vectors are linear combinations of the positions vectors of the nuclei expressed in Cartesian coordinates in the laboratory frame. Alternatively, one can start from the kinetic energy of the N nuclei given in the original momenta operators $\hat{p}_i = -i\hbar \nabla_{\mathbf{X}_i}$ and apply the chain rule to arrive at the same result.

Orthogonal vectors that are used in the literature are essentially of two types: Jacobi vectors (which are the most widely used) and Radau vectors (which have gained popularity more recently). In the following we will shortly define them. Note that combinations of these are possible, as will be discussed.

2.3.1 Jacobi vectors

One type of orthogonal vectors are *Jacobi vectors* which are defined by [36, 37]:

$$\begin{aligned}
 \vec{R}_1 &= \vec{X}_2 - \vec{X}_1 \\
 \vec{R}_2 &= \vec{X}_3 - \frac{m_1 \vec{X}_1 + m_2 \vec{X}_2}{m_1 + m_2} \\
 \vec{R}_3 &= \vec{X}_4 - \frac{m_1 \vec{X}_1 + m_2 \vec{X}_2 + m_3 \vec{X}_3}{m_1 + m_2 + m_3} \\
 &\vdots \\
 \vec{R}_{N-1} &= \vec{X}_N - \frac{\sum_{i=1}^{N-1} m_i \vec{X}_i}{\sum_{i=1}^{N-1} m_i} \\
 \vec{R}_N &= \frac{\sum_{i=1}^N m_i \vec{X}_i}{\sum_{i=1}^N m_i}
 \end{aligned} \tag{2.58}$$

$$\tag{2.59}$$

or, in more compact form, for the first $N - 1$ vectors:

$$\forall i \in \{1, \dots, N - 1\}, \quad \vec{R}_i = \vec{X}_{i+1} - \frac{\sum_{j=1}^i m_j \vec{X}_j}{\sum_{j=1}^i m_j} \tag{2.60}$$

Jacobi vectors have a simple geometrical interpretation. The first one is simply the distance vector between point 1 and 2. The following one starts from the center of mass of 1 and 2 and ends at point 3. The following one starts from the center of mass of 1, 2 and 3 and ends at point 4, etc... In general, the i^{th} vector starts from the center of mass of the first i points and ends at the $(i + 1)^{\text{th}}$ point. The last vector, \vec{R}_N , is the position of the center of mass.

The effective mass μ_i (for $i < N$) that is associated to each Jacobi vector \vec{R}_i is the reduced mass between the starting group of i points and that of the $(i + 1)^{\text{th}}$ endpoint:

$$\mu_i^{-1} = m_{i+1}^{-1} + M_i^{-1} \tag{2.61}$$

with $M_i = \sum_{j=1}^i m_j$. The effective mass associated to the center of mass is the total mass $M = M_N$. With the definitions in eqs. (2.58) and (2.61), the orthogonal kinematic rotation matrix (eq. (2.49)) which transforms the mass-weighted nuclear position vectors into effective-mass-weighted Jacobi vectors is defined by [34]:

$$\forall (i, j) \in \{1, \dots, N - 1\} \times \{1, \dots, N\}, \quad A_{ij} = \begin{cases} -\sqrt{\frac{m_j m_{i+1}}{M_i M_{i+1}}} & \text{if } j \leq i \\ \sqrt{\frac{M_i}{M_{i+1}}} & \text{if } j = i + 1 \\ 0 & \text{if } j > i + 1 \end{cases} \tag{2.62}$$

$$\forall j \in \{1, \dots, N\}, \quad A_{Nj} = \sqrt{\frac{m_j}{M}} \quad (2.63)$$

An illustration of Jacobi vectors is given in fig. 2.1a.

2.3.2 Radau vectors

Radau vectors, also known as *modified heliocentric* vectors [38, 39], are another type of orthogonal vectors which are particularly adapted when, among the set of N nuclei, there is one which is substantially heavier than the other $N - 1$. These vectors are named after Radau who first defined them in his studies of the orbital motion of planets around the Sun. Radau vectors are essentially distance vectors from one particular point (called *canonical center*) close to the designated heavy nucleus (the *heliocenter*) to each of the light ones (the *satellites*). Figure 2.1b shows an example where Radau vectors are used to describe the relative positions of the nuclei in a tetra-atomic system. The canonical center will be called K and it is defined as follows. Let O be the point associated to the heliocenter which we assume to be the N^{th} nucleus. Let G be the center of mass of all the N nuclei. Let the positions of these points in the laboratory frame be \vec{X}_O and \vec{X}_G , respectively. Then, the position of the canonical center \vec{X}_K is defined such that:

$$\vec{X}_G - \vec{X}_O = (1 + \alpha_O) (\vec{X}_K - \vec{X}_O) \quad (2.64)$$

with

$$\alpha_O = \sqrt{\frac{m_O}{M}} \quad (2.65)$$

with M the total mass of the molecule. It turns out that with this definition, the canonical point has a geometrical meaning. If we call D the center of mass of the $N - 1$ satellites, then the length of the segment $[KD]$ is the geometrical mean of those of $[OD]$ and $[GD]$, i.e. $KD^2 = OD \cdot GD$.

Given the position of the canonical center \vec{X}_K , the Radau vectors are simply:

$$\forall i \in \{1, \dots, N - 1\}, \quad \vec{R}_i = \vec{X}_i - \vec{X}_K \quad (2.66)$$

and \vec{R}_N is again the position of the center of mass of the molecule as in eq. (2.59). Each Radau vectors in eq. (2.66) is defined along with the associated effective mass, which is simply the mass of corresponding pointed satellite:

$$\forall i \in \{1, \dots, N - 1\}, \quad \mu_i = m_i \quad (2.67)$$

Again, the effective mass associated to \vec{R}_N is that of the molecule, M .

The definitions eqs. (2.66) and (2.67) are given as a result of an orthogonal transformation (in the sense of eq. (2.49)) whose matrix elements are:

$$\forall (i, j) \in \{1, \dots, N - 1\}^2, \quad A_{ij} = \delta_{ij} - \frac{\alpha_i \alpha_j}{\alpha_O + 1} \quad (2.68)$$

and

$$\forall j \in \{1, \dots, N\}, \quad A_{Nj} = A_{jN} = \alpha_j \quad (2.69)$$

with

$$\forall i \in \{1, \dots, N\}, \quad \alpha_i = \sqrt{\frac{m_i}{M}} \quad (2.70)$$

Note that $\alpha_N = \alpha_O$.

2.3.3 Combinations of orthogonal vectors

One is not necessarily bound to choose exclusively one or another type of orthogonal vectors. Combinations of these are possible by selecting a subset of n nuclei among the N of the whole molecule. The position vectors of these n nuclei can then be transformed to orthogonal vectors of a given type. From the point of view of the other $N - n$ nuclei, this subsystem can be simply represented by its center of mass carrying the mass of the subsystem. Another set of orthogonal vectors can then be used to represent the configuration of the supersystem of $N - n + 1$ points ($N - n$ nuclei not contained in the subsystem plus the center of mass of the latter). Figure 2.1c shows an example of how a mixture of Radau and Jacobi vectors can be used to characterize the relative positions of several atoms. This approach can be repeatedly applied as many times as desired on selected subsets of points. The kinetic energy is still guaranteed to have a “diagonal” form. An application of this strategy will be given in chapter 3.

2.3.4 Separation of the center of mass motion: the space-fixed frame of reference

The vector \vec{R}_N will always be chosen to be, whichever the choice of the other orthogonal or non-orthogonal vectors, that pointing to the center of mass of the whole molecule. The potential energy of the isolated molecule is invariant with respect to \vec{R}_N . The kinetic energy term associated to it is simply $P_N^2/2M$ and is uncorrelated to the relative motion described by the other vectors. In other words, the center of mass will move in the LF frame as a free particle whose equations of motion can be solved analytically.

It is then convenient to define a *space-fixed* (SF) frame of reference whose origin is located at the center of mass and whose axes are parallel to those of the LF frame. From the definition, the SF frame is an inertial frame of reference and the kinetic energy associated to the center of mass motion, i.e. to \vec{R}_N , is simply zero when expressed in it. Thus, in the SF frame, the total Hamiltonian is free of terms involving \vec{R}_N . The wavefunction can then be described as a function of $\vec{R}_1, \dots, \vec{R}_{N-1}$ only. In other words, we can reduce the dimensionality of the problem at hand from $3N$ to $3N - 3$ degrees of freedom by not including the center of mass in the description.

We take the advantage of this reduction and henceforth formulate the problem of the motion of N isolated nuclei of a molecular system in its SF frame of reference.

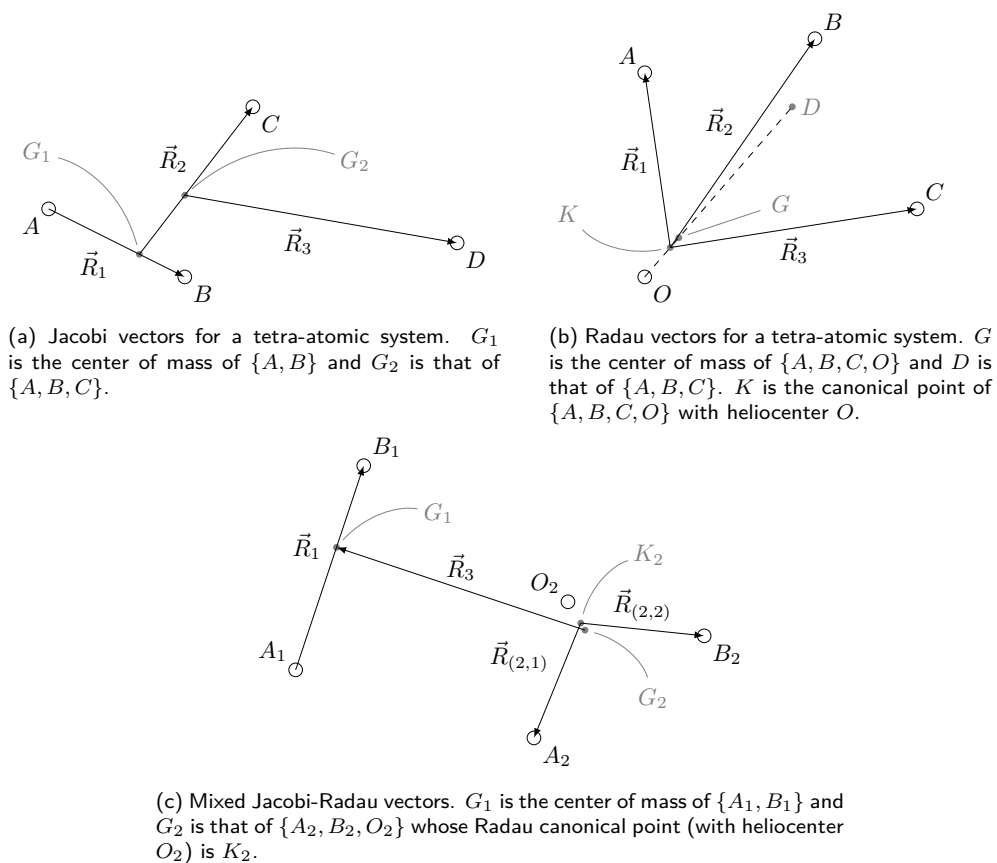


Figure 2.1: Various examples of orthogonal vectors characterizing the relative positions of N nuclei and for which the kinetic energy is diagonal in the corresponding conjugate momenta.

2.4 Polyspherical coordinates

By the term *polyspherical coordinates* [40–47] we designate a set of spherical coordinates representing a set of $N - 1$ relative position vectors in a given frame of reference. In other words, each vector \vec{R}_i , with $i \in \{1, \dots, N - 1\}$, is defined with a triplet of three coordinates (R_i, θ_i, ϕ_i) , i.e. a radial distance from the origin, a polar angle with respect to an axis and an azimuthal angle around that axis, with $0 \leq R_i$, $0 \leq \theta_i \leq \pi$ and $0 \leq \phi_i < 2\pi$:

$$\forall i \in \{1, \dots, N - 1\}, \quad \vec{R}_i \rightarrow (R_i, \theta_i, \phi_i) \quad (2.71)$$

Polyspherical coordinates belong to the class of *curvilinear coordinates*, that is, the map that defines them in terms of the original Cartesian coordinates is not linear. In order to be more specific about what are the axes from which the angles are measured, we first introduce an additional frame of reference describing the overall orientation of the molecule.

2.4.1 Separation of overall rotation: the body-fixed frame of reference

In section 2.3.4 we have specified the SF frame of reference and dropped, by its construction, the contribution of the center of mass G to the kinetic energy. An additional simplification of the description of the nuclear motion in a molecule is brought by the separation between its overall rotation and its deformation. Such a distinction takes the advantage that the potential energy is also invariant under change of orientation of the molecule (it is *isotropic*). Indeed, if such transformation in the three-dimensional space is called \mathcal{R} , we have:

$$V(\mathcal{R}(\vec{R}_1), \dots, \mathcal{R}(\vec{R}_{N-1})) = V(\vec{R}_1, \dots, \vec{R}_{N-1}) \quad (2.72)$$

where the vectors \vec{R}_i , $i \in \{1, \dots, N - 1\}$ are orthogonal or non-orthogonal relative position vectors (see section 2.3). As we will see, three degrees of freedom need to be specified for the overall orientation of the molecule. Hence, if we are not interested in rotations, we can further reduce the dimensionality of the problem from $3N - 3$ to $3N - 6$.

The separation of overall rotations from internal deformations is done by introducing a so-called *body-fixed* (BF) frame of reference. This frame is centred at the center of mass G of the molecule (like the SF frame) but its axes are now rotating with the molecule. It will allow to distinguish the internal deformations of the molecule from its overall rotation. There is in principle no unique way of defining these axes: for a rigid body, the principal axes of inertia are generally chosen, whereas for an *a priori* deformable molecular system, several other options are available (a known example in molecular physics is the Eckart frame [48]).

When using polyspherical coordinates, the following definition of the BF frame is preferred. For convenience, we will let $(\vec{e}_x, \vec{e}_y, \vec{e}_z)$ be the right-handed orthonormal basis of vectors defining the axes of the SF frame. Now, let also $(\vec{u}_x, \vec{u}_y, \vec{u}_z)$ be the

right-handed orthonormal basis of vectors orienting those of the BF frame. This basis is defined as follows:

- \vec{u}_z is aligned along \vec{R}_{N-1} ,
- \vec{u}_y is orthogonal to the plane $(O, \vec{R}_{N-1}, \vec{R}_{N-2})$, such that the triplet of vectors $(\vec{R}_{N-1}, \vec{R}_{N-2}, \vec{u}_y)$ is right-handed,
- As a consequence \vec{u}_x is such that \vec{R}_{N-1} lies in the positive (Gzx) half-plane.

Mathematically:

$$\vec{u}_z = \vec{R}_{N-1} / \|\vec{R}_{N-1}\| \quad (2.73)$$

$$\vec{u}_y = \vec{R}_{N-1} \times \vec{R}_{N-2} / \|\vec{R}_{N-1} \times \vec{R}_{N-2}\| \quad (2.74)$$

$$\vec{u}_x = \vec{u}_y \times \vec{u}_z \quad (2.75)$$

that is, in the BF frame, \vec{R}_{N-1} has no x or y components and \vec{R}_{N-2} has no y component.

Now, the orientation of the BF frame of reference can be described in terms of Euler angles (α, β, γ) , with the convention that (see e.g. [49]):

- α denotes a rotation angle around the z axis in the SF frame,
- β denotes a rotation angle around the y axis in the α -rotated frame,
- γ denotes a rotation angle around the z axis of the α - β -rotated frame.

We call E_2 the frame obtained by transformation of the SF axes by the first two Euler rotations by α and β . BF is therefore obtained by rotation of E_2 about its z axis by γ . Figure 2.2a gives an illustration of these angles and resulting frames. Let the following rotation matrices represent these subsequent rotations:

$$\begin{aligned} \mathcal{R}_z(\alpha) &= \begin{bmatrix} \cos \alpha & -\sin \alpha & 0 \\ \sin \alpha & \cos \alpha & 0 \\ 0 & 0 & 1 \end{bmatrix} & \mathcal{R}_y(\beta) &= \begin{bmatrix} \cos \beta & 0 & \sin \beta \\ 0 & 1 & 0 \\ -\sin \beta & 0 & \cos \beta \end{bmatrix} \\ \mathcal{R}_z(\gamma) &= \begin{bmatrix} \cos \gamma & -\sin \gamma & 0 \\ \sin \gamma & \cos \gamma & 0 \\ 0 & 0 & 1 \end{bmatrix} \end{aligned} \quad (2.76)$$

so that the rotation matrix from SF to BF i.e. the matrix of the BF basis $(\vec{u}_x, \vec{u}_y, \vec{u}_z)$ expressed in the SF basis $(\vec{e}_x, \vec{e}_y, \vec{e}_z)$ is $\mathcal{R}(\alpha, \beta, \gamma) = \mathcal{R}_z(\alpha)\mathcal{R}_y(\beta)\mathcal{R}_z(\gamma)$.

With the definition of the BF and E_2 axes given above, the Cartesian coordinates of the vectors \vec{R}_{N-1} and \vec{R}_{N-2} in the frames BF, E_2 and SF are related by:

$$\begin{bmatrix} R_{N-1}^{(\text{SF}),x} \\ R_{N-1}^{(\text{SF}),y} \\ R_{N-1}^{(\text{SF}),z} \end{bmatrix} = \mathcal{R}_z(\alpha)\mathcal{R}_y(\beta) \begin{bmatrix} 0 \\ 0 \\ R_{N-1}^{(E_2),z} \end{bmatrix} \quad (2.77)$$

$$\begin{bmatrix} 0 \\ 0 \\ R_{N-1}^{(E_2),z} \end{bmatrix} = \mathcal{R}_z(\gamma) \begin{bmatrix} 0 \\ 0 \\ R_{N-1}^{(BF),z} \end{bmatrix} = \begin{bmatrix} 0 \\ 0 \\ R_{N-1}^{(BF),z} \end{bmatrix} \quad (2.78)$$

$$\begin{bmatrix} R_{N-2}^{(SF),x} \\ R_{N-2}^{(SF),y} \\ R_{N-2}^{(SF),z} \end{bmatrix} = \mathcal{R}_z(\alpha)\mathcal{R}_y(\beta) \begin{bmatrix} R_{N-2}^{(E_2),x} \\ R_{N-2}^{(E_2),y} \\ R_{N-2}^{(E_2),z} \end{bmatrix} \quad (2.79)$$

$$\begin{bmatrix} R_{N-2}^{(E_2),x} \\ R_{N-2}^{(E_2),y} \\ R_{N-2}^{(E_2),z} \end{bmatrix} = \mathcal{R}_z(\gamma) \begin{bmatrix} R_{N-2}^{(BF),x} \\ 0 \\ R_{N-2}^{(BF),z} \end{bmatrix} \quad (2.80)$$

And for the components of the other vectors \vec{R}_i , $i \in \{1, \dots, N-3\}$:

$$\begin{bmatrix} R_i^{(SF),x} \\ R_i^{(SF),y} \\ R_i^{(SF),z} \end{bmatrix} = \mathcal{R}_z(\alpha)\mathcal{R}_y(\beta) \begin{bmatrix} R_i^{(E_2),x} \\ R_i^{(E_2),y} \\ R_i^{(E_2),z} \end{bmatrix} \quad (2.81)$$

$$\begin{bmatrix} R_i^{(E_2),x} \\ R_i^{(E_2),y} \\ R_i^{(E_2),z} \end{bmatrix} = \mathcal{R}_z(\gamma) \begin{bmatrix} R_i^{(BF),x} \\ R_i^{(BF),y} \\ R_i^{(BF),z} \end{bmatrix} \quad (2.82)$$

or equivalently:

$$\begin{bmatrix} R_i^{(SF),x} \\ R_i^{(SF),y} \\ R_i^{(SF),z} \end{bmatrix} = \mathcal{R}(\alpha, \beta, \gamma) \begin{bmatrix} R_i^{(BF),x} \\ R_i^{(BF),y} \\ R_i^{(BF),z} \end{bmatrix} \quad (2.83)$$

2.4.2 Specification of the angles

Inspired by eq. (2.77), the angles β and α are respectively chosen to be the polar and the azimuthal angles of \vec{R}_{N-1} in the SF frame. In the polyspherical parametrization eq. (2.71) we write then:

$$\theta_{N-1} = \beta \quad (2.84)$$

$$\phi_{N-1} = \alpha \quad (2.85)$$

This choice reads:

$$\begin{aligned} R_{N-1}^{(SF),x} &= R_{N-1} \sin \beta \cos \alpha \\ R_{N-1}^{(SF),y} &= R_{N-1} \sin \beta \sin \alpha \\ R_{N-1}^{(SF),z} &= R_{N-1} \cos \beta \end{aligned} \quad (2.86)$$

Thus, eq. (2.86) together with eqs. (2.79) and (2.81) realize a change of variable where, on the one hand, \vec{R}_{N-1} is expressed in spherical coordinates in the SF frame and, on the other hand, the E_2 Cartesian coordinates of the other $N-2$ vectors are used in

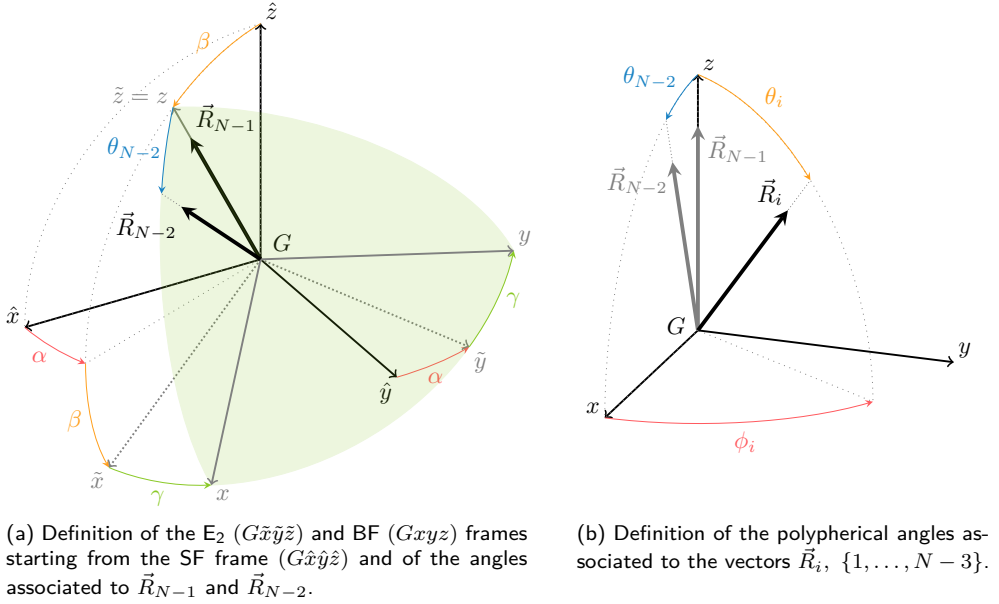


Figure 2.2: Definition of the polyspherical coordinates associated to $N - 1$ relative position vectors.

place of their SF Cartesian coordinates via the rotation matrix $\mathcal{R}_z(\alpha)\mathcal{R}_y(\beta)$. Since the determinant of this rotation matrix is 1, then the Jacobian J_{N-1} of this change of coordinates is the usual one for the transformation to spherical coordinates given in eq. (2.86):

$$J_{N-1} = R_{N-1}^2 \sin \beta \quad (2.87)$$

We call θ_{N-2} the angle from \vec{R}_{N-1} to \vec{R}_{N-2} . Since \vec{u}_z is aligned with \vec{R}_{N-1} (see eq. (2.73)), it is also aligned with the z -axis of the intermediate E_2 frame. Then θ_{N-2} can be seen as the polar angle of the vector \vec{R}_{N-2} in the E_2 frame. On the other hand, from the simplification given by eq. (2.80), we choose γ to be the azimuthal angle of \vec{R}_{N-2} in E_2 . We write then:

$$\phi_{N-2} = \gamma \quad (2.88)$$

This choice of the angles yields:

$$\begin{aligned} R_{N-2}^{(E_2),x} &= R_{N-2} \sin \theta_{N-2} \cos \gamma \\ R_{N-2}^{(E_2),y} &= R_{N-2} \sin \theta_{N-2} \sin \gamma \\ R_{N-2}^{(E_2),z} &= R_{N-2} \cos \theta_{N-2} \end{aligned} \quad (2.89)$$

We then operate the change of variables eq. (2.89) together with eq. (2.82) while keeping the coordinates R_{N-1} , α and β unchanged. In other words, the expressions

of the E_2 Cartesian coordinates of \vec{R}_{N-2} are given in terms of its spherical coordinates (still within E_2) and the E_2 Cartesian coordinates of the remaining $N-3$ vectors are replaced by their BF Cartesian coordinates via the rotation matrix $\mathcal{R}_z(\gamma)$. Note that the identification of γ as the azimuthal angle ϕ_{N-2} of \vec{R}_{N-2} in E_2 is consistent with the definition of the BF frame since it can be verified that, from eq. (2.89) and inverting eq. (2.80):

$$R_{N-2}^{(\text{BF}),z} = R_{N-2} \cos \theta_{N-2} \quad (2.90)$$

$$R_{N-2}^{(\text{BF}),x} = R_{N-2} \sin \theta_{N-2} \quad (2.91)$$

Again, since $\mathcal{R}_z(\gamma)$ is an orthogonal matrix, the change of coordinates realized with eqs. (2.82) and (2.89) is accompanied by a Jacobian J_{N-2} of a change to spherical coordinates given by eq. (2.89):

$$J_{N-2} = R_{N-2}^2 \sin \theta_{N-2} \quad (2.92)$$

Finally, the last change of coordinates consists in expressing the BF Cartesian coordinates of the vectors \vec{R}_i , with $i \in \{1, \dots, N-3\}$, in spherical coordinates (still within BF):

$$\begin{aligned} R_i^{(\text{BF}),x} &= R_i \sin \theta_i \cos \phi_i \\ R_i^{(\text{BF}),y} &= R_i \sin \theta_i \sin \phi_i \end{aligned} \quad (2.93)$$

$$R_i^{(\text{BF}),z} = R_i \cos \theta_i$$

while keeping the spherical coordinates of \vec{R}_{N-1} and \vec{R}_{N-2} unchanged. Figure 2.2b gives an illustration of eq. (2.93). The Jacobian characterizing this change of coordinates is:

$$J_{\text{BF}} = \prod_{i=1}^{N-3} R_i^2 \sin \theta_i \quad (2.94)$$

The Jacobian of the whole transformation from SF Cartesian coordinates to the so-defined polyspherical coordinates is the product of J_{N-1} , J_{N-2} and J_{BF} , that is:

$$J = \prod_{i=1}^{N-1} R_i^2 \sin \theta_i = \prod_{i=1}^{N-1} R_i^2 \prod_{j=1}^{N-2} \sin \theta_j \sin \beta \quad (2.95)$$

2.4.3 Summary

Polyspherical coordinates are a set of spherical coordinates $(R_i, \theta_i, \phi_i)_i$, with $i \in \{1, \dots, N-1\}$, whose each triplet represents a relative position vector. Given the definition of the frames of reference BF and E_2 in terms of \vec{R}_{N-1} and \vec{R}_{N-2} , these coordinates are, specifically:

- $\forall i \in \{1, \dots, N-1\}$, R_i is radial distance between the origin of SF/ E_2 /BF and the position of the i^{th} fictitious particle (i.e. length of the vector \vec{R}_i),

- $(\theta_{N-1}, \phi_{N-1}) = (\beta, \alpha)$ are the polar and azimuthal angles of \vec{R}_{N-1} in SF,
- $(\theta_{N-2}, \phi_{N-2}) = (\theta_{N-2}, \gamma)$ are the polar and azimuthal angles of \vec{R}_{N-2} in E_2 ,
- $\forall i \in \{1, \dots, N-3\}$, (θ_i, ϕ_i) are the polar and azimuthal angles of \vec{R}_i in BF.

The Jacobian of the transformation ρ from SF Cartesian coordinates to polyspherical coordinates

$$(R_i^{(\text{SF}),\xi})_{\substack{\xi=x,y,z \\ i \in \{1, \dots, N-1\}}} = \rho((R_i, \theta_i, \phi_i)_{i \in \{1, \dots, N-1\}}) \quad (2.96)$$

is

$$J_\rho = \prod_{i=1}^{N-1} R_i^2 \sin \theta_i = \prod_{i=1}^{N-1} R_i^2 \prod_{j=1}^{N-2} \sin \theta_j \sin \beta \quad (2.97)$$

2.4.4 Separation into subsystems

We mention that a separation into subsystems is also possible. For the scope of this thesis, we will briefly explain the procedure for the definition of one subsystem of polyspherical coordinates among the others defined in the standard way as above.

One can choose a vector \vec{R}_k (other than \vec{R}_{N-1}) to be along the z axis of an intermediate body-fixed frame of reference (which we will call BFs) and another vector⁸ \vec{R}_{k-1} (which is neither \vec{R}_{N-1} nor \vec{R}_{N-2}) to be in the zx plane of that frame. In other words, \vec{R}_k and \vec{R}_{k-1} define BFs like \vec{R}_{N-1} and \vec{R}_{N-2} define BF. Therefore, (θ_k, ϕ_k) play the role of (β, α) and ϕ_{k-1} plays the role of γ in the definition of the axes of BFs. Other vectors can then be expressed in spherical coordinates within BFs instead of BF. Since the passage from BF to BFs involves rotations by the Euler angles (from the perspective of BFs) θ_k, ϕ_k and ϕ_{k-1} , the Jacobian will not be different from eq. (2.97).

This choice will however have an impact on the expression of the kinetic energy in polyspherical coordinates. In chapter 3 we will show its derivation in the specific case of the tetra-atomic system H + HOD.

2.5 Molecular vibrations and normal modes

In sections 2.3 and 2.4 we have discussed particular types of curvilinear coordinates in order to describe arbitrary deformations of a molecular system. These are convenient when dealing with chemical reactions and scattering problems. Instead, vibrations in a molecule are merely small oscillatory displacements of nuclei around their equilibrium positions and it is often not necessary to use a coordinate system like the ones presented above to describe them. Except in some special cases, it is preferable to use simpler coordinates known as *normal modes* [33, 50]. These describe molecular vibrations in a convenient way since, as we will see, they allow to decompose the latter in simpler one-dimensional problems. They are one of the essential

⁸The index $k-1$ is chosen for analogy with the preceding discussion, as the indexing of the vectors can be always be redefined by permutation.

concepts in infrared spectroscopy, of which we present an application in chapter 4. Normal modes are defined in the following.

The Hamiltonian of a molecule containing N nuclei expressed in terms of their mass-weighted Cartesian coordinates⁹ $\mathbf{x}' = (x'_1, \dots, x'_{3N})$ in the laboratory-fixed frame of reference is given by:

$$\hat{H} = -\frac{\hbar^2}{2} \sum_{i=1}^{3N} \frac{\partial^2}{\partial x'_i{}^2} + V(\mathbf{x}') \quad (2.98)$$

Where V is the PES of the molecule. Let \mathbf{x}'_0 define a nuclear configuration at a stationary point on V , i.e. where its gradient with respect to the coordinates is zero, and let $\boldsymbol{\varepsilon} := \mathbf{x}' - \mathbf{x}'_0$ denote a displacement from that stationary point. For small $\boldsymbol{\varepsilon}$, one can expand the potential in a Taylor series up to second order:

$$\begin{aligned} V(\mathbf{x}') &= V(\mathbf{x}'_0) + \frac{1}{2} \sum_{i=1}^{3N} \sum_{j=1}^{3N} \varepsilon_i \varepsilon_j \frac{\partial^2 V}{\partial \varepsilon_i \partial \varepsilon_j}(\mathbf{x}'_0) + o(\|\boldsymbol{\varepsilon}\|^2) \\ &= V(\mathbf{x}'_0) + \frac{1}{2} \boldsymbol{\varepsilon}^\top \mathbf{H}_V(\mathbf{x}'_0) \boldsymbol{\varepsilon} + o(\|\boldsymbol{\varepsilon}\|^2) \end{aligned} \quad (2.99)$$

Where $\mathbf{H}_V(\mathbf{x}'_0)$ is the Hessian of V evaluated at the stationary point:

$$(\mathbf{H}_V(\mathbf{x}'_0))_{ij} = \frac{\partial^2 V}{\partial \varepsilon_i \partial \varepsilon_j}(\mathbf{x}'_0) \quad (2.100)$$

Since the Hessian is a symmetric matrix, it is diagonalizable and its eigenvectors are mutually orthogonal for the canonical dot product in \mathbb{R}^{3N} . Let $Q = (Q_{ij})$ be the orthogonal matrix whose columns \mathbf{q}_j , with $j \in \{1, \dots, 3N\}$, are distinct normalized eigenvectors of the Hessian and $K = \text{diag}(k_1, \dots, k_{3N})$ the diagonal matrix of the corresponding eigenvalues. With these, we have:

$$\mathbf{H}_V(\mathbf{x}'_0) = QKQ^\top \quad (2.101)$$

The \mathbf{q}_j are the so-called *normal modes* at the stationary point \mathbf{x}_0 . They represent specific collective small displacements of the nuclei from their equilibrium positions. Since Q depends on $\mathbf{H}_V(\mathbf{x}'_0)$, how normal modes combine these displacements depends on the shape of the V around the stationary point \mathbf{x}'_0 . Of the $3N$ eigenvalues, six of these (for linear molecules, five) will be zero and correspond to overall translations in the three dimensions and to overall rotations about three (resp. two) angles. If all remaining non-zero eigenvalues are positive, then \mathbf{x}'_0 corresponds to a local minimum on the surface. If there are n negative eigenvalues, we call it n^{th} -order saddle point.

⁹Here we index the nuclear coordinates from 1 to $3N$ without distinction between the x , y and z components of each nucleus, as was done in page 17. In addition to making the following computations lighter, this notation indicates that all these $3N$ coordinates contribute in a different way in normal modes. This is different from the definition of orthogonal vectors from original position vectors, where the x , y and z components transform in the same way.

Any arbitrary displacement ε can thus be decomposed as a linear combination of the normal modes:

$$\varepsilon = Q\boldsymbol{\eta} = \sum_{j=1}^{3N} \eta_j \mathbf{q}_j \quad (2.102)$$

By plugging eqs. (2.101) and (2.102) into eq. (2.99) and by dropping the terms beyond second order in $\|\varepsilon\|$, one has:

$$\begin{aligned} V(\mathbf{x}') - V(\mathbf{x}'_0) &= \frac{1}{2} \boldsymbol{\varepsilon}^\top \mathbf{H}_V(\mathbf{x}'_0) \boldsymbol{\varepsilon} = \frac{1}{2} \boldsymbol{\varepsilon}^\top Q K Q^\top \boldsymbol{\varepsilon} \\ &= \frac{1}{2} \boldsymbol{\eta}^\top K \boldsymbol{\eta} = \frac{1}{2} \sum_{i=1}^{3N} k_i \eta_i^2 \end{aligned} \quad (2.103)$$

The last line follows from diagonality of K . Moreover, we have:

$$\begin{aligned} \sum_{i=1}^{3N} \frac{\partial^2}{\partial x_i'^2} &= \sum_{i=1}^{3N} \frac{\partial^2}{\partial \varepsilon_i^2} = \sum_{i=1}^{3N} \frac{\partial}{\partial \varepsilon_i} \frac{\partial}{\partial \varepsilon_i} \\ &= \sum_{i=1}^{3N} \left(\sum_{j=1}^{3N} \frac{\partial \eta_j}{\partial \varepsilon_i} \frac{\partial}{\partial \eta_j} \right) \left(\sum_{k=1}^{3N} \frac{\partial \eta_k}{\partial \varepsilon_i} \frac{\partial}{\partial \eta_k} \right) \\ &= \sum_{i=1}^{3N} \left(\sum_{j=1}^{3N} (Q^\top)_{ji} \frac{\partial}{\partial \eta_j} \right) \left(\sum_{k=1}^{3N} (Q^\top)_{ki} \frac{\partial}{\partial \eta_k} \right) \\ &= \sum_{j=1}^{3N} \sum_{k=1}^{3N} \left(\sum_{i=1}^{3N} Q_{ij} Q_{ik} \right) \frac{\partial^2}{\partial \eta_j \partial \eta_k} = \sum_{j=1}^{3N} \sum_{k=1}^{3N} \delta_{jk} \frac{\partial^2}{\partial \eta_j \partial \eta_k} \\ &= \sum_{j=1}^{3N} \frac{\partial^2}{\partial \eta_j^2} \end{aligned} \quad (2.104)$$

where the third line follows from eq. (2.102) and the simplification in the fourth line follows from the orthogonality of the matrix Q .

In the case \mathbf{x}'_0 corresponds to a minimum on the PES (all non-zero eigenvalues of the Hessian are positive) we write $k_i = \omega_i^2$. With eqs. (2.103) and (2.104), the Hamiltonian is thus transformed as:

$$\hat{H} = \sum_{i=1}^{3N} \left(-\frac{\hbar^2}{2} \frac{\partial^2}{\partial \eta_i^2} + \frac{1}{2} \omega_i^2 \eta_i^2 \right) + V(\mathbf{x}'_0) \quad (2.105)$$

In other words, by a harmonic expansion of the potential and the decomposition of displacements in normal modes, the nuclear Hamiltonian is that of $3N$ independent harmonic oscillators, each of frequency $\omega_i/2\pi$. As a consequence, by labelling the non-zero-frequency modes from 1 to $3N - 6$, the vibrational energy of a molecule is

quantized and is given by:

$$E_{\mathbf{v}} = \sum_{i=1}^{3N-6} \hbar\omega_i \left(v_i + \frac{1}{2} \right) \quad (2.106)$$

where $\mathbf{v} := (v_1, \dots, v_{3N-6})$ is a multi-index specifying the overall vibrational state of the molecule and each $v_i \in \{0, 1, \dots\}$ labels a specific vibrational state for the i^{th} normal mode. In particular, the energy of the vibrational ground state $\mathbf{0}$ is:

$$E_0 = \sum_{i=1}^{3N-6} \frac{\hbar\omega_i}{2} \quad (2.107)$$

which is a finite non-zero quantity called *vibrational zero-point energy*.

Normal modes take a central place in vibrational spectroscopy as they allow to derive well-known selection rules of transitions between vibrational states using the algebra of the harmonic oscillator [50]. They also provide a convenient way of visualizing vibrations in a molecule, since one may assess whether the absorption of IR radiation will induce a transition or not by the sole inspection of their symmetry.

2.6 Numerical solution of the TDSE: the MultiConfigurational Time-Dependent Hartree method

Armed with the tools for describing nuclear configurations in a molecule, we now turn to the problem of solving the TDSE for the nuclear wavefunction. Except in very particular cases, no analytic solution of that equation can be found and one has to look for a numerical approximation which can be obtained with a computer. There exist several numerical methods for solving the TDSE [32, 51]. Of these we will mention the MultiConfigurational Time-Dependent Hartree (MCTDH) method [52–57] which is the one used in the work presented in chapter 3.

The MCTDH method is a scheme for solving the TDSE for systems involving multiple degrees of freedom, typically the nuclear coordinates in a molecule. In its fundamental definition, the wavefunction is written in a specific trial form with adjustable parameters. For a system depending on f degrees of freedom and time, the MCTDH ansatz is written as:

$$\Psi(q_1, \dots, q_n, t) = \sum_{i_1=1}^{n_1} \cdots \sum_{i_f=1}^{n_f} A_{i_1, \dots, i_f}(t) \prod_{k=1}^f \phi_{i_k}^{(k)}(q_k, t) \quad (2.108)$$

In other words, the total wavefunction Ψ is expanded as a linear combination of *configurations*, each being a *time-dependent Hartree product* of wavefunctions $\phi_{i_k}^{(k)}$ of one coordinate. The latter are thus called *single particle functions* (SPF) and are in turn expanded as:

$$\phi_{i_k}^{(k)}(q_k, t) = \sum_{j=1}^{N_k} c_{i_k, j}^{(k)}(t) \chi_j^{(k)}(q_k) \quad (2.109)$$

where for each $k \in \{1, \dots, f\}$, the $\chi_j^{(k)}$ are chosen orthonormal time-independent functions for the k^{th} degree of freedom, known as *primitive basis functions* (PBF).

Following this trial form, the time evolution of the wavefunction Ψ is completely determined by the time evolution of its expansion coefficients A_{i_1, \dots, i_f} and $c_{i_k, j}^{(k)}$. The way these change in time must be such that Ψ is as close as possible to the exact solution of the TDSE. This is done by invoking the Dirac-Frenkel variational principle (see e.g. [58] and references therein). One then obtains the MCTDH equations of motion, i.e. time differential equations with unknowns A_{i_1, \dots, i_f} and $c_{i_k, j}^{(k)}$.

Owing to the fact that the MCTDH method relies on a variational principle, the ansatz becomes closer and closer to the exact solution by increasing the number of terms in the expansion (namely, increasing the n_k and N_k). The convergence of the results depends, among other things, on the choice of coordinates in relation to the problem to solve, embodied in the Hamiltonian \hat{H} . However, adding more terms in eqs. (2.108) and (2.109) increases the number of differential equations in the A_{i_1, \dots, i_f} and $c_{i_k, j}^{(k)}$ coefficients to be solved, thus making the computations more and more time-consuming.

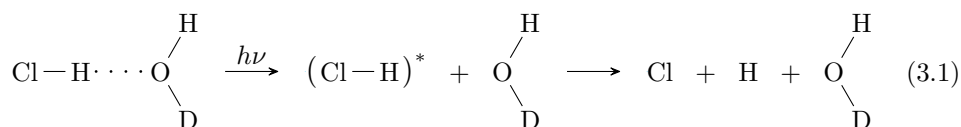
3

Study of the $\text{H} + \text{HOD} \longrightarrow \text{HOD} + \text{H} / \text{HOH} + \text{D}$ exchange reactions from the $(\text{HCl}) \cdots (\text{HOD})$ complex

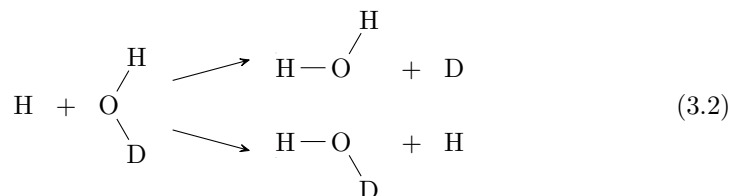
This chapter is dedicated to the study documented in the manuscript titled “Femtochemistry of bimolecular reactions from weakly bound complexes: computational study of the $\text{H} + \text{H}'\text{OD} \longrightarrow \text{H}'\text{OH} + \text{D} / \text{HOD} + \text{H}'$ exchange reactions” submitted to *The Journal of Chemical Physics* which can be read in appendix A.

The object of this study is the hypothetical gas phase reaction between an hydrogen atom with HOD (D denoting the ^2H deuterium isotope of hydrogen) that would arise from forming the weakly bound complex $(\text{HCl}) \cdots (\text{HOD})$ and photodissociating its HCl moiety. The reaction scheme is the following:

1. Photoexcitation of HCl in the complex. Its two atoms undergo homolytic dissociation and H is ejected against HOD:



2. Collision between H and HOD, possibly resulting in the “H-to-D” or the “H-to-H” exchange reactions:



In a first moment we will briefly review the main points and achievements of this work. Next, we will dedicate space to some of the concepts whose details were

omitted in the manuscript and which we will report in this chapter. Then, additional observations not presented in the manuscript will be provided. In particular, these are shown so as to provide answers to the reviewers who read the manuscript (see the introduction in appendix A). We will finally conclude this chapter, with suggestions on possible improvements of this work.

3.1 Summary of the manuscript in appendix A

The $(HCl) \cdots (H_2O)$ complex and its isotopologues are well-known in the literature. A large body of experimental and theoretical work, referenced in the paper, confirms that the two molecules are bound together by a single hydrogen bond, where HCl is the donor and H_2O is the acceptor.

The exchange reactions in eq. (3.2) can be expected to occur as a result of how the two molecules are oriented with respect to each other. The specific choice of the HOD isotopologue (instead of regular water) was made so as to have the two above-mentioned distinguishable reaction channels. The possible selectivity between the two is then one aspect we intended to inspect in this work.

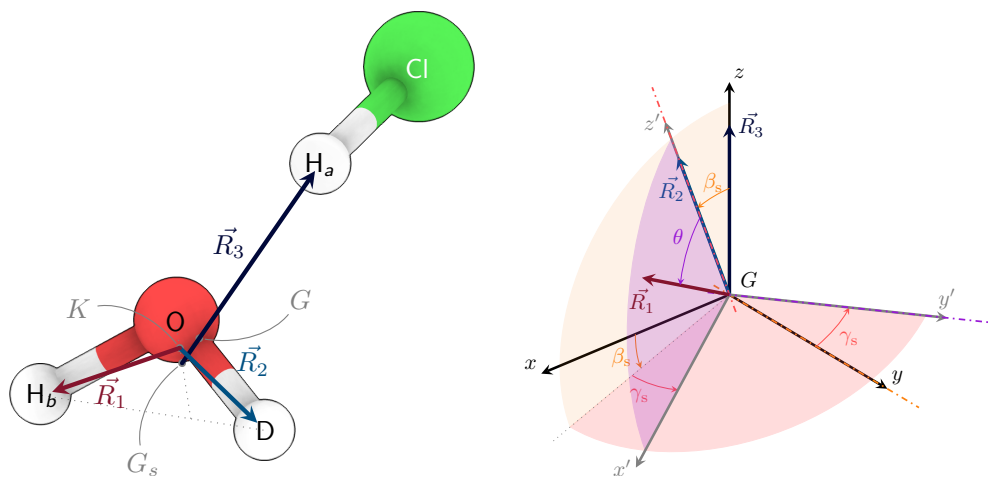
Because of the non-availability of the full surface of the complex with electronically excited HCl, the focus is shifted on $H + HOD$ only, whose H_3O ab initio PES is known instead. Proper initial conditions for this system are chosen to take into consideration the initial positions of the nuclei in the complex (see section 3.2.1) and to mimic the effective result of the HCl photodissociation (see section 3.2.2). In other words, the step in eq. (3.2) is described explicitly here, whereas the preceding step in eq. (3.1) will be considered implicitly in the initial conditions of the collision.

The relative positions of the atoms in the $H + HOD$ system – henceforth labelled H_a , H_b , O and D – is given by a set of three orthogonal vectors (in the sense of section 2.3) as shown in fig. 3.1a : one Jacobi vector \vec{R}_3 , from the center of mass of H_bOD to H_1 , and two Radau vectors \vec{R}_2 and \vec{R}_1 , from the canonical center of H_bOD to D and H_b respectively).

We choose the vectors \vec{R}_3 and \vec{R}_2 to define the orientation of the body-fixed (BF) frame of reference of the whole system (following section 2.4.1). \vec{R}_2 and \vec{R}_1 define the orientation of the “sub”-body-fixed (BFs) frame of the H_bOD subsystem (following section 2.4.4). With this choice, the three vectors are parametrized with polyspherical coordinates where, by the separation into subsystems $\{H_a\}$ and $\{H_bOD\}$, the orientation of BFs is given with respect to BF (see fig. 3.1b).

With the choice of these coordinates, we express the potential (see section 3.2.4) and derive the kinetic energy operator in terms of these (see section 3.2.3). With the knowledge of the ground and excited states potential energy curves of HCl we could estimate the initial momentum of H_a in terms of the polyspherical coordinates.

The MultiConfigurational Time-Dependent Hartree (MCTDH) method was used to propagate the wavepacket of the system (see section 2.6). For the definition of the initial state, a preliminary relaxation on the (adapted) ground state surface of the $(HCl) \cdots (H_2O)$ complex was necessary because of the low-double-well structure of the



(a) Orthogonal vectors \vec{R}_1 , \vec{R}_2 and \vec{R}_3 describing the relative positions of the nuclei H_a , H_b , O and D. The geometry of the $(HCl) \cdots (HOD)$ shown here corresponds to the global minimum on its PES.

(b) Parametrization of the vectors in terms of polyspherical coordinates. Note that the axes $(x'y'z')$ of the sub-body-fixed frame BFs are oriented with respect to (xyz) , those of the body-fixed frame BF.

Figure 3.1: The description of the $H_a + H_bOD$ geometry in terms of orthogonal Jacobi and Radau vectors and their parametrization in polyspherical coordinates. Reproduced from the manuscript in appendix A.

potential between two global minima (see section 3.2.1 for details) preventing from defining it “by hand” as a product of Gaussians. Both potentials for the relaxation and the propagation were adapted to a sum-of-products form suitable for its evaluation in MCTDH with the POTFIT procedure [59, 60].

By inspection of the wavepacket evolution over time, the only outcomes of the collision that could be observed were mostly the recoil of H_a from H_bOD and, to minor extent, both products of the exchange reactions in eq. (3.2). No abstraction reaction, i.e. of the type $H_a + H_bOD \longrightarrow H_aH_b + OD$ or $H_a + H_bOD \longrightarrow H_aD + OH_b$, are observed. The energy distribution of the wavepacket is a broad bell-shaped function of the collision energy whose maximum is located at 3.1 eV. The analysis of the energy- and time-resolved reaction probabilities confirm that the recoil of H_a is the most probable outcome over the whole range of collision energies, followed by “H-to-H” exchange and then by little “H-to-D” exchange (see fig. 3.2a). Thus, for the part that gives rise to new products, the reaction is selective. Vibrational zero-point energy effects are suspected to play a role in this selectivity. The timescale of the reaction is of the order of 10 fs (plus around 10 fs more for H_a to reach H_bOD , see fig. 3.2b).

Two additional propagations were performed. The first one starts with pre-excited OD vibrational mode in H_bOD . The obtained results show similarities with the

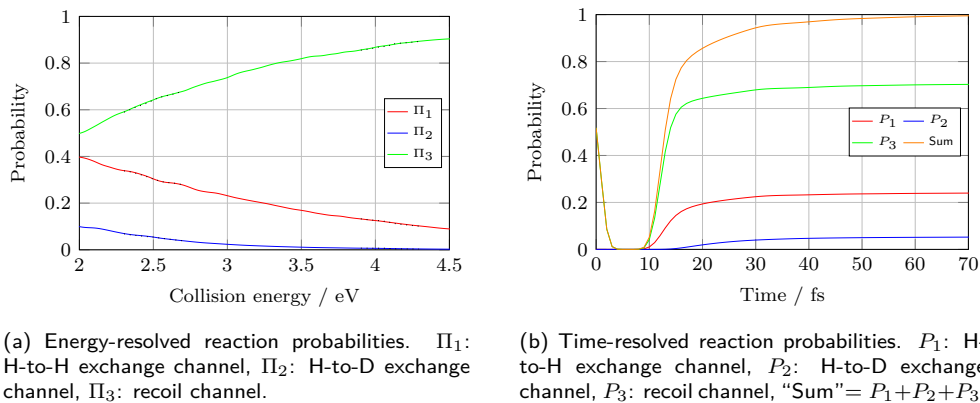


Figure 3.2: Energy- and time-resolved reaction probabilities for the $H_a + H_bOD$ collision with H_bOD in the vibrational ground state. Reproduced from the manuscript in appendix A.

previous ones with the exception that the reaction probabilities of “H-to-H” and “H-to-D” exchanges products are reversed, thus providing an example of mode-selective chemistry. The second one is carried out in the vibrational ground state of H_bOD but with lower momentum applied to H_a . The energy distribution of the wavefunction thus covered a range of collision energies around the reaction barrier height. The fine features observed in the exchange reaction probabilities follow the ones found in full bimolecular collision studies and are ascribable to shape resonances (more on this in section 3.3.1).

We want to stress that the situation studied here is conceptually different than that of the reaction $H + HOD$ studied in the framework of full bimolecular reactions and scattering experiments. Indeed, in the latter case, reaction probabilities are obtained by averaging over all possible orientations and impact parameters. In the present situation, the specificity of the initial conditions are determined, on the one hand, by the geometry of the complex in its electronic ground state and, on the other hand, by the relative collision energy stemming from the kinetic energy gained by H upon the dissociation of HCl. This is the main reason why we do not observe products of the abstraction reaction and that the reaction probabilities for the exchange (below 2 eV) are larger than in the full bimolecular case.

3.2 Supplementary information

3.2.1 The geometry of the $(HCl) \cdots (HOD)$ complex and the definition of the initial state

As already mentioned, $(HCl) \cdots (H_2O)$ is a complex which is formed via a hydrogen bond between the hydrogen atom of the HCl molecule (the H-bond donor) and the

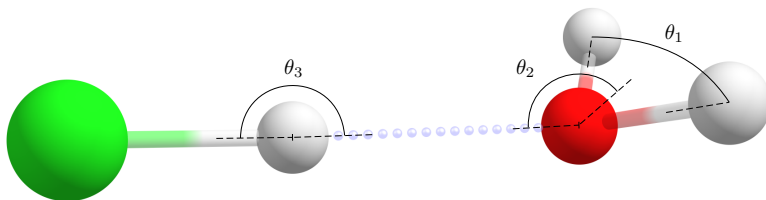


Figure 3.3: Global minimum energy structure of the $(\text{HCl}) \cdots (\text{H}_2\text{O})$ complex (geometry kindly provided by the authors of [61]).

oxygen of the HOD molecule (the H-bond acceptor). It has been long debated whether the complex is either planar, with C_{2v} symmetry, or bent such as in fig. 3.3, with C_s symmetry. An important paper by Mancini & Bowman [61] gives an answer to this problem. In their work, the authors calculated the full dimensional *ab initio* potential energy surface of the complex with special emphasis on the regions where intermolecular interactions play a key role on its shape. The geometry corresponding to the global minimum on this PES is given in fig. 3.3 and corresponds to the one obtained in previous works by optimization of the structure (see e.g. [62]). Instead, the planar geometry corresponds to a saddle point whose imaginary frequency normal mode is the “umbrella inversion” motion, where the angle θ_2 varies from above to below π . Thus, the relaxed potential along the imaginary frequency mode describes a double-well connecting the two global minima which are the symmetric of each other about the plane of the water molecule, as depicted in fig. 3.4.

The peculiar aspect in this case is that the barrier between the two minima is only 59 cm^{-1} high relative to those. Mancini & Bowman could obtain the one-dimensional ground state wavefunction along the inversion coordinate. Its calculated vibrational zero-point energy is 52 cm^{-1} above the top of the barrier and the wavefunction is delocalized over the two minima. These results are supported by the agreement between their calculated values of the rotational constant of the complex and experimentally measured values.

Now, concerning our study of the title reaction, since the geometry of the complex is crucial in the definition of the initial conditions, it was important to start from an initial state which reflected this unusual behaviour in the $(\text{HCl}) \cdots (\text{HOD})$ complex. The fact that the C_{2v} geometry does not correspond to a global minimum made us unable to postulate an initial state as a product of Gaussians of the normal modes. Moreover, the large spread along the inversion coordinate could not be easily estimated. It was then decided to proceed with a wavefunction relaxation on the PES of the complex by Mancini & Bowman.

However, the propagated wavefunction depends only on the relative coordinates of H_a , H_b , O and D, and cannot therefore describe the whole complex. Nevertheless, the electronegative chlorine atom plays a critical role (as hydrogen donor) in the stability of the complex and needed to be included in some way in order to obtain the proper position of H_a with respect to H_bOD . One can notice that, in the global minimum

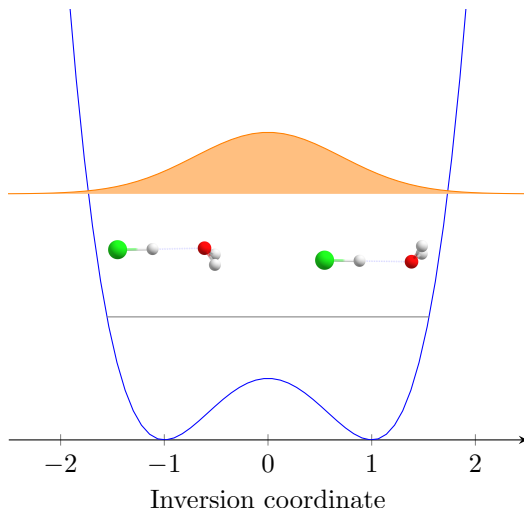


Figure 3.4: Schematic representation of the double-well potential (blue curve) of $(HCl) \cdots (HOD)$ along the inversion coordinate from one global minimum geometry with C_s symmetry to the other passing by the planar saddle point geometry. The vibrational zero-point energy (grey horizontal line) is above the inversion barrier. As a result, the wavefunction (orange) is delocalized over the two wells and is maximal at the planar geometry.

geometry of the complex, the angle $\theta_3 \approx \pi$, i.e. the atoms Cl, H_a and O are (almost) aligned. This is (necessarily) also the case for the planar C_{2v} geometry. On the other hand, the HCl bond length varies little from being isolated ($R_{HCl} = 1.275 \text{ \AA}$, from [63]) or bound in the complex ($R_{HCl} = 1.292 \text{ \AA}$ in the C_s geometry, $R_{HCl} = 1.289 \text{ \AA}$ in the C_{2v} saddle point geometry, from [61]).

Thus the adopted solution was to adapt Mancini's surface so as to account for the chlorine atom implicitly while being a function of the coordinates of the other four atoms only. This implicit inclusion consisted in deducing the position of the Cl atom from those of O and H_a based on the arguments above, namely it is aligned with the latter two and placed at a fixed distance from H_a .

If U is the potential of the complex as a function of position coordinates of all the five atoms and V the adapted potential described above, the relation between the two is (eqs. (22) and (23) in the manuscript):

$$V(\vec{x}_{H_a}, \vec{x}_{H_b}, \vec{x}_D, \vec{x}_O) = U(\vec{x}_{H_a}, \vec{x}_{H_b}, \vec{x}_D, \vec{x}_O, \underbrace{f(\vec{x}_{H_a}, \vec{x}_O)}_{= \vec{x}_{Cl}}) \quad (3.3)$$

with f defined as

$$f(\vec{x}_{H_a}, \vec{x}_O) = \vec{x}_{H_a} + \frac{\vec{x}_{H_a} - \vec{x}_O}{\|\vec{x}_{H_a} - \vec{x}_O\|} R_e \quad (3.4)$$

with $R_e = 1.292 \text{ \AA}$. The evaluation of the Cartesian coordinates of the atoms from

the polyspherical coordinates used in this study is discussed in section 3.2.4.

The Hamiltonian used for the relaxation included the modified potential V and the kinetic energy of $\text{H}_a + \text{H}_b\text{OD}$ given in eqs. (11) and (12) in the manuscript and discussed in more details in section 3.2.3. This means that we have neglected the kinetic energy of Cl and *de facto* rigidified the HCl molecule in the complex. In spite of this, the obtained relaxed wavefunction (ψ_g in the manuscript) used for the definition of the initial state of the propagation proved consistent with the fact that its modulus squared is maximal at the planar geometry and is delocalized over the double-well (see section 3.3.2).

3.2.2 HCl dissociation

In addition to what is described in the previous section, the definition of the initial state of the wavepacket propagation additionally involves the momentum gained by H_a upon dissociation of H_aCl . This section aims at providing a better understanding of how this is taken into consideration.

The adopted method for achieving this was to multiply the relaxed wavefunction ψ_g obtained by relaxation by an imaginary exponential:

$$\Psi_0(R_1, R_2, R_3, u, \alpha_s, \beta_s, \gamma_s) = \psi_g(R_1, R_2, R_3, u, \beta_s, \gamma_s) e^{-ip'_{\text{exc}}R_3/\hbar} \quad (3.5)$$

with $p'_{\text{exc}} > 0$ denoting a fixed momentum determined later. The effect of this is to shift the expectation value of the momentum along the R_3 coordinate from 0 to $-p'_{\text{exc}}$. Indeed we have:

$$\begin{aligned} \hat{P}_{R_3}\Psi_0 &= \hat{P}_{R_3}\psi_g e^{-ip'_{\text{exc}}R_3/\hbar} \\ &= \frac{\hbar}{i} \frac{\partial}{\partial R_3} \left(\psi_g e^{-ip'_{\text{exc}}R_3/\hbar} \right) \\ &= \frac{\hbar}{i} \frac{\partial \psi_g}{\partial R_3} e^{-ip'_{\text{exc}}R_3/\hbar} + \frac{\hbar}{i} \psi_g \left(-\frac{i}{\hbar} p'_{\text{exc}} \right) e^{-ip'_{\text{exc}}R_3/\hbar} \\ &= e^{-ip'_{\text{exc}}R_3/\hbar} \left(\hat{P}_{R_3}\psi_g - p'_{\text{exc}}\psi_g \right) \end{aligned} \quad (3.6)$$

so that:

$$\left\langle \Psi_0, \hat{P}_{R_3}\Psi_0 \right\rangle = \left\langle \psi_g, \hat{P}_{R_3}\psi_g \right\rangle - p'_{\text{exc}} \quad (3.7)$$

The choice of putting this momentum along the R_3 coordinate only is due to the fortuitous fact that the atoms Cl, H_a and O are aligned and that the vector \vec{R}_3 is *almost* equal to the vector $\vec{\text{OH}}_a$ (see fig. 3.1a). A more precise way of dealing with the question of the direction of ejection of the H_a atom towards H_bOD would involve the product with other imaginary exponentials of the other coordinates, analogous to that in eq. (3.5). We deliberately disregarded this aspect for it has a minor impact on the propagation in this particular case.

Thus, in our model, the effect of the photodissociation of H_a reduces to finding the value of p'_{exc} in eq. (3.5). This is determined in classical terms following two steps:

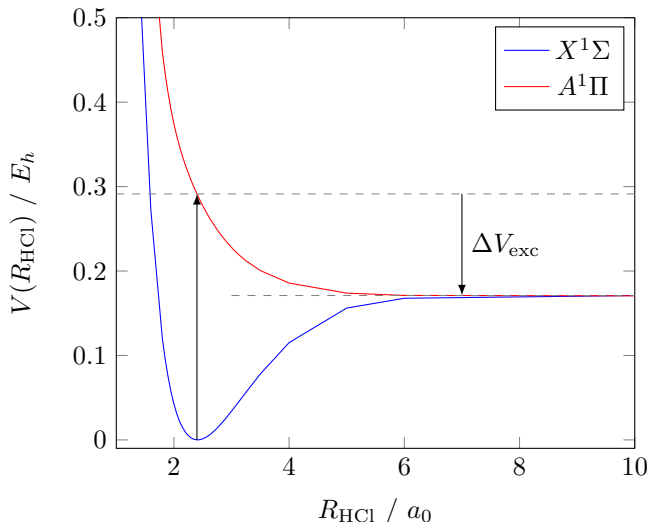


Figure 3.5: The ground and excited state potential energy curves of HCl (reproduced from [64], data provided with the courtesy of the authors).

1. Evaluation of the excess of potential energy gained by H_aCl (by absorption of a photon) which is converted into kinetic energy as the two atoms separate.
2. Expression of the momentum of H_a in the frame of reference attached to the system $H_a + H_bOD$.

We will show here some details of step 1 only. All the details of step 2 are given in the Appendix A of the manuscript.

In view of photodissociation, we assume that the interaction between the atoms of the isolated HCl molecule, in the vicinity of its equilibrium bond length, is unchanged upon complexation with HOD. In other words, the small modifications of the potential energy curves of HCl caused by the presence of the nearby HOD molecule are neglected. Thus, we look at the photodissociation of HCl as if it was isolated.

For this purpose, we have used the potential energy curves of HCl in its ground state (labelled $X^1\Sigma$) and first excited state (labelled $A^1\Pi$) calculated by Schmidt *et al.* [64] and reproduced in fig. 3.5. These correlate to the electronic ground states of the two atoms ($H(^2S) + Cl(^2P)$). The other dissociative states which do so too are not considered in this study as they have a different spin multiplicity than that of the ground state $X^1\Sigma$ (transitions to these from the ground state are spin-forbidden).

In our model, the excess of potential energy ΔV_{exc} is calculated as follows. We assume that, in virtue of the Frank-Condon approximation, the HCl molecule undergoes a vertical excitation from $X^1\Sigma$ to $A^1\Pi$ at its equilibrium bond length $R_{\text{HCl}} = 1.275 \text{ \AA}$. From this point, HCl will dissociate following the dissociative state towards infinite separation, thus gaining kinetic energy. Hence, ΔV_{exc} is the difference between the

value of the potential $A^1\Pi$ at infinite separation and that at the Frank-Condon bond length, as shown in fig. 3.5.

3.2.3 Derivation of the kinetic energy operator

The expression of the kinetic energy operator in polyspherical coordinates can be obtained in a systematic way [47] and we show here the main steps of its derivation. From the parametrization of the relative position vectors \vec{R}_1 , \vec{R}_2 and \vec{R}_3 in polyspherical coordinates $\vec{R}_3 \rightarrow (R_3, \beta, \alpha)$, $\vec{R}_2 \rightarrow (R_2, \beta_s, \gamma)$ and $\vec{R}_1 \rightarrow (R_1, \theta, \gamma_s)$, we will obtain the kinetic energy operator of the system in terms of elementary operators pre-implemented in the Heidelberg MCTDH package.

We recall that the vectors \vec{R}_1 , \vec{R}_2 and \vec{R}_3 are orthogonal relative position vectors in the sense of section 2.3, which means that the classical total kinetic energy in the space-fixed frame of reference (SF) has the diagonal form:

$$2T = \sum_{k=1}^3 \mu_k^{-1} \vec{P}_k \cdot \vec{P}_k \quad (3.8)$$

The basic idea behind the expression of the kinetic energy in terms of polyspherical coordinates is approach is to write the momentum vectors in terms of a radial linear momentum and an angular momentum:

$$\vec{P}_k = P_{R_k} \vec{e}_{R_k} - \frac{\vec{e}_{R_k} \times \vec{L}_k}{R_k} \quad (3.9)$$

where

$$\vec{e}_{R_k} = \vec{R}_k / R_k \quad (3.10)$$

$$\vec{L}_k = \vec{R}_k \times \vec{P}_k \quad (3.11)$$

$$P_{R_k} = \vec{e}_{R_k} \cdot \vec{P}_k \quad (3.12)$$

with $R_k = \|\vec{R}_k\|$. Here \vec{e}_{R_k} is the radial unit vector pointing to the k^{th} pseudo-particle, \vec{L}_k is its angular momentum and P_{R_k} the projection of its linear momentum along the radial axis. Plugging eq. (3.9) into eq. (3.8) yields:

$$2T = \sum_{k=1}^3 \mu_k^{-1} \left(P_{R_k}^2 + \frac{\vec{L}_k \cdot \vec{L}_k}{R_k^2} \right) \quad (3.13)$$

Note that $P_{R_k} = \partial T / \partial \dot{R}_k$, i.e. P_{R_k} is the conjugate momentum of the radial coordinate R_k . Now, the quantum kinetic energy operator is obtained by the quantization of the classical expression [41]:

$$2\hat{T} = \sum_{k=1}^3 \mu_k^{-1} \left(\hat{P}_{R_k}^\dagger \hat{P}_{R_k} + \frac{\hat{L}_k^\dagger \cdot \hat{L}_k}{R_k^2} \right) \quad (3.14)$$

where

$$\hat{\vec{L}}_k^\dagger \cdot \hat{\vec{L}}_k = \hat{L}_{k,x}^\dagger \hat{L}_{k,x} + \hat{L}_{k,y}^\dagger \hat{L}_{k,y} + \hat{L}_{k,z}^\dagger \hat{L}_{k,z} \quad (3.15)$$

$$\hat{P}_{R_k} = -i\hbar \frac{\partial}{\partial R_k} \quad (3.16)$$

$$\hat{P}_{R_k}^\dagger = -i\hbar \frac{1}{R_k} \frac{\partial}{\partial R_k} R_k \quad (3.17)$$

$$\hat{P}_{R_k}^\dagger \hat{P}_{R_k} = -\hbar^2 \frac{1}{R_k^2} \frac{\partial}{\partial R_k} R_k^2 \quad (3.18)$$

Note that the radial momenta operators \hat{P}_{R_k} are not Hermitian because they are conjugate to a curvilinear coordinate [35, 65]. We remind that the kinetic energy is computed in the SF frame. The angular momentum operators are thus evaluated in that frame too. However, the value of each dot product in eq. (3.15) is the same if calculated with the components projected along the axes of any other frame of reference F obtained by rotation of the SF axes:

$$\begin{aligned} \hat{\vec{L}}_k^\dagger \cdot \hat{\vec{L}}_k &= \hat{L}_{k,x}^\dagger \hat{L}_{k,x} + \hat{L}_{k,y}^\dagger \hat{L}_{k,y} + \hat{L}_{k,z}^\dagger \hat{L}_{k,z} \\ &= (\hat{L}_{k,x}^F)^\dagger (\hat{L}_{k,x}^F) + (\hat{L}_{k,y}^F)^\dagger (\hat{L}_{k,y}^F) + (\hat{L}_{k,z}^F)^\dagger (\hat{L}_{k,z}^F) \end{aligned} \quad (3.19)$$

$\hat{L}_{k,x}^F$, $\hat{L}_{k,y}^F$ and $\hat{L}_{k,z}^F$ may not be Hermitian, depending whether the corresponding \vec{R}_k is involved in the definition of the frame F [66, 67].

In the following, we use a separation into subsystems (see section 2.4.4 and [45]), where the vectors \vec{R}_2 and \vec{R}_1 define the subsystem-body-fixed frame BFs mentioned in the manuscript. It is essentially the frame of reference rotating with H_bOD within the body-fixed frame BF of the whole system. \vec{R}_2 gives the direction of its z' axis and \vec{R}_1 fixes the orientation of the $z'x'$ plane. An explicit definition is given in appendix B, page 120. The vector \vec{R}_3 is then associated to the relative motion between the subsystems $\{H_a\}$ and $\{H_bOD\}$.

The kinetic energy in eq. (3.14) can thus be recast in the following way:

$$2\hat{T} = \frac{1}{\mu_3} \hat{P}_{R_3}^\dagger \hat{P}_{R_3} + \frac{\hat{\vec{L}}_3^\dagger \cdot \hat{\vec{L}}_3}{\mu_3 R_3^2} + 2\hat{T}_{HOD} \quad (3.20)$$

where $2\hat{T}_{HOD}$ includes only the last two terms in the sum in eq. (3.14). The Hamiltonian T_{HOD} is the Hamiltonian of the triatomic HOD which has already been given in

[42, eq. 35b]. Adapting the notation to the present case gives:

$$\begin{aligned}
 2\hat{T}_{\text{HOD}} = & -\frac{\hbar^2}{\mu_1} \frac{1}{R_1^2} \frac{\partial}{\partial R_1} R_1^2 \frac{\partial}{\partial R_1} - \frac{\hbar^2}{\mu_2} \frac{1}{R_2^2} \frac{\partial}{\partial R_2} R_2^2 \frac{\partial}{\partial R_2} \\
 & - \hbar^2 \left(\frac{1}{\mu_1 R_1^2} + \frac{1}{\mu_2 R_2^2} \right) \left(\frac{1}{\sin \theta} \frac{\partial}{\partial \theta} \sin \theta \frac{\partial}{\partial \theta} + \frac{1}{\sin^2 \theta} \frac{\partial^2}{\partial \gamma_s^2} \right) \\
 & + \frac{1}{\mu_2 R_2^2} \left[\hat{L}_{1,2}^2 - 2(\hat{L}_{1,2})_z^2 \right. \\
 & \quad + \hbar \left(\frac{\partial}{\partial \theta} + \frac{1}{2} \cot \theta \right) \left((\hat{L}_{1,2})_+^{\text{BFs}} - (\hat{L}_{1,2})_-^{\text{BFs}} \right) \\
 & \quad + \frac{1}{2} \cot \theta \left((\hat{L}_{1,2})_+^{\text{BFs}} (\hat{L}_{1,2})_z^{\text{BFs}} + (\hat{L}_{1,2})_-^{\text{BFs}} (\hat{L}_{1,2})_z^{\text{BFs}} \right. \\
 & \quad \quad \left. \left. + (\hat{L}_{1,2})_z^{\text{BFs}} (\hat{L}_{1,2})_+^{\text{BFs}} + (\hat{L}_{1,2})_z^{\text{BFs}} (\hat{L}_{1,2})_-^{\text{BFs}} \right) \right]
 \end{aligned} \tag{3.21}$$

Where $\hat{L}_{1,2} = \hat{L}_1 + \hat{L}_2$ is the total angular momentum of the subsystem. In obtaining this expression, $\hat{L}_1^\dagger \cdot \hat{L}_1$ and $\hat{L}_2^\dagger \cdot \hat{L}_2$ are calculated using the components of the angular momenta along the BF axes.

Now, in order to calculate the term $\hat{L}_3^\dagger \cdot \hat{L}_3$, the angular momentum \hat{L}_3 is replaced by $\hat{J} - \hat{L}_1 - \hat{L}_2$, where \hat{J} is the total angular momentum. This dot product is evaluated using the BF components of \hat{J} and $\hat{L}_{1,2}$:

$$\begin{aligned}
 \hat{L}_3^\dagger \cdot \hat{L}_3 &= (\hat{J} - \hat{L}_{1,2})^\dagger \cdot (\hat{J} - \hat{L}_{1,2}) \\
 &= \hat{J}^2 + \hat{L}_{1,2}^2 - 2\hat{J}^\dagger \cdot \hat{L}_{1,2}
 \end{aligned} \tag{3.22}$$

In particular, using the fact that the BF components of \hat{J} are Hermitian [66, 67] and that $\hat{J}_\pm = \hat{J}_x \pm i\hat{J}_y$ and $\hat{L}_{k,\pm} = \hat{L}_{k,x} \pm i\hat{L}_{k,y}$:

$$\begin{aligned}
 \hat{J}^\dagger \cdot \hat{L}_{1,2} &= \hat{J}_x^\dagger (\hat{L}_{1,2})_x + \hat{J}_y^\dagger (\hat{L}_{1,2})_y + \hat{J}_z^\dagger (\hat{L}_{1,2})_z \\
 &= \hat{J}_x (\hat{L}_{1,2})_x + \hat{J}_y (\hat{L}_{1,2})_y + \hat{J}_z (\hat{L}_{1,2})_z \\
 &= \hat{J}_z (\hat{L}_{1,2})_z + \frac{1}{2} \left(\hat{J}_+ (\hat{L}_{1,2})_- + \hat{J}_- (\hat{L}_{1,2})_+ \right)
 \end{aligned} \tag{3.23}$$

Finally, since the z -axis of the BF frame is aligned with \vec{R}_3 , we have:

$$\hat{L}_{3,z} = 0 \tag{3.24}$$

so that:

$$\hat{J}_z = (\hat{L}_{1,2})_z \tag{3.25}$$

Thus the kinetic energy operator reads, up to this point:

$$2\hat{T} = -\hbar^2 \frac{1}{R_3^2} \frac{\partial}{\partial R_3} R_3^2 + \frac{\hat{J} + \hat{L}_{1,2}^2 - 2\hat{J}_z^2 - \hat{J}_+ (\hat{L}_{1,2})_- - \hat{J}_- (\hat{L}_{1,2})_+}{\mu_3 R_3^2} + 2\hat{T}_{\text{HOD}} \tag{3.26}$$

In obtaining this expression, the use of the polyspherical coordinates in place of SF Cartesian coordinates is associated to the following Jacobian (see eq. (2.95)):

$$J = R_1^2 R_2^2 R_3^2 \sin \theta \sin \beta_s \sin \beta \quad (3.27)$$

At this point, we change the form of \hat{T} by additional transformations. First, we recast the kinetic energy operator as:

$$\hat{T} = \hat{T}_{R_1} + \hat{T}_{R_2} + \hat{T}_{R_3} + \hat{T}_{\text{other}} \quad (3.28)$$

with, for $k \in \{1, 2, 3\}$

$$\hat{T}_{R_k} = -\frac{\hbar^2}{\mu_k} \frac{1}{R_k^2} \frac{\partial}{\partial R_k} R_k^2 \frac{\partial}{\partial R_k} \quad (3.29)$$

Next, we perform a change of function to simplify the kinetic energy operator. Let Φ be the solution of the TDSE with the kinetic energy given in eq. (3.28). We define the wavefunction Ψ such that:

$$\Phi(R_1, R_2, R_3, \beta_s, \gamma_s, \theta, t) = (R_1 R_2 R_3)^{-1} \Psi(R_1, R_2, R_3, \beta_s, \gamma_s, \theta, t) \quad (3.30)$$

It is trivial that

$$i\hbar \frac{\partial \Phi}{\partial t} = (R_1 R_2 R_3)^{-1} i\hbar \frac{\partial \Psi}{\partial t} \quad (3.31)$$

$$V\Phi = (R_1 R_2 R_3)^{-1} V\Psi \quad (3.32)$$

$$\hat{T}_{\text{other}}\Phi = (R_1 R_2 R_3)^{-1} \hat{T}_{\text{other}}\Psi \quad (3.33)$$

since the operators V and \hat{T}_{other} do not differentiate with respect to the radial coordinates and contain at most a multiplication by a function of these. On the other hand, it is easy to check that, for any $k \in \{1, 2, 3\}$

$$\hat{T}_{R_k}\Phi = -\frac{\hbar^2}{2\mu_k} \frac{1}{R_k^2} \frac{\partial}{\partial R_k} R_k^2 \frac{\partial \Psi}{\partial R_k} \quad (3.34)$$

$$= -\frac{\hbar^2}{2\mu_k} (R_1 R_2 R_3)^{-1} \frac{\partial^2 \Psi}{\partial R_k^2} \quad (3.35)$$

$$= (R_1 R_2 R_3)^{-1} \hat{T}'_{R_k} \Psi \quad (3.36)$$

where we have defined

$$\hat{T}'_{R_k} = -\frac{\hbar^2}{2\mu_k} \frac{\partial^2}{\partial R_k^2} \quad (3.37)$$

Hence, by plugging the ansatz of eq. (3.30) into the TDSE, we obtain:

$$i\hbar \frac{\partial \Psi}{\partial t} = \left(\hat{T}'_{R_1} + \hat{T}'_{R_2} + \hat{T}'_{R_3} + \hat{T}_{\text{other}} + V \right) \Psi \quad (3.38)$$

Equation (3.38) follows from the fact that the factor $(R_1 R_2 R_3)^{-1}$ cancels out from both sides of the TDSE. By this change of function, we have removed the singularity

in $R_k = 0$, simplifying the kinetic energy operator and allowing to use the sin-DVR representation of the wavefunction Ψ along the R_1 , R_2 and R_3 coordinates.

Now, an additional change of variable $u = u(\theta) = \cos \theta$ is carried out by keeping all the other coordinates identical. As a consequence, we have:

$$\sin \theta = \sqrt{1 - u^2} \quad (3.39)$$

$$\cot \theta = \frac{u}{\sqrt{1 - u^2}} \quad (3.40)$$

$$\frac{\partial \Psi}{\partial \theta} = \frac{\partial u}{\partial \theta} \frac{\partial \Psi}{\partial u} = -\sin \theta \frac{\partial \Psi}{\partial u} = -\sqrt{1 - u^2} \frac{\partial \Psi}{\partial u} \quad (3.41)$$

$$\sin \theta \frac{\partial \Psi}{\partial \theta} = -(1 - u^2) \frac{\partial \Psi}{\partial u} \quad (3.42)$$

$$\frac{\partial}{\partial \theta} \sin \theta \frac{\partial \Psi}{\partial \theta} = \sqrt{1 - u^2} \frac{\partial}{\partial u} (1 - u^2) \frac{\partial \Psi}{\partial u} \quad (3.43)$$

$$\frac{1}{\sin \theta} \frac{\partial}{\partial \theta} \sin \theta \frac{\partial \Psi}{\partial \theta} = \frac{\partial}{\partial u} (1 - u^2) \frac{\partial \Psi}{\partial u} \quad (3.44)$$

As a result, twice the kinetic energy operator in eq. (3.38) is:

$$\begin{aligned} 2\hat{T} = & -\frac{\hbar^2}{\mu_1} \frac{\partial^2}{\partial R_1^2} - \frac{\hbar^2}{\mu_2} \frac{\partial^2}{\partial R_2^2} - \frac{\hbar^2}{\mu_3} \frac{\partial^2}{\partial R_3^2} \\ & + \frac{1}{\mu_3 R_3^2} \left(\hat{J}^2 + \hat{L}_{1,2}^2 - 2\hat{J}_z^2 - \hat{J}_+ (\hat{L}_{1,2})_- - \hat{J}_- (\hat{L}_{1,2})_+ \right) \\ & - \hbar^2 \left(\frac{1}{\mu_1 R_1^2} + \frac{1}{\mu_2 R_2^2} \right) \left(\frac{\partial}{\partial u} \left((1 - u^2) \frac{\partial}{\partial u} \right) + \frac{1}{1 - u^2} \frac{\partial^2}{\partial \gamma_s^2} \right) \\ & + \frac{1}{\mu_2 R_2^2} \left[\hat{L}_{1,2}^2 - 2(\hat{L}_{1,2})_z^2 \right. \\ & \quad \left. - \hbar \left(\sqrt{1 - u^2} \frac{\partial \Psi}{\partial u} - \frac{u}{2\sqrt{1 - u^2}} \right) \left((\hat{L}_{1,2})_+^{\text{BFs}} - (\hat{L}_{1,2})_-^{\text{BFs}} \right) \right. \\ & \quad \left. + \frac{u}{2\sqrt{1 - u^2}} \left((\hat{L}_{1,2})_+^{\text{BFs}} (\hat{L}_{1,2})_z^{\text{BFs}} + (\hat{L}_{1,2})_-^{\text{BFs}} (\hat{L}_{1,2})_z^{\text{BFs}} \right. \right. \\ & \quad \left. \left. + (\hat{L}_{1,2})_z^{\text{BFs}} (\hat{L}_{1,2})_+^{\text{BFs}} + (\hat{L}_{1,2})_z^{\text{BFs}} (\hat{L}_{1,2})_-^{\text{BFs}} \right) \right] \quad (3.45) \end{aligned}$$

which is the kinetic energy reported in the manuscript. By carrying out the change of function and the change of variable, the underlying dot product in the Hilbert space is:

$$\langle \Psi, \Psi' \rangle = \int \bar{\Psi} \Psi' \rho d\tau \quad (3.46)$$

with

$$\rho = \sin \beta_s \sin \beta \quad (3.47)$$

3.2.4 From polyspherical to Cartesian coordinates: evaluation of the potential energy

The potential energy surface of H_3O of Chen *et al.* [68] is given as a function of internuclear distances, which are in turn easily calculated from the Cartesian coordinates of the positions of nuclei in the space-fixed frame of reference. Since here the system is described with the orthogonal vectors \vec{R}_1 , \vec{R}_2 and \vec{R}_3 , in turn parametrized by the scalar internal coordinates R_1 , R_2 , R_3 , β_s , γ_s and $u = \cos\theta$, one needs to express the Cartesian coordinates as functions of the latter to calculate the potential at a given geometry. The relation between the two is derived in appendix B.

3.3 Additional unreported results

3.3.1 Wavepacket propagation at low collision energy

At the end of the manuscript in appendix A we report the results of a propagation at “low” collision energy. This is done by choosing a momentum p_{exc} lower than expected from the dissociation of HCl. This propagation was carried out primarily as a way of making contact with the results obtained by Fu & Zhang [69] from full bimolecular collisions. The presence of shape resonance peaks in the calculated energy-resolved flux shows the overlap between our work and theirs.

We show in fig. 3.6 the plots of the reduced densities of the wavefunction at different times in this propagation at low collision energy. The observations we can make from these are the following:

- Overall, the wavepacket is slower than in the main propagation, as it needs 10 fs before H_a reaches HOD (this delay time was 6 fs in the main propagation),
- At the moment of the collision, we see that it splits at the entrance barrier (figs. 3.6b and 3.6c at 10 fs),
- A large part of the incoming wavepacket is reflected back towards the entrance channel (figs. 3.6b and 3.6c at 20 fs), while a smaller part of it successfully reaches the H-to-H and H-to-D channels (fig. 3.6a),
- Part of the wavefunction remains trapped in the potential well of the H_aH_bOD intermediate for long times (figs. 3.6b and 3.6c at 50 fs).

The splitting at the entrance barrier is explained by the fact that the wavefunctions contain components with collision energies above and below the barrier height. Up to some tunnelling, the latter have insufficient energy to overcome the barrier and are readily reflected back by it. This fact is conceptually different from the recoil observed in the main propagation: there, the whole wavepacket passes beyond that entrance barrier but is readily repelled by the repulsion wall of the oxygen atom.

The permanence of the wavefunction in the potential well of H_aH_bOD is the cause of the longer timescales of the reaction. Indeed, it escapes little by little from that

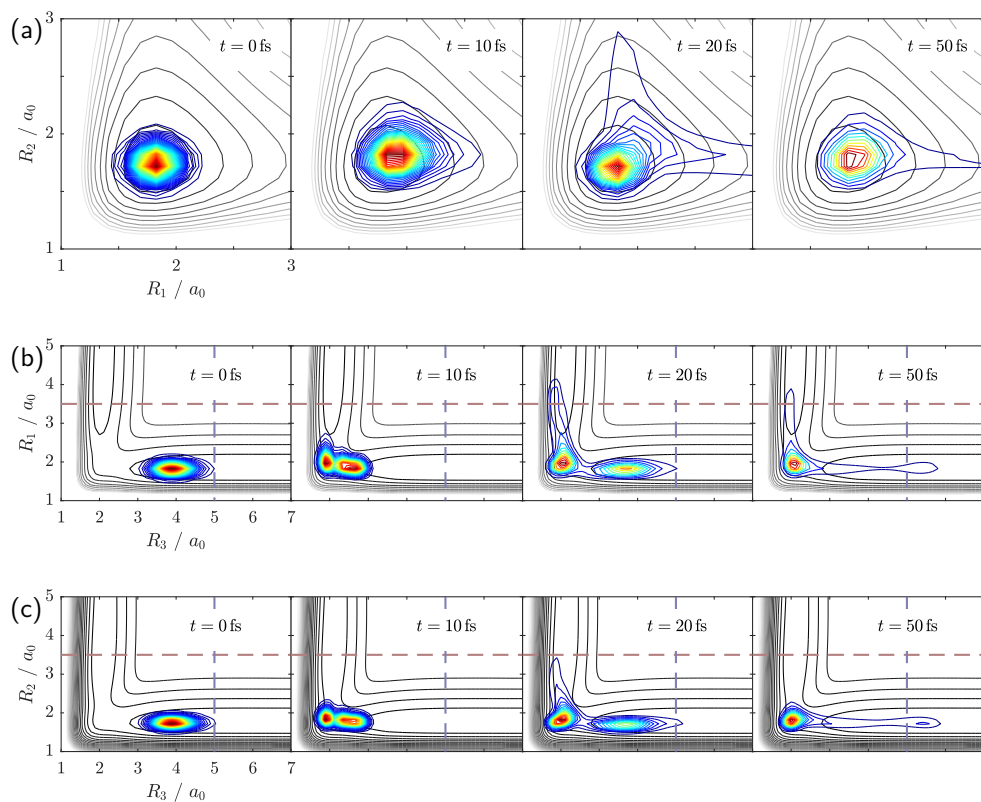


Figure 3.6: Snapshots of the reduced densities (coloured contours) of the wavepacket in the low collision energy propagation. These are given as functions of different pairs of radial coordinates: (a) R_1 and R_2 , (b) R_3 and R_1 and (c) R_3 and R_2 . Note that the densities shown at $t = 50 \text{ fs}$ is multiplied by 10. These are overlaid over cuts of the PES (grey-scaled contours) where the fixed coordinates equal their expectation value in the initial state. The dashed lines denote the beginning of a complex absorbing potential.

well and flows towards either of the three channels (recoil or exchanges). This permanence is also the reason of the appearance of the resonance peaks in the reaction probabilities, in particular in that corresponding to “H-to-H” exchange.

3.3.2 Propagation along the angular coordinates

The manuscript focuses on the dependence of the wavepacket on the radial coordinates, i.e. on how it moves along these. Indeed, the separation of any of the hydrogen or deuterium atom from the heavy oxygen simply corresponds to either coordinate R_1 , R_2 or R_3 going to infinity. However, little has been said about the motion of the wavepacket along the angular coordinates θ , β_s and γ_s . We will focus here on the dependence of the wavepacket on β_s and γ_s during the main propagation.

We recall that β_s is the angle between \vec{R}_3 and \vec{R}_2 , i.e. the polar angle of \vec{R}_2 in the E_2 frame (its definition is given in section 2.4.1). It can be seen as the angle $\widehat{H_a O D}$. Instead, γ_s is the angle characterizing the rotation of \vec{R}_1 around \vec{R}_2 . It is the azimuthal angle of \vec{R}_1 in the frame we could call “ E_2s ”, i.e. the intermediate frame obtained by rotation of the BF axes by Euler rotations by $\alpha_s = \gamma$ and β_s . It is related to the dihedral angle φ between $\overrightarrow{OH_a}$ and $\overrightarrow{OH_b}$ around the axis drawn by the O–D bond, namely, we have roughly $\gamma_s \approx \pi - \varphi$. Note that, if $\gamma_s = 0$, all the four atoms lie in the same plane whereas, if $\gamma_s = \pm \pi/2$, the two planes containing H_aOD and H_bOD respectively are perpendicular. Note also that the wavepacket is 2π -periodic along the γ_s coordinate. Figure 3.7 shows its reduced density as a function of the two coordinates β_s and γ_s at different times in the main propagation.

The influence of the shape of the PES of the $(HCl) \cdots (H_2O)$ complex on the initial state, discussed in section 3.2.1, can be put in connection to the leftmost panel, at $t = 0$. The maximum of the reduced density is located along the $\gamma_s = 0$ axis. In addition, the density is symmetric about that axis and is broadly spread over the γ_s coordinate. This observation confirms that the method of implicit inclusion of the Cl atom in the $(HCl) \cdots (H_2O)$ potential (eqs. (3.3) and (3.4)) is sufficient to obtain an initial state consistent with the fact that the complex is most likely planar and that its wavefunction is spread over large displacements of H_a from the plane of H_bOD .

By following the motion of the wavepacket in the (β_s, γ_s) coordinates over time, one notices that it does not move much until the collision between H_a and O occurs, at $t = 6$ fs. The peak of the reduced density then quickly moves to larger values of $|\gamma_s|$. This is accompanied by a slight shift towards smaller β_s . Knowing that most of the wavefunction goes back to the entrance channel (i.e. the recoil channel) this peak may indicate that, after the collision, the H_a atom is scattered away from H_bOD outside its plane.

We can then look at the propagation of the wavepacket in the (R_3, γ_s) coordinates in order to analyse this aspect. Contour plots of the reduced densities as functions of these coordinates are shown in fig. 3.8. What emerges from these is that the displacement of the wavepacket from $\gamma_s = 0$ to $|\gamma_s| > 0$ indeed happens after the collision at $t = 6$ fs. From the rightmost panel, i.e. at $t = 14$ fs, it can be seen that the part of the wavefunction describing recoil is mostly away from the plane $\gamma_s = 0$. This however seems to concern the reacting part too: the small peak around $R_3 \approx 2.7 a_0$ which corresponds to the H_a which is successfully “stuck” to the oxygen atom, is also located at values of γ_s far from 0.

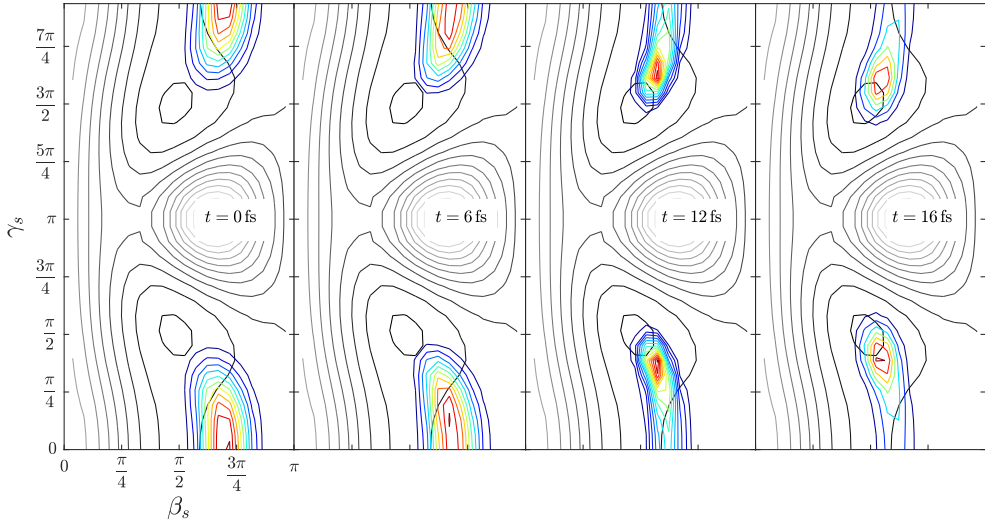


Figure 3.7: Reduced density (coloured contour lines) of the wavepacket of the main propagation as a function of the angular coordinates β_s and γ_s at different times. The black contour lines correspond to the cut of the potential energy surface at the expectation values of the other coordinates at $t = 0$.

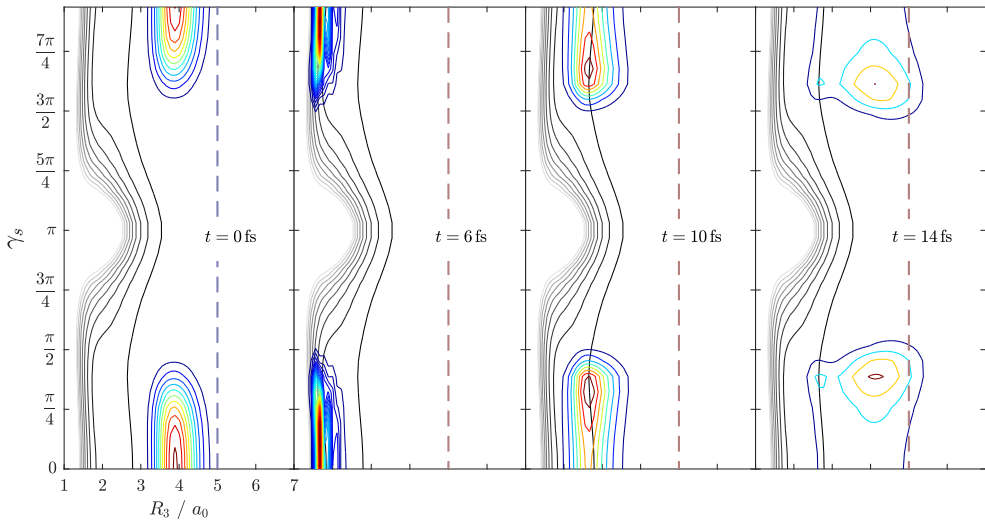


Figure 3.8: Reduced density (coloured contour lines) of the wavepacket of the main propagation as a function of the coordinates R_3 and γ_s at different times. The black contour lines correspond to the cut of the potential energy surface at the expectation values of the other coordinates at $t = 0$. The dashed line indicates the beginning of the complex absorbing potential.

3.4 Discussion: the presence of the Cl atom

As explained in the article and in this chapter, the chlorine atom was considered to play a role only in the definition of the initial conditions of the exchange reactions in eq. (3.2). In the present dynamical study we do not follow the fate of the Cl atom and focus our attention on the other $H_a + H_bOD$ subsystem. Because of this approximation, two aspects of the studied reaction have been neglected, namely how the incoming hydrogen atom H_a is accelerated towards H_bOD and whether the interaction between the Cl atom and the reacting subsystem has an influence on the results. We shall discuss them in what follows.

3.4.1 The acceleration of H_a

The hydrogen atom H_a is given the momentum gained upon *full* dissociation of H_aCl . However, it actually gains this momentum on its way to dissociation, as it is accelerated by the $A^1\Pi$ repulsive excited state of HCl. The (corrected) momentum p'_{exc} used in eq. (3.5) corresponds to the situation where the distance R_{HCl} is infinitely large. Since H_bOD is at a finite distance from H_a , the latter may not have gained all this momentum before the collision, i.e. it may encounter the potential wall of the oxygen atom before being fully accelerated by the dissociation. This approximation implies that the simulated collisions between H_a and H_bOD in the propagations (both from vibrational ground and excited state of H_bOD) are limit cases, i.e. the calculated p'_{exc} is an upper bound of what it should be. Including somehow the interaction of Cl with H_bOD in the calculation of the initial momentum p'_{exc} would yield lower collision energies. The adopted approximation is however acceptable if the potential of repulsion between Cl and H_a becomes negligible in the vicinity of the reaction region, i.e. in a set of geometries close to that of the H_3O intermediate.

The question can be addressed by analyzing fig. 3.9. By assuming that $R_3 \approx R_{OH_a}$, $\theta_3 \approx \pi$ (see fig. 3.3) and $R_{H_aCl} + R_{OH_a} = \text{constant}$, the superposition of the red and green potentials shown in the figure are a rough estimate of the total potential of H_aH_bOD along the dissociation/collision coordinate. At the Franck-Condon point, the potential describing the $H_a + H_bOD$ interaction is negligible when compared with the potential in the repulsive $A^1\Pi$ state of H_aCl . Conversely, at the opposite “turning point” on the potential wall of H_3O (around $R_{HCl} - R_{HCl}^{eq} \approx 2.5 a_0$), it is the potential of the $A^1\Pi$ state which is much smaller than the latter. Between these two points, the two potentials cross at around 0.72 eV.

What this fig. 3.9 reveals is that the repulsive potential of H_aCl should not be neglected if we were to look at the wavepacket hovering above the entrance barrier (around $R_{HCl} - R_{HCl}^{eq} \approx 1.5 a_0$). However, the initial potential energy allows it to reach the above-mentioned turning point where this repulsion is instead extinguished. As a consequence, it is correct to say that the wavepacket does not have the momentum p'_{exc} before it reaches the barrier of $H_a + H_bOD \rightarrow H_aH_bOD$, but it is still fair to consider that it gains a kinetic energy very close to ΔV_{exc} (see section 3.2.2 and fig. 3.5) before reaching the following repulsive wall. Given how the barrier height in H_3O compares

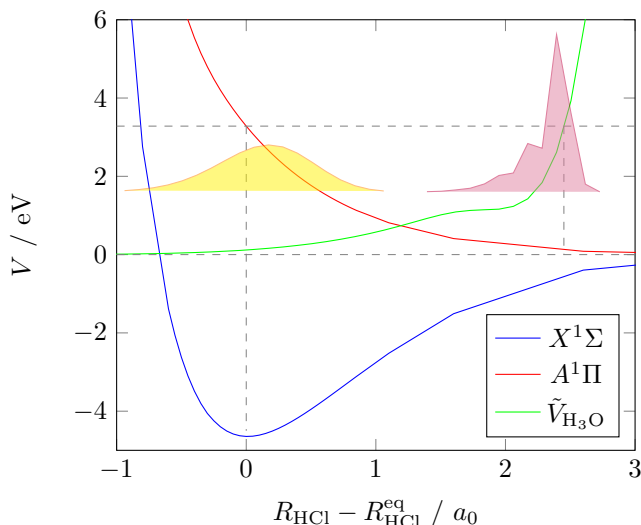


Figure 3.9: Ground (blue) and excited (red) states potentials of HCl, cut of the potential of H₃O (green) and the reduced density of the wavepacket along R_3 at $t = 0$ fs (yellow) and $t = 6$ fs (purple) in the main propagation. The zero in abscissa is the Franck-Condon point of H₂Cl. The cut of the H₃O potential, originally a function of the radial distance R_3 at fixed values of the other coordinates (expectation values at $t = 0$ fs), has been flipped and shifted horizontally by the expectation value of R_3 at $t = 0$ fs. The zero in the ordinate corresponds to the asymptotic values of the potentials at $R_{\text{HCl}} \rightarrow \infty$ and infinitely separated H + H₂O. Dashed lines mark the zeros, the Franck-Condon point and the “turning point”.

to that kinetic energy (about a factor of 2), we do not expect major variations in the computed energy-resolved reaction probabilities shown in fig. 3.2a.

If the acceleration of H_a along the H_aCl dissociation curve was taken into account, we can expect that the time-resolved reaction probabilities will look different than in fig. 3.2b. In particular, the initial delay time needed for H_a and H_bOD to encounter will be longer. However, the risetimes of these reaction probabilities would not be much longer than those reported (≈ 10 fs), as the wavepacket would anyway have too much energy to remain trapped in the H₃O potential well. The order of selectivity would be preserved as well (recoil > H-to-H exchange > H-to-D exchange).

3.4.2 Backscattering of H_a

Within the short times of the collision and subsequent exchange reactions or recoil, the chlorine atom, because of its mass, has not moved much from its initial position (about 0.07 Å in 10 fs). Therefore, fig. 3.9 may suggest that the recoiling part of the wavepacket will be pushed back again by the HCl repulsive potential towards the reaction region. In other words, the presence of the Cl atom would provoke multiple

collisions.

However figs. 3.7 and 3.8 show that after the first collision the wavepacket is mostly scattered at a different angles than $\gamma_s = 0$, that is, the recoiling H_a takes another direction than that where it came from (i.e. along the Cl–O axis). As a result, Cl would merely deflect the H_a nucleus but will not push it back in the reaction region.

The energy distribution function Δ of the wavepacket (fig. 5a. in the manuscript), is a broadly spread bell-shaped function of the collision energy. This indicates that the autocorrelation function from which it is calculated decays very quickly from $t = 0$ fs and, more importantly, remains close to zero for the entire propagation. Hence, the wavepacket never revisits its original location at $t = 0$ fs, thus supporting the fact that multiple collisions will not occur.

3.5 Conclusion and outlook

In this work we have explored the possibility of inducing a bimolecular reaction between a hydrogen atom and a HOD molecule from a hydrogen-bound complex precursor, $(HCl) \cdots (HOD)$, and simulated the femtosecond dynamics of the collision. In this chapter we summarized the main results shown in the manuscript in appendix A, detailed some of the important considerations about the studied system and provided additional information concerning how these results were obtained. Furthermore, other unreported results were presented in order to support the interpretations we originally provide. Although this study is grounded on some approximations, we hope that the observations we made here regarding these results may convince the reader of their correctness.

This model can certainly be improved. In the future we plan to change it so as to bring new insights on the role of the Cl atom in the dynamics. It is clear that the latter does not move a lot during the wavepacket propagation, owing to its mass and the short timescales of the exchange reactions and the recoil. In the limit of infinite mass of Cl, its position can be seen as the origin of a stationary repulsive potential. Therefore, it is our intention to add more degrees of freedom describing, for example, the position of the Cl atom relative to H_a . The potential to use could be a superposition of the H_3O potential used here with the spherical HCl repulsive $A^1\Pi$ state potential (somewhat as depicted in fig. 3.9). All of this would be done to test and justify the approximation regarding the neglect of Cl. We may expect, though, that the high energy of the wavepacket and the increase in the dimensionality of the model will bring extra challenges regarding the required computational resources.

4

Design of a matrix isolation setup and application to the IR spectroscopy of $(\text{HCl}) \cdots (\text{H}_2\text{O})$ complexes

The reaction discussed in chapter 3 involves the formation of the $(\text{HCl}) \cdots (\text{HOD})$ hydrogen-bound complex as a preliminary condition. Although it has served only as a starting point for the reaction, it was our intention to study this complex (and its isotopologues) from an experimental standpoint. It is the aim of this chapter to present the work that has been done from this perspective. Namely, we present the design of a new matrix isolation setup used in combination with our infrared spectroscopy facilities for the study of weakly bound complexes. This has been successfully applied for a number of systems [70]. We will focus, towards the end of the chapter, on the preliminary results that we have obtained on the $(\text{HCl}) \cdots (\text{H}_2\text{O})$ complex and various isotopically substituted analogues.

4.1 General concepts

4.1.1 Infrared spectroscopy of weakly bound complexes

Vibrational spectroscopy encompasses all the spectroscopic techniques based on the coupling between the vibrational motion of molecules and light. Of these, infrared (IR) spectroscopy is an ubiquitous technique exploiting the interaction of the electric field of IR radiation with the electric dipole moment of a molecule which oscillates as it vibrates.

Molecular vibrations are usually described in terms of normal modes, i.e. collective small displacements of the nuclei from their equilibrium positions (see section 2.5). If the displacements of the nuclei in a vibrational normal mode are accompanied by a change in dipole moment, then it will give rise to an absorption band in the IR spectrum. The larger this change in dipole moment, the stronger the band.

In the case of weakly bound complexes, we can distinguish two groups of modes.

Consider, for example, a complex of two non-linear molecules, each having respectively N_1 and N_2 nuclei. If taken on their own, each molecule would feature $3N_1 - 6$ and $3N_2 - 6$ normal modes, respectively. Now, the complex of the two has in total $N_1 + N_2$ nuclei, thus giving rise to $3(N_1 + N_2) - 6$ normal modes. By subtraction, we can deduce that complexation of two molecules gives rise to 6 modes in addition to those associated to each individual, isolated subunit. These 6 extra modes can be referred to as large amplitude *intermolecular* normal modes and are associated to hindered rotations and translations of one molecule as a whole with respect to the other. The other ones originate from the normal modes of each single molecule, describing their own vibrations within the complex. These are called *intramolecular* normal modes.

Intramolecular modes in a complex will slightly differ from the normal modes of the isolated molecules. From the perspective of one molecule, its PES is slightly modified by the presence of another one nearby. As a consequence, in the IR spectrum, the bands associated to intramolecular modes are more or less shifted with respect to those of the isolated monomer which typically lie in the mid-infrared region (MIR, from 4000 to 400 cm^{-1}). By their nature, the observation of these bands provide an indirect probe of the existence of a complex. On the other hand, the PES is in general significantly flatter along intermolecular modes and their vibrational frequencies lie in a lower range, typically in the far-infrared (FIR, from 400 to 10 cm^{-1}) [70–74]. Bands associated to intermolecular modes are direct signatures of complexes. These are of particular importance as they provide direct information about the large amplitude motion along the intermolecular potential and the interaction between molecules. In particular, along intermolecular modes, the potential is shallow and deviates from ideal harmonicity to a larger extent than along intramolecular modes. This greatly affects the complex dissociation energy, where the intermolecular vibrational zero-point energy plays a non-negligible role. While the theoretical description of anharmonicity in complexes is an active area of research, it is also worth mentioning that direct probing of intermolecular interactions in the FIR region is difficult, in particular because of the narrow choice of radiation sources suitable for that scope. Obtaining this valuable information about these interactions represents thus a major challenge, both from theoretical and experimental standpoints.

Although weak interactions are a manifestly crucial ingredient for the existence of condensed matter and biological processes, the isolation of a weakly bound complex of two molecules, the smallest system whose existence relies on these interactions, is a non-trivial task. The challenge is to bring the two molecules together and keep them in the shallow intermolecular potential energy well for a sufficient amount of time. This is hardly possible at room temperature, since the relative kinetic collision energy is too high for the complex to have a sufficient lifetime and therefore to be observable. In Bally's words [75], these are "of fleeting existence under ambient conditions". Hence, this excess of energy has to be withdrawn from the two molecules as they approach. Several techniques have been developed to that end. Matrix isolation is one of them and will be at the heart of this chapter. Other techniques worth mentioning are the supersonic jet expansion technique [29] and helium nanodroplets isolation (HENDI) [76].

4.1.2 The matrix isolation technique

Matrix isolation is an experimental technique of preparation of a sample for spectroscopic purposes [75], originally developed by Pimentel [77]. It consists in preparing a crystalline cold solid, the so-called *matrix*, containing molecules of the sample to analyse, also referred to as the *dopant* or *guest*, at low concentration. The matrix is typically made of an inert gas like Ne, Ar, Xe or N₂, kept below its melting point. This is generally called *matrix host*. Solid para-hydrogen can also be used, as discussed in chapter 5. The inertness of the matrix material, the low concentration and the low diffusion coefficient of the dopant within it are what makes the sample molecules *isolated* from one another.

This technique has proven to be a useful extension of traditional gas phase spectroscopy of single molecules, as it allows to analyse unstable species as well as reaction intermediates. In particular, isolated complexes of two or a few more molecules can also be observed, provided the existence of binding intermolecular interactions. Indeed, the excess relative kinetic energy between the two encountering molecules is withdrawn by their environment, i.e. the matrix kept at cryogenic temperature, thus allowing them to form a complex.

The low temperature also tends to simplify the IR spectra, as the populations in the excited vibrational and rotational states is reduced in favour of the ground state. This suppresses possible hot bands, i.e. allowed transitions originating from excited vibrational states, and reduces the number of rotational transitions within each vibrational transition, as only the ground rotational state is populated in the limit $T \rightarrow 0$ K. In addition, it is possible to prepare matrices containing larger amounts of diluted guest molecules than in gas phase, with significant improvements of the signal-to-noise ratio. This becomes especially advantageous when it comes to exploring the intermolecular signatures in the FIR region, where the availability of intense broadband light sources in that spectral range is limited. Matrix isolation can indeed be used in combination with conventional Fourier Transform Infrared (FTIR) spectrometers (see e.g. [78]), as the intrinsic low sensitivity of this type of instruments, in particular in the FIR, is compensated by the high concentration of sample one can achieve by this technique. Otherwise, tunable and intense THz/FIR lasers exist but can explore only a narrow range of frequencies in the electromagnetic spectrum. Alternatively, for special cases, one could consider using highly demanded large-scale facilities such as synchrotrons like the AILES infrared beamline at SOLEIL in France [73, 74, 79] or free-electron lasers like the FELIX laboratory in the Netherlands [80].

Although the interaction between the host material and the guest molecules is weak, it still has a small noticeable influence on the IR spectrum of the latter, depending on the strength of that interaction. Indeed, IR bands associated to vibrational transitions in a matrix isolated monomer are shifted compared to the same bands observed in gas phase. These shifts are part of so-called *matrix effects* caused by host-guest interaction and their magnitude varies from one matrix host to another. Note that in some cases, like in a Kr or N₂ matrix, several bands may arise from the same vibrational transition in a molecular system due to its placement in the

crystal lattice (or more precisely which interstitial or substitutional site it occupies). These *site splittings* are seldom observed in Ne or para-hydrogen matrices. Moreover, neon has proven to be one of the least perturbing host materials, as the positions of the matrix isolated and gas phase water monomer bands differ by only $+8.3\text{ cm}^{-1}$ ($+2.3\%$) for the ν_1 band, $+0.8\text{ cm}^{-1}$ ($+0.5\%$) for ν_2 and $+3.7\text{ cm}^{-1}$ ($+1.0\%$) for ν_3 [71]. Similar small shifts are observed in para-hydrogen, whereas they can be up to one order of magnitude larger in other noble gas matrices.

In practical terms, the preparation of a matrix consists in slowly depositing the gas phase mixture of host and guest molecules on a cold support – a process that we will henceforth call *matrix deposition*. The support is generally an optical window or a gold plated mirror. This is attached to a *cryostat* (literally, a cold thermostat) whose purpose is to maintain the temperature sufficiently low for the host material to solidify and retain it over the whole duration of the experiment. The inclusion of a temperature probe and a heater coupled to feedback electronics allows for controlling the temperature of the sample. An *inlet system* is the apparatus whose function is to channel the host and guest gases from the source containers to the cold support, thus realizing the deposition. Depending on their nature, the host and guest gases can either be mixed together in one same flask or deposited from separate ones.

A sample in a matrix can additionally be exposed to external stimuli. Several examples can be found in the literature, the most typical being irradiation by UV light [75, 81]. Of these, annealing is the most relevant for the scope of this work. Thanks to the control of the matrix temperature, the latter can be adjusted to a higher value than during the deposition phase. As a consequence, the matrix becomes softer and guest molecules acquire more freedom to move through it. The enhanced diffusion increases the chances that two monomers initially isolated in the matrix will encounter and form a complex. Hence, annealing has an impact on the recorded spectra, as monomer bands decrease in intensity whereas that of those corresponding to complexes increase. The assignment of the spectral bands is therefore facilitated by this intervention.

4.2 Design of a matrix deposition setup for FTIR spectroscopy

This section will present the design of the new matrix deposition setup in our laboratory. As a starting point, we will give an overview of the pre-existing equipment so as to understand the constraints of development of the setup. Next, we will focus on two of its main components, i.e. the gate valve and the inlet system. An overview of the whole assembly will then conclude this section.

All the parts the setup is made of were designed with the SOLIDWORKS 2017 Computer Aided Design (CAD) program. In this section, some of the figures show captures of the three-dimensional models drawn with the program, in particular the final result in fig. 4.5, page 65. These models were eventually transcribed to technical dimensional drawings which were then given to the machine shop of the department for their production. These are shown in appendix C.

4.2.1 Description of the starting available equipment

The matrix isolation setup described here has been designed for the instruments that were available in our laboratory at the beginning of the present Ph.D. project.

We use a closed-cycle helium cryostat (Advanced Research Systems, model DE-204) as the cooling instrument for forming and preserving the matrix. The “head” of the cryostat encloses a gas expander. Helium is flown through the expander along sealed, thermally insulated pipes. The circulation is operated by a dedicated compressor. The expander is the cooling component of the cryostat and withdraws heat from a so-called *cold tip* or *cold end*. This is the coldest point in the cryostat and it is where the object the experimenter wants to cool down is placed. An oxygen-free high conductivity (OFHC) copper sample holder is firmly screwed on this cold end, with an indium gasket interposed between the two to guarantee good thermal conduction. An optical window of caesium iodide (CsI, IR transparent down to approx. 200 cm^{-1}) or potassium bromide (KBr, IR transparent down to approx. 400 cm^{-1}) is mounted on the holder. This is where the matrix will be deposited. The cold end, with the attached sample holder, is surrounded by a *radiation shield*, i.e. a metallic cylindrical cover attached to a part of the cryostat which undergoes less intense cooling. Its function is to protect the sample and the cold end from blackbody radiation emitted by the surrounding objects of the laboratory at room temperature, thus limiting *radiative heating* of the sample. On top of all this, an additional rigid *vacuum shroud*, i.e. a cylindrical vacuum tight metallic enclosure, is mounted on the cryostat with sealing elastomer o-rings. Note that this shroud can be manually rotated about its axis. Under operation of the cryostat, the air contained within the shroud is evacuated by a pair of oil and turbomolecular vacuum pumps so as to reach pressures down to an order of magnitude of 10^{-6} mbar. Pumping that space prevents air molecules to freeze on the cold parts of the cryostat and, in particular, on the sample optical window. Otherwise, these would prevent the cryostat from reaching the lowest possible temperature and compromise the quality of the sample and thus of the recorded spectra. In addition, the rarefied environment inside the vacuum shroud prevents diffusion of heat from the outside to the sample (*collisional heat transfer*). The present cryostat can reach temperatures down to 3.9 K without load or exposition of the cold end to ambient light.

For the cryostat to be used for spectroscopic applications, the radiation shield and the vacuum shroud are tailored such that a beam of IR light can pass through the sample. The radiation shield has two openings on either side of the sample holder and the vacuum is equipped with four ports placed at the same height as these. On two of these, a pair of vacuum sealed optical windows of the same material as the sample window are mounted. The two others were originally covered by blank flanges. As we will see further, one of these ports will be used by the matrix deposition apparatus.

The laboratory is equipped with a Bruker Vertex 80v Fourier Transform Infrared (FTIR) spectrometer. No modification have been made on it, except from the sample compartment lid which has been replaced by a pair of aluminum boards. These allow for the placement of the cryostat inside it in such a way that the IR beam passes

through the sample on the cooled optical window.

A structure made of aluminum profiles holds the cryostat suspended above the experimental table where the spectrometer is laid. This structure is uncoupled from the table, preventing vibrations of the cryostat to propagate through the latter. The cryostat is oriented vertically, a pulley allows for adjusting its height and it can be moved horizontally across the table. In this way, the cryostat can be moved between two set positions, one being inside the sample compartment of the FTIR instrument and the other one being free space on the opposite side of the table. That space is where the matrix deposition will be carried out.

4.2.2 General requirements and constraints

The matrix deposition setup which we are going to describe is inspired from the design used by Andersen in the now decommissioned Max-Lab in Lund [71].

The above-mentioned spectrometer is a shared facility also used in a number of different projects and could hence not be modified. Thus, the matrix deposition could not be carried out *in situ* in the sample compartment. It was therefore decided to use the available space of the spectrometer table for this operation, as mentioned in the previous subsection.

This separation of the experiments in two steps – the deposition and the measurement – poses several technical challenges, in particular because the matrix deposition hardware, i.e. the inlet system, needs to be detachable from the cryostat. The following considerations needed to be borne in mind in its design:

- The access to the inner space of the vacuum shroud must be given by an opening of sufficient width for the inlet system to penetrate inside it.
- Since the inlet system and the cryostat must be detachable from each other, the latter must be able to operate independently. Since this requires the volume delimited by the vacuum shroud to be evacuated, that opening must be shut and vacuum-sealed when necessary.
- As the deposition must be done when the cryostat is cold (i.e. when it is evacuated) the access point cannot be opened directly to open air and the inlet system needs to be inserted through it without breaking the vacuum.
- When connected to the cryostat, the inlet system must be movable in order to, on the one hand, reach the cooled sample window and, on the other hand, be in a position such that the access point can be closed. This degree of freedom of the inlet system must guarantee vacuum tightness of its enclosure.
- Because of limited space in the spectrometer sample compartment and the fact that the vacuum shroud of the cryostat is held in place only by friction with a pair of sealing o-rings, the extra hardware added to it (for compliance with the previous considerations) must be sufficiently compact (for the whole to fit in the compartment) and light (to prevent the shroud to fall off).

- The width of the tubes at the end of the inlet system (those from which the host and guest gases are “sprayed” on the cold support) must be of an adequate width so as not to be a bottleneck of the flow of molecules but also to realize a directed beam.

In addition to these constraints, the following features were desirable in the inlet system:

- In order to realize the deposition of the host gas and two different guest gases from separate sources, the inlet system should have three separate channels – one for the host gas and two for the guest samples. This would allow for simultaneous deposition of deuterated and non-deuterated samples. Premixing and depositing them from the same tube would otherwise give erroneous results, as deuterium atoms may be exchanged by regular protium.
- The host gas should be pre-cooled as it flows towards the cryostat. This reduces the heat load that the cryostat has to compensate for as the gas sticks to the cold support. In addition, the host gas channel is the main potential source of impurities, since most matrix matter comes from it. A cold trap would then act as a cryopump where impurities, in particular water, are caught before being deposited.
- The flow of the various gases should be controllable.
- It should be possible to control the placement of the tubes with accuracy, in particular for optimally choosing the distance from their end to the optical support.

The designed setup is made of three main parts: a gate valve, the inlet system and a moving tray. We refer to fig. 4.5 for a global view of the whole matrix deposition setup. Detail of its parts will be given in the following. Note that the choice of o-rings and corresponding hosting grooves have been determined based on various recommendations from o-rings manufacturers, in particular those given by M-Seals and Parker Hannifin in their respective catalogues.

4.2.3 Gate valve

The vacuum shroud features, in addition to optical windows, two blank flanges at the level of the sample, each covering a hole. It was therefore decided to replace one of these by a component guaranteeing the access to the inlet system and acting as the shutter when the cryostat needs to be moved.

A *gate valve* is a component which joins or separates two volumes by extracting or inserting a separation wall between these. This type of valves is ubiquitous in vacuum technology and is the kind of component that is used here as the interface between the vacuum shroud and the inlet system. However, commercial solutions were not suitable for our purposes, as suppliers generally sell bulky valves for large vacuum

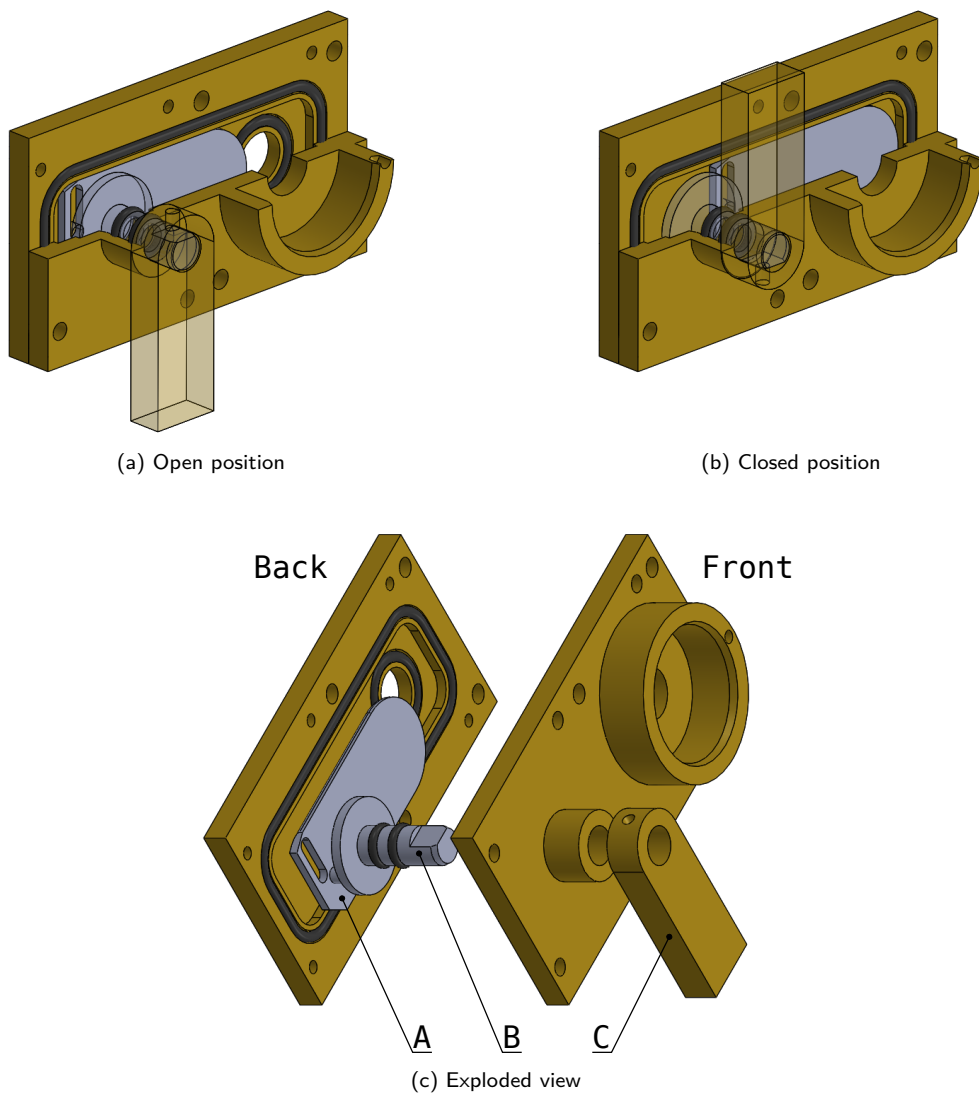


Figure 4.1: Computer model of the gate valve. (A) Shutter, (B) Cam, (C) Lever.

chambers. Given the size of the openings in the vacuum shroud, we needed to build a custom one.

The adopted solution follows a design similar to that proposed by Wahl *et al.* [82]. Our version is shown in fig. 4.1. This compact gate valve consists in a brass case made in two parts which we call “back” and “front”. An o-ring is hosted in a rectangular groove in the inner side of the back part. Six screws press the two parts together so as to keep the contour of the case vacuum tight. A hole of $\varnothing 1$ cm pierces the two parts, realizing the access passage for the inlet system tubes. The whole case is fixed against the vacuum shroud, replacing one of the blank flanges and pressing an o-ring hosted in its own groove on the shroud.

On the inner side of the back part, a space delimited by the rectangular groove is cleared and an additional groove and o-ring surround the piercing hole. This rectangular space hosts a stainless steel plate which slides along the long side. This piece is the *shutter* whose function is to close the passing hole. In its closed position (fig. 4.1b) it presses the circular o-ring and seals the vacuum shroud. In its open position (fig. 4.1a), it only covers a small part of that o-ring so as to prevent it from escaping from its groove.

The position of the shutter is controlled by a *cam*. This stainless steel part is made of a circular disk, a shaft sticking out from the center of one of its faces and an eccentric small pin. The latter is inserted in a slot drilled in the shutter. Via that pin, the rotational motion of the cam is converted into translational motion of the shutter. In other words, by rotating the shaft by half a turn, the pin drives the shutter from one position to the other. The shaft of the cam goes through a hole through the front part of the brass case where it can be manually accessed. A pair of o-rings on the cam shaft seal off the inside of the case from this hole. An additional lever is mounted on the cam for effortless operation.

Finally, the outer side of the front part of the case features a cylindrical lip, coaxial with the access hole. This is the connection point with the inlet system described in the next subsection.

4.2.4 Inlet system

The inlet system, in its simplest conceptualization, is nothing but a set of three tubes kept together side by side. The gaseous host and guest samples are introduced in one end so as to exit from the other. These eventually reach and settle on the cold support so as to form the matrix. The existence of the other components in this inlet system is ascribed to the various constraints due to working with vacuum. The assembly is shown in fig. 4.2.

To start, we have a stainless steel “interface” (in appendix C, it is called “static tube”) which is the component which is plugged on the gate valve, at the access point of the cryostat. This features a short cylindrical protuberance (with a groove around it hosting an o-ring) on the center of a disk. A longer threaded shaft, coaxial with the protuberance, is machined on the opposite side of the disk. A cylindrical hole is pierced through the two. The protuberance fits inside the lip of the valve and is used

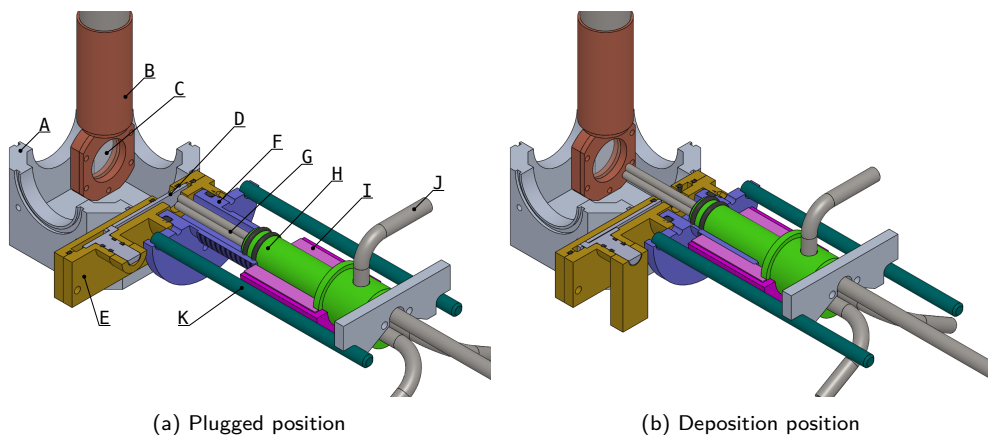


Figure 4.2: Partial cut view of the computer model of the inlet system, plugged on the gate valve mounted on the vacuum shroud of the cryostat. (A) Vacuum shroud, (B) Cryostat cold end, (C) Sample optical window, (D) Gate valve shutter, (E) Gate valve case, (F) Inlet system static interface, (G) Inlet tubes, (H) Inlet system sliding cylinder, (I) Positioning knob, (J) Pumping/venting tube, (K) Guide rails.

to plug the inlet system to the gate valve. The tubes of the inlet system are instead inserted from the threaded shaft side.

Another component is a hollow stainless steel “cylinder” (the “sliding tube” in appendix C) which slides along the hole of the interface. This part is capped at the wider end. Near the edge of the narrower opposite open end, a pair of o-rings are retained by two small grooves. Now, by inserting this cylinder inside the interface, o-rings are pressed against the latter, thus sealing off the volume contained inside the interface and the cylinder from the ambient air. This volume is therefore vacuum tight when the interface is plugged on the gate valve. An L-shaped tube soldered on the side of the cylinder is used for its evacuation and venting.

The position of the cylinder along the static interface is finely controlled by a knob that wraps the former. It has an inner thread which fits with that of the interface. When the two threaded parts are engaged, rotating the knob forces the cylinder to move along the hole. The outer shell of the knob is knurled so as to increase grip, hence easing its handling. Additional rails, united with the interface, guide the sliding cylinder so as to secure the longitudinal displacements.

The moving cylinder is the part that acts as a feedthrough of the matrix gases to deposit. Three piping tubes of diameter $\varnothing 1/4''$ are soldered on through-holes on the end cap of the cylinder. The gases source flasks will be connected on these. On the other side of this cap end, i.e. in the inside of the cylinder, narrower $\varnothing 1/8''$ tubes are welded. These extend the outer wider tubes inside the sealed volume, reaching a point beyond the edge of the cylinder. It is from that end that the deposited gases will be “shot” towards the cold optical window of the cryostat.

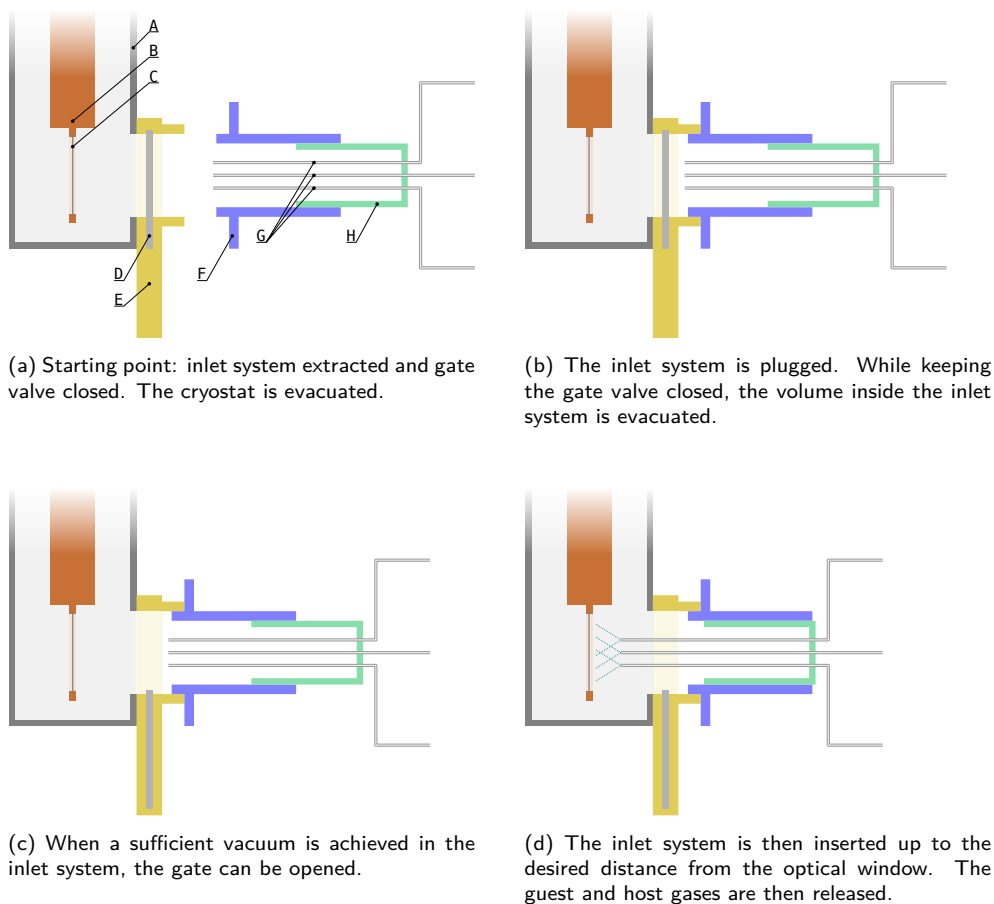


Figure 4.3: Schematic representation of the matrix isolation setup and main steps of the deposition procedure. When the deposition is over, the same shown steps are followed backwards. (A) Vacuum shroud, (B) Cryostat cold end, (C) Sample optical window, (D) Gate valve shutter, (E) Gate valve case, (F) Inlet system static interface, (G) Inlet tubes, (H) Inlet system sliding cylinder.

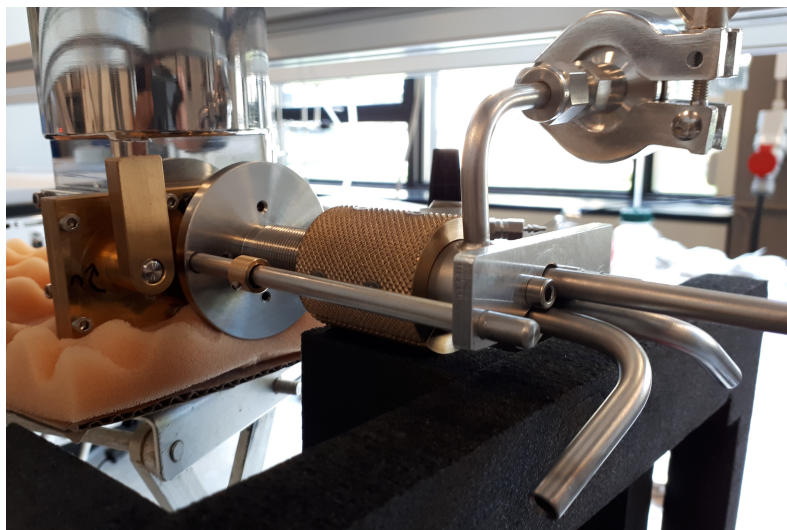


Figure 4.4: Photography of the inlet system plugged into the gate valve on the cryostat vacuum shroud.

Figure 4.2 shows the three-dimensional computer model of the inlet system when plugged on the gate valve at two different positions. When the sliding cylinder is withdrawn to the maximum (i.e. its pair of o-rings is at the edge of the threaded tube of the interface, see fig. 4.2a), the shutter of the gate valve can be kept closed and the deposition tubes end lie a little behind it. After opening the valve, the sliding cylinder can be pushed inside the interface (by turning the knob) and the deposition tubes can penetrate inside the volume of the vacuum shroud, eventually reaching the optical window (fig. 4.2b). Figure 4.3 is a simplified schematic of the inlet system showing the subsequent steps of usage of the inlet system. Finally, a picture of the real inlet system is shown in fig. 4.4.

4.2.5 Complete setup

The core of the deposition setup is made of the inlet system and the gate valve described above. What remains at this point are the connections to the source host and guest gases containers and a structure which carries these and the inlet system itself. A horizontally sliding tray was made for the latter purpose. With this, manual plugging of the inlet system on the gate valve and their separation are done in a practical and systematic way. The final result is shown in a capture of the three-dimensional computer model in fig. 4.5.

Of the three inlet system lines, two are used for piping the guest gases. Each is connected with standard $\varnothing 1/4'$ stainless steel tubing via metering valves (Swagelok SS-SS4-A-VH) for fine adjustment of the gas flow. Additional pumping/venting ports

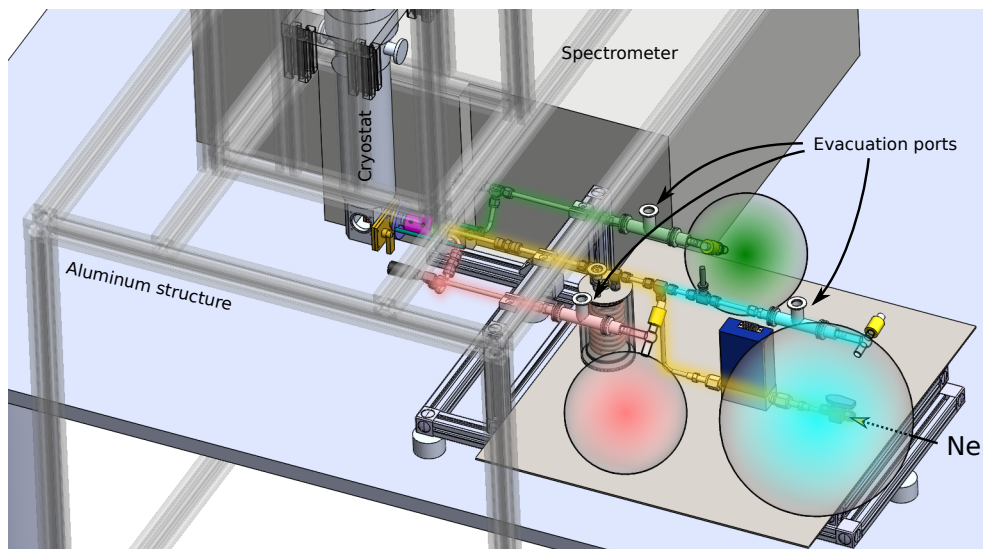


Figure 4.5: Overview of the whole matrix isolation experiments setup. Each gas channel is shaded with a different colour.

are included.

The host gas line is made of two branches, one that uses another metering valve (Swagelok SS-SS4) and the other featuring a flow mass controller (mks, GM50A type). The former is intended to be connected to a large gas flask containing enriched parahydrogen (see chapter 5) and the latter is connected to a neon gas cylinder. A coiled portion of tubing connects the union of the two branches and the remaining port of the inlet system. That portion is contained in a dewar which can be filled with liquid nitrogen and acts thus as a cold trap. With this, high melting point impurities (in particular water) in the host gas are caught before getting deposited on the cold support. Additionally, the cold trap lowers the temperature of the host gas before it reaches the latter, thus lowering the heat load that the cryostat has to compensate for. This line is also equipped with pumping and venting ports.

4.3 Application to the FTIR matrix isolation spectroscopy of (HCl)⋯(H₂O) in neon

The matrix deposition setup has successfully been applied to a number of studies of matrix isolated complexes in the MIR region [70]. In the following, we show the preliminary results of the study of the (HCl)⋯(H₂O) complex, henceforth noted (HCl)(H₂O) for simplicity, and its isotopologues in that region. Note that this is (up to a deuterium atom) the initial state complex used in the work presented in chapter 3. We will first give an overview of the known features of this complex. This complements the discussion in section 3.2.1, although the details mentioned in what follows are more spectroscopy-oriented. After a brief description of the followed experimental procedure (synthesis, deposition and measurements), the recorded spectra will be shown and tentative assignments of the observed signals will be given.

4.3.1 Introduction

Hydrogen chloride is a corrosive gas which has a pungent smell. It is best known in water solution as hydrochloric acid or as muriatic acid. Even though it is a well-known compound, there is still work carried out until recently concerning its interaction with water molecules and its microsolvation in water [61, 83–87].

The HCl molecule is IR active, with the band center of the H³⁵Cl fundamental vibrational transition at 2885.9775 cm⁻¹ [88]. Its rotational constant in the vibrational ground state is 10.5909 cm⁻¹ [63]. The two stable isotopes of the chlorine atom, ³⁵Cl and ³⁷Cl, have natural abundances of about 75% and 25% respectively. Thus, the band origin of H³⁷Cl lies about 2 cm⁻¹ below that of H³⁵Cl and its spectral lines have an intensity three times smaller. Concerning complexes containing HCl, it is expected to observe multiple neighbouring peaks each corresponding to the same vibrational transition in the different isotopologues.

A number of studies exist on HCl, its oligomers and its complexes with water in various matrices [81, 89–97]. Concerning HCl only, the spectral signature of the monomer, dimer, trimer and some higher order oligomers were observed in neon in the MIR [95, 96] as well as in the FIR [97]. Additional information on these spectra was provided by studies on ionized HCl oligomers [81].

For the mixed complex of HCl and H₂O in matrices, spectra were observed in less inert host materials such as nitrogen and argon [89–91, 93, 94]. A dedicated survey of (HCl)(H₂O) in neon is surprisingly missing. In their respective studies, Andrews & Bohn [95] and Forney *et al.* [81] assign a weak band in their spectra to the complex with water. Yet, their focus is on HCl oligomers and water is seen merely as an impurity. The more extensive analyses in other matrices assign a band to the 1:1 mixed complex and reveal that HCl is the hydrogen-bond donor in the complex with water. In particular, it was understood that it is not in the binary complex that HCl dissociates to form the ionic pair (Cl⁻, H₃O⁺).

Other techniques have been used so as to observe infrared spectra of this complex

as well as larger mixed oligomers. These include supersonic jet expansions combined with FTIR [98, 99], cavity ringdown spectroscopy [100, 101] and helium nanodroplets isolation laser spectroscopy [84, 85, 102]. A large body of computational investigations on these complexes have been carried out as well [61, 62, 86, 87, 103–113], some of which indicate that four water molecules are needed to dissociate HCl and form a stable Solvated Ion Pair (SIP) [87, 108–111].

The preliminary work presented in the following aims at identifying the spectral features of the (HCl)(H₂O) complex and its isotopologues in a neon matrix. In addition to be an interesting test case for the deposition apparatus shown in section 4.2, this study provides additional data characterizing the complex. Furthermore, it is the first step towards the study of this complex in the challenging FIR region, in particular in view of its peculiar behaviour explained in section 3.2.1 concerning its “effective” planarity, in spite of the fact that its global minimum energy geometry is not [61].

4.3.2 Experimental details

HCl gas was synthesized *in vacuo* by dropwise addition of concentrated sulphuric acid on KCl powder. The formed HCl vapours were caught in a liquid nitrogen cooled cold trap. These were then thawed and directly collected in a special gas flask equipped with a “finger”, i.e. a protuberance which can be cooled in order to freeze the contained sample. Its deuterated version, DCl, was obtained following this same procedure using deuterated sulphuric acid-d₂ (99.5% of deuterium) in place of the regular one. The inner walls of the glassware were rinsed with D₂O prior to the synthesis and transfer to its storage flask. Water vapour was collected by degassing Milli-Q liquid water. Similarly, D₂O (99.99% deuterium) vapour was obtained from the liquid. A sample of equilibrium amount of HOD gas was obtained by degassing a mixture containing equal amounts of D₂O and H₂O.

The matrix isolation setup described earlier was used. This was equipped with caesium iodide (CsI) windows both on the vacuum shroud along the beam path and the cold support. In all cases, the gases were deposited from separate inlet ports (no premixing). When using a deuterated sample, the corresponding port to which the source flask was connected was flushed with D₂O vapour prior to evacuation.

The relative amounts of guest gases were controlled by preliminarily filling the respective source flasks at selected pressures (of the order of 0.5 – 1 mbar) and opening the metering valves by the same number of turns (one and a half). An excess of the host gas, neon in this case, was co-deposited with the guest molecules. Each deposition was carried out over 60 minutes as soon as the cold support reached 4.14 ± 0.02 K. The heat load of the settling gases increased it to 4.32 ± 0.02 K during deposition.

The measurements of the IR spectra were taken on the Bruker Vertex 80v spectrometer in the MIR region using the internal blackbody radiation source (globar), a germanium-coated potassium bromide (KBr/Ge) beamsplitter and a liquid nitrogen cooled HgCdTe (MCT) detector at a spectral resolution of 0.6 cm^{-1} . Each single channel spectrum is an average of 1600 scans. The temperature of the matrix during

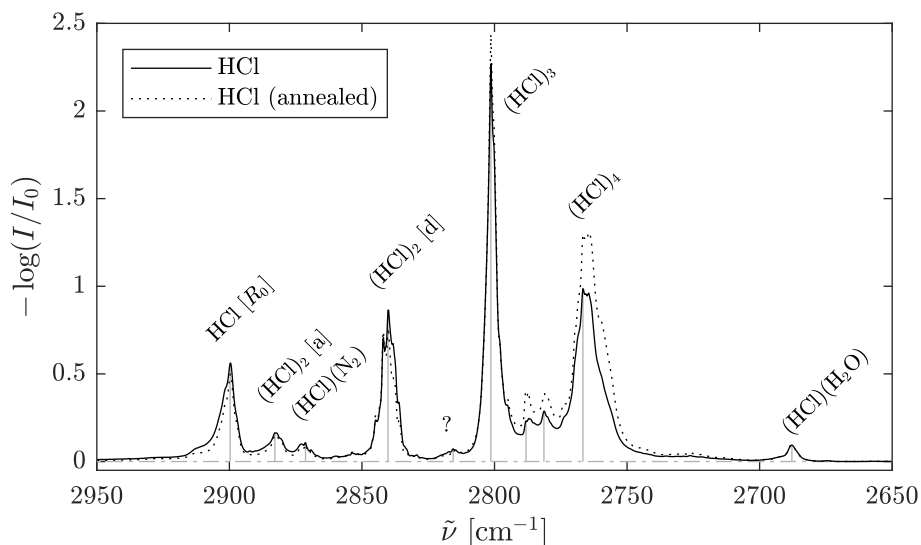


Figure 4.6: MIR absorption spectrum of HCl in a neon matrix at 4.3 K.

measurements was 4.30 ± 0.02 K. In some cases, we annealed the matrix at 8.5 K. The matrix was then cooled again and spectra taken when the temperature fell down again to 4.3 K. Background spectra were taken after removal of the matrix, with the cryostat warmed up at room temperature.

4.3.3 Preliminary results

Owing to the fact that, in the $(\text{HCl})(\text{H}_2\text{O})$ complex, HCl acts as the hydrogen-bond donor, we will focus on the spectrum of the perturbed HCl subunit in the complex and show spectra of matrices in the HCl stretching region and below, i.e. between 3000 and 2300 cm^{-1} . Analogously, the same will be done for complexes with DCI in the region between 2200 and 1700 cm^{-1} . Table 4.1 (for HCl) and table 4.2 (for DCI) summarize the bands assignments discussed in this subsection. These assignments were supported by *ab initio* calculations which are detailed in appendix D.

HCl only

The spectrum of HCl deposited with neon in the MIR region between 2950 and 2650 cm^{-1} is given in fig. 4.6. It features several strong bands, the most prominent being at 2899.5 cm^{-1} , 2839.9 cm^{-1} , 2801.4 cm^{-1} and 2766.7 cm^{-1} .

We confidently assign the peak at 2899.5 cm^{-1} to the R_0 rovibrational transition of the HCl monomer. As mentioned above, the band center in gas phase is 2885.309 cm^{-1} . The R_0 line in gas phase is then expected at 2901 cm^{-1} . We rule out

the possibility that it corresponds to a transition concerning the HCl stretching in larger oligomers or complexes as these are expected to lie below that of the monomer. In fact, in a binary hydrogen-bonded complex of the type A–H···B, where A–H is the hydrogen-bond donor and B is the acceptor, the A–H bond is weakened and elongated by the latter [114]. The weakening results in a smaller bond force constant and the corresponding IR band is red-shifted with respect to the monomer band. This is also observed in larger oligomers, where the size of the red-shift generally increases with the number of subunits, due to hydrogen bond cooperativity (see below).

Thus, the peaks at 2839.9 cm^{-1} , 2801.4 cm^{-1} and 2766.7 cm^{-1} are assigned to the (HCl)₂ donor stretching mode, the (HCl)₃ doubly-degenerate stretching mode and to a (HCl)₄ mode, respectively. In particular, the assignment of the trimer and tetramer bands is suggested by the increase in intensity upon annealing, accompanied by the decrease of that of the monomer band and the somewhat stable intensity of the donor mode in the dimer. This indicates that, as the matrix is annealed, monomers and dimers diffuse in the medium and encounter, thus forming the larger trimers and tetramers.

Another argument for the assignment of the bands at 2801.4 cm^{-1} and 2766.7 cm^{-1} comes from the fact that these trimers and tetramers have cyclic structures where each HCl subunit is simultaneously a donor and an acceptor (see e.g. [115]). Thus, the cooperativity of the hydrogen bonds polarizes even further the H–Cl bonds which is why, even at low concentrations, the absorption of these bands is so strong (see also appendix D). Since the weaker features at 2788.1 cm^{-1} and 2781.4 cm^{-1} grow like the band at 2766.7 cm^{-1} upon annealing, these are also tentatively assigned to tetramers and possibly pentamers.

Going back to the higher part of the spectrum, we assign the weak band at 2882.8 cm^{-1} to the acceptor stretching mode in (HCl)₂. Note that elsewhere [81, 95] it was assigned to the impurity-induced non-rotating HCl monomer. We motivate our assignment by the fact that this band is much less shifted than the donor mode in the dimer. Our calculations (see appendix D) predict a red-shift of 15.3 cm^{-1} and a band intensity which is about a fifth lower than that of the latter. This is consistent with the fact that the perturbations undergone by the acceptor subunit upon complexation are minor and its vibrational band is significantly less shifted compared to that of the donor.

The other neighbouring short peak at 2871.3 cm^{-1} is assigned to the (HCl)(N₂) complex by Andrews & Bohn [95], as they could show that this band increases in intensity with the concentration of N₂ in the matrix. Its existence in our spectra is then most likely due to the presence of a minor amount of N₂ in the source sample.

The peak at 2687.8 cm^{-1} is assigned to the HCl stretching in the (HCl)(H₂O) complex, as in [95]. This is due to some residual water which was also present in the matrix (the water stretching and bending regions, not shown here, display a few weak peaks of the water monomer and dimer). This last assignment will be evident in what follows.

HCl and H₂O

In the HCl stretching region under consideration, no bands are observed for H₂O in Neon. We show in figs. 4.7 and 4.8 the spectra of neon matrices with HCl and H₂O at different concentrations, along with that of HCl only, shown before. Note that the spectra are all normalized to the height of the HCl monomer line for better comparison.

The most noticeable effect arising from the addition of water is the overall decrease in intensity of all the features described so far in the HCl spectrum, except the peak at 2687.8 cm⁻¹ which, instead, grows substantially. This behaviour confirms the assignment of this band to the stretching of HCl in the (HCl)(H₂O) complex. Indeed, by increasing the proportion of water in the matrix, the likelihood of forming mixed (HCl)_n(H₂O)_m complexes increases at the expense of forming less HCl oligomers.

A few minor features around the 1:1 mixed complex modestly appear as the proportions of water and HCl are varied. Comparison with results from supersonic jet FTIR and helium nanodroplets isolation experiments suggests that the extra peaks at 2759.9 cm⁻¹ growing below the tetramer band and the weak feature at 2745.0 cm⁻¹ may be associated to the complexes (HCl)₂(H₂O) [84, 85, 99] and (HCl)₃(H₂O) [84, 116], respectively. Moreover, there is also a pair of broad features around 2533.0 cm⁻¹ (with two components centred at 2538.4 cm⁻¹ and 2527.3 cm⁻¹) and 2401.6 cm⁻¹ which grow with increasing proportion of water, as shown in fig. 4.8. We tentatively assign these to (HCl)₂(H₂O), again, and (HCl)(H₂O)₂, respectively. The relative intensities of these bands scale with the proportion of HCl and H₂O, consistently with the work of Fárník *et al.* [99]. More work is needed to make the assignment of these weak features more definitive.

HCl and water isotopologues

The spectra of matrices with HCl and either HOD or D₂O are given in fig. 4.9 and fig. 4.10, along with those of the single compounds HCl, HOD and D₂O. The spectrum of HCl with H₂O, taken from figs. 4.7 and 4.8, is also plotted there for direct comparison.

The transitions associated to the O–D stretching modes of HOD, D₂O and their own complexes are located in the region we have considered so far. These are listed in table 4.1 and we refer to the dedicated literature for their assignment [117]. Note that the spectrum of HOD is actually that of a mixture of H₂O, HOD and D₂O in equilibrium proportions 1:2:1 (see e.g. [118]), thus the presence of peaks proper to D₂O in this region.

The spectra of the mixtures contain the same features, at the same (normalized) intensities, arising from HCl and its oligomers. Additional peaks from monomeric or dimeric forms of deuterated water complexes are also present. Note, in particular, that the HCl trimer band coincides with the D₂O monomer band at 2801.5 cm⁻¹, thus the persistence of the sharp and intense peak in the HCl/D₂O spectrum.

We focus our attention to the region 2675 – 2700 cm⁻¹ shown in the inset of fig. 4.9, i.e. around the (HCl)(H₂O) band assigned previously. By closely comparing

4.3. Application to the FTIR matrix isolation spectroscopy of $(\text{HCl})(\text{H}_2\text{O})$ in neon

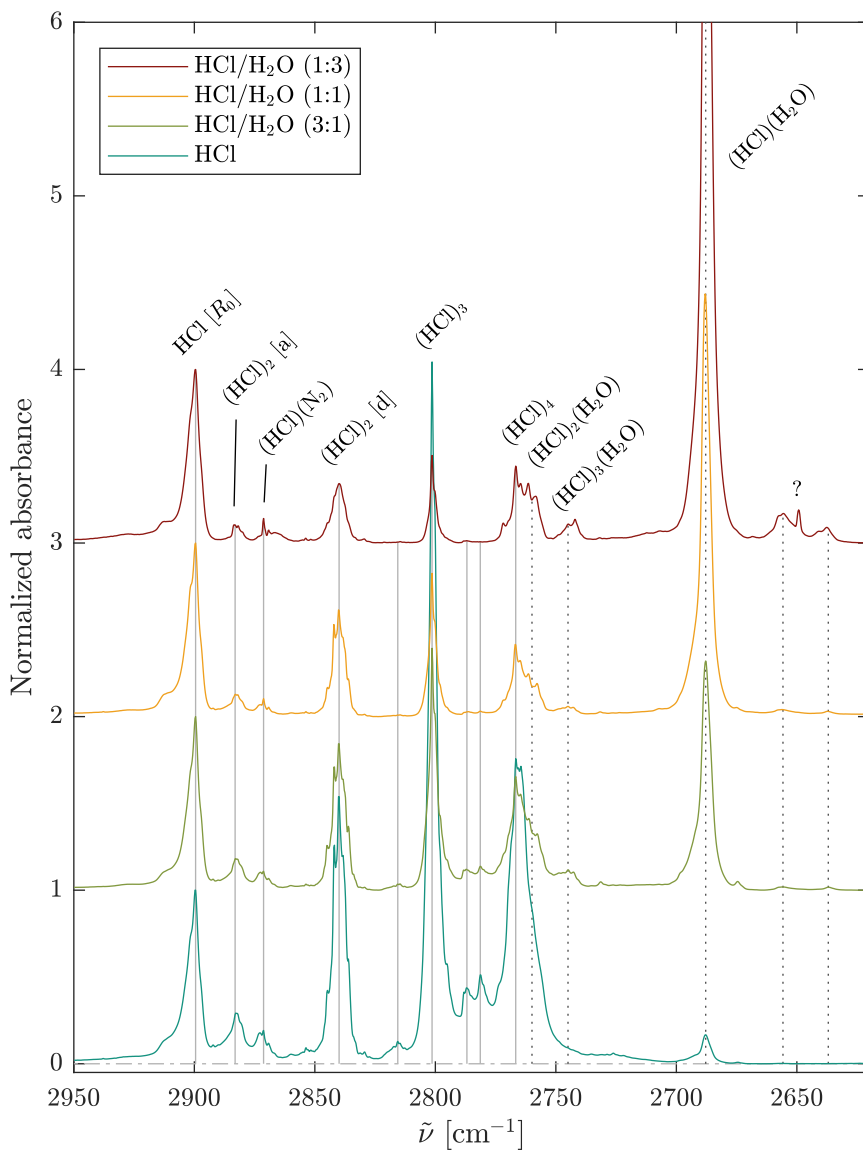


Figure 4.7: MIR absorption spectra of neon matrices with HCl and H_2O at 4.3 K in different proportions (marked parenthetically in the legend). Spectra normalized to the height of the HCl monomer band. Solid grey lines denote persistent HCl features, whereas dotted black lines indicate the appearance of new bands upon addition of water.

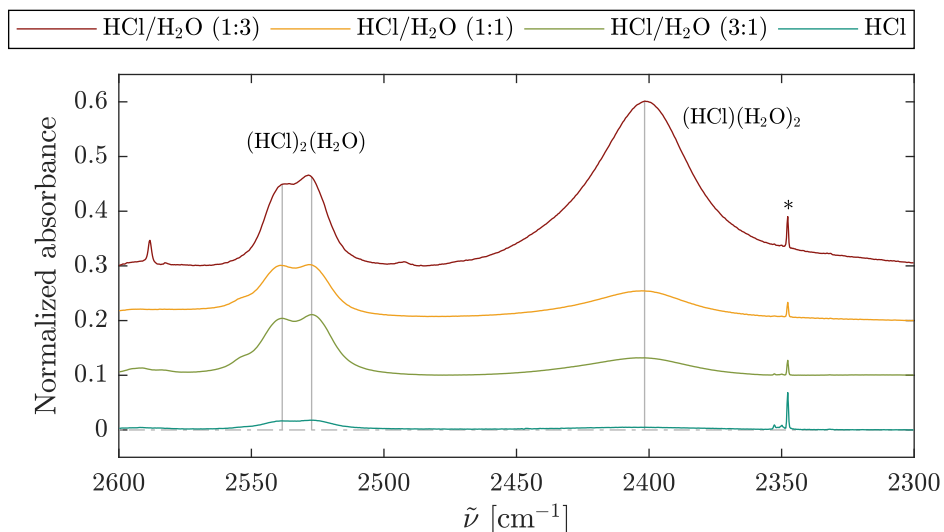


Figure 4.8: Continuation of fig. 4.7 in the $2300 - 2600 \text{ cm}^{-1}$ region. The absorbances are normalized to the height of the HCl monomer band. The peak marked with an asterisk is due to residual CO_2 .

the spectra of the $\text{HCl}/\text{H}_2\text{O}$, HCl/HOD and $\text{HCl}/\text{D}_2\text{O}$ mixtures, one notices the existence of peaks shifted to the blue or the red with respect to the $(\text{HCl})(\text{H}_2\text{O})$ band. In particular, the spectrum of the HCl/HOD also contains the latter band and a second one red-shifted at 2684.9 cm^{-1} . On the other hand, the spectrum of the $\text{HCl}/\text{D}_2\text{O}$ has this new band and another one, very close but blue-shifted with respect to $(\text{HCl})(\text{H}_2\text{O})$, at 2689.0 cm^{-1} .

We assign these new bands as follows: the one at 2684.9 cm^{-1} to the HCl stretching mode in the $(\text{HCl})(\text{HOD})$ complex and the one at 2689.0 cm^{-1} to the same mode in $(\text{HCl})(\text{D}_2\text{O})$. The unresolved shoulder on the right-hand side of the 2684.9 cm^{-1} band could be assigned to the corresponding ^{37}Cl isotopologue. The assignment of the peak at 2684.9 cm^{-1} is justified by the fact that it is mostly prominent in the spectrum of the HCl/HOD mixture. It also persists in the $\text{HCl}/\text{D}_2\text{O}$ mixture: the D_2O sample was not completely free from regular water, as the presence of some HOD in its spectrum shows (see bottom of fig. 4.9). The peak at 2689.0 cm^{-1} is observed in the $\text{HCl}/\text{D}_2\text{O}$ mixture only. The relatively high intensity of the $(\text{HCl})(\text{H}_2\text{O})$ peak in the HCl/HOD mixture may be caused by the overlap of absorbance from both $(\text{HCl})(\text{H}_2\text{O})$ and $(\text{HCl})(\text{D}_2\text{O})$ present in the matrix. More experiments in which one varies the proportions of $\text{H}_2\text{O}/\text{HOD}/\text{D}_2\text{O}$ could help in making these assignments more definitive.

Back to the big picture, the peak at 2666.3 cm^{-1} is clearly a new feature that is the most intense in the $\text{HCl}/\text{D}_2\text{O}$ mixture. We are unfortunately unable to assign

4.3. Application to the FTIR matrix isolation spectroscopy of $(\text{HCl})(\text{H}_2\text{O})$ in neon

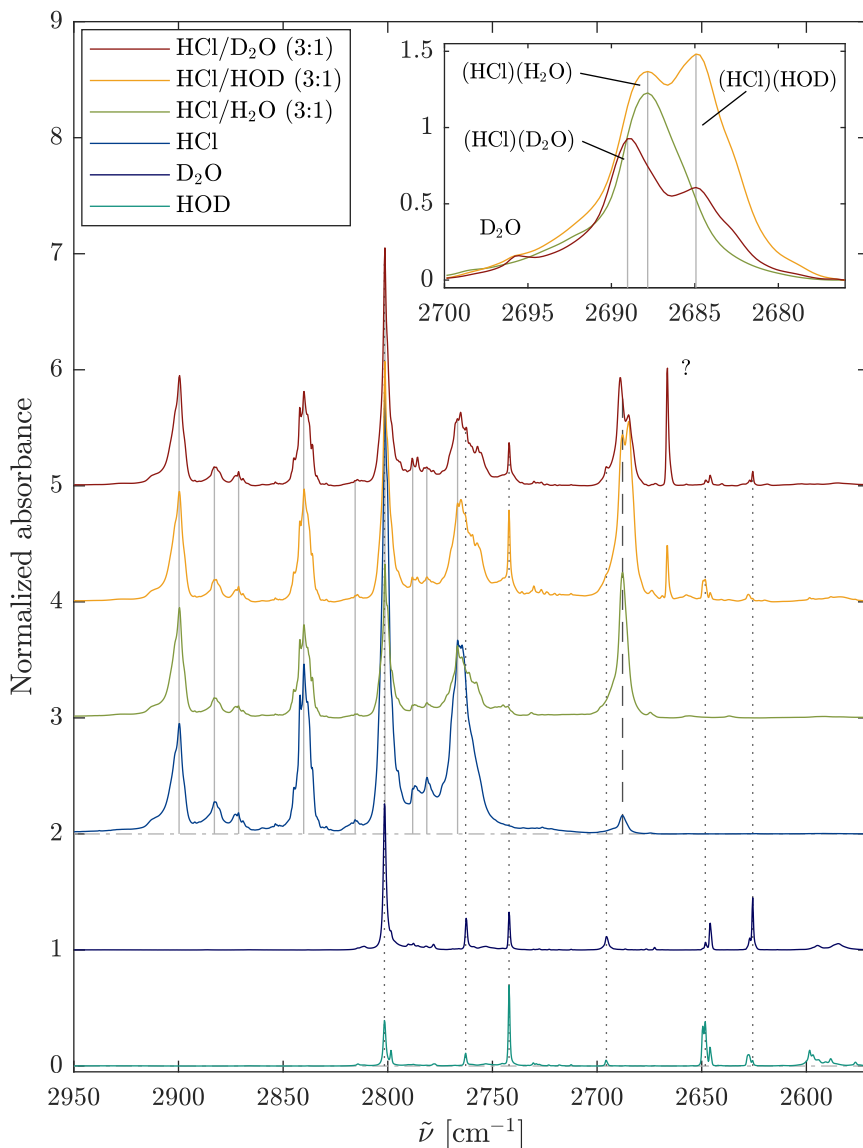


Figure 4.9: MIR absorption spectra of neon matrices with HCl, water isotopologues and mixtures of these at 4.3 K. The spectra of HCl and of the mixtures are normalized to the height of the HCl monomer band. In the main chart, solid grey lines denote persistent HCl features, dotted black lines indicate contributions from HOD, D₂O and their oligomers and the dashed line gives the position of the $(\text{HCl})(\text{H}_2\text{O})$ complex.

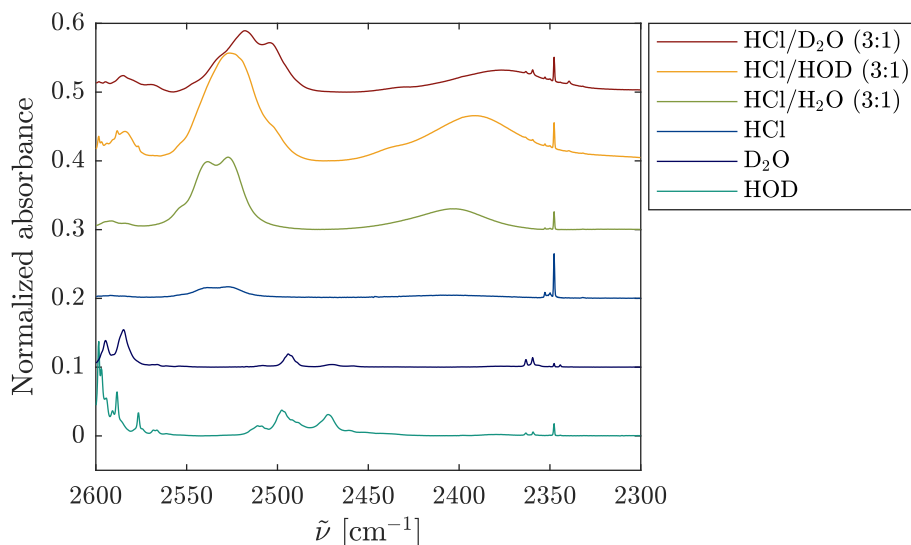


Figure 4.10: Continuation of fig. 4.9 in the $2300 - 2600\text{ cm}^{-1}$ region. The spectra of HCl and of the mixtures are normalized to the height of the HCl monomer band.

this band. What seems clear is that this band stems from the presence of D₂O and HCl together in the matrix. More experiments should be carried out to check how its intensity is dependent on the concentrations of the two molecules. However, it is surprising that no analogous peak is observed in the regular HCl/H₂O matrix.

The broad bands at lower energy associated with (HCl)₂(H₂O) (doublet at 2527.3 and 2538.3 cm⁻¹) and (HCl)(H₂O)₂ (at 2401.7 cm⁻¹) are red-shifted by deuteration of water. With D₂O, the doublet is red-shifted to 2517.9 and 2504.1 cm⁻¹ whereas the lower band is located at approximately 2374 cm⁻¹. Based on the previous assignments, these could be associated to (HCl)₂(D₂O) and (HCl)(D₂O)₂. With HOD, i.e. with the mixture of H₂O, HOD and D₂O in 1:2:1 proportions, the doublet appears red-shifted to approximately 2526.3 cm⁻¹ and blurred, whereas the lower band is located at 2390.8 cm⁻¹. These contain overlapping contributions from ternary complexes containing all three water isotopologues, so it is hard to make definitive assignments.

4.3. Application to the FTIR matrix isolation spectroscopy of $(\text{HCl})(\text{H}_2\text{O})$ in neon

Table 4.1: Assignments of IR spectral bands of neon matrices containing HCl, H_2O , HOD and D_2O .

Position / cm^{-1}	Assignment	Ref.
2899.6	HCl [R_0]	[96]
2882.8	$(\text{HCl})_2$, acceptor	TW
2871.3	$(\text{HCl})(\text{N}_2)$	[96]
2840.1	$(\text{HCl})_2$, donor	[96]
2815.6	?	
2801.4	$(\text{HCl})_3$	[95–97]
2801.7	D_2O	[117]
2788.1	<i>$(\text{HCl})_5$</i>	[99]
2781.4	<i>$(\text{HCl})_5$</i>	[99]
2766.7	$(\text{HCl})_4$	[96]
2762.9	$(\text{D}_2\text{O})(\text{H}_2\text{O})$	[117]
2762.6	$(\text{D}_2\text{O})_2$	[117]
2759.9	<i>$(\text{HCl})_2(\text{H}_2\text{O})$</i>	[84, 85, 99]
2745.0	<i>$(\text{HCl})_3(\text{H}_2\text{O})$</i>	[84, 116]
2742.3	HOD	[117]
2695.8	D_2O	[117]
2689.0	$(\text{HCl})(\text{D}_2\text{O})$	TW
2687.8	$(\text{HCl})(\text{H}_2\text{O})$	[96]
2684.9	$(\text{HCl})(\text{HOD})$	TW
2655.6	?	
2666.3	?	
2649.2	?	
2648.8	$(\text{HOD})(\text{H}_2\text{O})$	[117]
2648.3	$(\text{HOD})(\text{HOD})$	[117]
2646.2	$(\text{HOD})(\text{D}_2\text{O})$	[117]
2637.6	?	
2625.7	$(\text{D}_2\text{O})_2$	[117]
2538.4	<i>$(\text{HCl})_2(\text{H}_2\text{O})$</i>	[84, 85, 99]
2527.3	<i>$(\text{HCl})_2(\text{H}_2\text{O})$</i>	[84, 85, 99]
2517.9	<i>$(\text{HCl})_2(\text{D}_2\text{O})$</i>	TW
2504.1	<i>$(\text{HCl})_2(\text{D}_2\text{O})$</i>	TW
2401.6	<i>$(\text{HCl})(\text{H}_2\text{O})_2$</i>	[84, 85, 99]
2374	<i>$(\text{HCl})(\text{D}_2\text{O})_2$</i>	TW

TW: this work. Tentative assignments in italic. Missing assignments marked with question marks.

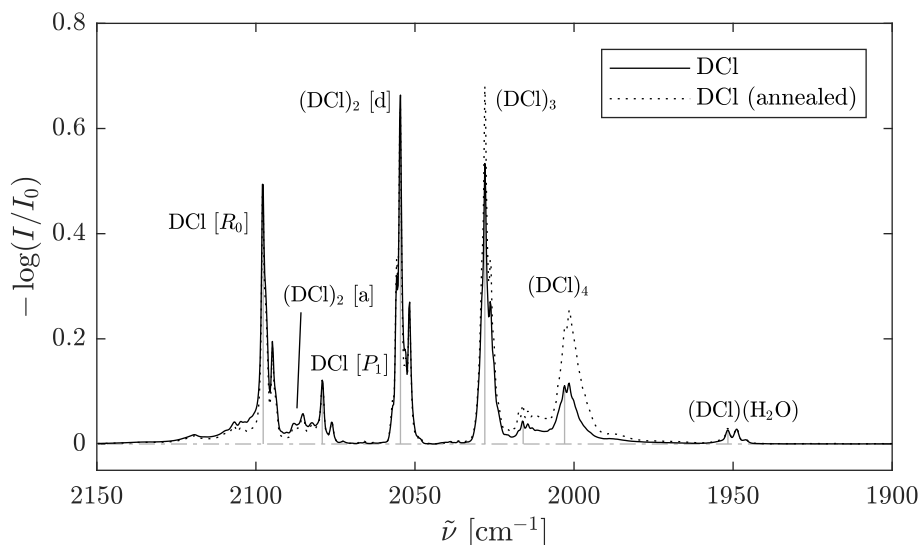


Figure 4.11: MIR absorption spectrum of DCl in a neon matrix at 4.3 K.

DCl and its complexes with H₂O, HOD and D₂O

The spectra of DCl alone (fig. 4.11), with water or with its deuterated isotopologues (figs. 4.12 and 4.13) are very similar to those containing HCl. The assignments of the bands in these spectra are given in table 4.2 of which we give justifications in the following.

In these DCl spectra, the bands arising from either ³⁵Cl and ³⁷Cl isotopologues of DCl are better resolved than in spectra containing regular HCl and we can easily distinguish the D³⁵Cl and D³⁷Cl monomer *R*₀ lines at 2097.8 cm⁻¹ and 2094.8 cm⁻¹, respectively. The pattern of intense bands at lower energies reproduces that in the HCl spectra. These bands correspond to the (DCl)₂ donor stretching, (DCl)₃ and (DCl)₄. In particular, fig. 4.11 shows once again how annealing of the matrix containing only DCl causes the larger oligomers to form from monomers or dimers. However, the assignment of peaks within these bands, which arise from isotopic shifts, is harder than for the monomer, since their intensities do not follow progressions dictated by the expected natural abundance. The presence of residual regular HCl (witnessed by the presence of HCl-related signals in the region discussed earlier) may also be a reason of the complication of the spectrum.

The smaller features between 2090 and 2075 cm⁻¹ deserve a more attentive discussion. We tentatively assign the pair of lines at 2079.1 and 2076.1 cm⁻¹ to the *P*₁ transitions of D³⁵Cl and D³⁷Cl, respectively. Given that the rotational constant of D³⁵Cl is $\tilde{B}_{D^{35}Cl} = 5.45 \text{ cm}^{-1}$, the *P*₁ line is expected to lie at a position about $4\tilde{B}_{D^{35}Cl}$ lower than the *R*₀ line – the same holds for D³⁷Cl whose rotational constant

4.3. Application to the FTIR matrix isolation spectroscopy of (HCl)(H₂O) in neon

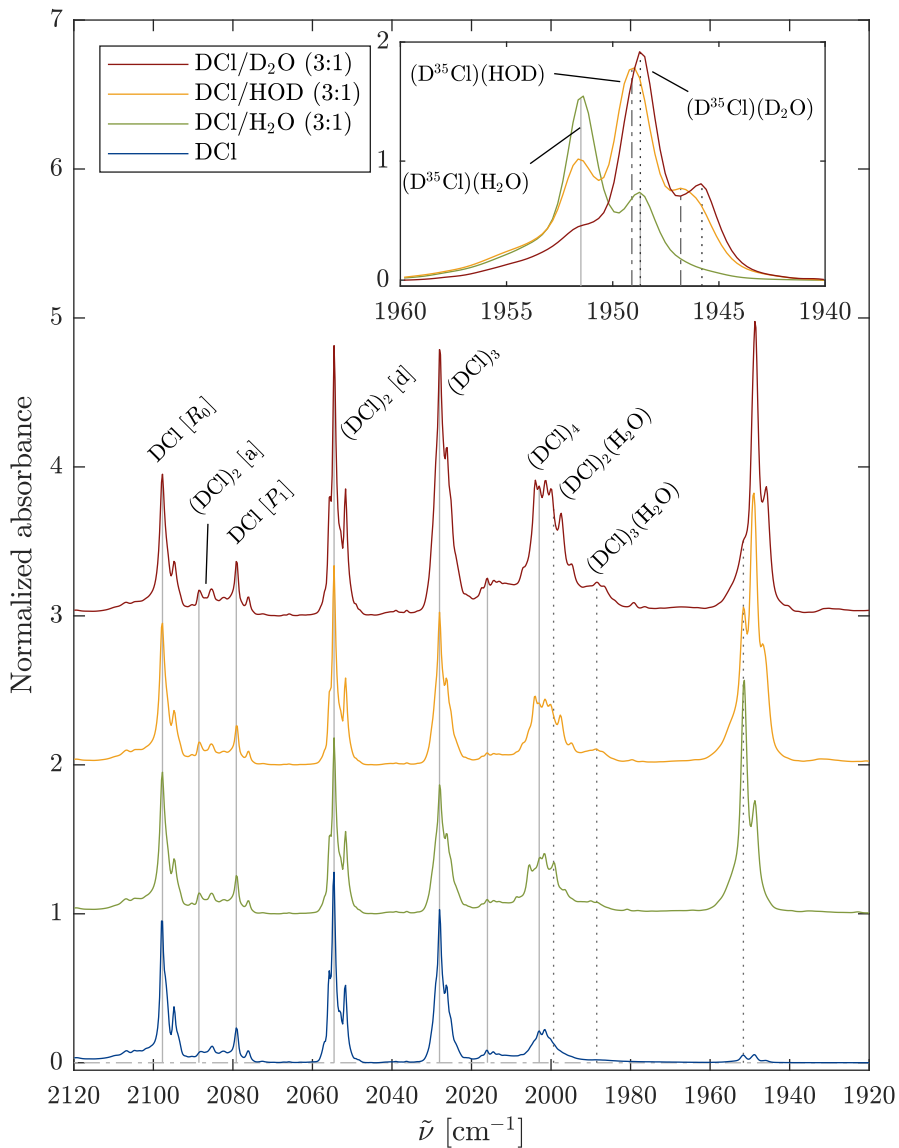


Figure 4.12: MIR absorption spectra of neon matrices with DCl, water isotopologues and mixtures of these at 4.3 K. These are normalized to the height of the DCl monomer band. In the main chart, solid grey lines denote persistent DCl features, whereas dotted black lines indicate the appearance of the new bands upon addition of water. In the inset, each of the ³⁵Cl/³⁷Cl isotopic pair is indicated by two lines of the same kind (solid, dashed or dotted). Note that the alignment of the (D³⁷Cl)(H₂O) and (D³⁵Cl)(D₂O) lines purely coincidental.

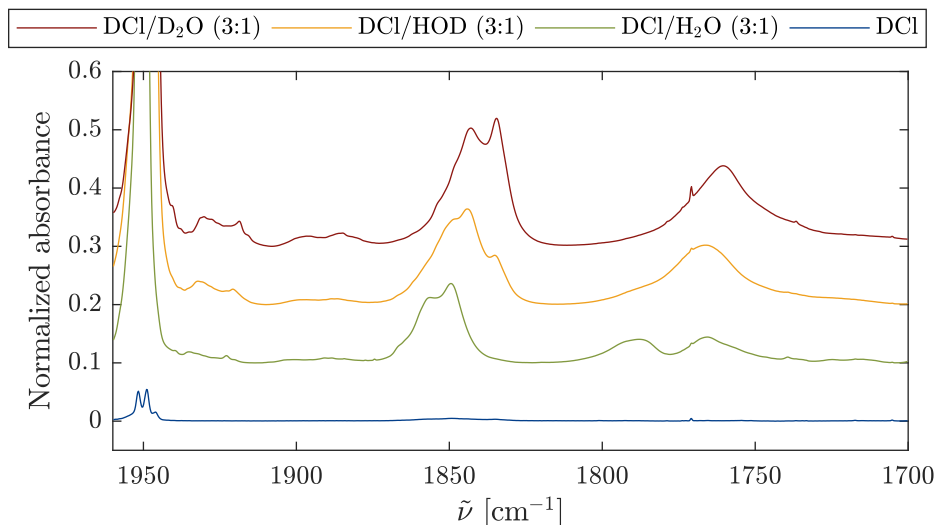


Figure 4.13: Continuation of fig. 4.12 in the 1970 – 1700 cm^{-1} region. Spectra normalized to the height of the DCl monomer band.

is $\tilde{B}_{\text{D}^{37}\text{Cl}} = 5.43 \text{ cm}^{-1}$. This is somewhat consistent with the observation, where the distance between the R_0 lines and the tentatively assigned P_1 lines is 18.7 cm^{-1} for both D^{35}Cl and D^{37}Cl . Note that P_1 lines were also observed in argon matrices at 16 K [94]. However, the temperature at the time of our measurements was $T = 4.3 \text{ K}$, and the populations of the three-fold degenerate $J = 1$ rotational excited state is therefore estimated to be only 7.8%, i.e. about 11 to 12 times smaller than the population of the rotational ground state. Thus, these observed lines are maybe too intense to be assigned to the P_1 transitions. In addition, we cannot exclude that these peaks arise as a result of complexation with residual traces of nitrogen, as discussed in the case of HCl. To confirm this assignment of the P_1 lines we would need to make additional experiments aiming at verifying the temperature dependence of their intensity. On the other hand, the features at 2088.4 cm^{-1} are assigned to the $(\text{DCl})_2$ acceptor by analogy with the HCl spectrum.

By addition of water and its deuterated analogues (which do not absorb on their own in this region), one notices again the growth of the band corresponding to the 1:1 complex, at 1951.5 cm^{-1} . The detailed assignment is shown in the inset of fig. 4.12, where this time the chlorine isotopologues can be distinguished by the 3:1 intensity ratios. Additional bands below the HCl tetramer band also grow by addition of water and some level of isotopic shift by replacement of the latter by HOD or D_2O can be noticed. This confirms the fact that these are associated to complexes containing water. In line with the HCl spectra, we make a rough assignment of the band at 1999 cm^{-1} to the $(\text{DCl})_2(\text{H}_2\text{O})$ and the band at 1988.5 cm^{-1} to the $(\text{DCl})_3(\text{H}_2\text{O})$,

without making any distinction between isotopologues containing deuterium or either $^{35}\text{Cl}/^{37}\text{Cl}$ isotopes.

Broad bands at lower energy, below that of the 1:1 complex, are observed as well by addition of water (fig. 4.13). The first one is found at around 1853 cm^{-1} (with two components at 1856.4 and 1849.6 cm^{-1}) and the second one is now split into two at about 1789 cm^{-1} and 1766 cm^{-1} . The relative ratios between these two signals is inverted by having more water than DCl in the matrix (not shown). Analogously to the case of HCl, one could therefore associate the first doublet at 1853 cm^{-1} with the $(\text{DCl})_2(\text{H}_2\text{O})$ complex and the second pair at about 1789 cm^{-1} and 1766 cm^{-1} to $(\text{DCl})(\text{H}_2\text{O})_2$. Both are subject to isotopic red-shifts by deuteration of water.

4.4 Conclusion and outlook

The constructed matrix deposition setup has successfully been applied to the matrix isolation spectroscopy of a number of hydrogen chloride/water complexes and various deuterated analogues in the MIR region. The setup can be used on a daily basis thanks to its association with the closed-cycle cryostat. The presence of separate inlet tubes and of the cold trap allows for the deposition of deuterated species without recombination with non-deuterated ones.

A rather good understanding of the spectra of HCl, DCl and their mixtures with H_2O , HOD and D_2O has been reached in the HCl and DCl stretching regions. The major achievement is the identification of the spectral bands corresponding to the perturbed HCl/DCl stretching mode within their complexes with one molecule of $\text{H}_2\text{O}/\text{HOD}/\text{D}_2\text{O}$. More experiments are needed to fully understand some of the features which were not assigned – or only tentatively to e.g. larger complexes, partially deuterated species or mixed $^{35}\text{Cl}/^{37}\text{Cl}$ isotopologues. Moreover, the H_2O stretching and bending regions ($3900 - 3400\text{ cm}^{-1}$ and $1800 - 1550\text{ cm}^{-1}$) should also deserve some attention, as they include perturbed acceptor bands.

Ultimately, the FIR region is where we aim at observing signatures of intermolecular modes in these complexes. We foresee many challenges including the intrinsic presence of HCl oligomers in the matrix which will have to be distinguished from the unpredicted spectral signature of the $(\text{HCl})(\text{H}_2\text{O})$ complex. The observation of bands associated to intermolecular vibrations, in particular because they are a direct probe of complexation, could provide additional insight on the delocalized character of the wavefunction over the double-well intermolecular potential (see section 3.2.1). For studies in this spectral region, para-hydrogen has proven to be an ideal matrix host for this investigation [119, 120]. This matrix host will be used in the future for that scope, as another setup has been developed for its synthesis. Its description is the subject of the next chapter.

Table 4.2: Assignments of spectra of neon matrices containing DCl, H₂O, HOD and D₂O

Position / cm ⁻¹	Assignment
2097.8	D ³⁵ Cl [<i>R</i> ₀]
2094.8	D ³⁷ Cl [<i>R</i> ₀]
2088.4	<i>(D³⁵Cl)₂</i> [a]
2085.4	<i>(D³⁷Cl)₂</i> [a]
2079.1	<i>D³⁵Cl</i> [<i>P</i> ₁]
2076.1	<i>D³⁷Cl</i> [<i>P</i> ₁]
2054.5	(D ³⁵ Cl) ₂ [d]
2051.7	(D ³⁷ Cl) ₂ [d]
2028.0	(D ³⁵ Cl) ₃
2026.2	(D ³⁵ Cl) ₂ (D ³⁷ Cl)
2016.1	(D ³⁵ Cl) ₄
2014.5	(D ³⁵ Cl) ₃ (D ³⁷ Cl)
2008.6	<i>(DCl)₂(H₂O)</i>
2005.5	<i>(DCl)₂(H₂O)</i>
2003.0	(D ³⁵ Cl) ₄
2001.6	(D ³⁵ Cl) ₃ (D ³⁷ Cl)
1999.3	?
1996.6	?
1951.5	(D ³⁵ Cl)(H ₂ O)
1949.1	(D ³⁵ Cl)(HOD)
1948.8	(D ³⁷ Cl)(H ₂ O)
1948.7	(D ³⁵ Cl)(D ₂ O)
1946.8	(D ³⁷ Cl)(HOD)
1945.9	(D ³⁷ Cl)(D ₂ O)
1856.4	<i>(DCl)₂(H₂O)</i>
1849.6	<i>(DCl)₂(H₂O)</i>
1844.2	<i>(DCl)₂(HOD)</i>
1843.1	<i>(DCl)₂(D₂O)</i>
1834.6	<i>(DCl)₂(D₂O)</i>
1789	<i>(DCl)(H₂O)₂</i>
1866.5	<i>(DCl)(HOD)₂</i>
1766	<i>(DCl)(H₂O)₂</i>
1860.5	<i>(DCl)(D₂O)₂</i>

TW: this work. Tentative assignments in italic. Missing assignments marked with question marks.

5

Para-hydrogen enrichment setup

Among the materials that can be used for matrix isolation experiments, para-hydrogen is one of these. In this chapter we will explain what it is and why solid para-hydrogen is a convenient host material, in particular in infrared spectroscopy. After presenting the fundamental characteristics of para-hydrogen and some of its properties as a solid, we will describe the apparatus that we have built in our laboratory for its production and demonstrate the quality of the matrices that we can form in our experiments.

5.1 Nuclear spin isomers of molecular hydrogen: para-hydrogen and ortho-hydrogen

Molecular hydrogen, H_2 , exist in two forms which differ only by how the spins of its nuclei are mutually oriented. Since the hydrogen nucleus is a fermion, with spin $1/2$, the total wavefunction of H_2 is antisymmetric upon permutation of the two nuclei. This fact has a dramatic effect on the quantum states a molecule of H_2 can be found in, as will be shown here in a similar way as done by McQuarrie [121].

Let us write, at first, the total wavefunction of H_2 as the product of an electronic, a vibrational and a rotational wavefunction, without taking nuclear spin into account:

$$\Phi = \psi_{\text{elec}}\psi_{\text{vib}}\psi_{\text{rot}} \quad (5.1)$$

For H_2 in the electronic ground state, exchanging the nuclei has no effect on ψ_{elec} and is therefore symmetric upon this operation. Similarly, the vibrational wavefunction ψ_{vib} depends on the distance between the two nuclei which remains unchanged by permutation, making it symmetric too. However, the rotational wavefunction ψ_{rot} may be affected by particle permutation. In the rigid rotor approximation, this is a spherical harmonic depending on two polar angles θ and ϕ . Permutation of the nuclei

is equivalent to rotation about the z -axis¹ by π , i.e. $\psi_{\text{rot}}(\theta, \phi)$ is replaced by $\psi_{\text{rot}}(\theta, \phi + \pi)$, which in turn equals $(-1)^J \psi_{\text{rot}}(\theta, \phi)$, where J is the rotational quantum number. Thus, the rotational wavefunction is symmetric (respectively antisymmetric) upon permutation of the nuclei for states with even (respectively odd) quantum number J .

Now, the nuclear wavefunction can be in either of the following four states:²

$$|1, 1\rangle = |\uparrow\uparrow\rangle \quad (5.2)$$

$$|1, 0\rangle = \frac{1}{\sqrt{2}} (|\uparrow\downarrow\rangle + |\downarrow\uparrow\rangle) \quad (5.3)$$

$$|1, -1\rangle = |\downarrow\downarrow\rangle \quad (5.4)$$

$$|0, 0\rangle = \frac{1}{\sqrt{2}} (|\uparrow\downarrow\rangle - |\downarrow\uparrow\rangle) \quad (5.5)$$

These states on the left-hand side are written as $|S, M_S\rangle$, with S denoting the total spin of the H_2 nuclei and M_S its projection along the z -axis. The states in the linear combinations on the right-hand side indicate the projections along the z -axis of the spin of each individual nucleus, where \uparrow means ‘up’ and \downarrow means ‘down’.³ The first three states correspond to a total spin of 1 and are called triplet states. The fourth one has spin 0 and is known as a singlet state. The set of triplet states and, on the other hand, the singlet state correspond to the cases where the individual nuclear spins are respectively said to be “parallel” (they “add up” to one) and “antiparallel” (they “cancel each other out”). Hydrogen with parallel spins is called *ortho-hydrogen* or $o\text{-H}_2$. With antiparallel spins, it is called *para-hydrogen* or $p\text{-H}_2$.

It is important to notice that triplet states (eqs. (5.2) to (5.4)) are unchanged upon nuclei permutation, whereas the singlet state (eq. (5.5)) changes sign if they are exchanged. Thus, if the total wavefunction is written as a product of electronic, vibrational, rotational and nuclear spin wavefunctions, the only situations that can arise are exclusively the following:

- Rotational state with J even (symmetric) and nuclear singlet state (antisymmetric);
- Rotational state with J odd (antisymmetric) and nuclear triplet state (symmetric).

From this we arrive to the following conclusion: in the electronic and vibrational ground states, para-hydrogen can only be in rotational states with even quantum number, whereas ortho-hydrogen exists only in rotational states with odd quantum number. This fact has a profound implication on the proportions of ortho- and para-forms in a given sample of H_2 at equilibrium, as well as on its macroscopic properties [122].

¹An axis contained in the midplane orthogonal to the H–H axis.

²These are eigenstates of the magnitude squared \hat{S}^2 and z -component \hat{S}_z of the spin operator of the compound system of the two nuclei.

³The chemists’ notation uses $|\alpha\rangle$ and $|\beta\rangle$ in place of $|\uparrow\rangle$ and $|\downarrow\rangle$

5.1. Nuclear spin isomers of molecular hydrogen: *para*-hydrogen and *ortho*-hydrogen

At a given temperature T , a molecule in an ensemble can be found in any of its accessible quantum states with a probability that follows Boltzmann's statistics. In general, if E_n is the n^{th} eigenvalue of the total molecular Hamiltonian and g_n is the number of states with that same n^{th} eigenvalue (also known as degeneracy), the probability p_n of finding a molecule with energy E_n is

$$p_n = \frac{g_n \exp\left(-\frac{E_n}{kT}\right)}{\sum_{m=0}^{+\infty} g_m \exp\left(-\frac{E_m}{kT}\right)} \quad (5.6)$$

where k is the Boltzmann constant. In particular, the probability to find a *para*-hydrogen molecule is proportional to the sum of the p_n 's corresponding to rotational states with even quantum number J . Similarly, for *ortho*-hydrogen, the sum is over rotational states with odd quantum number J . As a result, the ratio between the amounts of *para* and *ortho* forms in a sample of H_2 is:

$$\frac{N_{\text{para}}}{N_{\text{ortho}}} = \frac{p_{\text{para}}}{p_{\text{ortho}}} = \frac{\sum_{J \text{ even}} (2J+1) \exp\left(-\frac{BJ(J+1)}{kT}\right)}{3 \sum_{J \text{ odd}} (2J+1) \exp\left(-\frac{BJ(J+1)}{kT}\right)} \quad (5.7)$$

where $B = \hbar^2/2I$ is the rotational constant of H_2 in the vibrational ground state (I is its moment of inertia). The factor 3 in the numerator corresponds to the degeneracy of the triplet states. The factor $(2J+1)$ in the sums is the degeneracy of the corresponding J^{th} rotational state.

As a result, one finds that at room temperature $N_{\text{para}}/N_{\text{ortho}} \approx 1/3$. A sample of hydrogen with these proportions is called "normal" hydrogen, denoted n- H_2 . However, this ratio increases as T decreases. Since the lowest $J = 0$ rotational state can be occupied by *para*-hydrogen only, $N_{\text{para}}/N_{\text{ortho}} \rightarrow \infty$ as $T \rightarrow 0$. This means that only *para*-hydrogen can be found at $T = 0$. At slightly higher temperatures, traces of *ortho*-hydrogen are present. Figure 5.1 shows how these proportions vary with temperature for a sample at thermal equilibrium.

These considerations are valid for any sample of H_2 at thermal equilibrium. Yet, at any temperature, *ortho*-to-*para* spin transition is quantum mechanically forbidden for an isolated molecule. Therefore, the conversion can only occur via an indirect mechanism as shown in section 5.3. This is in fact an advantage: if one is able to produce a sample of hydrogen with different *ortho*/*para* proportions than in n- H_2 , then it is possible to keep it as it is even at room temperature. In other words, it is possible to keep a metastable mixture of o- H_2 and p- H_2 with the desired proportions at any temperature.

In practical terms, the back-conversion of p- H_2 to o- H_2 does occur at room temperature, though it takes of the order of days to observe any significant degradation of the prepared sample. The occurrence of back-conversion is due to the presence of

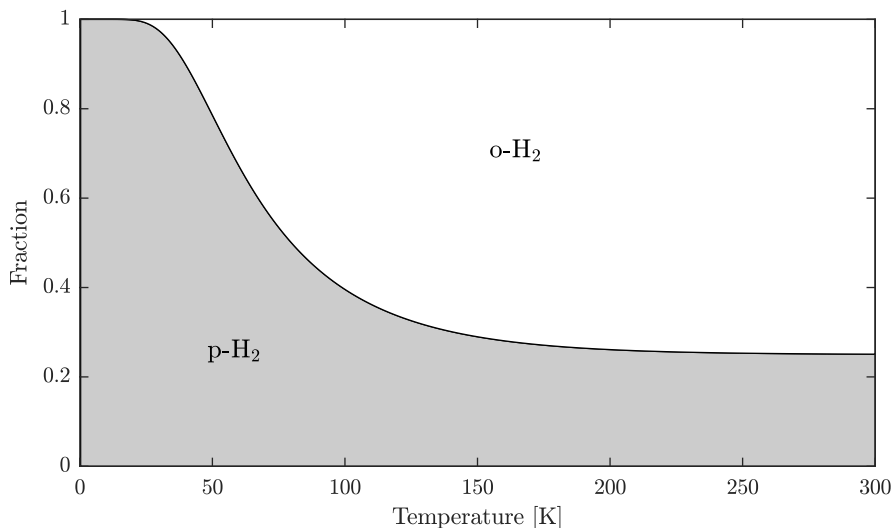


Figure 5.1: Proportions at equilibrium of o-H₂ and p-H₂ as a function of temperature according to Boltzmann's statistics, using the fact that $p_{para} + p_{ortho} = 1$ and eq. (5.7).

impurities, in particular molecular oxygen [123]. Back-conversion in the solid state is also known to be slow [124] and is hence hardly noticeable in the time-scale of matrix isolation experiments (≈ 1 day).

5.2 Para-hydrogen as a host matrix

As mentioned in section 4.1.2, in matrix isolation spectroscopy the inert host material interacts weakly with the guest molecules it encloses. As a consequence, the matrix will have a more or less pronounced influence on the aspect of the IR spectrum of the guest molecules, although this effect is minor in neon and para-hydrogen, as mentioned earlier.

In addition to these perturbations, the translational and rotational motions of molecules trapped in the matrix are not totally free as in gas phase. These are instead coupled, giving rise to so-called “rotation-translation coupling” (RTC) states and related transitions between these [125]. In particular, these show up in the FIR spectrum of the water monomer in neon matrices [120]. When studying complexes with water, these RTC bands may overlap with bands stemming from intermolecular vibrational transitions. Although neon proves suitable for matrix isolation, it is desirable to avoid this situation and use another matrix host in which RTC bands of water (and potentially of the other moiety of the complex) do not arise.

In solid para-hydrogen, this type of interactions with guest molecules are partic-

ularly weak to the point that RTC bands of monomeric water do not arise in the FIR region. The reasons can be ascribed to the particular properties of solid para-hydrogen which have been extensively reviewed by Silvera [124]. Its applications to matrix isolation spectroscopy is also discussed in a recent review by Tsuge & Lee [126]. Solid para-hydrogen is transparent in the FIR region below $\approx 300\text{ cm}^{-1}$ and is therefore suitable for the exploration of intermolecular vibrational transitions in weakly bound complexes.

Para-hydrogen solidifies at temperatures around $T = 14\text{ K}$ at atmospheric pressure (the triple point is located at $T = 13.8\text{ K}$ and $p = 7.041\text{ kPa}$ [122]). Solid p-H₂ exists in a hexagonal close-packed crystal structure with a large distance between closest neighbours of 3.793 \AA . Because of this and the fact that the hydrogen molecule has an almost spherical charge distribution (owing to the short interatomic distance of 0.74 \AA), the single H₂ molecules in the solid are (almost) free rotors distributed in the crystal lattice. Because of the lightness of H₂, each molecule vibrates around the equilibrium lattice points with large amplitude motion (even at zero Kelvin, for it is called a “quantum solid”). It is the softness of this solid that prevents the RTC bands of monomeric water to show up.

The hydrogen molecule (either *ortho* or *para*) has a non-zero quadrupole moment. However, each molecule of solid para-hydrogen is in the rotational ground state $J = 0$ associated with a spherical rotational wavefunction. In other words, all para-hydrogen molecules in the lattice are randomly oriented. Thus, the rotationally averaged quadrupole moment in solid para-hydrogen is zero. Owing to this fact, dipole-quadrupole or quadrupole-quadrupole interactions of guest molecules with the matrix host are very weak.

In the context of matrix isolation, it is important to have the largest proportion of para-hydrogen for this reason. Ortho-hydrogen exists essentially in the $J = 1$ rotational state, resulting in a non-zero rotationally averaged quadrupole moment. For this, it does interact with guest molecules. In other words, ortho-hydrogen traces can be seen as undesired guest molecules in the para-hydrogen matrix. It is therefore required that the conversion procedure leaves a proportion of ortho-hydrogen which is negligible compared to what will be the concentration of guest molecules to be studied in the matrix.

5.3 Catalytic *ortho-para* hydrogen conversion

As mentioned in section 5.1, the conversion from one form of hydrogen to the other involves a forbidden spin transition. This means that, as temperature is lowered, o-H₂ does not convert to p-H₂ on its own but can, at most, do so very slowly only because of the presence of contaminants. A sample of n-H₂, at equilibrium at room temperature, is hence a metastable mixture of o-H₂ and p-H₂ at lower temperature.

In order to obtain pure para-hydrogen, a sample of normal hydrogen must be cooled to cryogenic temperatures (see fig. 5.1) and put in conditions which allow the conversion to happen so that the equilibrium *ortho-para* proportions can be reached

at that temperature. The mechanism making this possible is the interaction of a H_2 molecule with a paramagnetic compound. Its magnetic field, extending over a small region around it, is inhomogeneous over the hydrogen molecule and interacts most with the closest atom of the two, allowing it to flip its nuclear spin. Thus, the paramagnetic compound acts as a catalyst in the ortho-para conversion. This mechanism was explained theoretically by Wigner [127] and further refined by Harrison & McDowell [128] for a solid catalyst. Various paramagnetic solids have been known as ortho-para conversion catalysts [129]. Ferric oxide (Fe_2O_3) powder will be our choice from now on.

It is also worth mentioning that, when high p- H_2 enrichment degree is desired, i.e. when very low temperatures must be reached, a limitation to the conversion efficiency is the slow self-diffusion of hydrogen molecules in its solid. When the converter is cooled down to temperatures below the triple point of H_2 , hydrogen freezes on the catalyst. However, only the molecules in the first adsorption layer interact with the magnetic field cast by the catalyst at its surface and undergo a ortho-para spin transition. For the other o- H_2 molecules to be converted, they would need to diffuse through the solid and reach the surface of catalyst. The latter is a time-limiting step. However, this difficulty is simply overcome by repeatedly melting and freezing hydrogen around the triple point. As a result, the molecules that did not come into contact with the catalyst one first time are able to do so in the subsequent ones. In the limit of many repetitions, all H_2 molecules will have reached the catalyst at least once. This technique will be used with our ortho-para hydrogen converter described in the following.

Several enrichment setups are documented in the literature. The choice of one or the other depends on many factors proper to the intended use (enrichment quality, produced amounts, application, practical handling, costs, etc. . .). Some authors [130, 131] use a design based on flowing n- H_2 thorough the catalyst powder at low temperature. Instead, we designed and built an ortho-para hydrogen converter in our laboratory, schematically shown in fig. 5.2, which relies on another – somewhat simpler – approach which will be presented here.

A large glass flask is first filled with the desired amount of n- H_2 to be treated. This is connected to an assembly of glass tubes equipped with a pressure gauge and several valves. The assembly is connected to a custom made vessel containing the Fe_2O_3 catalyzer where the conversion takes place.

More specifically, the vessel is made of Oxygen-Free High Conductivity (OFHC) copper and has a 1/2' diameter steel pipe on the top. The latter realizes the connection between the vessel and the glass tubes assembly through a flexible hose. The vessel parts are braized together so as to guarantee vacuum tightness and is itself firmly screwed on the cold end of a closed-cycle He cryostat (Advanced Research Systems, model DE-202AI) used to lower its temperature. An indium gasket is pressed between the vessel and the cold end for improved thermal conduction. As in the other cryostat mentioned in chapter 4, a radiation shield protects the vessel from surrounding black-body radiation. The vacuum shroud has been redesigned. It consists in a stainless steel cylinder with a welded flat cap. A hole is drilled in its center and an ISO-KF 25

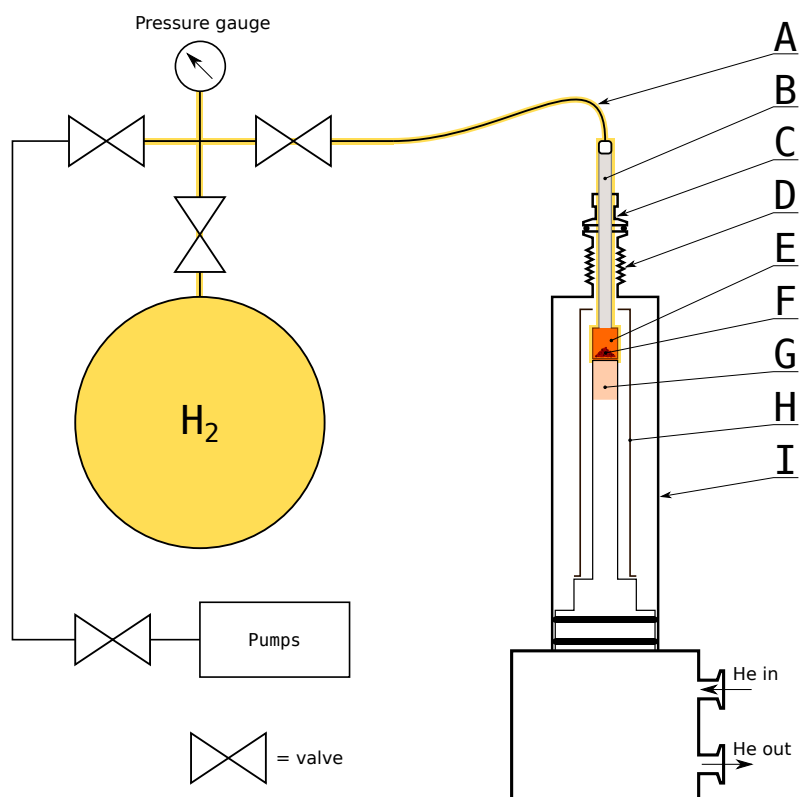


Figure 5.2: Schematic representatin of the ortho-para hydrogen converter use in our lab. Initially, a given amount of normal hydrogen is contained in the large round glass flask (H_2) while the rest of the setup is evacuated. The elements highlighted in yellow are the ones occupied by hydrogen during the conversion. (A) Flexible pipe, (B) Steel 1/2' tube, (C) Swagelok Ultratorr 1/2' pipe feedthrough with ISO-KF 25 mounting interface, (D) ISO-KF 25 flexible hose soldered on the vacuum shroud, (E) OFHC copper vessel, (F) Fe_2O_3 catalyzer, (G) Cryostat cold end, (H) Radiation shield, (I) Vacuum shroud.

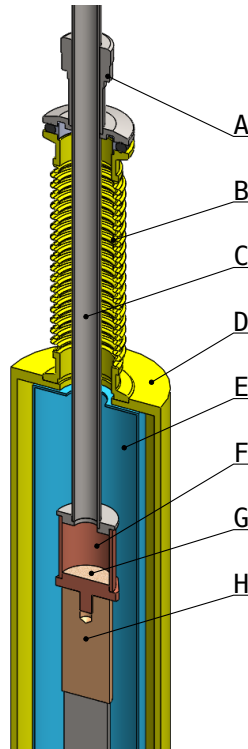


Figure 5.3: Detailed cut view of the ortho-para hydrogen converter vessel mounted on the cryostat. (A) Swagelok Ultratorr 1/2' pipe feedthrough with ISO-KF 25 mounting interface [clamp not shown] (B) ISO-KF 25 flexible hose soldered on the vacuum shroud, (C) Steel 1/2' tube, (D) Vacuum shroud, (E) Radiation shield, (F) OFHC copper vessel, (G) Fe_2O_3 catalyzer position, (H) Cryostat cold tip.

flexible hose is welded on it. A pipe feedthrough seals the hose at the other end and is where the steel pipe of the vessel sticks out from the evacuated volume. A detailed view of the components of the para-hydrogen converter is given in fig. 5.3. Dimensional drawings of the parts it is made of are given in appendix C.

The conversion procedure relies on controlling the temperature of the vessel only. A temperature probe (silicon diode) and an heating element (resistive cartridge) are placed on the cold end of the cryostat and are connected to a temperature controller (Lake Shore, model 335). Through closed-loop feedback control scheme, the controller adjusts the amount of current needed delivered to the heating element so as to compensate the cooling power of the cryostat, thus keeping the temperature of the vessel at a specified desired temperature.

A PC is used as an interface between the experimenter and the controller. A custom-made program called *Temperature Control Program* (TCP), written in C++

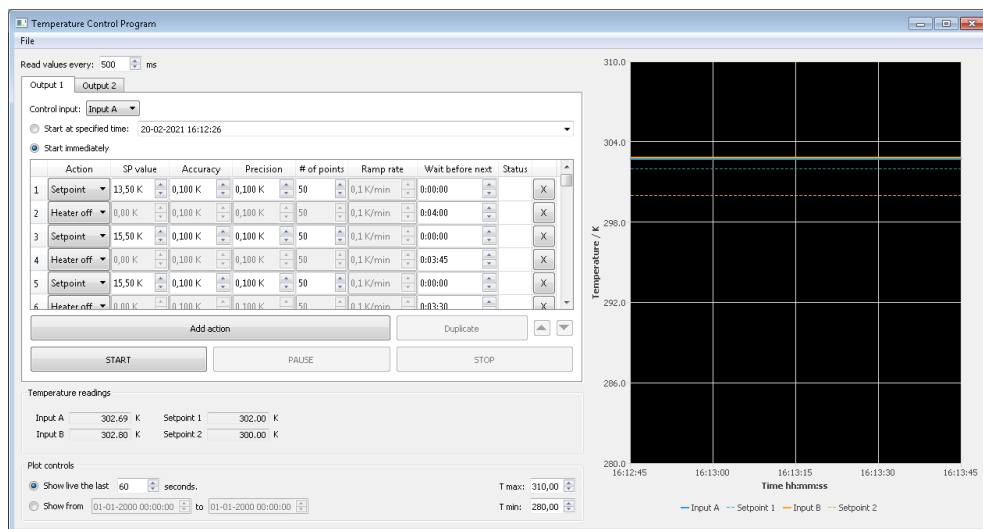


Figure 5.4: Screenshot of the custom-made Temperature Control Program used for the automatic recirculation of hydrogen in the ortho-para converter.

with the Qt framework (version 5.12), is used for this scope (see screenshot in fig. 5.4). It consists in a Graphical User Interface (GUI) displaying the current temperature of the copper vessel. In separate panel of the interface, the user can fill a table with “tasks”, such as changing the setpoint temperature, waiting for a certain time or switching the heater off. Once a series of tasks is created, the execution of these is started, manually or automatically at a specified time of the day, and the tasks are completed one after the other without further input from the user. The TCP program was originally created for the automation and control of the ortho-para hydrogen conversion procedure only, but proved also useful for managing the matrix isolation experiments on the FTIR spectrometer.

Armed with this setup, the ortho-para hydrogen conversion procedure is rather simple. As explained earlier, high fraction of para-hydrogen is obtained by repeatedly freezing and thawing the sample of normal hydrogen onto the catalyst simply by setting the temperature of the vessel slightly below and above that of the triple point of H_2 . These steps are repeated at will until all molecules have been into contact with the ferric oxide powder. After a series of cycles, the converted hydrogen is then frozen on the catalyst one last time. After pumping away the remaining vapour pressure, the so-obtained para-hydrogen is slowly thawed (in the vicinity of the triple point) and collected in the original glass flask. The latter is then closed and moved to the deposition setup. Figure 5.5 shows the evolution of the temperature of the copper vessel over time during this procedure.

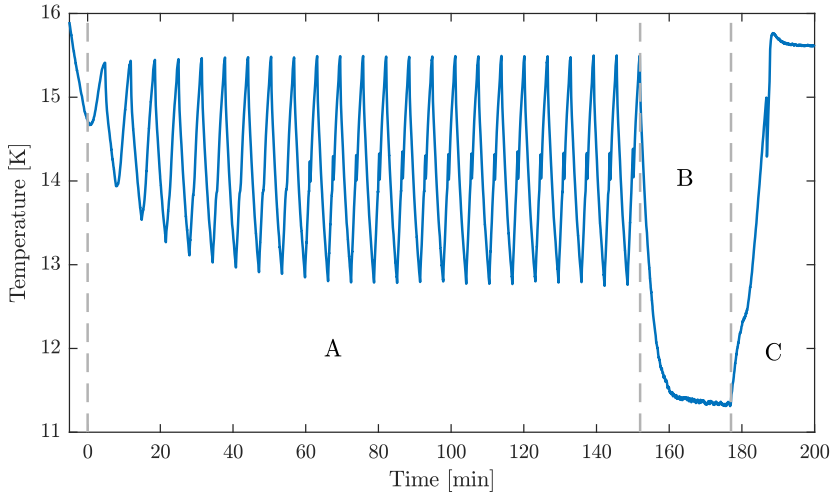


Figure 5.5: Evolution of the temperature of the copper vessel over time during the para-hydrogen enrichment procedure. (A) Freeze-thaw cycles, (B) Freezing period, (C) Slow thawing and recollection of the enriched para-hydrogen. The zero of time corresponds to the beginning of the recirculation procedure.

5.4 Enrichment quality assessment

After preparation of para-hydrogen with the procedure detailed above, it can be deposited on the sample window of the matrix isolation apparatus described in chapter 4. The quality of the enrichment can be assessed by inspection of the NIR spectrum of such a para-hydrogen matrix between 4100 cm^{-1} and 4900 cm^{-1} . Several characteristic bands of the IR spectrum which depend on the concentrations of o-H₂ and p-H₂ are present in this region [130–132]. Two spectra taken in our lab, one of n-H₂ and another of enriched p-H₂, are shown in fig. 5.6.

The features that are worth noting are the $S_1(0)$ band at 4485.9 cm^{-1} and the $Q_1(0)$ band at 4152.9 cm^{-1} . In normal hydrogen, the $S_1(0)$ band is weak while the $Q_1(0)$ is rather prominent. In para-hydrogen, the former drastically increases in intensity, giving rise to a sharp peak, while the latter is barely noticeable. A measure of the p-H₂ enrichment of the prepared sample is given by the ratio:

$$\rho = \frac{I_Q}{I_S} \quad (5.8)$$

where I_Q is the integrated absorbance of the $Q_1(0)$ band and I_S is that of $S_1(0)$. According to Table I in [130], a proportion of 0.19% of ortho-hydrogen is left in the sample when $\rho = 0.021$. For highly para-hydrogen enriched samples, the residual proportion of ortho-hydrogen is approximately ten times the value of ρ . In the present

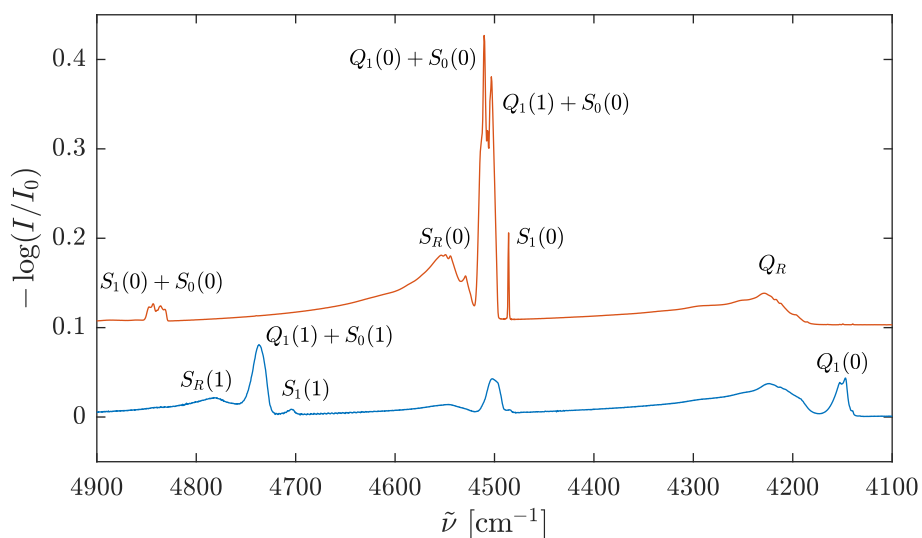


Figure 5.6: NIR absorption spectra of solid normal hydrogen (blue) and para-hydrogen (red) deposited on a CsI window in the matrix isolation apparatus in our laboratory. For visualization purposes, the latter spectrum has been rescaled so that its Q_R band intensity matches that of the former. The assignments of the various bands follow [130].

case, a value of $3.8 \cdot 10^{-3}$ is obtained, indicating that the proportion of remaining o-H₂ is roughly 0.04% of the whole sample, which means that the fraction of p-H₂ in the enriched sample is larger than 99.95%. The automated procedure for enriching para-hydrogen enables systematic reproducibility of this result.

It is furthermore possible to estimate the thickness of the para-hydrogen matrices that can be made with our deposition system. The methods described by Tam & Fajardo [133] (later refined in [134]) are based on the same NIR spectrum of the matrix discussed here. We were able to deposit various matrices with thickness of about 0.5 to 1.0 mm [70].

5.5 Outlook

The ortho-para hydrogen converter described in this chapter enables to obtain enriched high-purity para-hydrogen for matrix isolation experiments. The robust design and the automatic procedure allows for the preparation of this matrix host in a systematic way. In combination with the new matrix deposition apparatus (chapter 4), matrix isolation spectroscopy experiments of weakly bound complexes in para-hydrogen in the FIR region below 300 cm^{-1} can now be carried out routinely.

Conclusion and perspectives

In this project, weakly bound complexes, in particular $(\text{HCl}) \cdots (\text{HOD})$, occupied a central place both from the theoretical and the experimental standpoints. On the one hand, we have shown a computational study of the bimolecular exchange reactions $\text{H} + \text{H}'\text{OD} \longrightarrow \text{HOD} + \text{H}' / \text{HOH}' + \text{D}$, where the complex $(\text{HCl}) \cdots (\text{HOD})$ is used to define the initial conditions of the reaction. On the other hand, we have developed experimental setups for the characterization of weakly bound complexes and applied it to the study of $(\text{HCl}) \cdots (\text{H}_2\text{O})$. The designed para-hydrogen enrichment setup gives the future opportunity to look at its spectral signature in the challenging FIR region.

The computational quantum dynamics work shows that initiating a bimolecular reaction from the weakly bound complex precursor gives rise to a collision characterized by a particularly large collision energy and a well-defined orientation of the reactants. Indeed, as a consequence of the high energy, the collision mostly yields a rebound of the incoming hydrogen atom against HOD. However, because of orientation, some exchange is observed but no abstraction occurs. We have argued that Cl plays no role in the collision process.

There are many ways one could expand on this work. From the example given in this thesis, it would be interesting to extend it to other systems. One could, for example, look at analogous reactions by changing one nucleus in the complex at a time. Hence, starting with the complex $(\text{HX}) \cdots (\text{HOD})$, with X being a different halogen atom, may reveal what is the influence of the halogen atom on the reaction (as a spectator atom or by the amount of collisional kinetic energy gained by the hydrogen atom from the dissociation of HX). The choices are limited to the availability of relevant PES's. Another natural choice would be to revisit cases where the femtochemistry has been studied experimentally, like in the original works of Zewail et al. with $(\text{HI}) \cdots (\text{CO}_2)$ [13, 14] and in particular $(\text{HBr}) \cdots (\text{I}_2)$ [15, 16]. We mention that this has been attempted with the latter system and appendix E gives an overview of the related work.

On the experimental side, the development of instrumentation and methods for the study of weakly bound complexes, i.e. the matrix isolation setup and the para-hydrogen enrichment setup, were successfully accomplished. In particular, the spectrum of the $(\text{HCl}) \cdots (\text{H}_2\text{O})$ complex in solid neon matrices was revealed in the MIR region in the HCl stretching region. The same was achieved for deuterated isotopologues, in particular $(\text{DCl}) \cdots (\text{H}_2\text{O})$. New important insights on the intermolecular PES will be provided by the future study of these complexes in the FIR region, where bands associated to intermolecular vibrations are expected to be observed and, to our knowledge, have not been reported yet. Para-hydrogen is an ideal matrix host for this type of study in the FIR range, in particular for its transparency in this region. These are now possible thanks to the development of the new dedicated enrichment setup.

A

Manuscript submitted to The Journal of Chemical Physics

The following is the manuscript submitted to *The Journal of Chemical Physics* in its original form on October 29, 2020. It was sent back to us on December 9, 2020 for revision. The main concerns that the reviewers raised regarded the following aspects:

- In the initial conditions, the initial momentum of H_a (which is, in terms of the used coordinates, up to a correction factor, that along R_3) is calculated in the case when H_aCl is fully dissociated. However, in this work, this initial momentum is given to H_a when it is in the position defined by the complex geometry in its ground state. It is therefore disputed that H_aCl fully dissociates (and that H_a gains all the momentum it could from that photodissociation) before H_a and H_bOD collide.
- The Cl atom is absent and plays no role in the dynamics. Within the short time-scale of the reaction (exchange or recoil), the chlorine atom (whose mass is 35 atomic mass units) does not move significantly far from H_bOD due to its large mass compared to that of the others. Thus it is thought that Cl is sufficiently close to H_aH_bOD to interact with the latter and, as a consequence, have an impact on the wavepacket propagation. In other words, the assumption no. 3 in section IV is disputed. In particular, for the large part of the wavepacket that recoils into the entrance channel, it is argued that the H_a atom will bounce again against the chlorine atom, thus inducing multiple re-collisions between H_a and H_bOD .

We acknowledge and thank the reviewers for their pertinent remarks. Some of these points can be answered with results obtained from the present model and which were not presented in this article in its original form. These are presented in chapter 3. In order to fully address the reviewer's concerns we suggest possible improvements to

the model in the conclusion of that chapter.

Femtochemistry of bimolecular reactions from weakly bound complexes: computational study of the $\text{H} + \text{H}'\text{OD} \longrightarrow \text{H}'\text{OH} + \text{D} / \text{HOD} + \text{H}'$ exchange reactions

Alexandre Voute,¹ Fabien Gatti,² Klaus B. Møller,¹ and Niels E. Henriksen¹

¹*Department of Chemistry, Technical University of Denmark, Kemitorvet 206, 2800 Kongens Lyngby, Denmark*

²*ISMO, Institut des Sciences Moléculaires d'Orsay - UMR 8214 CNRS/Université Paris-Saclay, F-91405 Orsay, France*

(Dated: October 29, 2020)

A full-dimensional wavepacket propagation describing the bimolecular exchange reactions $\text{H} + \text{H}'\text{OD} \longrightarrow \text{H}'\text{OH} + \text{D} / \text{HOD} + \text{H}'$ initiated by photolysis of HCl in the hydrogen-bound complex $(\text{HCl}) \cdots (\text{HOD})$ is reported. The dynamics of this reaction is carried out with the MCTDH method on an *ab initio* potential energy surface (PES) of H_3O and the initial state is derived from the ground state wavefunction of the complex obtained by relaxation on its own electronic ground state *ab initio* PES. The description of the system makes use of polyspherical coordinates parametrizing a set of Radau and Jacobi vectors. The calculated energy- and time-resolved reaction probabilities show, owing to the large collision energies at play stemming from the photolysis of HCl , that the repulsion between oxygen in the $\text{H}'\text{OD}$ molecule and the incoming hydrogen atom is the main feature of the collision and leads to non-reactive recoil. However, both exchange processes are still observable, with a preference in $\text{O}-\text{H}'$ bond dissociation over that of $\text{O}-\text{D}$. The selectivity is reversed upon vibrational pre-excitation of the $\text{O}-\text{D}$ stretching mode in the $\text{H}'\text{OD}$ molecule.

I. INTRODUCTION

The vast majority of chemical reactions rely on the encounter between molecules. At the elementary molecular level, the collision between two molecules, possibly giving rise to new compounds, is the basic phenomenon where molecules exchange atoms and energy.¹ As is known, the outcome of a single bimolecular collision depends on the initial quantum state of the reactants and the shape of the potential energy surface (PES) in which they lie. Other conditions are also crucial, such as their relative orientations, the collision impact parameter and the relative translational kinetic energy.

Molecular crossed-beam scattering experiments,^{2–5} where a molecule conveyed in one beam with a selected translational kinetic energy scatters due to the sole interaction with a single molecule from the other beam, provide a deep understanding of bimolecular reactions. In these specific conditions, one can quantify the energy required for a given reaction to succeed, characterize whether a collision is elastic or inelastic and, in the latter case, determine how energy is redistributed within the molecules. Yet, the influence of the relative orientations and the impact parameter on the outcome of these collisions can not be readily discerned, as the molecules in the beam are randomly distributed. With the emergence of “transition state spectroscopy”,^{6,7} the nature of the reaction in the vicinity of the barrier could be elucidated for some cases by fixing these geometrical aspects. One of the methods used to achieve this geometrical restriction is to form weakly-bound complexes of the reactants.

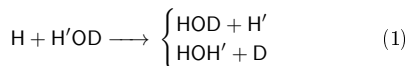
The use of weakly bound atom-molecule aggregates in chemical reactions can be traced back to the work of Jouvet and Soep⁸ who studied the photochemistry

of the $\text{Hg} \cdots \text{Cl}_2$ atom-molecule van der Waals complex. Later, complexes of two molecules were used by Wittig et al. such as $(\text{HBr}) \cdots (\text{CO}_2)^{9,10}$, $(\text{H}_2\text{S}) \cdots (\text{CO}_2)^{11}$, $(\text{HI}) \cdots (\text{CO}_2)^{12}$, $(\text{N}_2\text{O}) \cdots (\text{HI})^{13}$, $(\text{OCS}) \cdots (\text{DI})^{14}$. These groups took the advantage of bringing different molecules close to each other thanks to their weak mutual interaction, ranging from van der Waals interactions to the stronger hydrogen-bonds. It is then by irradiating the formed complex with light that they would trigger a reaction involving the two moieties. In the case of two molecules $\text{A}-\text{B}$ and C , one forms the weakly bound complex $\text{A}-\text{B} \cdots \text{C}$, then irradiates the system with light so as to photodissociate $\text{A}-\text{B}$. As a result, the fragment A is ejected away from the whole system and B is thrown against C . The collision of B with C is then the bimolecular elementary process of interest. What is special here is that the initial positions of the colliding molecules are given by the geometry of the starting complex and that the collisional process takes place in the electronic ground state of the latter, provided that the fragment A is far enough from the two others, $\text{B} + \text{C}$, and that B is formed in its electronic ground state.

In these works, the measured physical quantities were given as functions of the photodissociating continuous wave laser frequency, preventing the observation of time-dependent quantities. Eventually, sub-picosecond time-resolved analysis of bimolecular reactions from predefined initial conditions were accomplished by Zewail and collaborators who exploited the idea of using weakly bound complexes in pump-probe laser femtochemistry experiments. Here, a first short laser pulse (“pump”) initiates the process by photodissociating one of the molecules of the complex (in the example above, $\text{A}-\text{B}$), thus setting a “zero of time” of the reaction to be observed. A second, delayed, laser pulse (“probe”) is beamed on the

system. The response of the latter by interaction with the probe pulse gives then an indication of the status of the system at a given time after the pump pulse. This procedure is ubiquitous in Zewail’s pioneering work and has been applied to a large number of studies of more common unimolecular dynamics. The situation described here is conceptually the same if one considers the complex as a single “supermolecule” where the collisional process unfolds internally. The first experiments of this kind carried out by Zewail’s group involved the complexes $(\text{H})\cdots(\text{CO}_2)^{15,16}$ and $(\text{HBr})\cdots(\text{I}_2)^{17,18}$. Since then, this and other groups explored or revisited this class of reactions^{19–24} and similar ones relying on charge transfer between the moieties of the complex upon photoexcitation by the pump pulse.^{25–30}

One of the prototypical examples of bimolecular reactions is the pair of exchange reactions:



These exchange reactions have been studied only from a theoretical standpoint,^{31–36} whereas the competing “abstraction” reactions $\text{H} + \text{H}'\text{OD} \longrightarrow \text{HH}' + \text{DO}$ or $\text{HD} + \text{H}'\text{O}$ have received a lot of attention in both theory^{4,31–36} and experiments.^{4,37–42} In the context of the ideas explained above, we explore, in this paper, the possibility of initiating the exchange reactions (1) starting from the hydrogen-bond complex $(\text{HCl})\cdots(\text{HOD})$ by breaking the HCl moiety with an appropriate short laser pulse. The approach we adopt is based on quantum mechanics where we solve numerically the time-dependent Schrödinger equation (TDSE) for the nuclear wavefunction, aiming at predicting how the nuclei involved in the reaction will move. In particular, one of our main goals here is to calculate time-dependent reaction probabilities along the exchange and recoil channels of the above-mentioned reaction. To the best of our knowledge, no time-resolved experiments on that exchange reactions and no study of such reactions occurring from the use of the $(\text{HCl})\cdots(\text{HOD})$ complex seem to have ever been conducted. With this paper, our hope is to revive the interest in the femtochemistry of these “precursor-initiated” bimolecular reactions, which have received attention from experimentalists until twenty years ago but have lacked theoretical studies.⁴³ As will be shown, the development of new accurate *ab initio* PESs and efficient algorithms for solving the TDSE in recent years have made it possible to come back to these.

We structure this work as follows. First, we will briefly review the existing work regarding the $(\text{HCl})\cdots(\text{HOD})$ complex and the photodissociation of HCl . Next, we explain how the nuclear coordinates of the reacting system $\text{H} + \text{H}'\text{OD}$ are described in terms of polyspherical coordinates whose choice determines the form of the kinetic energy operator to be used. Subsequently, we will be in the position of specifying the initial state used for the time propagation given the assumptions invoked in this study.

Details on the computational aspects of the simulations are then provided. Finally, we present and discuss the results we have obtained.

II. THE STARTING COMPLEX $(\text{HCl})\cdots(\text{HOD})$ AND THE PHOTODISSOCIATION OF HCl

The complex $(\text{HCl})\cdots(\text{H}_2\text{O})$ and its various isotopologues are known in the literature. Experimentalists could observe it in a variety of conditions by many methods, including Fourier transform microwave (FTMW) spectroscopy in supersonic jets,^{44–46} Fourier transform infrared (FTIR) spectroscopy in supersonic jets,^{47,48} inert matrices^{49–54} and Helium nanodroplets,^{55–57} time-of-flight mass spectrometry and velocity-map imaging used to observe vibrational predissociation of the complex^{58,59} and infrared cavity ringdown spectroscopy.^{60,61} Many theoretical analyses using *ab initio* electronic structure methods^{62–76} were published as well.

It is established that HCl is the hydrogen-bond donor in the binary complex while remaining non-ionized. *Ab initio* methods indicate the existence of three noteworthy stationary points on the potential energy surface. Two of them are identical global minima with C_s geometries (as in fig. 1), one being the image of the other by reflection through the plane of the water molecule. The other one is a saddle point with planar C_{2v} geometry (where HCl and H_2O are now coplanar) connecting the two minima and whose imaginary frequency normal mode is the oscillation between one such geometry to the other. The minimum energy path on the PES going through these three points describes a double-well potential curve. However, the barrier between the two C_s geometries turns out to be smaller than the vibrational zero-point energy. As a consequence, the vibrational ground state wavefunction is delocalized over that double-well and the planar C_{2v} geometry is the most likely to be observed. With the calculation of the potential energy surface for this system at the CCSD(T)/aug-cc-pvtz level of theory, Mancini and Bowman could accurately calculate the barrier height and obtain the vibrational ground state wavefunction and zero-point energy by the diffusion Monte Carlo method.⁷⁴

Excited states potential energy surfaces of the complex, in particular of $(\text{HCl}^*)\cdots(\text{H}_2\text{O})$ where HCl dissociates, are instead not available. However, the photodissociation of HCl alone is known and is not expected to differ much when occurring within the complex because of the relatively weak bond between the water molecule and the hydrogen halide. This aspect will be further discussed when defining the initial state. According to the work of Schmidt *et al.*,⁷⁷ the first allowed electronic transition originating from the electronic ground state $X^1\Sigma$ is the $A^1\Pi \leftarrow X^1\Sigma$, with vertical energy 7.9274 eV corresponding to 156.40 nm. When corrected with the vibrational zero-point energy of HCl ,⁷⁸ the effective vertical transition energy becomes 7.7434 eV, cor-

responding to 160.12 nm. The potential curve of the $A^1\Pi$ state is characteristic of an exponential-decay-like unbound state correlating to ground state $\text{Cl}(^2P)$ and $\text{H}(^2S)$. The difference ΔV_{exc} in energy between the Franck-Condon geometry and the infinitely separated Cl and H is $\Delta V_{\text{exc}} = 3.2825$ eV. Were these two atoms considered as classical particles, by conservation of momentum they would then gain opposite partial momenta of magnitude $p_{\text{exc}} = \sqrt{2\mu\Delta V_{\text{exc}}}$, as shown in appendix A. It is important to note that these quantities are given in the space-fixed frame of reference of HCl.

These considerations, will be important for the definition of the initial state of $\text{H} + \text{HOD}$, as will be done in section IV. In order to be specific, we first discuss in the following section how nuclear configurations are defined in this study.

III. CHOICE OF COORDINATES AND HAMILTONIAN

As in any many-body dynamical problem, the choice of the coordinates describing the system is crucial. A balance has to be found between convenience (for analysis and interpretation of the results) and tractability of the equations of motion. In molecules, the nuclei move with respect to one another, so that distances between pairs of them and various angles are, at first sight, the most natural coordinates to choose. It turns out that this very choice is not optimal in general, in particular when molecules contain more than three atoms. Indeed, distance vectors do not yield a convenient kinetic energy operator to work with, as the number of terms coupling the conjugated momenta associated to each vector scales with the square of the number of atoms. However, one can judiciously work with another set of vectors which, by design, make these crossed terms disappear. Such vectors, in the context of molecular many-body dynamics, are called “orthogonal vectors” (this does *not* mean they are perpendicular) since they “diagonalize” the kinetic energy operator. By this we mean that the kinetic energy is expressed simply as the sum of momenta squared (weighted by their associated masses) without mixed terms. For this reason, as detailed in the following, we choose a non-trivial set of orthogonal vectors to describe the molecular system. These are parameterized in spherical coordinates and, by the polyspherical approach,⁷⁹ we find the expression of the kinetic energy operator used in this study.

From now on, we call H_a the hydrogen atom belonging to HCl and H_b the one belonging to HOD (see fig. 1). G is the center of mass of $\text{H}_a\text{H}_b\text{OD}$, G_s is the center of mass of the *subsystem* H_bOD and K is its so-called “canonical point” with O being the heliocenter, as defined

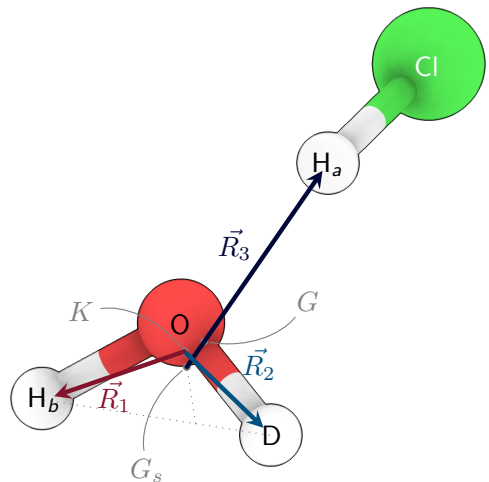


Figure 1. Minimum potential energy geometry of the $(\text{HCl})\cdots(\text{HOD})$ complex and the vectors describing the relative positions of the atoms H_a , H_b , D and O. The shown points are: G , the center of mass of $\{\text{H}_a, \text{H}_b, \text{D}, \text{O}\}$; G_s , the center of mass of the *subsystem* $\{\text{H}_b, \text{D}, \text{O}\}$; K , the Radau canonical point of $\{\text{H}_b, \text{D}, \text{O}\}$ with heliocenter O. Some lengths are exaggerated for visualization purposes (to make G , G_s and K distinguishable).

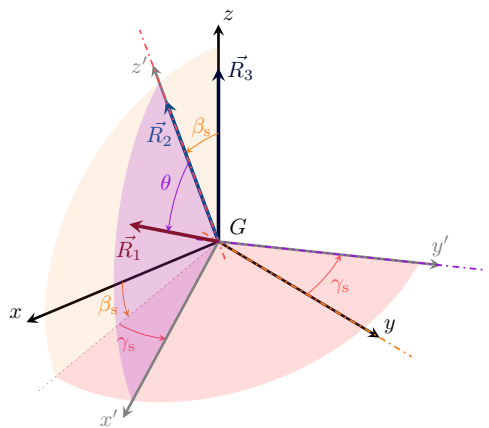


Figure 2. The three vectors \vec{R}_1 , \vec{R}_2 and \vec{R}_3 of fig. 1 and definition of the angles β_s , γ_s and θ between them in the BF and BF's frames of reference. The coordinate system $(Gxyz)$ is attached to the body-fixed frame BF, whereas $(Gx'y'z')$ is attached to the “subsystem”-body-fixed frame BF's. In the text, $u = \cos \theta$

by Radau.^{80,81} . These points are defined such that:

$$\vec{x}_G = \frac{m_H \vec{x}_{H_a} + m_H \vec{x}_{H_b} + m_O \vec{x}_O + m_D \vec{x}_D}{2m_H + m_O + m_D} \quad (2)$$

$$\vec{x}_{G_s} = \frac{m_H \vec{x}_{H_b} + m_O \vec{x}_O + m_D \vec{x}_D}{m_H + m_O + m_D} \quad (3)$$

$$\vec{x}_K - \vec{x}_O = (1 + \alpha_O)^{-1} (\vec{x}_{G_s} - \vec{x}_O) \quad (4)$$

$$\alpha_O = \sqrt{\frac{m_O}{m_H + m_O + m_D}} \quad (5)$$

Since we are not interested in the fate of the chlorine atom after HCl has dissociated, the wavefunction for which we will solve the time-dependent Schrödinger equation will not depend on its coordinates. As will be shown later, these will play a role only in obtaining the initial state in the computations. We focus here on the other atoms of the molecular system $H_a + H_bOD$, shown in fig. 1 with the points we have just defined. The relative positions of these four atoms are given by three vectors \vec{R}_1 , \vec{R}_2 and \vec{R}_3 , also shown in the figure and defined as follows:

$$\vec{R}_1 = \vec{x}_{H_b} - \vec{x}_K \quad (6)$$

$$\vec{R}_2 = \vec{x}_D - \vec{x}_K \quad (7)$$

$$\vec{R}_3 = \vec{x}_{H_a} - \vec{x}_{G_s} \quad (8)$$

We call α , β and γ the three Euler angles of the overall rotation of the system. The rotating body-fixed (BF) frame of reference is chosen such that its z -axis is aligned along the \vec{R}_3 vector and the x -axis is in the plane defined by \vec{R}_2 and \vec{R}_3 (with \vec{R}_2 being oriented towards positive x). By this choice, α and β are given by the spherical angles of \vec{R}_3 with respect to a given lab frame of reference and γ is defined in such a way that (for small values γ) \vec{R}_2 lies in the $(xz, x > 0)$ semi-plane. As will be clearer later, we write $\gamma = \alpha_s$ for convenience. Finally, as shown in fig. 2, we call β_s , γ_s and θ the angle from \vec{R}_3 to \vec{R}_2 , the rotation angle of \vec{R}_1 around \vec{R}_2 and the angle from \vec{R}_2 to \vec{R}_1 , respectively. We define for convenience a “subsystem”-body-fixed (BFs) frame of reference attached to H_bOD , whose z' -axis is aligned along \vec{R}_2 and the x' -axis is such that (for small values of θ) \vec{R}_1 is in the $(x'z', x' > 0)$ semi-plane. As the Euler angles α , β and $\gamma = \alpha_s$ define the overall orientation of the system, they will be called “external” coordinates, as opposed to R_1, R_2, R_3 ,

β_s, γ_s and θ which will be called “internal” coordinates ($R_k = \|\vec{R}_k\|, k \in \{1, 2, 3\}$).

\vec{R}_1, \vec{R}_2 (which are Radau vectors within H_bOD) and \vec{R}_3 (Jacobi vector) are said to be “orthogonal” in the sense that the classical expression of the kinetic energy in the space-fixed frame of reference of H_aH_bOD (i.e. whose origin is the center of mass G and the axes do not rotate with respect to any given lab-fixed frame of reference) is a linear combination of the squares of their conjugate momenta \vec{P}_1, \vec{P}_2 and \vec{P}_3 , respectively. This gives:

$$T = \sum_{k=1}^3 \frac{\vec{P}_k^2}{2\mu_k} \quad (9)$$

with μ_k ($k \in \{1, 2, 3\}$) being masses depending on the problem. With our particular choice of vectors:

$$\mu_1 = m_H \quad \mu_2 = m_D \quad \mu_3 = \frac{m_H(m_H + m_O + m_D)}{2m_H + m_O + m_D} \quad (10)$$

that is, the masses associated to the Radau vectors are the masses of the “satellite” atoms H_a and D of H_bOD and the one of the Jacobi vector is the reduced mass of H_a and H_bOD . The study of the $H_a + H_bOD$ system is therefore equivalent to that of three fictive particles with these three masses, respectively. It is worth noting that, owing to the heavier mass of oxygen than those of the other atoms, these vectors can be roughly interpreted as the distance vectors from O to $H_a/D/H_b$, respectively. This is also the reason why this choice of vectors is suitable for the description of the exchange processes in eq. (1), since each of the regions of the configuration space corresponding to $R_k \rightarrow +\infty$ (for $k \in \{1, 2, 3\}$) describes an exchange reaction ($k = 1$ or 2) or recoil ($k = 3$). Note also that the abstraction reactions channels would correspond to regions where *pairs* of radial coordinates tend to infinity *simultaneously*.

We choose to parametrize these vectors with poly-spherical coordinates, where each vector is described by spherical coordinates (one distance and two angles) with respect to a frame of reference moving with other vectors: \vec{R}_1, \vec{R}_2 and \vec{R}_3 are respectively defined by the triplets of coordinates (R_1, γ_s, θ) , (R_2, α_s, β_s) and (R_3, α, β) (see fig. 2). By using a separation into two subsystems⁸² with the two Radau coordinates for the water-d1 molecule,⁸³ which can be seen as a very particular case of the systematic approach of Gatti and Lung,^{79,84,85} twice the quantized form of the kinetic energy operator of this system reads:

$$\begin{aligned}
2\hat{T} &= -\frac{\hbar^2}{\mu_3} \frac{\partial^2}{\partial R_3^2} + \frac{\hat{L}_3^\dagger \cdot \hat{L}_3}{\mu_3 R_3^2} + 2\hat{T}_{\text{HOD}} \\
&= -\frac{\hbar^2}{\mu_3} \frac{\partial^2}{\partial R_3^2} + \frac{(\hat{J} - \hat{L}_{1,2})^\dagger \cdot (\hat{J} - \hat{L}_{1,2})}{\mu_3 R_3^2} + 2\hat{T}_{\text{HOD}} \\
&= -\frac{\hbar^2}{\mu_3} \frac{\partial^2}{\partial R_3^2} + \frac{\hat{J}^\dagger \cdot \hat{J} + \hat{L}_{1,2}^\dagger \cdot \hat{L}_{1,2} - 2\hat{J}^\dagger \cdot \hat{L}_{1,2}}{\mu_3 R_3^2} + 2\hat{T}_{\text{HOD}} \\
&= -\frac{\hbar^2}{\mu_3} \frac{\partial^2}{\partial R_3^2} + \frac{\hat{J}^2 + \hat{L}_{1,2}^2 - 2\hat{J}_z^2 - \hat{J}_+(\hat{L}_{1,2})_- - \hat{J}_-(\hat{L}_{1,2})_+}{\mu_3 R_3^2} + 2\hat{T}_{\text{HOD}}
\end{aligned} \tag{11}$$

where \dagger denotes the Hermitian conjugate of the operator, which appears here since we work with conjugate momenta of curvilinear coordinates (see e.g. refs. 86–88). Here \hat{T}_{HOD} is the kinetic energy of HOD in the space-fixed frame of reference:

$$\begin{aligned}
2\hat{T}_{\text{HOD}} &= -\frac{\hbar^2}{\mu_1} \frac{\partial^2}{\partial R_1^2} - \frac{\hbar^2}{\mu_2} \frac{\partial^2}{\partial R_2^2} + \hbar^2 \left(\frac{1}{\mu_1 R_1^2} + \frac{1}{\mu_2 R_2^2} \right) \left(\frac{\partial}{\partial u} (1-u^2) \frac{\partial}{\partial u} + \frac{1}{1-u^2} \frac{\partial^2}{\partial \gamma_s^2} \right) \\
&\quad + \frac{1}{\mu_2 R_2^2} \left[\hat{L}_{1,2}^2 - 2(\hat{L}_{1,2})_z^2 + \hbar \left(-\sqrt{1-u^2} \frac{\partial}{\partial u} + \frac{1}{2} \frac{u}{\sqrt{1-u^2}} \right) \left((\hat{L}_{1,2})_+^{\text{BFs}} - (\hat{L}_{1,2})_-^{\text{BFs}} \right) \right. \\
&\quad \left. + \frac{u}{2\sqrt{1-u^2}} \left((\hat{L}_{1,2})_+^{\text{BFs}} (\hat{L}_{1,2})_z^{\text{BFs}} + (\hat{L}_{1,2})_-^{\text{BFs}} (\hat{L}_{1,2})_z^{\text{BFs}} \right. \right. \\
&\quad \left. \left. + (\hat{L}_{1,2})_z^{\text{BFs}} (\hat{L}_{1,2})_+^{\text{BFs}} + (\hat{L}_{1,2})_z^{\text{BFs}} (\hat{L}_{1,2})_-^{\text{BFs}} \right) \right]
\end{aligned} \tag{12}$$

where we have carried out a change of variable $u = \cos \theta$. In eq. (11), \hat{J} and $\hat{L}_{1,2} = \hat{L}_1 + \hat{L}_2$ are respectively vector operators of the total angular momentum and the angular momentum of H_bOD (corresponding to the fictive particles 1 and 2 together). \hat{J}^2 , \hat{J}_z and \hat{J}_\pm are the magnitude squared, the z -component and the ladder operators of the angular momentum of $\text{H}_a\text{H}_b\text{OD}$. $\hat{L}_{1,2}^2$ and $(\hat{L}_{1,2})_z$ are the magnitude squared and the z -component of $\hat{L}_{1,2}$ in the space-fixed frame of reference. In eq. (12), the operators $(\hat{L}_{1,2})_+^{\text{BFs}}$, $(\hat{L}_{1,2})_-^{\text{BFs}}$ and $(\hat{L}_{1,2})_z^{\text{BFs}}$ are the lowering, raising and z -component of the angular momentum $\hat{L}_{1,2}$ projected on the (BFs) frame of reference axes (still expressed within the space-fixed frame of reference).

The kinetic energy operator \hat{T} , written as in eqs. (11) and (12), can be implemented in the Heidelberg MCTDH package which will be introduced in section V. The correctness of the operator \hat{T}_{HOD} and its implementation have been tested numerically as explained in appendix B.

IV. DEFINITION OF THE INITIAL STATE

As our main focus is on the collision between H_a and H_bOD , the wavefunction Ψ of the system $\text{H}_a\text{H}_b\text{OD}$ will be a function of the internal coordinates R_1 , R_2 , R_3 , β_s , γ_s and u as well as the external angle α_s . For a fixed

orientation ($\alpha, \beta, \gamma = \alpha_s$), there is a one-to-one relation between these internal coordinates and the space-fixed Cartesian coordinates \vec{x}_{H_a} , \vec{x}_{H_b} , \vec{x}_{O} of the atoms in $\text{H}_a + \text{H}_b\text{OD}$. The definition of the initial state Ψ_0 of the system $\text{H}_a + \text{H}_b\text{OD}$ is specified as a result of the following assumptions:

1. the transition from the complex ground state to its excited state $(\text{H}_a\text{Cl}^*) \cdots (\text{H}_b\text{OD})$ is vertical (Franck-Condon approximation);
2. the hydrogen-bond is disregarded in the photodissociation process of H_2Cl , as the intermolecular binding energy is small with respect to the excess energy ΔV_{exc} ;
3. the dissociation of H_2Cl is fast enough so that, as it “slides down” the H_2Cl dissociation potential curve, the wavefunction does not spread significantly;
4. after dissociation, the Cl atom is far enough from the other atoms not to interact with them.

The first assumption is invoked so that the (ro-)vibrational ground state wavefunction of the complex, which we call ψ_g , is taken as a starting point for building the initial state Ψ_0 . In other words, the excitation is so fast that the complex retains its geometry as it transits to the electronic excited state. The second one allows to consider that the photodissociation of H_2Cl

occurs independently of the presence of the neighbouring H_bOD molecule. This has two corollaries: (a) the potential energy curves of the $X^1\Sigma$ and $A^1\Pi$ states of H_aCl remain the same as when it is isolated and (b) the centers of masses of the two molecules keep the same distance at all times. Now, as we will be observing the collision occurring between H_a and H_bOD in the space-fixed frame of these four atoms (and not the frame of the whole complex, which included Cl), we must correct the partial momentum of the released hydrogen atom. The relative momentum between H_a and H_bOD becomes:

$$p'_{\text{exc}} = \left(1 - \frac{m_{\text{H}}}{2m_{\text{H}} + m_{\text{D}} + m_{\text{O}}}\right) p_{\text{exc}} \quad (13)$$

as shown in appendix A. The classical translational kinetic energy of collision is then, in the frame of reference of $\text{H}_a + \text{H}_b\text{OD}$, $E_{\text{coll}} = \Delta V_{\text{exc}}(m_{\text{Cl}}/m_{\text{HCl}})(m_{\text{HOD}}/m_{\text{H}_2\text{OD}}) = 3.03 \text{ eV}$. With the third assumption, we consider that the H_a and Cl are well separated before any collision between H_a and H_bOD has ever occurred, so that H_a has gained all the momentum it could get from the dissociation. Moreover, since the wavefunction is considered to spread only a little, we then use the same wavefunction at Franck-Condon geometry to which we “add” the momentum it has gained. Since the atoms Cl , H_a and O in the complex are aligned and G almost coincides with oxygen, we consider that the momentum of H_a is entirely converted into momentum along the R_3 coordinate. Last, the fourth assumption justifies our choice not to include Cl in the wavefunction.

In view of these approximations, the initial state of the propagation is defined as:

$$\begin{aligned} \Psi_0(R_1, R_2, R_3, u, \alpha_s, \beta_s, \gamma_s) \\ = \psi_g(R_1, R_2, R_3, u, \beta_s, \gamma_s) e^{-ip'_{\text{exc}}R_3/\hbar} \end{aligned} \quad (14)$$

In addition, the propagation is performed in the rotational ground state $J = 0$.

V. COMPUTATIONAL DETAILS

This study has been carried out with the Multi-Configuration Time-Dependent Hartree method (MCTDH),^{89–93} more precisely the Heidelberg MCTDH package (version 8.5.11).⁹⁴ The wavefunction Ψ to be propagated is defined over a grid in the internal coordinates R_1 , R_2 , R_3 , β_s , γ_s and u plus the overall rotation angle $\gamma = \alpha_s$. The chosen wavefunction ansatz is:

$$\begin{aligned} \Psi(R_1, R_2, R_3, u, \alpha_s, \beta_s, \gamma_s, t) \\ = \sum_{i_1=0}^{n_1} \sum_{i_2=0}^{n_2} \sum_{i_3=0}^{n_3} A_{i_1, i_2, i_3}(t) \varphi_{i_1}^{(1)}(R_1, u, t) \varphi_{i_2}^{(2)}(R_2, R_3, t) \\ \times \varphi_{i_3}^{(3)}(\alpha_s, \beta_s, \gamma_s, t) \end{aligned} \quad (15)$$

That is, we use three sets of combined-modes single-particle functions (SPF). The SPFs are defined, for $i_1 \in \{1, \dots, n_1\}$, $i_2 \in \{1, \dots, n_2\}$ and $i_3 \in \{1, \dots, n_3\}$, as:

$$\varphi_{i_1}^{(1)}(R_1, u, t) = \sum_{j_1=0}^{N_{1,1}} \sum_{j_2=0}^{N_{1,2}} c_{i_1, j_1, j_2}^{(1)}(t) \chi_{j_1}^{(1,1)}(R_1) \chi_{j_2}^{(1,2)}(u) \quad (16)$$

$$\varphi_{i_2}^{(2)}(R_2, R_3, t) = \sum_{j_1=0}^{N_{2,1}} \sum_{j_2=0}^{N_{2,2}} c_{i_2, j_1, j_2}^{(2)}(t) \chi_{j_1}^{(2,1)}(R_2) \chi_{j_2}^{(2,2)}(R_3) \quad (17)$$

and

$$\begin{aligned} \varphi_{i_3}^{(3)}(\alpha_s, \beta_s, \gamma_s, t) \\ = \sum_{j=0}^{N_{3,1}} \sum_{k=0}^{N_{3,2}} \sum_{m=0}^{N_{3,3}} c_{i_3, j, k, m}^{(3)}(t) \chi_{j, k, m}^{(3)}(\alpha_s, \beta_s, \gamma_s) \end{aligned} \quad (18)$$

The functions $\chi_j^{(\kappa)}(q_\kappa)$ – where κ is a multi-index labelling a coordinate in a mode, e.g. $\kappa = (2, 1)$ labels the coordinate R_2 – are the time-independent primitive basis functions (PBF). These functions, for the coordinates R_1 , R_2 , R_3 and u , are chosen to be the discrete variable representation (DVR) associated with particle-in-a-box eigenfunctions:

$$\chi_j^\kappa(q_\kappa) = \sqrt{\frac{2}{L_\kappa}} \sin\left(\frac{\pi j(q_\kappa - q_\kappa^{\min})}{L_\kappa}\right) \quad (19)$$

where the coordinate q_κ takes values between q_κ^{\min} and q_κ^{\max} , and $L_\kappa = q_\kappa^{\max} - q_\kappa^{\min}$. For the angular coordinates we choose the DVR associated with an expansion in Wigner rotation matrix elements which are non-direct product functions of the three angles:

$$\chi_{j, k, m}^{(3)}(\alpha_s, \beta_s, \gamma_s) = \sqrt{\frac{2(j+1)}{8\pi^2}} D_{j, k, m}^j(\alpha_s, \beta_s, \gamma_s) \quad (20)$$

where

$$D_{m, k}^j(\alpha_s, \beta_s, \gamma_s) = e^{-im\gamma_s/\hbar} d_{m, k}^j(\cos \beta_s) e^{-ik\alpha_s/\hbar} \quad (21)$$

the functions $d_{m, k}^j$ are Jacobi polynomials.⁹⁵

The discrete points where the wavefunction and the potential energy operators are evaluated in coordinate space are determined by the DVR algorithm built into the MCTDH program. These correspond to Gaussian quadrature points specific to the type of PBF used for each degree of freedom. The number of grid points N_κ along a given coordinate equals the number of primitive functions used in the expansions in eqs. (16) to (18). The parameters of the grid/PBF expansions are given in table I.

The ground state wavefunction ψ_g of the complex $(\text{H}_a\text{Cl}) \cdots (\text{H}_b\text{OD})$ was obtained by improved relaxation⁹⁶ on the potential energy surface by Mancini and Bowman⁷⁴ with implicit inclusion of the Cl atom. By “implicit” we mean that the position of the Cl atom is deduced

Table I. Definition of the grid and of the corresponding primitive basis.

κ	Coord.	PBF type ¹	N_κ	Range	Units ²	n_i
(1, 1)	R_1	sin	30	[1.0, 5.0]	a_0	20
(1, 2)	u	sin	20	[-0.99, 0.6]	–	–
(2, 1)	R_2	sin	40	[1.0, 5.0]	a_0	25
(2, 2)	R_3	sin	55	[1.0, 7.0]	a_0	–
(3, 1)	α_s	k	1	–	–	16
(3, 2)	β_s	wigner	20	–	–	–
(3, 3)	γ_s	exp	31	[0, 2π]	rad	–

¹ **sin** = particle in a box eigenfunctions ; **wigner** = Wigner rotation matrix elements ; **exp** = imaginary exponentials with periodic boundary conditions ; **k** = K -rotational quantum number in the Wigner-DVR

² $a_0 = 1 \text{ Bohr} = 0.529 \text{ \AA}$

by the position of the other ones H_a , H_b , D and O. To be specific, the potential energy function V used in this relaxation is a function of the coordinates \vec{x}_{H_a} , \vec{x}_{H_b} , \vec{x}_D , \vec{x}_O (or, equivalently, as a function of the internal coordinates, since the potential is invariant by overall rotation and translation) and its definition is related to the original potential energy surface of the complex U by:

$$V(\vec{x}_{H_a}, \vec{x}_{H_b}, \vec{x}_D, \vec{x}_O) = U(\vec{x}_{H_a}, \vec{x}_{H_b}, \vec{x}_D, \vec{x}_O, \underbrace{f(\vec{x}_{H_a}, \vec{x}_O)}_{=\vec{x}_{Cl}}) \quad (22)$$

with f defined as

$$f(\vec{x}_{H_a}, \vec{x}_O) = \vec{x}_{H_a} + \frac{\vec{x}_{H_a} - \vec{x}_O}{\|\vec{x}_{H_a} - \vec{x}_O\|} R_e \quad (23)$$

In other words, the chlorine atom is placed along the (OH_a) axis, behind the hydrogen atom at a fixed distance $R_e = 1.29 \text{ \AA}$ corresponding to the equilibrium bond length of HCl in the $(HCl) \cdots (H_2O)$ complex at the C_s geometry. The kinetic energy operator used for the relaxation is the one in eq. (11), thus missing some terms related to the HCl elongation and rotation which are neglected. However, this procedure still allows to obtain a physically reasonable ground state wavefunction ψ_g without explicit consideration of the Cl coordinates which are not of interest in the subsequent collision between H_a and H_bOD . We could indeed obtain a wavefunction with C_{2v} symmetry, with expectation values of the coordinates in agreement with the ground state geometry found by Mancini and Bowman. The potential was reconstructed as a sum of products of “one particle” (also called “natural”) potentials – a suitable form for the evaluation of its action on the MCTDH ansatz (eq. (15)) – with the POTFIT program.^{97–99} A narrow relevant region including the double-well potential was considered for the fit. Contraction along the mode (R_2, R_3) was performed whereas, for the modes (R_1, u) and (β_s, γ_s) , 213 and 166 natural potentials were respectively included for the fit and, after a few fitting iterations, the rms error in the relevant regions was 20.7 meV.

The wavefunction ψ_g obtained above is then multiplied by the imaginary exponential as in eq. (14) so as to obtain the initial state for the subsequent dynamics of the $H_a + H_bOD$ collision, for which we used the H_2O potential energy surface of Chen *et al.*¹⁰⁰ (of the three version presented in the paper, the NN1 was chosen). The latter was POTFITTED over a region corresponding to energies below 6.1 eV (the reference being at the $H + H_2O$ asymptote). The mode (R_2, R_3) was again contracted and, for the other modes, we used 191 and 77 natural potentials for the fit. The obtained rms error in the relevant region was, after several iterations, 14.3 meV.

Additional complex absorbing potentials (CAPs) were added at the ends of the three reaction channels in which the wavefunction had more likelihood to exit: the $H_aOD + H_b$ and $H_aHO_b + D$ exchange channels (which we label “1” and “2”, respectively) and the $H_a + H_bOD$ recoil channel (“3”). In practice, the CAPs were placed at the ends of the grid for large values of R_1 , R_2 and R_3 and were of the form (for $k \in \{1, 2, 3\}$):

$$\Theta_k(R_k) = -i\eta_k \cdot \Gamma(R_k - R_k^0) \cdot (R_k - R_k^0)^2 \quad (24)$$

where Γ is the Heaviside step function, R_k^0 is the starting point of the k^{th} CAP and η_k its strength. The lengths (i.e. $\max(R_k) - R_k^0$) of the CAPs were set to $1.5 a_0$ at the ends of channels “1” and “2” and to $2 a_0$ for channel “3”. The strengths were chosen by an automatized optimization procedure – included in the MCTDH package – in order to minimize the reflection on and transmission through these.^{101–103} Due to the limited range of values taken by R_3 and the fact that the initial state is located in the region covered by the third CAP, the latter was activated only a few femtoseconds after the beginning of the propagation, i.e. when the wavepacket would mostly be outside that region.

Time-resolved reaction probabilities $P_k(t)$ with $k \in \{1, 2, 3\}$ for the three outcomes listed above (two exchanges and one recoil) were calculated by accumulation in time of the probability current along each of the three channels. The latter were evaluated by taking the expectation value of the flux operators \hat{F}_k defined as the following commutator¹⁰⁴ (for $k \in \{1, 2, 3\}$):

$$\hat{F}_k = \left[\hat{H}, \Gamma(R_k - R_k^0) \right] = \left[\hat{T}, \Gamma(R_k - d) \right] \quad (25)$$

with $\hat{H} = \hat{T} + \hat{V}_{H+H_2O}$ and $d = 3.5 a_0$. In the following we call “interaction region” the portion of the configuration space where, for $k \in \{1, 2, 3\}$, $0 < R_k < d$. The reaction probability in each channel k is then given by:

$$P_k(t) = \int_0^t \langle \Psi(\tau) | \hat{F}_k | \Psi(\tau) \rangle d\tau + P_k(0) \quad (26)$$

where $P_k(0)$ is the probability of finding the system in the region where $R_k < d$ at $t = 0$.

In addition, energy-resolved reactions probabilities along the three channels were calculated too. The computation of these quantities depend on the energy distribution $\Delta(E)$ of the wavefunction which is determined by

the (inverse) energy-time Fourier transform of the wavefunction autocorrelation function:

$$\begin{aligned} \Delta(E) &= \frac{1}{2\pi\hbar} \int_{-\infty}^{+\infty} \langle \Psi(0) | \Psi(\tau) \rangle e^{iE\tau/\hbar} d\tau \\ &= \frac{1}{\pi\hbar} \operatorname{Re} \left(\int_0^T \langle \Psi(0) | \Psi(\tau) \rangle e^{iE\tau/\hbar} d\tau \right) \end{aligned} \quad (27)$$

where T is the final time of the propagation. In the following, we will represent energy-dependent quantities as functions of the collision energy between H_a and H_bOD . The energy axes are thus shifted by 0.498389 eV corresponding to the vibrational zero-point energy of the latter. This energy is calculated by improved relaxation of H_bOD on the same surface we use for the dynamics (where H_a is fixed, far away from H_bOD , see appendix B for details). In order to calculate the reaction probabilities, one needs the energy-dependent fluxes $\phi_k(E)$ for $k \in \{1, 2, 3\}$ at the end of each channel. These can be computed thanks to the CAPs:^{92,93}

$$\phi_k(E) = \frac{2}{\pi\hbar} \operatorname{Re} \left(\int_0^T g_k(\tau) e^{iE\tau/\hbar} d\tau \right) \quad (28)$$

with:

$$\begin{aligned} g_k(\tau) &= \int_0^{T-\tau} \langle \Psi(t) | \Theta_k | \Psi(t+\tau) \rangle d\tau \\ &+ \frac{1}{2} \langle \Psi(T-\tau) | \Gamma(R_k - R_k^0) | \Psi(T) \rangle \end{aligned} \quad (29)$$

Eventually, the energy-resolved reaction probabilities are given by:

$$\Pi_k(E) = \frac{\phi_k(E)}{\Delta(E)} \quad (30)$$

Because of the presence of CAPs, the norm of the wavefunction would eventually decrease during the propagation. We let it proceed until the former would fall below 10^{-3} , for which a propagation time of 130 fs is sufficient.

The convergence of our results was checked by inspection of (1) the squares of absolute values of the expansion coefficients $c_{i,j,k,m}^{(\kappa)}(t)$ and the populations at the ends of the grid and (2) the magnitude of the natural weights (i.e. the eigenvalues of the one-mode density matrices $\sum_{i_k} |\varphi_{i_k}^{(\kappa)}\rangle \langle \varphi_{i_k}^{(\kappa)}|$). It was required that, over the entire propagation, the smallest value of each of the quantities in (1) and (2) was below 10^{-3} and 10^{-4} , respectively. In addition, we required that the sum of the energy-resolved reaction probabilities would be as close as possible to unity within a 1% error over the largest possible collision energy range. The precision constraint was satisfied by further increasing the number of SPF. The coverage of a larger portion of the energy spectrum was made possible by carrying out additional propagations at slightly higher or lower collision energy (namely by increasing or

decreasing ρ'_{exc} – we chose 16 a.u. and 22 a.u., respectively) and then joining the respective calculated reaction probabilities Π_i^{\oplus} and Π_i^{\ominus} to the main one Π_i^0 by using smooth switching sigmoid-type functions:

$$\begin{aligned} \Pi_i(E) &= \Pi_i^{\ominus}(E)(1-s(E-\epsilon_{\ominus}))(1-s(E-\epsilon_{\oplus})) \\ &+ \Pi_i^0(E)s(E-\epsilon_{\ominus})(1-s(E-\epsilon_{\oplus})) \\ &+ \Pi_i^{\oplus}(E)s(E-\epsilon_{\ominus})s(E-\epsilon_{\oplus}) \end{aligned} \quad (31)$$

where $s(E) = (1 + \exp(-E/\epsilon))^{-1}$, the junction extent is $\epsilon = 0.1$ and the junction points are $(\epsilon_{\ominus}, \epsilon_{\oplus}) = (2.5, 4.1)$ eV.

The chosen parameters to achieve the desired level of precision are the ones given in table I.

VI. RESULTS AND DISCUSSION

A. Main results

We first look at the evolution of the nuclear wavepacket over time. The most relevant coordinates for tracking the present process in eq. (1) are the radial ones R_1 , R_2 and R_3 (since, as noted in section III, they roughly correspond to the O–H_b, O–D and O–H_a bond distances, respectively). Figure 3 displays three contour plots of cuts of the potential energy surface of H_2O as functions of different pairs of these coordinates. In these cuts, the angular coordinates u , β_s and γ_s as well as, in turns, R_1 , R_2 or R_3 , were chosen as their respective expectation value at $t = 0$. On top of the PES cuts, the marginal probability densities (also known as “reduced densities”) are represented at different times during the propagation. These were evaluated by integrating $|\Psi(t)|^2$ with respect to all but two radial coordinates over the entire grid. The marginal probabilities are, at $t = 0$, Gaussian-like functions of the radial coordinates located around $\langle R_1 \rangle = 1.81 a_0$, $\langle R_2 \rangle = 1.78 a_0$ and $\langle R_3 \rangle = 4.0 a_0$. This reflects the fact that the initial state describes the H_a atom and the H_bOD molecule as separated bodies. Note, though, that the wavepacket is not infinitely far from the interaction region: it is indeed lying on the uphill slope of the PES leading to the $\text{H}_a\text{H}_b\text{DO}$ transient (a saddle point $[\text{H}_a(\text{H}_b\text{OD})]^\ddagger$ and a shallow local minimum $\text{H}_a\text{H}_b\text{OD}$ behind it). As time unfolds, because of the initial momentum $-\rho'_{\text{exc}}$ in the direction of \vec{R}_3 , the wavepacket approaches the interaction region. As shown in figs. 3b and 3c, it quickly reaches $\langle R_3 \rangle \approx 1.6 a_0$, crossing many high-lying contour lines of the repulsive potential wall, yet keeping the H_bOD molecule undisturbed (see fig. 3a). Around 12 fs, the wavepacket is almost entirely rejected back from where it came, i.e. in the non-reactive recoil channel “3”. There is just a small fraction of the wavepacket that stands out and manages to enter the reactive channel “1” corresponding to the H_a/H_b exchange (see figs. 3a and 3b at 12 fs). During this time, no O–D dissociation seems to be observable (fig. 3c). The abstraction reactions are also totally absent.

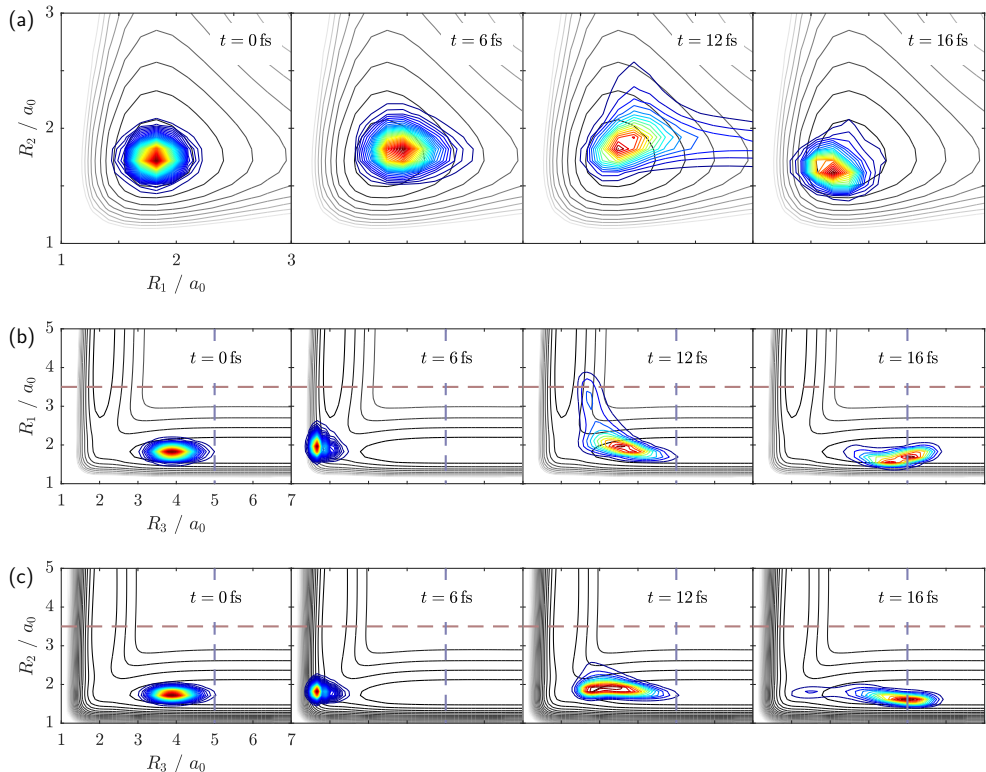


Figure 3. Snapshots of the reduced densities (coloured contours) of the wavepacket as functions of different pairs of radial coordinates: (a) R_1 and R_2 , (b) R_3 and R_1 and (c) R_3 and R_2 . These are overlaid over cuts of the PES (grey-scaled contours) where the fixed coordinates equal their expectation value in the initial state. The dashed lines denote the beginning of a complex absorbing potential.

The computation of time-resolved fluxes through delimiting surfaces in the three channels gives a more quantitative description of the process. The time evolution of the expectation value of the flux operators in eq. (25) are shown in fig. 4a. The negative flux across the delimiting surface at $R_3 = d = 3.5 a_0$ observed at early times is due to the approaching of H_a to the H_bOD molecule: the wavefunction is flowing inside the interaction region. Shortly after, the flux across that same surface and the one placed at the $O-H_b$ dissociation channel sharply peak to positive values and simultaneously with a 4:1 ratio. It is only 3 to 4 fs later that the flux in the $O-D$ dissociation channel starts increasing moderately, followed by a slow decay (see inset in the figure).

These fluxes show that the recoil is the most probable outcome of the collision, followed by H_a/H_b exchange, and very little H_a/D exchange is observable. This is made clear by integrating the fluxes as in eq. (26). These integrals are shown in fig. 4b (the negative of the integral

of F_3 over the entrance phase was taken as $P_3(t=0)$). After the delay time needed for H_a to reach the collision partner, the reaction probabilities P_1 and P_3 steeply increase: the probability of finding the system in the recoil channel goes from almost zero to 90% of its maximal value in the timespan between $t = 9$ fs to $t = 15$ fs. The rising of the probability of H_a/H_b exchange increases in the same fashion. Instead, the probability of H_a/D exchange P_2 starts increasing at slightly later moment and is slower than the others: the increase to 90% of its asymptotic value occurs in the timespan between $t = 11$ fs to $t = 38$ fs. As time tends to infinity, the total reaction probabilities reach $P_1 = 24.1\%$, $P_2 = 5.4\%$ and $P_3 = 70.5\%$.

An insight on the contributions of the different energy components of the wavepacket to this process can be obtained by the evaluation of the energy-resolved fluxes at the end of each reaction channel. These and the wavepacket energy distribution $\Delta(E)$ are shown in fig. 5a. As

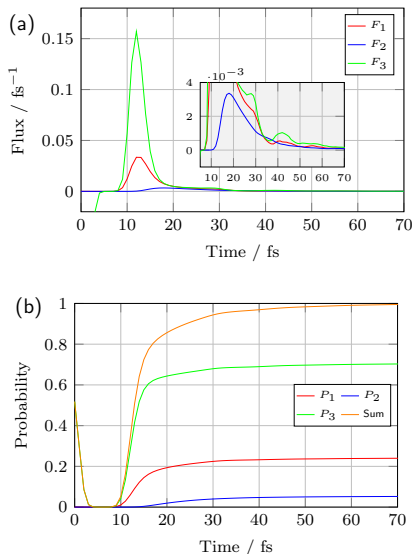


Figure 4. Time-resolved (a) fluxes through the dividing surfaces at $R_k = d = 3.5 a_0$ and (b) corresponding reaction probabilities as defined in eq. (26), with H_bOD initially in its vibrational ground state.

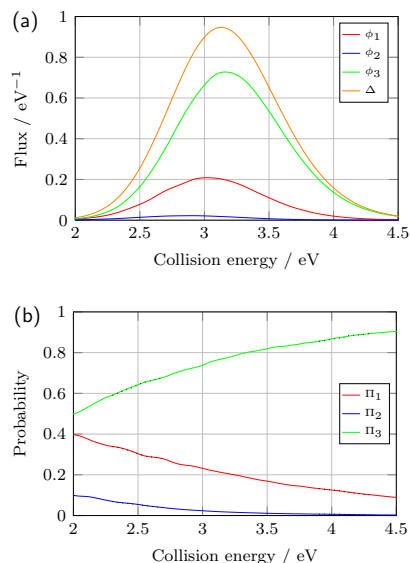


Figure 5. Energy-resolved (a) fluxes and wavepacket energy distribution Δ and (b) reaction probabilities. The dotted lines represent the original data around the junction points which has been smoothed with switching functions.

anticipated, the energy distribution of the wavepacket is a broad Gaussian-like function centered at 3.1 eV. The fluxes evaluated at the ends of the three channels are also smooth, bell-shaped functions of the collision energy, each having its maximum at a slightly higher or lower value. It can again clearly be seen from the values taken by ϕ_3 that the most probable outcome of the collision is the recoil of H_a against H_bOD . On the other hand, within the fraction of successful exchange reactions, the one involving the dissociation of the $\text{O}-\text{H}_b$ bond with subsequent departure of H_b is the most favoured and very little dissociation of the $\text{O}-\text{D}$ bond would be observed.

A clearer comparison of these fluxes can be discussed by computing the energy-resolved reaction probabilities as in eq. (30). These are shown in fig. 5b. We see, as in the time-dependent picture, that the recoil is the most prominent outcome. This becomes more and more the case as the collision energy increases, starting from almost 50% of probability at 2 eV and reaching 90% at 4.5 eV. Conversely, the likelihood that either of the exchange reactions would occur decreases monotonically with collision energy: in that same range, Π_1 (H_a/H_b exchange) goes from 40% to 4.5% and Π_2 (H_a/D exchange) falls from 5% to 0.5%.

The overall reaction probabilities are evaluated by taking the integrals of ϕ_1 , ϕ_2 and ϕ_3 over all the energies (the integral of Δ is one). In total, if the experiment were to be repeated infinitely many times, the recoil would occur 76.5% of the time against only 21.2% and 2.3% of exchange reactions releasing a protium or a deuterium, respectively, which is consistent with the values obtained from the time-resolved fluxes. The discrepancy between the two sets of values is probably due to the fact that the flux ϕ_3 is overestimated at the tails of the energy distribution, making the sum of the three fluxes larger than the latter (which is why we performed additional propagations at lower and higher collision energies for the calculation of energy-resolved probabilities). The overestimation seemed to be larger with a longer CAP in the recoil channel “3”.

As H_a approaches H_bOD , the regions of the H_3O PES explored by the wavepacket are characterized by the presence of a barrier whose geometry at the saddle point is of C_s symmetry. The latter is followed by a shallow local minimum with a geometry of C_{3v} symmetry. The energies of these two are, respectively, 0.888 eV and 0.789 eV above the $\text{H} + \text{H}_2\text{O}$ asymptote.¹⁰⁰ From that C_{3v} intermediate, the paths leading to the departure of either hydrogen atom originally bound to the oxygen are the same as the one just described, backwards. Now, even though the collision energy here is well beyond the barrier, it appears that the exchange would fail most of the time and recoil would occur, in particular for the high energy components of the wavefunction. The collision is so intense that the kinetic energy stored in the R_3 degree of freedom – as H_a is quickly approaching H_bOD – seems not to have sufficient time to redistribute within the H_2DO transient. Little energy is passed to the $\text{O}-\text{H}_b$ and $\text{O}-\text{D}$ bonds. The

collision is dominated by the repulsion between H_a and O, suggesting a hard-sphere-like behaviour of the collision moieties. The hard-sphere character of the collision can also be ascribed to the very short rise-time in the probability of recoil.

Nevertheless, a small fraction of the wavefunction succeeds in following either exchange process as in eq. (1). Protium-to-protium exchange is clearly preferred to protium-to-deuterium. Yet, the direction of attack of H_a towards H_bOD is along the C_2 axis of the latter, so H_b and D are geometrically equivalent prior to the collision. H_b and D being isotopes, for any position of H_a in that axis the potential energy on either bond dissociation channel is the same.

A possible explanation of the difference in exchange reaction probabilities could be a manifestation of vibrational zero-point energy effects within the H_aH_bOD transient. Indeed, the normal modes of the HOD molecule alone are localized, featuring distinct O–H and O–D stretching modes with well-separated vibrational frequencies (3707.47 cm^{-1} and 2723.68 cm^{-1} , respectively¹⁰⁵). Their contributions to the overall vibrational zero-point energy are therefore substantially different. By the harmonic approximation, their difference can be estimated at 491.895 cm^{-1} , i.e. 0.0609872 eV . This suggests that more energy is required to dissociate the O–D bond than the O–H one. This analogy can be applied to the $[H_aH_bOD]^\ddagger$ saddle point structures on the PES. The geometries at the saddle points of H_3O with C_s symmetry are very similar to the one at the C_{3v} local minimum, the main difference being that one of the hydrogen atoms (the one in the symmetry plane) is a bit farther than the other two from the oxygen. The imaginary frequency normal mode is essentially the stretching of the bond in that plane. The vibrational zero-point energy at that saddle point stems from contributions of the other normal modes. Now, the electronic barriers from the H_aH_bOD local minimum to the $[(H_aOD)H_b]^\ddagger$ and $[(H_aOH_b)D]^\ddagger$ saddle points are the same, but the vibrational zero-point energies are different, resulting in an effective barrier height difference. This is supported by inspection of harmonic frequencies calculated at the MP2/aug-cc-pvtz level of theory with the Gaussian16 quantum chemistry package,¹⁰⁶ where this difference is estimated at 492.62 cm^{-1} , that is 0.0611 eV .

However, this difference is much smaller than the collision energies at play in the present case. As a result, if it had a role in the selectivity between the two exchange outcomes, one would expect the ratio Π_1/Π_2 to be close or at least approach unity from above for higher and higher collision energies. This is not the observed trend (that ratio is significantly larger than 1 and increases with the collision energy).

B. Propagation from vibrationally pre-excited HOD

In order not to entirely reject the possibility that vibrational zero-point energy effects play a role in the selectivity between either reaction channels (among what is left aside recoil), we ran an additional propagation in the same conditions as described above, except that the initial state was excited to the first OD-stretching mode vibrational state of HOD. The excitation is applied to the relaxed ground state geometry wavefunction ψ_g by using a harmonic oscillator raising ladder operator (the excitation energy is 2824.5 cm^{-1} in the harmonic approximation¹⁰⁷) along the R_2 coordinate (which is approximately the same as the actual OD-stretching normal mode coordinate). The time evolution of the marginal probability densities for this propagation are shown in fig. 6. Initially, the wavepacket is located in the same region as before, in the recoil channel, but it now features a node and a larger spread along the R_2 coordinate as a result of the vibrational excitation. The collision occurs in the same way as in the previous case with the exception that there is now a much larger fraction of the wavepacket that goes into the O–D bond dissociation reaction channel (see fig. 6a at $t = 12\text{ fs}$ and compare the tails of the marginal probability densities in fig. 6b and fig. 6c). Recoil is still predominant and the O–H bond dissociation is again observable, yet in minor proportion compared to the O–D bond dissociation.

By the look of the time-resolved fluxes and reaction probabilities (fig. 7) it is clear that recoil is still the main observed outcome, with a steep rise of P_3 , the time-integrated flux in the recoil channel, from nearly zero to 90% of its asymptotic value (63.2%) within the timespan between 8 fs to 16 fs. The selectivity between H_a/H_b and H_a/D exchange reactions is reversed. The flux F_1 in the O– H_b bond dissociation channel peaks at the same time as the one along the recoil channel. The flux F_2 along the O–D bond dissociation channel increases again 3 to 4 fs later but is now more prominent than in the previous propagation. The integrals P_1 and P_2 of the fluxes F_1 and F_2 increase with the same time constants as in the previous propagation. The final values are respectively 12.0% and 24.8%.

The energy-resolved data is shown in fig. 8. The tails of the reaction probabilities in fig. 8a are obtained by the same technique as explained in the previous section, by setting p'_{exc} to 17.5 a.u. and 20.5 a.u., and choosing the junction points to be $(\epsilon_{\ominus}, \epsilon_{\oplus}) = (2.7, 3.9)\text{ eV}$. The collision energy distribution Δ is essentially unchanged from the previous propagation and the fluxes preserve the same bell-shaped feature, though the magnitude of ϕ_2 is now larger than ϕ_1 over the whole relevant energy range (see fig. 8a). The resulting reaction probabilities (fig. 8b) show the same energy dependence, i.e. the probability of recoil Π_3 increases with energy (from 44% to 87.5% in the shown range) and the probabilities of both exchange reaction success Π_1 or Π_2 decrease monotonically (from 21% to 6.5% for the former and from 35%

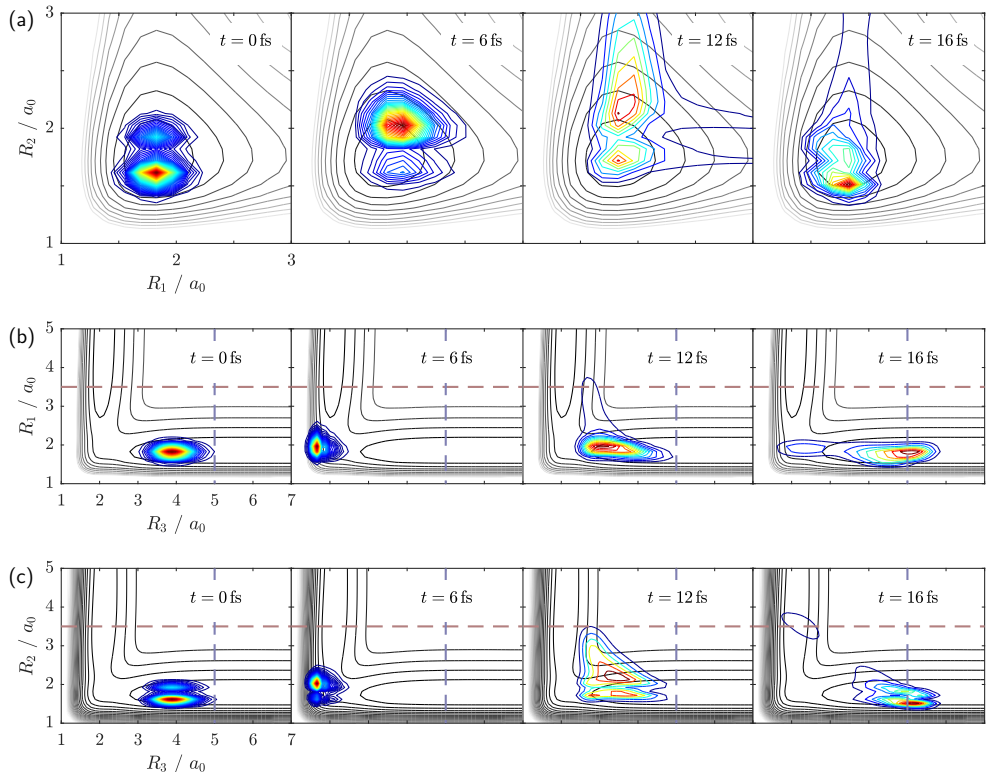


Figure 6. Same as fig. 3, with initial OD-stretching mode excitation of HOD.

to 9% for the latter). A noteworthy difference with the situation with the vibrational ground state of HOD, apart from the fact that now Π_1 and Π_2 are reversed, is that the ratio Π_1/Π_2 does tend to one (from below). The overall energy-integrated reaction probabilities are 69% for the recoil, 11.5% for the H_a/H_b exchange and 19.5% for the H_a/D exchange, again fairly close to the values calculated in the time-dependent picture, given the uncertainty explained earlier.

By exciting the OD-stretching mode, the vibrational energy of HOD, thus that of the H_aH_bOD transient, are increased by one quantum carried by the OD bond. As a result, the effective barrier height at the $[(H_aOD)H_b]^\ddagger$ saddle point is increased and is now larger than at the other $[(H_aOH_b)D]^\ddagger$ point. This fact eventually makes the O– H_b bond harder to break. Moreover, this propagation matches better the expectation that the vibrational energy within the H_aH_bOD transient plays less and less a role as the collision energy increases, since the difference in effective barrier height becomes negligible. One last point about this propagation is that it is an interesting illustration of how one could control the selectivity of the

reaction by changing the quantum state of its colliding moieties, also known as mode-selective chemistry.^{40–42}

C. Propagation at lower collision energy

Finally, in order to connect our study to pre-existing work on these exchange reactions,³² another propagation, this time at lower collision energy, was carried out. The value of p'_{exc} was lowered to 11 atomic units so that the collision energy distribution of the wavepacket would cover a range centered at the exchange reaction barrier height. The time-resolved fluxes and reaction probabilities are shown in fig. 9. The timescale of the reaction is visibly longer, as there is still 5% of chances of finding the system inside the interaction region at $t = 100$ fs (see fig. 9b). The recoil probability P_3 evolves in two steps: a neat increase between 15 and 22 fs and another slower one at later times. These correspond respectively to the first peak in flux F_3 at 19 fs and the following slow undulating decrease which matches with the flux F_1 on the O–H bond dissociation channel (see fig. 9a). This

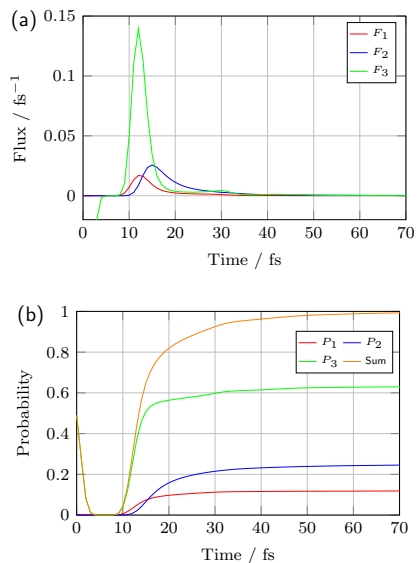


Figure 7. Time-resolved (a) fluxes and (b) reaction probabilities as is fig. 4, with initial OD-stretching mode excitation of HOD.

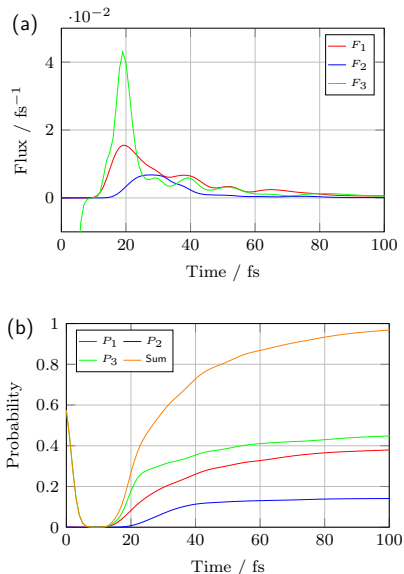


Figure 9. Time-resolved (a) fluxes and (b) reaction probabilities for the exchange reaction at low collision energy.

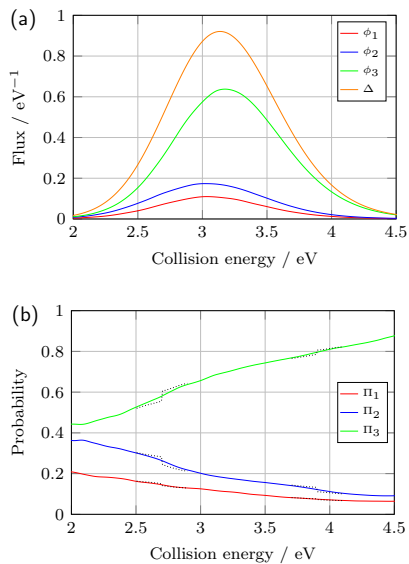


Figure 8. Energy-resolved (a) fluxes and wavepacket energy distribution Δ and (b) reaction probabilities, with initial OD-stretching mode excitation of HOD. The dotted lines represent the original data around the junction points which has been smoothed with switching functions.

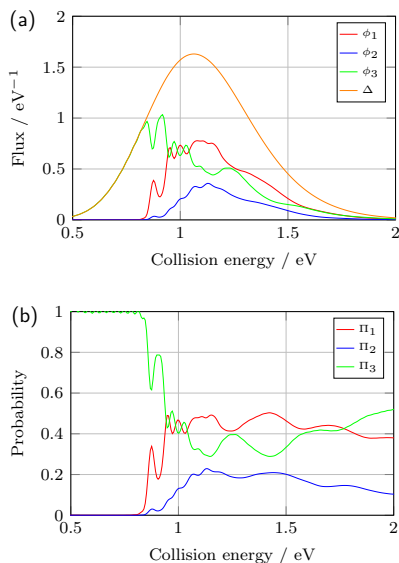


Figure 10. Energy-resolved (a) fluxes and wavepacket energy distribution Δ and (b) reaction probabilities for the low collision energy propagation.

suggests that the first fast phase corresponds to the portion of the wavepacket that is immediately reflected by the potential barrier and that the second one is due to the other portion which is retained in the interaction region and eventually splits into two parts which mainly go either towards the recoil channel or the O–H_b bond dissociation channel. This splitting is confirmed by inspection of the wavepacket (not shown). Furthermore, we do not observe abstraction reactions. The energy-resolved fluxes are richer in features than in the propagations carried out above (fig. 10a). The reaction probabilities shown in fig. 10b support the previous argument, as most of the components of the wavepacket with energies below the barrier height are reflected with certainty and, for the ones above it, there is a competition mostly between recoil and O–H_b bond dissociation. The shift in the onset of Π_2 relative to that of Π_1 is consistent with the higher barrier for O–D dissociation.

The positions of the features at 0.92, 0.96 and 1.0 eV in fig. 10b are close to the ones found by Fu and Zhang³² on a similar PES¹⁰⁸ and are ascribed to shape resonances¹⁰⁹ due to the shape of the potential around the C_{3v} local minimum after the barrier. The differences in the magnitudes between our propagation and their study is due to the fact that their results are obtained by averaging over different orientations and impact parameters, whereas our study involves a well-defined initial wavefunction describing a specific geometrical arrangement of the atoms. The latter is favourable for a backside attack of the H_a against the oxygen, which explains why both H_a/H_b and H_a/D exchange reaction probabilities obtained here are overall twice as large as in their full-collision study. The ratio between reaction probabilities of either exchange processes (channels “1” vs. “2”) is consistent with their results.

VII. CONCLUSION

Femtochemistry experiments of bimolecular reactions initiated by intramolecular photolysis of weakly bound complexes are now between twenty and thirty years old and have not further been studied in detail. In this attempt of reviving the interest in these, we studied the selectivity of the exchange reactions $\text{H} + \text{H}'\text{OD} \rightarrow \text{HOD} + \text{H}' / \text{H}'\text{OH} + \text{D}$ initiated by preforming the $(\text{HCl}) \cdots (\text{HOD})$ hydrogen-bound complex and photodissociating the HCl moiety. The latter causes a release of a considerable amount of energy in the form of translational collision energy between its hydrogen atom and the HOD partner. Because of the magnitude of that energy, the repulsion between the approaching hydrogen and the oxygen belonging to the latter dominates in this collisional process, mainly leading to recoil. However, hydrogen-to-hydrogen and hydrogen-to-deuterium exchange processes can still be observed, with a distinguishable preference of the former to the latter. This selectivity can be controlled by changing the vibrational

state of HOD. We tentatively ascribe the selectivity to vibrational effects in virtue of the fact that O–H and O–D vibrations contribute in different amounts to the vibrational zero-point energy of the H₂DO transient. The time-scales of the recoil and exchange processes are very short: less than 6 fs for recoil and protium-to-protium exchange and less than 27 fs for protium-to-deuterium exchange. Finally, our results were compared to previous full-collision studies of the title reaction at lower collision energies. We find, in particular, an enhanced probability for the exchange reactions to occur.

ACKNOWLEDGMENTS

The authors are grateful to Hans-Dieter Meyer, Markus Schröder and Steve Ndengué for their support in using MCTDH, Joel Bowman and Qi Yu for providing the potential energy surface of $(\text{HCl}) \cdots (\text{H}_2\text{O})$ and help in its usage, Johan Schmidt and Gunnar Nyman for providing the potential energy curves of HCl, Jun Chen for providing the potential energy surface of H₃O and help in its usage and the DTU Computing Center for access to the High Performance Computing services. The rendering of $(\text{HCl}) \cdots (\text{HOD})$ in fig. 1 was made with Speck (<http://www.tyro.github.io/speck/>).

DATA AVAILABILITY

The data that support the findings of this study are available from the corresponding author upon request.

Appendix A: Calculation of the initial momentum \vec{p}'_{ex}

In this appendix we refer to fig. 11. For convenience, we replace the atoms Cl and H_a by two points A and B as well as the center of mass of H_bOD by a point C . These points carry masses $m_A = m_{\text{Cl}}$, $m_B = m_{\text{H}_a}$ and $m_C = m_{\text{H}_b\text{OD}}$, respectively. We call G_0 , G_1 and G_2 the centers of masses of the groups of points $\{A, B, C\}$, $\{A, B\}$ and $\{B, C\}$, respectively, and define the space-fixed frames of reference \mathcal{F}_0 , \mathcal{F}_1 and \mathcal{F}_2 centered at these points. We recall the definitions of the points: for any arbitrary point X in space, we have

$$\vec{G}_0\vec{X} = \frac{m_A\vec{A}\vec{X} + m_B\vec{B}\vec{X} + m_C\vec{C}\vec{X}}{m_A + m_B + m_C} \quad (\text{A1})$$

$$\vec{G}_1\vec{X} = \frac{m_A\vec{A}\vec{X} + m_B\vec{B}\vec{X}}{m_A + m_B} \quad (\text{A2})$$

$$\vec{G}_2\vec{X} = \frac{m_B\vec{B}\vec{X} + m_C\vec{C}\vec{X}}{m_B + m_C} \quad (\text{A3})$$

We denote by $\vec{p}'_X^{(n)}$ the classical momentum of the point

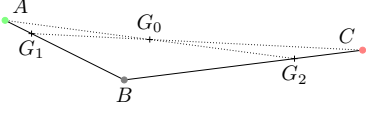


Figure 11. Simplified representation of the generic A–B...C complex and the associated centers of masses: G_0 is the center of mass of $\{A, B, C\}$, G_1 is the center of mass of $\{A, B\}$ and G_2 is the center of mass of $\{B, C\}$. In this work, $A = \text{Cl}$, $B = \text{H}_a$ and $C = \text{G}_s$ (see fig. 1). Here, the positions of the points A, B and C, as well as their weights, are arbitrarily chosen for visualization purposes.

X in the frame \mathcal{F}_n , that is:

$$\vec{p}_X^{(n)} = m_X \frac{d\overrightarrow{G_n X}}{dt} \quad (\text{A4})$$

We assume, on the one hand, that the whole system is initially at rest in \mathcal{F}_0 (and therefore also in \mathcal{F}_1 and \mathcal{F}_2) and, on the other hand, that the interaction between H_aCl and H_bOD (hence between $\{A, B\}$ and C) does not play a role in the dissociation and the dynamics (except for their placement with respect to each other). Thus, the sub-

sequent dissociation of $\{A, B\}$ at total zero momentum in \mathcal{F}_1 implies $\vec{p}_A^{(1)} = -\vec{p}_B^{(1)}$. Moreover, the conversion of the excess potential energy ΔV_{exc} (see section II) in kinetic energy yields:

$$\Delta V_{\text{exc}} = \frac{(\vec{p}_A^{(1)})^2}{2m_A} + \frac{(\vec{p}_B^{(1)})^2}{2m_B} = \frac{(\vec{p}_B^{(1)})^2}{2} \left(\frac{1}{m_A} + \frac{1}{m_B} \right) \quad (\text{A5})$$

As a consequence:

$$p_{\text{exc}} := \left\| \vec{p}_B^{(1)} \right\| = \sqrt{2\mu_{AB}\Delta V_{\text{exc}}} \quad (\text{A6})$$

with $\mu_{AB}^{-1} = m_A^{-1} + m_B^{-1}$.

Again, since we assume that $\{A, B\}$ and C do not interact, the momenta of G_1 and C are zero in \mathcal{F}_0 , that is:

$$\vec{p}_{G_1}^{(0)} = \vec{p}_C^{(0)} = \vec{0} \quad \text{i.e.} \quad \frac{d\overrightarrow{G_0 G_1}}{dt} = \frac{d\overrightarrow{G_0 C}}{dt} = \vec{0} \quad (\text{A7})$$

We are now in the position of calculating the translational collision energy between B and C in the frame of reference \mathcal{F}_2 . The latter is given by:

$$E_{\text{coll}} = \frac{(\vec{p}_B^{(2)})^2}{2m_B} + \frac{(\vec{p}_C^{(2)})^2}{2m_C} = \frac{1}{2}m_B \left(\frac{d\overrightarrow{G_2 B}}{dt} \right)^2 + \frac{1}{2}m_C \left(\frac{d\overrightarrow{G_2 C}}{dt} \right)^2 \quad (\text{A8})$$

The two derivatives can be expressed in terms of $\vec{p}_B^{(1)}$ by using eqs. (A3), (A4) and (A7):

$$\begin{aligned} \frac{d\overrightarrow{G_2 B}}{dt} &= \frac{d}{dt} (\overrightarrow{G_2 G_1} + \overrightarrow{G_1 B}) = \frac{d}{dt} \left(\frac{1}{m_B + m_C} (m_B \overrightarrow{B G_1} + m_C \overrightarrow{C G_1}) \right) + \frac{\vec{p}_B^{(1)}}{m_B} \\ &= \frac{m_B}{m_B + m_C} \frac{d\overrightarrow{B G_1}}{dt} + \frac{m_C}{m_B + m_C} \frac{d\overrightarrow{C G_1}}{dt} + \frac{\vec{p}_B^{(1)}}{m_B} \\ &= -\frac{\vec{p}_B^{(1)}}{m_B + m_C} + \frac{m_C}{m_B + m_C} \underbrace{\frac{d}{dt} (\overrightarrow{C G_0} + \overrightarrow{G_0 G_1})}_{=\vec{0}} + \frac{\vec{p}_B^{(1)}}{m_B} \\ &= \vec{p}_B^{(1)} \left(\frac{1}{m_B} - \frac{1}{m_B + m_C} \right) \end{aligned}$$

and

$$\begin{aligned} \frac{d\overrightarrow{G_2 C}}{dt} &= \frac{d}{dt} (\overrightarrow{G_2 G_1} + \overrightarrow{G_1 C}) = \frac{d}{dt} \left(\frac{1}{m_B + m_C} (m_B \overrightarrow{B G_1} + m_C \overrightarrow{C G_1}) \right) + \underbrace{\frac{d}{dt} (\overrightarrow{G_1 G_0} + \overrightarrow{G_0 C})}_{=\vec{0}} \\ &= -\frac{\vec{p}_B^{(1)}}{m_B + m_C} + \frac{m_C}{m_B + m_C} \underbrace{\frac{d}{dt} (\overrightarrow{C G_0} + \overrightarrow{G_0 G_1})}_{=\vec{0}} = -\frac{\vec{p}_B^{(1)}}{m_B + m_C} \end{aligned}$$

Plugging these relations back into eq. (A8) and by using eq. (A6):

$$\begin{aligned}
E_{\text{coll}} &= \frac{1}{2}m_B \left(\vec{p}_B^{(1)} \left(\frac{1}{m_B} - \frac{1}{m_B + m_C} \right) \right)^2 + \frac{1}{2}m_C \left(-\frac{\vec{p}_B^{(1)}}{m_B + m_C} \right)^2 \\
&= \frac{\|\vec{p}_B^{(1)}\|^2}{2} \left(m_B \left(\frac{1}{m_B} - \frac{1}{m_B + m_C} \right)^2 + m_C \left(\frac{1}{m_B + m_C} \right)^2 \right) \\
&= \frac{p_{\text{exc}}^2}{2} \left(m_B \left(\frac{m_C}{m_B(m_B + m_C)} \right)^2 + m_C \left(\frac{1}{m_B + m_C} \right)^2 \right) \\
&= \Delta V_{\text{exc}} \cdot \mu_{AB} \cdot \left(\frac{m_C}{m_B + m_C} \right)^2 \cdot \left(\frac{1}{m_B} + \frac{1}{m_C} \right) \\
&= \Delta V_{\text{exc}} \cdot \frac{m_A m_B}{m_A + m_B} \cdot \frac{m_C^2}{(m_B + m_C)^2} \cdot \frac{m_B + m_C}{m_B m_C}
\end{aligned}$$

that is

$$E_{\text{coll}} = \Delta V_{\text{exc}} \cdot \frac{m_A}{m_A + m_B} \cdot \frac{m_C}{m_B + m_C} \quad (\text{A9})$$

Finally, we need to determine the initial conjugated momentum \vec{p}_3 associated to the orthogonal vector \vec{R}_3 . Since we have simply $\vec{R}_3 = \vec{C}\vec{B}$, then by eqs. (A1) and (A2):

$$\vec{R}_3 = \frac{1}{m_C} \left((m_A + m_B + m_C) \overrightarrow{G_0\vec{B}} - (m_A + m_B) \overrightarrow{G_1\vec{B}} \right) \quad (\text{A10})$$

Therefore,

$$\begin{aligned}
\vec{p}_3 &= \mu_3 \frac{d\vec{R}_3}{dt} \\
&= \mu_3 \cdot \frac{1}{m_C} \left((m_A + m_B + m_C) \frac{d\overrightarrow{G_0\vec{B}}}{dt} - (m_A + m_B) \frac{d\overrightarrow{G_1\vec{B}}}{dt} \right) \\
&= \mu_3 \cdot \frac{1}{m_C} \left((m_A + m_B + m_C) \left(\underbrace{\frac{d\overrightarrow{G_0\vec{G}_1}}{dt}}_{=\vec{0}} + \frac{d\overrightarrow{G_1\vec{B}}}{dt} \right) - (m_A + m_B) \frac{d\overrightarrow{G_1\vec{B}}}{dt} \right) \\
&= \frac{m_B m_C}{m_B + m_C} \cdot \frac{d\overrightarrow{G_1\vec{B}}}{dt} \\
&= \frac{m_C}{m_B + m_C} \cdot \vec{p}_B^{(1)}
\end{aligned}$$

and finally we obtain:

$$p'_{\text{exc}} := \|\vec{p}_3\| = \frac{m_C}{m_B + m_C} \cdot p_{\text{exc}} \quad (\text{A11})$$

Appendix B: Correctness of the kinetic energy operator and calculation of the zero-point energy of HOD

Before proceeding to any of the simulations that are presented in this article, we made sure that the (not self-evident) kinetic energy operator \hat{T}_{HOD} in eq. (12) and its implementation in the MCTDH package was correct by preliminary numerical tests on HOD. To that end, we

modified the PES of the system H₃O by Chen *et al.*¹⁰⁰ by fixing the R_3 , β_s and γ_s coordinates such that H_a would be far from HOD. The resulting effective surface is, in fact, the one of regular water expressed as a function of R_1 , R_2 and u . This surface was adapted in the MCTDH format with POTFIT on a grid with the same specifications as in table I for these coordinates, without mode combinations and by including all possible natural

potentials. The Hamiltonian of HOD was then taken as the sum of this potential and the kinetic energy operator \hat{T}_{HOD} . A block relaxation was carried out in order to calculate the first 11 rotational excited states of HOD. The rotational lines listed in the MARVEL database^{110–112}, taken as an experimental reference, could unequivocally be assigned to energy differences between the calculated eigenstates.

The vibrational zero-point energy of HOD could be calculated by an improved relaxation on that same modified surface and by keeping only the terms of \hat{T}_{HOD} depending on R_1 , R_2 and u (thus forcing the molecule to be in its rotational ground state). The obtained value is 0.498389 eV.

REFERENCES

- N. E. Henriksen and F. Y. Hansen, *Theories of Molecular Reaction Dynamics: The Microscopic Foundation of Chemical Kinetics*, 2nd ed. (Oxford University Press, 2018).
- D. R. Herschbach, 'Molecular Dynamics of Elementary Chemical Reactions (Nobel Lecture),' *Angew. Chem. Int. Ed.* **26**, 1221–1243 (1987).
- U. Gerlach-Meyer, K. Kleinermanns, E. Linnebach, and J. Wolfrum, 'Experimental determination of total reactive cross sections for $\text{H} + \text{D}_2(\nu = 0) \rightarrow \text{HD} + \text{D}$ at $E_{\text{cm}} = 2.11$ and 1.54 eV,' *J. Chem. Phys.* **86**, 3047 (1987).
- C. Xiao, X. Xu, S. Liu, T. Wang, W. Dong, T. Yang, Z. Sun, D. Dai, X. Xu, D. H. Zhang, and X. Yang, 'Experimental and Theoretical Differential Cross Sections for a Four-Atom Reaction: $\text{HD} + \text{OH} \rightarrow \text{H}_2\text{O} + \text{D}$,' *Science* **333**, 440–442 (2011).
- T. Yang, J. Chen, L. Huang, T. Wang, C. Xiao, Z. Sun, D. Dai, X. Yang, and D. H. Zhang, 'Extremely short-lived reaction resonances in $\text{Cl} + \text{HD}(\nu = 1) \rightarrow \text{DCI} + \text{H}$ due to chemical bond softening,' *Science* **347**, 60–63 (2015).
- D. M. Neumark, 'Transition state spectroscopy of bimolecular chemical reactions,' *Ann. Rev. Phys. Chem.* **43**, 153–176 (1992).
- D. M. Neumark, 'Transition State Spectroscopy,' *Science* **272**, 1446–1447 (1996).
- C. Jouvet and B. Soep, 'Photochemistry in van der Waals complexes: Observation of the intermediate state of the $\text{Hg} \cdots \text{Cl}_2$ reaction,' *Chem. Phys. Lett.* **96**, 426–428 (1983).
- S. Buelow, G. Radhakrishnan, J. Catanzarite, and C. Wittig, 'The use of van der Waals forces to orient chemical reactants: The $\text{H} + \text{CO}_2$ reaction,' *J. Chem. Phys.* **83**, 444–445 (1985).
- G. Radhakrishnan, S. Buelow, and C. Wittig, 'Orienting reactants using van der Waals precursors: $\text{OCO} \cdots \text{HBr} + h\nu \rightarrow \{\text{OCO} \leftarrow \text{H}\} + \text{Br} \rightarrow \text{CO} + \text{OH} + \text{Br}$,' *J. Chem. Phys.* **84**, 727–738 (1986).
- J. Rice, G. Hoffmann, and C. Wittig, 'Photoinitiated $\text{H} + \text{CO}_2 \rightarrow \text{OH} + \text{CO}$ reactions: OH distributions and three-body interactions in $\text{CO}_2\text{H}_2\text{S}$ complexes,' *J. Chem. Phys.* **88**, 2841 (1988).
- Y. Chen, G. Hoffmann, D. Oh, and C. Wittig, ' $\text{H} + \text{CO}_2 \rightarrow \text{OH} + \text{CO}$: Yield versus HI photolysis wavelength and OH rotational distributions under single-collision conditions and with CO_2HI complexes,' *Chem. Phys. Lett.* **159**, 426–434 (1989).
- E. Böhmer, S. K. Shin, Y. Chen, and C. Wittig, 'Photoinitiated H- and D-atom reactions with N_2O in the gas phase and in $\text{N}_2\text{O} \cdots \text{HI}$ and $\text{N}_2\text{O} \cdots \text{DI}$ complexes,' *J. Chem. Phys.* **97**, 2536–2547 (1992).
- E. Böhmer, K. Mikhaylichenko, and C. Wittig, 'Reactions of hot deuterium atoms with OCS in the gas phase and in OCS \cdots DI complexes,' *J. Chem. Phys.* **99**, 6545–6552 (1993).
- N. F. Scherer, L. R. Khundkar, R. B. Bernstein, and A. H. Zewail, 'Real-time picosecond clocking of the collision complex in a bimolecular reaction: The birth of OH from $\text{H} + \text{CO}_2$,' *J. Chem. Phys.* **87**, 1451 (1987).
- N. F. Scherer, C. Sipes, R. B. Bernstein, and A. H. Zewail, 'Real-time clocking of bimolecular reactions: Application to $\text{H} + \text{CO}_2$,' *J. Chem. Phys.* **92**, 5239–5259 (1990).
- M. Gruebele, I. R. Sims, E. D. Potter, and A. H. Zewail, 'Femto-second probing of bimolecular reactions: The collision complex,' *J. Chem. Phys.* **95**, 7763–7766 (1991).
- I. R. Sims, M. Gruebele, E. D. Potter, and A. H. Zewail, 'Femto-second real-time probing of reactions. VIII. The bimolecular reaction $\text{Br} + \text{I}_2$,' *J. Chem. Phys.* **97**, 4127–4148 (1992).
- S. I. Ionov, G. A. Brucker, C. Jaques, L. Valachovic, and C. Wittig, 'Subpicosecond OH production from photoexcited $\text{CO}_2 \cdots \text{HI}$ complexes,' *J. Chem. Phys.* **97**, 9486 (1992).
- S. I. Ionov, P. I. Ionov, and C. Wittig, 'Time-resolved studies of photoinitiated reactions in binary and larger (N_2O) $_m$ (HI) $_n$ ($m \geq 1$, $n \geq 1$) complexes,' *Faraday Discuss. Chem. Soc.* **97**, 391 (1994).
- C. Jaques, L. Valachovic, S. Ionov, E. Böhmer, Y. Wen, J. Segall, and C. Wittig, 'Photoinitiated processes in complexes - subpicosecond studies of $\text{CO}_2 \cdots \text{HI}$ and stereospecificity in $\text{Ar} \cdots \text{HX}$,' *J. Chem. Soc. Faraday. Trans.* **89**, 1419–1425 (1993).
- S. A. Wright, M. F. Tuchler, and J. McDonald, 'Picosecond observation of electronic quenching. $\text{Br}(^2P_{1/2}) + \text{I}_2(\nu = 0) \rightarrow \text{Br}(^2P_{3/2}) + \text{I}_2(\nu > 0)$ by geometrically restricted reaction,' *Chem. Phys. Lett.* **226**, 570–576 (1994).
- M. F. Tuchler, S. Wright, and J. D. McDonald, 'Real time study of bimolecular interactions: Direct detection of internal conversion involving $\text{Br}(^2P_{1/2}) + \text{I}_2$ initiated from a van der Waals dimer,' *J. Chem. Phys.* **106**, 2634–2645 (1997).
- R. Wester, A. E. Bragg, A. V. Davis, and D. M. Neumark, 'Time-resolved study of the symmetric S_N2 -reaction $\text{I}^- + \text{CH}_3\text{I}$,' *J. Chem. Phys.* **119**, 10032–10039 (2003).
- P. Y. Cheng, D. Zhong, and A. H. Zewail, 'Transition states of charge-transfer reactions: Femtosecond dynamics and the concept of harpooning in the bimolecular reaction of benzene with iodine,' *J. Chem. Phys.* **103**, 5153–5156 (1995).
- D. Zhong, S. Ahmad, P. Y. Cheng, and A. H. Zewail, 'Femtosecond nucleophilic substitution reaction dynamics,' *J. Am. Chem. Soc.* **119**, 2305–2306 (1997).
- O. K. Abou-Zied and J. D. McDonald, 'Picosecond real time study of the bimolecular reaction $\text{O}(^3P) + \text{C}_2\text{H}_4$ and the unimolecular photodissociation of CH_3CHO and H_2CO ,' *J. Chem. Phys.* **109**, 1293–1301 (1998).
- P. Farmanara, V. Stert, W. Radloff, S. Skowronek, and A. Gonzalez-Ureña, 'Ultrafast dynamics and energetics of the intracuster harpooning reaction in $\text{Ba} \cdots \text{FCH}_3$,' *Chem. Phys. Lett.* **304**, 127–133 (1999).
- V. Stert, P. Farmanara, W. Radloff, F. Noack, S. Skowronek, J. Jimenez, and A. González Ureña, 'Real-time study of the femtosecond harpooning reaction in $\text{Ba} \cdots \text{FCH}_3$,' *Phys. Rev. A* **59**, R1727–R1730 (1999).
- V. Stert, P. Farmanara, H.-H. Ritzke, W. Radloff, K. Gasmí, and A. Gonzalez-Ureña, 'Femtosecond time-resolved electron spectroscopy of the intracuster reaction in $\text{Ba} \cdots \text{FCH}_3$,' *Chem. Phys. Lett.* **337**, 299–305 (2001).
- B. Fu and D. H. Zhang, 'Full-dimensional quantum dynamics study of exchange processes for the $\text{D} + \text{H}_2\text{O}$ and $\text{D} + \text{HOD}$ reactions,' *J. Chem. Phys.* **136**, 194301 (2012).
- B. Fu and D. H. Zhang, 'Full-Dimensional Quantum Dynamics Study of the $\text{H} + \text{H}_2\text{O}$ and $\text{H} + \text{HOD}$ Exchange Reactions,' *J. Phys. Chem. A* **116**, 820–825 (2012).
- B. Fu, Y. Zhou, and D. H. Zhang, 'Shape resonance in the $\text{H} + \text{D}_2\text{O} \rightarrow \text{D} + \text{HOD}$ reaction: a full-dimensional quantum dynamics study,' *Chem. Sci.* **3**, 270–274 (2012).
- B. Fu and D. H. Zhang, 'Mode specificity in the $\text{H} + \text{H}_2\text{O} \rightarrow \text{H}_2 + \text{OH}$ reaction: A full-dimensional quantum dynamics study,' *J. Chem. Phys.* **138**, 184308 (2013).
- D. H. Zhang, M. Yang, and S.-Y. Lee, 'Branching ratio in the $\text{HD} + \text{OH}$ reaction: A full-dimensional quantum dynamics study

- on a new ab initio potential energy surface,' *J. Chem. Phys.* **114**, 8733–8736 (2001).
- ³⁶D. H. Zhang, M. Yang, and S.-Y. Lee, 'Breakdown of the Spectator Model for the OH Bonds in Studying the H + H₂O Reaction,' *Phys. Rev. Lett.* **89**, 103201 (2002).
- ³⁷A. Sinha, M. C. Hsiao, and F. F. Crim, 'Bond-selected bimolecular chemistry: H + HOD($4\nu_{OH}$) \longrightarrow OD + H₂,' *J. Chem. Phys.* **92**, 6333–6335 (1990).
- ³⁸A. Sinha, M. C. Hsiao, and F. F. Crim, 'Controlling bimolecular reactions: Mode and bond selected reaction of water with hydrogen atoms,' *J. Chem. Phys.* **94**, 4928–4935 (1991).
- ³⁹R. B. Metz, J. D. Thoemke, J. M. Pfeiffer, and F. F. Crim, 'Selectively breaking either bond in the bimolecular reaction of HOD with hydrogen atoms,' *J. Chem. Phys.* **99**, 1744–1751 (1993).
- ⁴⁰M. J. Bronikowski, W. R. Simpson, B. Girard, and R. N. Zare, 'Bond-specific chemistry: OD:OH product ratios for the reactions H + HOD(100) and H + HOD(001),' *J. Chem. Phys.* **95**, 8647–8648 (1991).
- ⁴¹M. J. Bronikowski, W. R. Simpson, and R. N. Zare, 'Effect of reagent vibration on the H + HOD reaction: An example of bond-specific chemistry,' *J. Chem. Phys.* **97**, 2194–2203 (1993).
- ⁴²M. J. Bronikowski, W. R. Simpson, and R. N. Zare, 'Comparison of reagent stretch vs bend excitation in the H + D₂O reaction: an example of mode-selective chemistry,' *J. Chem. Phys.* **97**, 2204–2208 (1993).
- ⁴³N. E. Henriksen, 'Femtochemistry – some reflections and perspectives,' *Chem. Phys.* **442**, 2–8 (2014).
- ⁴⁴Z. Kisiel, E. Białkowska-Jaworska, L. Pszczołkowski, A. Milec, C. Struniewicz, R. Moszynski, and J. Sadlej, 'Structure and properties of the weakly bound trimer (H₂O)₂HCl observed by rotational spectroscopy,' *J. Chem. Phys.* **112**, 5767–5776 (2000).
- ⁴⁵Z. Kisiel, B. A. Pietrewicz, P. W. Fowler, A. C. Legon, and E. Steiner, 'Rotational spectra of the less common isotopomers, electric dipole moment and the double minimum inversion potential of H₂O...HCl,' *J. Phys. Chem. A* **104**, 6970–6978 (2000).
- ⁴⁶A. C. Legon and L. C. Willoughby, 'Identification and molecular geometry of a weakly bound dimer (H₂O...HCl) in the gas phase by rotational spectroscopy,' *Chem. Phys. Lett.* **95**, 449–452 (1983).
- ⁴⁷M. Fárník, M. Weimann, and M. A. Suhm, 'Acidic protons before take-off: A comparative jet Fourier transform infrared study of small HCl- and HBr-solvent complexes,' *J. Chem. Phys.* **118**, 10120–10136 (2003).
- ⁴⁸M. Weimann, M. Fárník, and M. A. Suhm, 'A first glimpse at the acidic proton vibrations in HCl-water clusters via supersonic jet FTIR spectroscopy,' *PCCP* **4**, 3933–3937 (2002).
- ⁴⁹B. S. Ault and G. C. Pimentel, 'Infrared spectrum of the water-hydrochloric acid complex in solid nitrogen,' *J. Chem. Phys.* **77**, 57–61 (1973).
- ⁵⁰G. P. Ayers and A. D. E. Pullin, 'The i.r. spectra of matrix isolated water species – II. The characterisation of non-rotating monomer water species in an argon matrix by xenon doping: The matrix isolated spectra of H₂O-HCl and (CH₃)₂O-H₂O as model compounds for water dimer spectra,' *Spectrochimica Acta part A* **32**, 1641–1650 (1976).
- ⁵¹C. Amirand and D. Maillard, 'Spectrum and structure of water-rich water-hydracid complexes from matrix isolation spectroscopy: evidence for proton transfer,' *J. Mol. Struct.* **176**, 181–201 (1988).
- ⁵²A. Engdahl and B. Nelander, 'Axial motion of water-hydrogen halide and water-halogen complexes in argon matrices,' *J. Chem. Phys.* **84**, 1981–1987 (1986).
- ⁵³A. J. Barnes, 'Molecular complexes of the hydrogen halides studied by matrix isolation infrared spectroscopy,' *J. Mol. Struct.* **100**, 259–280 (1983).
- ⁵⁴A. Schriver, B. Silvi, D. Maillard, and J. P. Perchard, 'Structure of water-hydrochloric acid complexes in argon and nitrogen matrices from infrared spectra,' *J. Chem. Phys.* **81**, 2095–2102 (1977).
- ⁵⁵S. D. Flynn, D. Skvortsov, A. M. Morrison, T. Liang, M. Y. Choi, G. E. Doublerly, and A. F. Vilesov, 'Infrared Spectra of HCl-H₂O Clusters in Helium Nanodroplets,' *J. Phys. Chem. Lett.* **1**, 2233–2238 (2010).
- ⁵⁶A. M. Morrison, S. D. Flynn, T. Liang, and G. E. Doublerly, 'Infrared Spectroscopy of (HCl)_m(H₂O)_n Clusters in Helium Nanodroplets: Definitive Assignments in the HCl Stretch Region,' *J. Phys. Chem. A* **114**, 8090–8098 (2010).
- ⁵⁷M. Ortlieb, Ö. Birer, M. Letzner, G. W. Schwaab, and M. Havenith, 'Observation of Rovibrational Transitions of HCl, (HCl)₂, and H₂O-HCl in Liquid Helium Nanodroplets,' *J. Phys. Chem. A* **111**, 12192–12199 (2007).
- ⁵⁸B. E. Casterline, A. K. Mollner, L. C. Ch'Ng, and H. Reisler, 'Imaging the state-specific vibrational predissociation of the hydrogen chloride-water hydrogen-bonded dimer,' *J. Phys. Chem. A* **114**, 9774–9781 (2010).
- ⁵⁹B. E. Rocher-Casterline, A. K. Mollner, L. C. Ch'Ng, and H. Reisler, 'Imaging H₂O photofragments in the predissociation of the HCl-H₂O hydrogen-bonded dimer,' *J. Phys. Chem. A* **115**, 6903–6909 (2011).
- ⁶⁰A. J. Huneycutt, R. J. Stickland, F. Hellberg, and R. J. Saykally, 'Characterization of gas-phase HCl-H₂O clusters using pulsed infrared cavity ringdown spectroscopy,' *Methods for Ultrasensitive Detection II* **4634**, 70 (2002).
- ⁶¹A. J. Huneycutt, R. J. Stickland, F. Hellberg, and R. J. Saykally, 'Infrared cavity ringdown spectroscopy of acid-water clusters: HCl-H₂O, DCl-D₂O, and DCl-(D₂O)₂,' *J. Chem. Phys.* **118**, 1221–1229 (2003).
- ⁶²M. E. Alikhani and B. Silvi, 'Ab initio study of (H₂O)_{1,2}-HCl: Accurate energetic and frequency shift of HCl,' *PCCP* **5**, 2494–2498 (2003).
- ⁶³M. J. Packer and D. C. Clary, 'Interaction of HCl with water clusters: (H₂O)_nHCl, n = 1–3,' *J. Chem. Phys.* **99**, 14323–14333 (1995).
- ⁶⁴Z. Latajka and S. Scheiner, 'Structure, energetics, and vibrational spectrum of H₂O-HCl,' *J. Chem. Phys.* **87**, 5928–5936 (1987).
- ⁶⁵M. M. Szcześniak, S. Scheiner, and Y. Bouteiller, 'Theoretical study of H₂O-HF and H₂O-HCl: Comparison with experiment,' *J. Chem. Phys.* **81**, 5024–5030 (1984).
- ⁶⁶Y. Hannachi, B. Silvi, and Y. Bouteiller, 'Structure and vibrational properties of water hydrogen halide complexes,' *J. Chem. Phys.* **94**, 2915–2922 (1991).
- ⁶⁷S. Re, Y. Osamura, Y. Suzuki, and H. F. Schaefer, 'Structures and stability of hydrated clusters of hydrogen chloride, HCl(H₂O)_n, n = 1–5,' *J. Chem. Phys.* **109**, 973–977 (1998).
- ⁶⁸G. M. Chaban, R. B. Gerber, and K. C. Janda, 'Transition from Hydrogen Bonding to Ionization in (HCl)_n(NH₃)_n and (HCl)_n(H₂O)_n Clusters: Consequences for Anharmonic Vibrational Spectroscopy,' *J. Phys. Chem. A* **105**, 8323–8332 (2001).
- ⁶⁹E. M. Cabaleiro-Lago, J. M. Hermida-Ramón, and J. Rodríguez-Otero, 'Computational study of the dissociation of H-X acids (X = F, Cl, Br, I) in water clusters,' *J. Chem. Phys.* **117**, 3160–3168 (2002).
- ⁷⁰S. Odde, B. J. Mhin, S. Lee, H. M. Lee, and K. S. Kim, 'Dissociation chemistry of hydrogen halides in water,' *J. Chem. Phys.* **120**, 9524–9535 (2004).
- ⁷¹X. Zhang, Y. Zeng, X. Li, L. Meng, and S. Zheng, 'Comparison in the complexes of oxygen-containing σ -electron donor with hydrogen halide and dihalogen molecules,' *J. Mol. Struct. (Theochem)* **950**, 27–35 (2010).
- ⁷²E. Perlt, S. A. Berger, A. M. Kelterer, and B. Kirchner, 'Anharmonicity of Vibrational Modes in Hydrogen Chloride-Water Mixtures,' *J. Chem. Theory Comput.* **15**, 2535–2547 (2019).
- ⁷³H. Liu, R. Man, Z. Wang, J. Liao, X. Li, S. Ma, and P. Yi, 'Study on the cooperativity of hydrogen bonds between H₂Y and HX (X=F, Cl, Br; Y=O, S, Se),' *J. Theo. Comp. Chem.* **13**, 1450037 (2014).
- ⁷⁴J. S. Mancini and J. M. Bowman, 'Communication: A new ab initio potential energy surface for HCl-H₂O, diffusion Monte

- Carlo calculations of D_0 and a delocalized zero-point wavefunction,' *J. Chem. Phys.* **138**, 121102 (2013).
- ⁷⁵J. S. Mancini and J. M. Bowman, 'Effects of Zero-Point Delocalization on the Vibrational Frequencies of Mixed HCl and Water Clusters,' *J. Phys. Chem. Lett.* **5**, 2247–2253 (2014).
- ⁷⁶J. S. Mancini and J. M. Bowman, 'Isolating the spectral signature of H_3O^+ in the smallest droplet of dissociated HCl acid,' *PCCP* **17**, 6222–6226 (2015).
- ⁷⁷J. A. Schmidt, M. S. Johnson, M. M. Grage, and G. Nyman, 'On the origin of the asymmetric shape of the HCl photodissociation cross section,' *Chem. Phys. Lett.* **480**, 168–172 (2009).
- ⁷⁸K. K. Irikura, 'Experimental Vibrational Zero-Point Energies: Diatomic Molecules,' *J. Phys. Chem. Ref. Data* **36**, 389–397 (2007).
- ⁷⁹F. Gatti and C. Iung, 'Exact and constrained kinetic energy operators for polyatomic molecules: The polyspherical approach,' *Phys. Rep.* **484**, 1–69 (2009).
- ⁸⁰R. Radau, 'Sur une transformation des équations différentielles de la dynamique,' *Annales Scientifiques de l'École Normale Supérieure* **5**, 311–375 (1868).
- ⁸¹F. T. Smith, 'Modified Heliocentric Coordinates for Particle Dynamics,' *Phys. Rev. Lett.* **45**, 1157–1160 (1980).
- ⁸²G. Brocks, A. V. D. Avoird, B. T. Sutcliffe, and J. Tennyson, *Mol. Phys.* **50**, 1025 (1983).
- ⁸³M. J. Bramley and T. Carrington, Jr., *J. Chem. Phys.* **99**, 8519 (1993).
- ⁸⁴F. Gatti, C. Iung, M. Menou, Y. Justum, A. Nauts, and X. Chapuisat, 'Vector parametrization of the N-atom problem in quantum mechanics. I. Jacobi vectors,' *J. Chem. Phys.* **108**, 8804 (1998).
- ⁸⁵F. Gatti, 'Vector parametrization of the N-atom problem in quantum mechanics. III. Separation into two sub-systems,' *J. Chem. Phys.* **111**, 7225 (2010).
- ⁸⁶A. Nauts and X. Chapuisat, 'Momentum, quasi-momentum and hamiltonian operators in terms of arbitrary curvilinear coordinates, with special emphasis on molecular hamiltonians,' *Mol. Phys.* **55**, 1287–1318 (1985).
- ⁸⁷H. Essen, 'Quantization and independent coordinates,' *Am. J. Phys.* **46**, 983–988 (1978).
- ⁸⁸A. Nauts and F. Gatti, 'Unusual commutation relations in physics,' *Am. J. Phys.* **78**, 1365–1375 (2010).
- ⁸⁹H.-D. Meyer, U. Manthe, and L. S. Cederbaum, 'The multi-configurational time-dependent Hartree approach,' *Chem. Phys. Lett.* **165**, 73–78 (1990).
- ⁹⁰U. Manthe, H.-D. Meyer, and L. S. Cederbaum, 'Wave-packet dynamics within the multiconfiguration Hartree framework: General aspects and application to NOCI,' *J. Chem. Phys.* **97**, 3199–3213 (1992).
- ⁹¹U. Manthe, H.-D. Meyer, and L. S. Cederbaum, 'Multiconfigurational time-dependent Hartree study of complex dynamics: Photodissociation of NO_2 ,' *J. Chem. Phys.* **97**, 9062–9071 (1992).
- ⁹²M. Beck, A. Jäckle, G. A. Worth, and H.-D. Meyer, 'The multiconfiguration time-dependent Hartree (MCTDH) method: a highly efficient algorithm for propagating wavepackets,' *Phys. Rep.* **324**, 1–105 (2000).
- ⁹³F. Gatti, B. Lasorne, H.-D. Meyer, and A. Nauts, *Applications of Quantum Dynamics in Chemistry*, Vol. 98 (Springer International Publishing, 2017) pp. XIV, 429.
- ⁹⁴G. A. Worth, M. H. Beck, A. Jäckle, O. Vendrell, and H.-D. Meyer, The MCTDH Package, Version 8.2, (2000). H.-D. Meyer, Version 8.3 (2002), Version 8.4 (2007). O. Vendrell and H.-D. Meyer Version 8.5 (2013). Version 8.5 contains the ML-MCTDH algorithm. Used version: 8.5.11 (2019). See <http://mctdh.uni-hd.de/>.
- ⁹⁵M. Abramowitz and I. Stegun, *Handbook of Mathematical Functions* (Dover Publ., 1973).
- ⁹⁶H.-D. Meyer, F. Le Quéré, C. Léonard, and F. Gatti, 'Calculation and selective population of vibrational levels with the Multiconfiguration Time-Dependent Hartree (MCTDH) algorithm,' *Chem. Phys.* **329**, 179–192 (2006).
- ⁹⁷A. Jäckle and H. Meyer, 'Product representation of potential energy surfaces,' *J. Chem. Phys.* **104**, 7974–7984 (1996).
- ⁹⁸A. Jäckle and H.-D. Meyer, 'Product representation of potential energy surfaces. II,' *J. Chem. Phys.* **109**, 3772–3779 (1998).
- ⁹⁹F. Gatti and H.-D. Meyer, 'Intramolecular vibrational energy redistribution in Toluene: A nine dimensional quantum mechanical study using the MCTDH algorithm,' *Chem. Phys.* **304**, 3–15 (2004).
- ¹⁰⁰J. Chen, X. Xu, X. Xu, and D. H. Zhang, 'A global potential energy surface for the $\text{H}_2 + \text{OH} \rightarrow \text{H}_2\text{O} + \text{H}$ reaction using neural networks,' *J. Chem. Phys.* **138**, 154301 (2013).
- ¹⁰¹U. V. Riss and H.-D. Meyer, 'Calculation of resonance energies and widths using the complex absorbing potential method,' *J. Phys. B* **26**, 4503 (1993).
- ¹⁰²U. V. Riss and H. D. Meyer, 'Reflection-free complex absorbing potentials,' *J. Phys. B* **28**, 1475–1493 (1995).
- ¹⁰³U. V. Riss and H. Meyer, 'Investigation on the reflection and transmission properties of complex absorbing potentials,' *J. Chem. Phys.* **105**, 1409–1419 (1996).
- ¹⁰⁴W. H. Miller, S. D. Schwartz, and J. W. Tromp, 'Quantum mechanical rate constants for bimolecular reactions,' *J. Chem. Phys.* **79**, 4889–4898 (1983).
- ¹⁰⁵J. Tennyson, P. F. Bernath, L. R. Brown, A. Campargue, A. G. Császár, L. Daumont, R. R. Gamache, J. T. Hodges, O. V. Naumenko, O. L. Polyansky, L. S. Rothman, R. A. Toth, A. C. Vandaele, N. F. Zobov, S. Fally, A. Z. Fazliev, T. Furtenbacher, I. E. Gordon, S.-M. Hu, S. N. Mikhailenko, and B. A. Voronin, 'IUPAC critical evaluation of the rotational-vibrational spectra of water vapor. Part II,' *J. Quant. Spectrosc. Radiat. Transfer* **111**, 2160–2184 (2010).
- ¹⁰⁶M. J. Frisch, G. W. Trucks, H. B. Schlegel, G. E. Scuseria, M. A. Robb, J. R. Cheeseman, G. Scalmani, V. Barone, G. A. Petersson, H. Nakatsuji, X. Li, M. Caricato, A. V. Marenich, J. Bloino, B. G. Janesko, R. Gomperts, B. Mennucci, H. P. Hratchian, J. V. Ortiz, A. F. Izmaylov, J. L. Sonnenberg, D. Williams-Young, F. Ding, F. Lipparini, F. Egidi, J. Goings, B. Peng, A. Petrone, T. Henderson, D. Ranasinghe, V. G. Zakrzewski, J. Gao, N. Rega, G. Zheng, W. Liang, M. Hada, M. Ehara, K. Toyota, R. Fukuda, J. Hasegawa, M. Ishida, T. Nakajima, Y. Honda, O. Kitao, H. Nakai, T. Vreven, K. Throssell, J. A. Montgomery, Jr., J. E. Peralta, F. Ogliaro, M. J. Bearpark, J. J. Heyd, E. N. Brothers, K. N. Kudin, V. N. Staroverov, T. A. Keith, R. Kobayashi, J. Normand, K. Raghavachari, A. P. Rendell, J. C. Burant, S. S. Iyengar, J. Tomasi, M. Cossi, J. M. Millam, M. Klene, C. Adamo, R. Cammi, J. W. Ochterski, R. L. Martin, K. Morokuma, O. Farkas, J. B. Foresman, and D. J. Fox, 'Gaussian 16 Revision C.01,' (2016), Gaussian Inc. Wallingford CT.
- ¹⁰⁷D. F. Dinu, M. Podewitz, H. Grothe, K. R. Liedl, and T. Loerting, 'Toward Elimination of Discrepancies between Theory and Experiment: Anharmonic Rotational-Vibrational Spectrum of Water in Solid Noble Gas Matrices,' *J. Phys. Chem. A* **123**, 8234–8242 (2019).
- ¹⁰⁸M. Yang, D. H. Zhang, M. A. Collins, and S.-Y. Lee, 'Ab initio potential-energy surfaces for the reactions $\text{OH} + \text{H}_2 \leftrightarrow \text{H}_2\text{O} + \text{H}$,' *J. Chem. Phys.* **115**, 174–178 (2001).
- ¹⁰⁹F. Fernández-Alonso and R. N. Zare, 'Scattering resonances in the simplest chemical reaction,' *Ann. Rev. Phys. Chem.* **53**, 67–99 (2002).
- ¹¹⁰T. Furtenbacher, A. G. Császár, and J. Tennyson, 'MARVEL: measured active rotational-vibrational energy levels,' *J. Mol. Spec.* **245**, 115 – 125 (2007).
- ¹¹¹T. Furtenbacher and A. G. Császár, 'The role of intensities in determining characteristics of spectroscopic networks,' *J. Mol. Struct.* **1009**, 123 – 129 (2012).
- ¹¹²T. Furtenbacher and A. G. Császár, 'MARVEL: Measured active rotational-vibrational energy levels. II. Algorithmic improvements,' *J. Quant. Spectrosc. Radiat. Transfer* **113**, 929 – 935 (2012).

B

Cartesian coordinates of $\text{H} + \text{HOD}$ from polyspherical coordinates

The PESs of H_3O by Chen *et al.* [68] and $(\text{HCl}) \cdots (\text{HOD})$ by Mancini & Bowman [61] used in the work presented in chapter 3 and appendix A are provided as FORTRAN routines. The first takes atom-atom distances as input arguments and the second takes Cartesian coordinates of the atoms (from which distances are calculated internally) to compute the value of the potential for a given nuclear configuration of $\text{H}_a\text{H}_b\text{OD}$. Given that, in the presented work, the positions of the atoms in the body-fixed (BF) frame of reference are determined by the values of the internal coordinates R_1 , R_2 , R_3 , θ , β_s and γ_s , one needs to retrieve the distances between one another. As the potential is invariant upon overall rotation of the system, it is sufficient to express the Cartesian coordinates of the atoms in the BF frame.

In order to simplify the notation in the following derivation, we will call O , A , B and C the points in space associated to the positions of the atoms O , H_a , H_b and D , respectively (see fig. 3.1a). K is the Radau canonical point of H_bOD , with O as the heliocenter, as defined in the study. The centers-of-mass of $\text{H}_a\text{H}_b\text{OD}$ and H_bOD are called here G and G' (called G and G_s in fig. 3.1a).

We recall the definitions of the orthogonal vectors \vec{R}_1 , \vec{R}_2 and \vec{R}_3 :

$$\vec{R}_1 = \overrightarrow{KB} \quad (\text{B.1})$$

$$\vec{R}_2 = \overrightarrow{KC} \quad (\text{B.2})$$

$$\vec{R}_3 = \overrightarrow{G'A} \quad (\text{B.3})$$

with

$$\overrightarrow{OK} = (1 + \alpha_O)^{-1} \overrightarrow{OG'} \quad (\text{B.4})$$

with $\alpha_O = \sqrt{m_O / (m_O + m_B + m_C)}$. The points G' and G are defined such that, for

any point X :

$$(m_O + m_B + m_C)\overrightarrow{G'X} = m_O\overrightarrow{OX} + m_B\overrightarrow{BX} + m_C\overrightarrow{CX} \quad (\text{B.5})$$

$$m\overrightarrow{GX} = m_O\overrightarrow{OX} + m_A\overrightarrow{AX} + m_B\overrightarrow{BX} + m_C\overrightarrow{CX} \quad (\text{B.6})$$

$$= (m_O + m_B + m_C)\overrightarrow{G'X} + m_A\overrightarrow{AX} \quad (\text{B.7})$$

where we have defined for convenience $m = m_O + m_A + m_B + m_C$.

Since G is the origin of the BF frame of reference, our aim is to find the expressions of the vectors \overrightarrow{GO} , \overrightarrow{GA} , \overrightarrow{GB} and \overrightarrow{GC} as functions of \vec{R}_1 , \vec{R}_2 and \vec{R}_3 . These give the position of O , A , B and C relative to that origin. It will then be possible to introduce the polyspherical coordinates in the expressions of their Cartesian components.

We start by locating the points G' and K with respect to G and O . By eq. (B.7), taking $X = G'$

$$m\overrightarrow{GG'} = m_A\overrightarrow{AG'} = -m_A\vec{R}_3 \quad (\text{B.8})$$

Where we have used eq. (B.3). Thus, by splitting $\overrightarrow{GG'}$ at O :

$$\overrightarrow{OG'} = -\overrightarrow{GO} - \frac{m_A}{m}\vec{R}_3 \quad (\text{B.9})$$

Moreover, because of eq. (B.4), we have:

$$\begin{aligned} \overrightarrow{KG'} &= \overrightarrow{KO} + \overrightarrow{OG'} = \left(1 - \frac{1}{1 + \alpha_O}\right)\overrightarrow{OG'} = \frac{\alpha_O}{1 + \alpha_O}\overrightarrow{OG'} \\ &= -\frac{\alpha_O}{1 + \alpha_O}\left(\overrightarrow{GO} + \frac{m_A}{m}\vec{R}_3\right) \end{aligned} \quad (\text{B.10})$$

Then one readily has, by taking $X = O, A, B, C$ in eq. (B.6):

$$m\overrightarrow{GO} = \vec{0} \quad + m_A\overrightarrow{AO} \quad + m_B\overrightarrow{BO} \quad + m_C\overrightarrow{CO} \quad (\text{B.11})$$

$$m\overrightarrow{GA} = m_O\overrightarrow{OA} \quad + \vec{0} \quad + m_B\overrightarrow{BA} \quad + m_C\overrightarrow{CA} \quad (\text{B.12})$$

$$m\overrightarrow{GB} = m_O\overrightarrow{OB} \quad + m_A\overrightarrow{AB} \quad + \vec{0} \quad + m_C\overrightarrow{CB} \quad (\text{B.13})$$

$$m\overrightarrow{GC} = m_O\overrightarrow{OC} \quad + m_A\overrightarrow{AC} \quad + m_B\overrightarrow{BC} \quad + \vec{0} \quad (\text{B.14})$$

Each of the vectors on the right-hand side of these equations is split and expressed in terms of the orthogonal vectors and \overrightarrow{GO} :

$$\begin{aligned} \overrightarrow{OA} &= \overrightarrow{OG'} + \overrightarrow{G'A} = -\overrightarrow{GO} - \frac{m_A}{m}\vec{R}_3 + \vec{R}_3 \\ &= -\overrightarrow{GO} + \left(1 - \frac{m_A}{m}\right)\vec{R}_3 \end{aligned} \quad (\text{B.15})$$

$$\begin{aligned}
\overrightarrow{OB} &= \overrightarrow{OK} + \overrightarrow{KB} = (1 + \alpha_O)^{-1} \overrightarrow{OG'} + \vec{R}_1 \\
&= -(1 + \alpha_O)^{-1} \left(\overrightarrow{GO} + \frac{m_A}{m} \vec{R}_3 \right) + \vec{R}_1 \\
&= -\frac{1}{1 + \alpha_O} \overrightarrow{GO} - \frac{m_A}{m(1 + \alpha_O)} \vec{R}_3 + \vec{R}_1
\end{aligned} \tag{B.16}$$

$$\begin{aligned}
\overrightarrow{OC} &= \overrightarrow{OK} + \overrightarrow{KC} = (1 + \alpha_O)^{-1} \overrightarrow{OG'} + \vec{R}_2 \\
&= -\frac{1}{1 + \alpha_O} \overrightarrow{GO} - \frac{m_A}{m(1 + \alpha_O)} \vec{R}_3 + \vec{R}_2
\end{aligned} \tag{B.17}$$

$$\begin{aligned}
\overrightarrow{AB} &= \overrightarrow{AG'} + \overrightarrow{G'K} + \overrightarrow{KB} = -\vec{R}_3 + \frac{\alpha_O}{1 + \alpha_O} \left(\overrightarrow{GO} + \frac{m_A}{m} \vec{R}_3 \right) + \vec{R}_1 \\
&= \frac{\alpha_O}{1 + \alpha_O} \overrightarrow{GO} - \left(1 - \frac{\alpha_O}{1 + \alpha_O} \frac{m_A}{m} \right) \vec{R}_3 + \vec{R}_1
\end{aligned} \tag{B.18}$$

$$\begin{aligned}
\overrightarrow{AC} &= \overrightarrow{AG'} + \overrightarrow{G'K} + \overrightarrow{KC} = -\vec{R}_3 + \frac{\alpha_O}{1 + \alpha_O} \left(\overrightarrow{GO} + \frac{m_A}{m} \vec{R}_3 \right) + \vec{R}_2 \\
&= \frac{\alpha_O}{1 + \alpha_O} \overrightarrow{GO} - \left(1 - \frac{\alpha_O}{1 + \alpha_O} \frac{m_A}{m} \right) \vec{R}_3 + \vec{R}_2
\end{aligned} \tag{B.19}$$

$$\overrightarrow{BC} = \overrightarrow{BK} + \overrightarrow{KC} = -\vec{R}_1 + \vec{R}_2 \tag{B.20}$$

By plugging eqs. (B.15) to (B.17) into eq. (B.11) and some rearrangement, one obtains:

$$\begin{aligned}
\overrightarrow{GO} &= -\frac{m_B}{m} \left(1 - \frac{m_A}{m} - \frac{m_B + m_C}{m(1 + \alpha_O)} \right)^{-1} \vec{R}_1 \\
&\quad - \frac{m_C}{m} \left(1 - \frac{m_A}{m} - \frac{m_B + m_C}{m(1 + \alpha_O)} \right)^{-1} \vec{R}_2 \\
&\quad - \frac{m_A}{m} \vec{R}_3
\end{aligned} \tag{B.21}$$

Finally, plugging eqs. (B.15) to (B.20) into the remaining eqs. (B.12) to (B.14) yields:

$$\begin{aligned}
m\overrightarrow{GA} &= -\left(m_O + \frac{\alpha_O(m_B + m_C)}{1 + \alpha_O} \right) \overrightarrow{GO} - m_B \vec{R}_1 - m_C \vec{R}_2 \\
&\quad + \left[(m_B + m_C) \left(1 - \frac{\alpha_O}{1 + \alpha_O} \frac{m_A}{m} \right) + m_O \left(1 - \frac{m_A}{m} \right) \right] \vec{R}_3
\end{aligned} \tag{B.22}$$

$$\begin{aligned}
m\overrightarrow{GB} &= \frac{\alpha_O m_A - m_O}{1 + \alpha_O} \overrightarrow{GO} + (m_O + m_A + m_C) \vec{R}_1 - m_C \vec{R}_2 \\
&\quad - m_A \left(1 - \frac{\alpha_O m_A - m_O}{(1 + \alpha_O)m} \right) \vec{R}_3
\end{aligned} \tag{B.23}$$

$$m\overrightarrow{GC} = \frac{\alpha_O m_A - m_O}{1 + \alpha_O} \overrightarrow{GO} - m_B \vec{R}_1 + (m_O + m_A + m_B) \vec{R}_2$$

$$-m_A \left(1 - \frac{\alpha_O m_A - m_O}{(1 + \alpha_O)m} \right) \vec{R}_3 \quad (\text{B.24})$$

We do not replace \vec{OG} by its expression in eq. (B.21) as it would needlessly complicate these expressions.

Now we are in the position to compute the Cartesian components of these vectors in the body-fixed frame of reference through those of \vec{R}_1 , \vec{R}_2 and \vec{R}_3 . The BF frame is defined by its origin G and its orthonormal basis of vectors $\mathcal{B} = (\vec{u}_x, \vec{u}_y, \vec{u}_z)$. For any $k \in \{1, 2, 3\}$ we define the column matrix $\mathbf{R}_k = [R_k^{(\text{BF}),x} \ R_k^{(\text{BF}),y} \ R_k^{(\text{BF}),z}]^\top$ of the BF coordinates of \vec{R}_k . By definition of the BF frame, its unit vector \vec{u}_z is aligned with \vec{R}_3 , so that:

$$\mathbf{R}_3 = R_3 \begin{bmatrix} 0 \\ 0 \\ 1 \end{bmatrix} \quad (\text{B.25})$$

Let β_s be the angle between \vec{R}_3 and \vec{R}_2 . The unit vector \vec{u}_x is oriented in such a way that \vec{R}_2 is contained in the $(G, \vec{u}_z, \vec{u}_x)$ plane. More precisely, for small values of β_s , \vec{R}_2 lies in its first quadrant. Thus:

$$\mathbf{R}_2 = R_2 \begin{bmatrix} \sin \beta_s \\ 0 \\ \cos \beta_s \end{bmatrix} \quad (\text{B.26})$$

Obtaining the BF coordinates of \vec{R}_1 is more involved because the vectors \vec{R}_2 and \vec{R}_1 define the subsystem-body-fixed frame BFs which we specify in the following. We refer to section 2.4.4 for a general discussion and to fig. 3.1b for an illustration of this specific case.

Let the axes of this BF frame be oriented with a right-handed basis of orthonormal vectors $\mathcal{B}' = (\vec{u}'_x, \vec{u}'_y, \vec{u}'_z)$. These are chosen to be such that:

- \vec{u}'_z is aligned along \vec{R}_2 ,
- \vec{u}'_y is orthogonal to the plane $(G, \vec{R}_2, \vec{R}_1)$ such that the triplet $(\vec{R}_2, \vec{R}_1, \vec{u}'_y)$ is right-handed,

Like for the definition of the BF axes from rotations of the SF axes (see section 2.4.1), those of BFs are obtained by rotations of the BF axes. Thus, we need three Euler angles $\tilde{\alpha}$, $\tilde{\beta}$ and $\tilde{\gamma}$ defining the orientation of those new axes. In order to follow the definitions above, these are chosen such that $\tilde{\alpha}$ and $\tilde{\beta}$ are the azimuthal and polar angles of \vec{R}_2 in the BF frame. The intermediate frame obtained by the first two Euler rotations of the BF axes will be called E_2 s. Next, $\tilde{\gamma}$ is chosen to be the azimuthal angle of \vec{R}_1 in the E_2 s frame.

Note that \vec{R}_2 is by definition in the $(G, \vec{u}_z, \vec{u}_x)$ plane of BF, so its azimuthal angle in that frame is zero. Hence the first Euler angle is simply $\tilde{\alpha} = 0$. The polar angle of \vec{R}_2 in BF is the angle between \vec{R}_3 and \vec{R}_2 , therefore the second Euler angle is $\tilde{\beta} = \beta_s$.

Finally, the “rotation angle of \vec{R}_1 around \vec{R}_2 ”, as defined in the manuscript and as shown in fig. 3.1b, is in fact the third Euler angle orienting the BFs axes, thus we write we write $\tilde{\gamma} = \gamma_s$.

Therefore, for any vector \vec{X} , its coordinates $X^{(\text{BF}),\xi}$ and $X^{(\text{BFs}),\xi}$ (with $\xi = x, y, z$) in the frames BF and BF_s, respectively, are related by:

$$\begin{bmatrix} X^{(\text{BF}),x} \\ X^{(\text{BF}),y} \\ X^{(\text{BF}),z} \end{bmatrix} = \mathcal{R}(0, \beta_s, \gamma_s) \begin{bmatrix} X^{(\text{BFs}),x} \\ X^{(\text{BFs}),y} \\ X^{(\text{BFs}),z} \end{bmatrix} \quad (\text{B.27})$$

Let θ be the angle from \vec{R}_2 and \vec{R}_1 . Then, using eq. (B.27) with $\vec{X} = \vec{R}_1$ and the definition of the Euler rotation matrices in eq. (2.76), we have:

$$\begin{aligned} \mathbf{R}_1 &= \begin{bmatrix} R_1^{(\text{BF}),x} \\ R_1^{(\text{BF}),y} \\ R_1^{(\text{BF}),z} \end{bmatrix} = \begin{bmatrix} \cos \beta_s & 0 & \sin \beta_s \\ 0 & 1 & 0 \\ -\sin \beta_s & 0 & \cos \beta_s \end{bmatrix} \begin{bmatrix} \cos \gamma_s & -\sin \gamma_s & 0 \\ \sin \gamma_s & \cos \gamma_s & 0 \\ 0 & 0 & 1 \end{bmatrix} \begin{bmatrix} R_1 \sin \theta \\ 0 \\ R_1 \cos \theta \end{bmatrix} \\ &= R_1 \begin{bmatrix} \sin \theta \cos \beta_s \cos \gamma_s + \cos \theta \sin \beta_s \\ \sin \theta \sin \gamma_s \\ -\sin \theta \sin \beta_s \cos \gamma_s + \cos \theta \cos \beta_s \end{bmatrix} \end{aligned} \quad (\text{B.28})$$

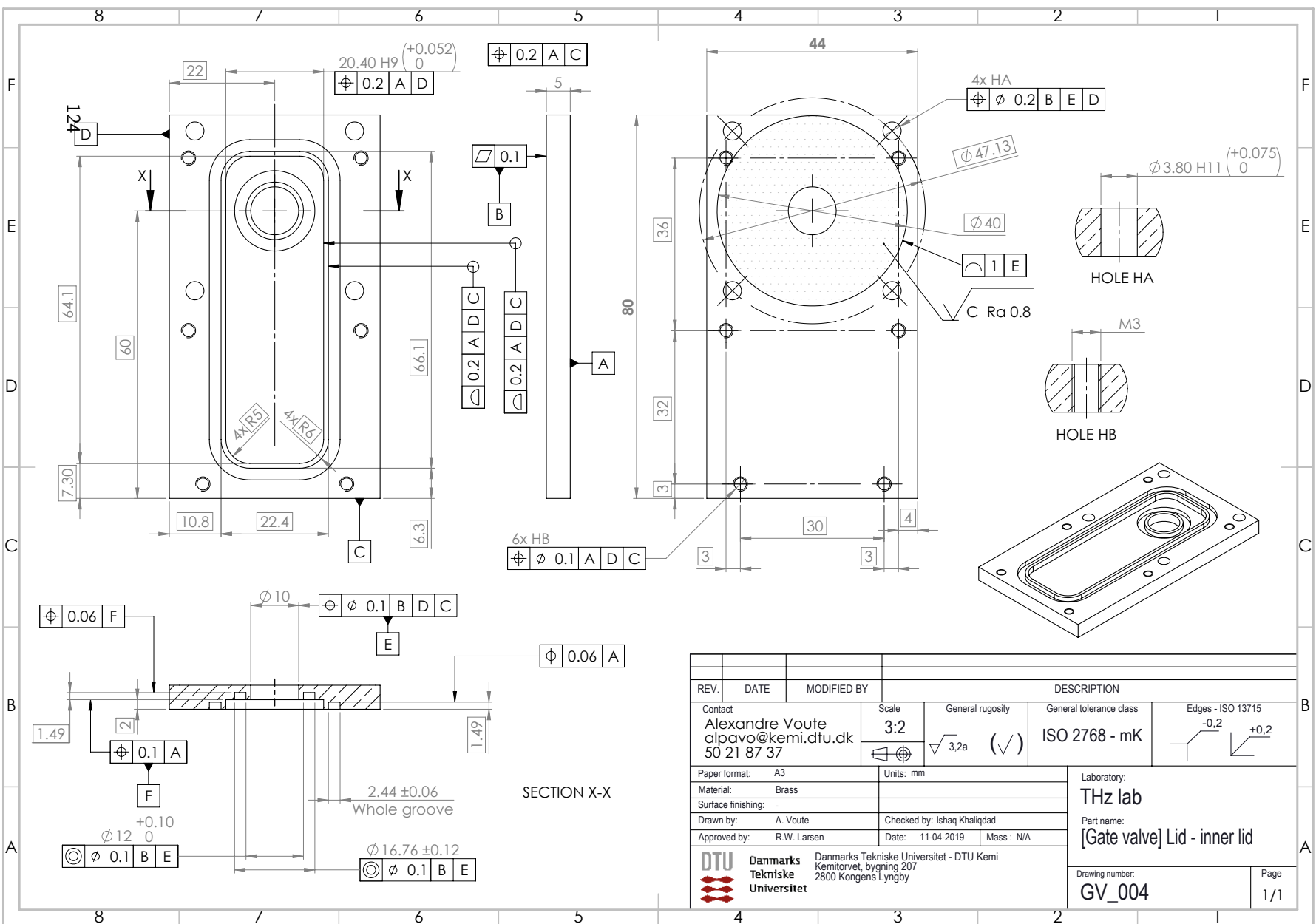
By first calculating the BF Cartesian coordinates of each vector with eqs. (B.25), (B.26) and (B.28), one can finally obtain the BF Cartesian coordinates of the nuclei with eqs. (B.21) to (B.24) and finally compute the potential.

C

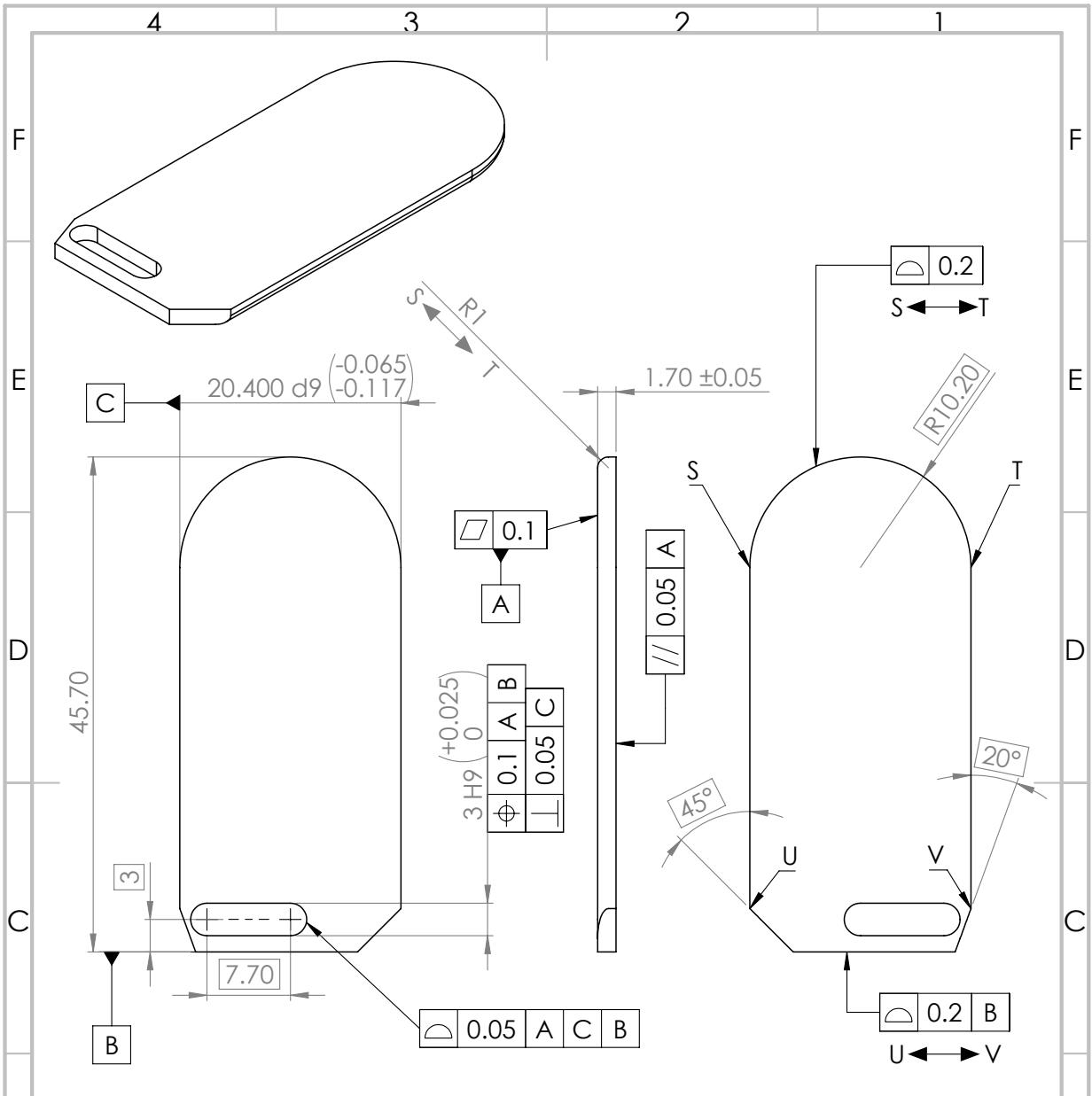
Technical drawings

In this appendix we report the technical drawings of the various parts of the setups which have been designed for the matrix isolation experiments in the laboratory. These drawings were provided to the machine shop of the Department of Chemistry of DTU for the fabrication and assembly of these components.

- pages 124 to 129 : Gate valve
- pages 130 to 139 : Inlet system
- pages 140 to 147 : Parahydrogen enrichment setup



REV.	DATE	MODIFIED BY	DESCRIPTION			
Contact Alexandre Voute alpavo@kemi.dtu.dk 50 21 87 37			Scale 3:2	General roughness $\sqrt{3.2a}$ (✓)	General tolerance class ISO 2768 - mK	Edges - ISO 13715 -0.2 $+0.2$
Paper format: A3			Units: mm		Laboratory: THz lab	
Material: Brass					Part name: [Gate valve] Lid - inner lid	
Surface finishing: -					Part name: [Gate valve] Lid - inner lid	
Drawn by: A. Voute			Checked by: Ishaq Khalilqdad			
Approved by: R.W. Larsen			Date: 11-04-2019		Mass: N/A	
DTU Danmarks Tekniske Universitet 			Danmarks Tekniske Universitet - DTU Kemi Kemitorvet, bygning 207 2800 Kongens Lyngby		Drawing number: GV_004	
						Page 1/1



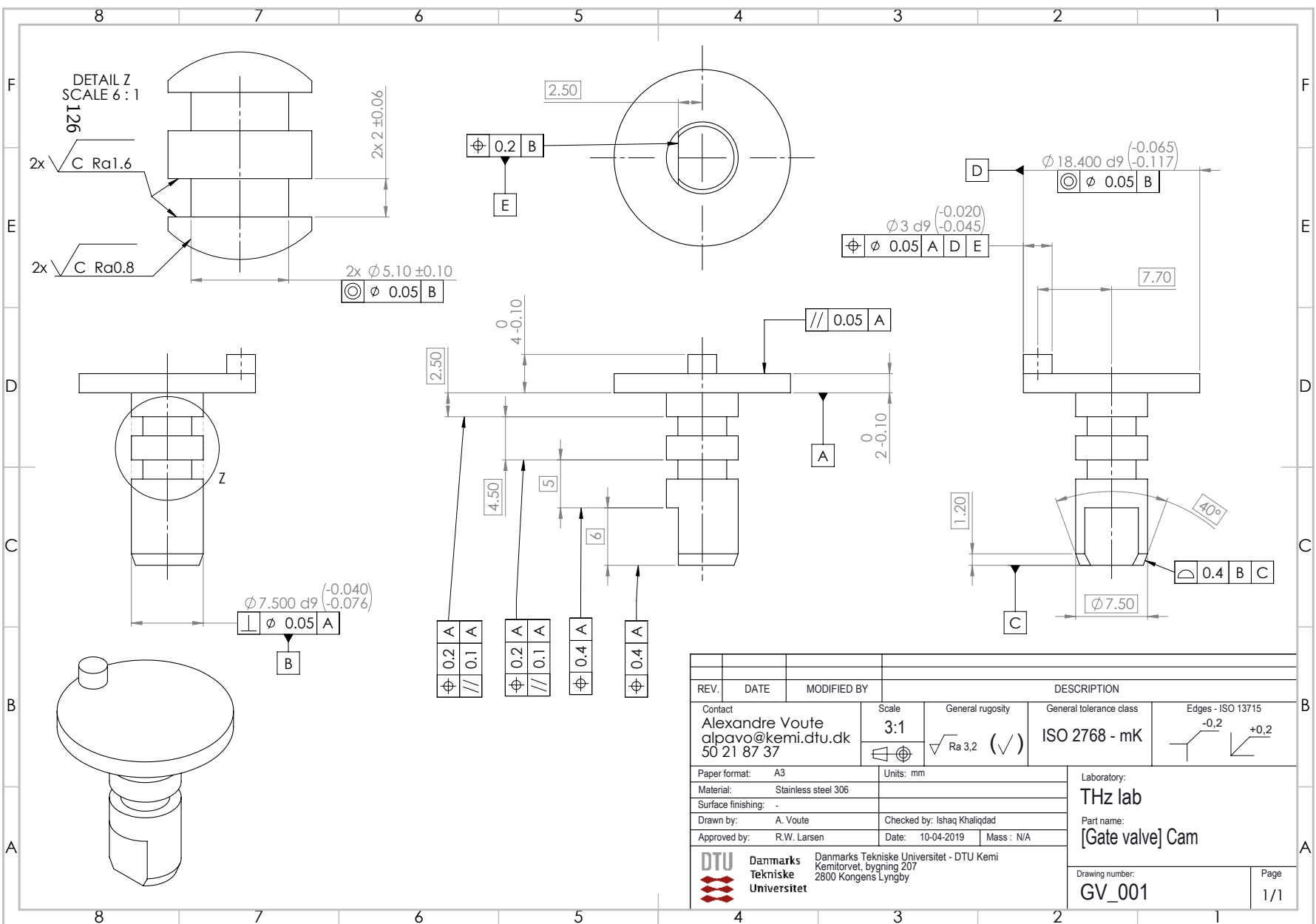
2	10-09-2019	A. Voute	Corrected version
1		A. Voute	Original version

REV.	DATE	MODIFIED BY	DESCRIPTION
------	------	-------------	-------------

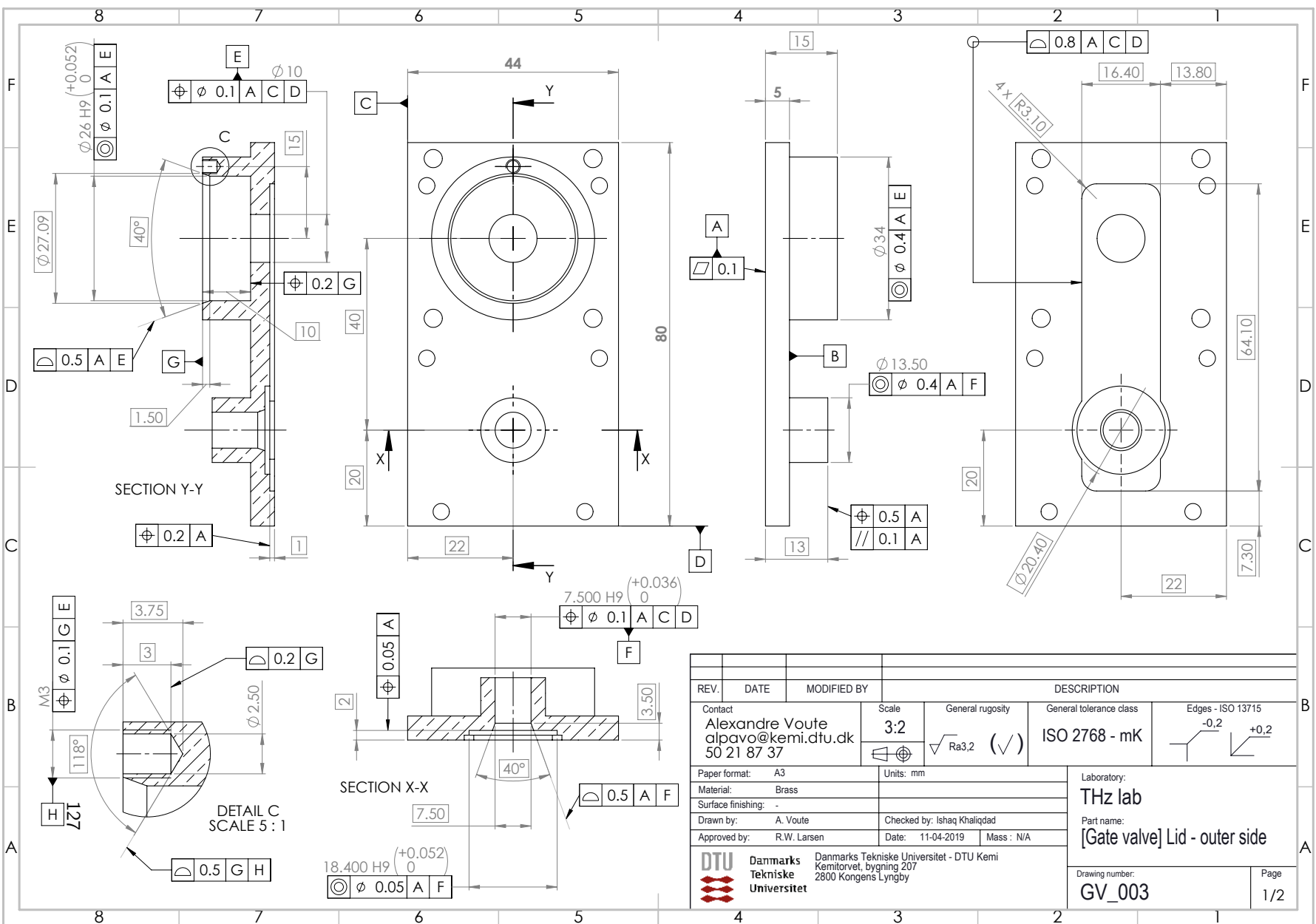
Contact Alexandre Voute alpavo@kemi.dtu.dk 50 21 87 37	Scale	General rugosity	General tolerance class	Edges - ISO 13715
	2:1	$\sqrt{Ra 3,2}$ (✓)	ISO 2687 - mK	$-0,2$ $+0,2$

Paper format: A4	Units: mm	Laboratory: THz lab
Material: Stainless steel 304		Part name: [Gate valve] Shutter V2
Surface finishing: -		
Drawn by: A. Voute	Checked by: Ishaq Khaliqdad	
Approved by: R.W. Larsen	Date: 11-04-2019	Mass: N/A

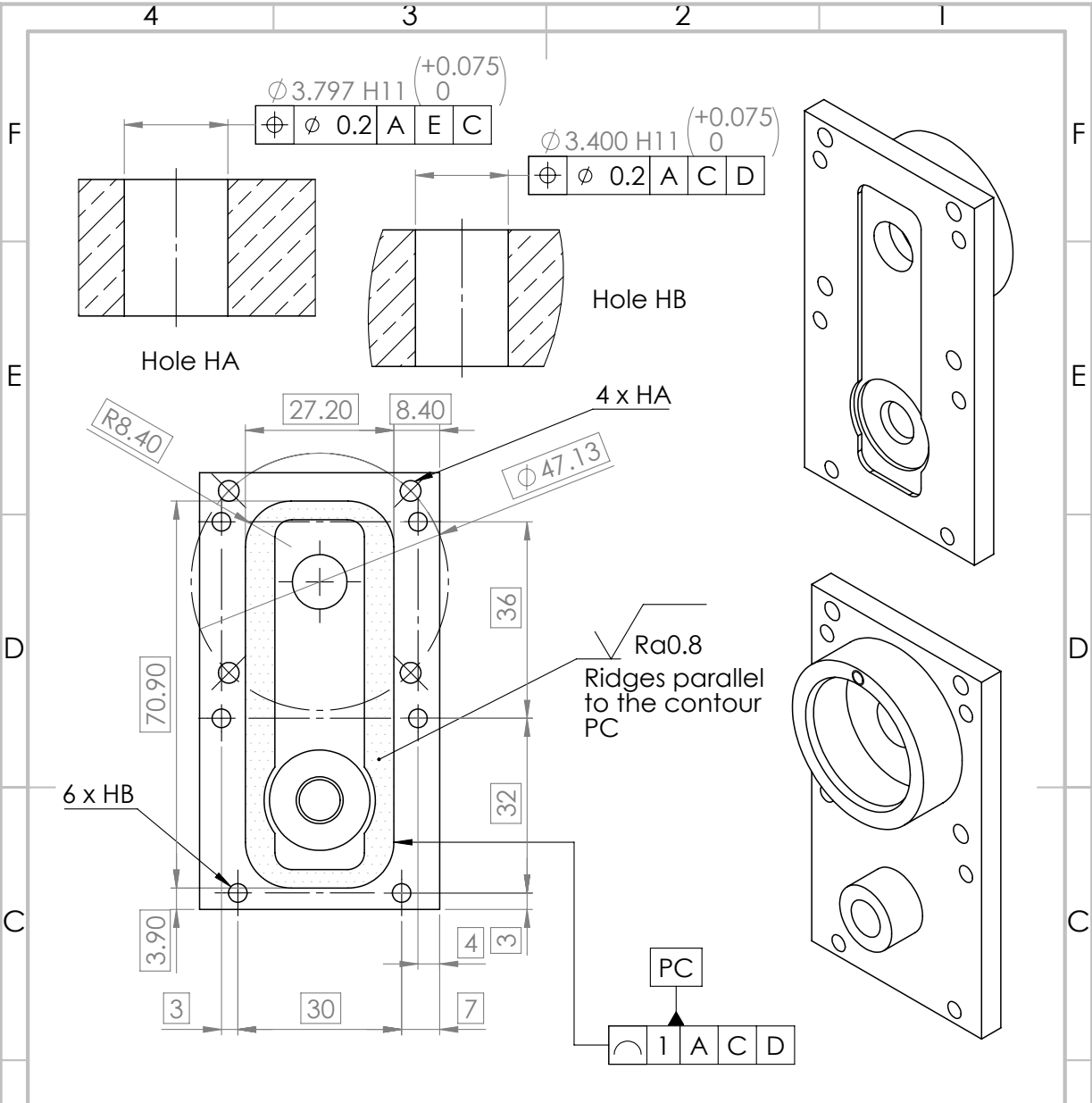
Danmarks Tekniske Universitet Danmarks Tekniske Universitet - DTU Kemi Kemitorvet, bygning 207 2800 Kongens Lyngby	Drawing number: GV_002	125	Page 1/1
--	------------------------	-----	----------



REV.	DATE	MODIFIED BY	DESCRIPTION				
			Contact	Scale	General rugosity	General tolerance class	Edges - ISO 13715
			Alexandre Voute	3:1	√ Ra 3.2 (✓)	ISO 2768 - mK	-0.2 / +0.2
			alpavo@kemi.dtu.dk	Units: mm			
			50 21 87 37				
Paper format: A3			Laboratory:		THz lab		
Material: Stainless steel 306			Surface finishing: -		Part name:		
Drawn by: A. Voute			Checked by: Ishaq Khalilqdad		[Gate valve] Cam		
Approved by: R.W. Larsen			Date: 10-04-2019		Mass: N/A		
DTU Danmarks Tekniske Universitet Kemitorvet, bygning 207 2800 Kongens Lyngby			Danmarks Tekniske Universitet - DTU Kemi		Drawing number:		
					GV_001		
					Page		
					1/1		



REV.	DATE	MODIFIED BY	DESCRIPTION			
Contact Alexandre Voute alpavo@kemi.dtu.dk 50 21 87 37			Scale 3:2	General rugosity $\sqrt{Ra3.2}$ (✓)	General tolerance class ISO 2768 - mK	Edges - ISO 13715 -0.2 +0.2
Paper format: A3			Units: mm		Laboratory: THz lab	
Material: Brass					Part name: [Gate valve] Lid - outer side	
Surface finishing: -					Drawing number: GV_003	
Drawn by: A. Voute			Checked by: Ishaq Khalilqdad		Page 1/2	
Approved by: R.W. Larsen			Date: 11-04-2019		Mass: N/A	
DTU Danmarks Tekniske Universitet 			Danmarks Tekniske Universitet - DTU Kemi Kemitorvet, bygning 207 2800 Kongens Lyngby			

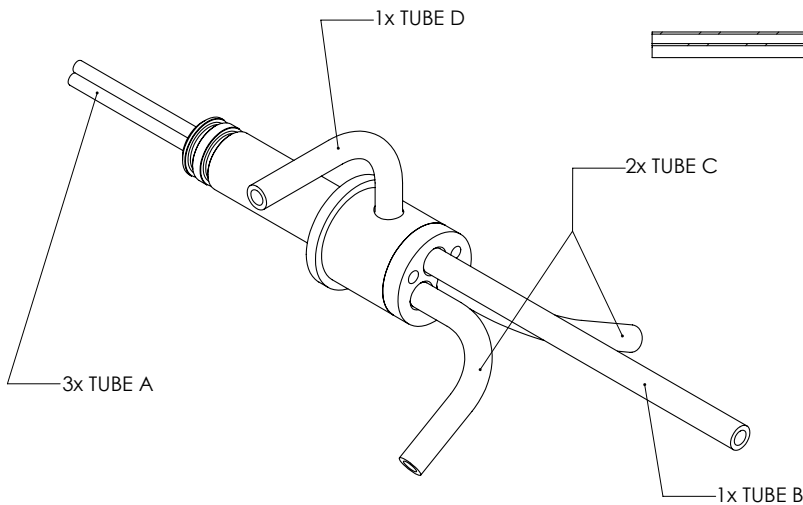
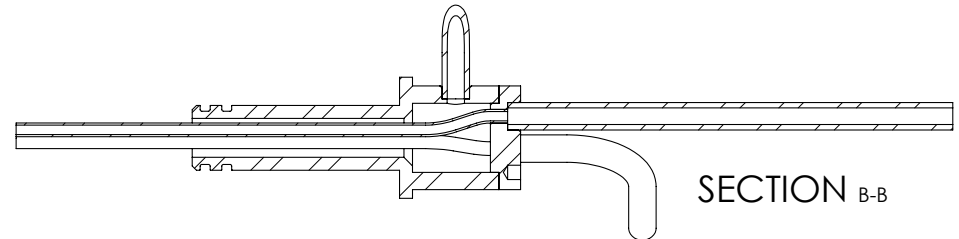
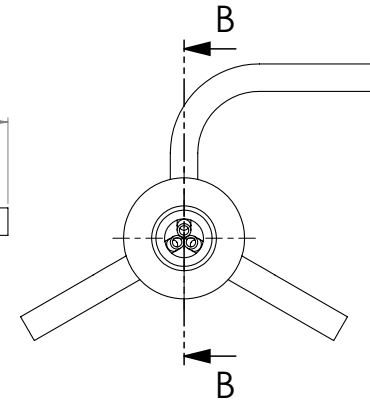
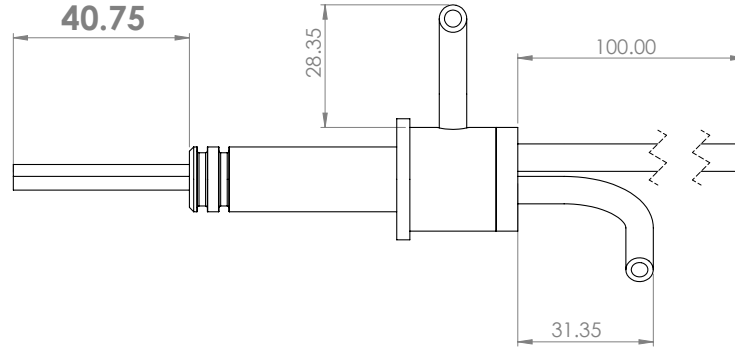
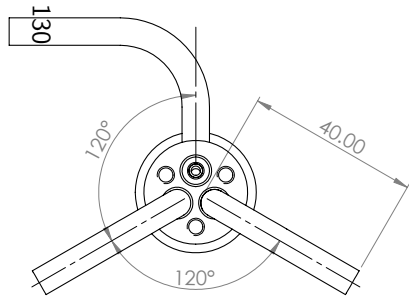


REV.	DATE	MODIFIED BY	DESCRIPTION

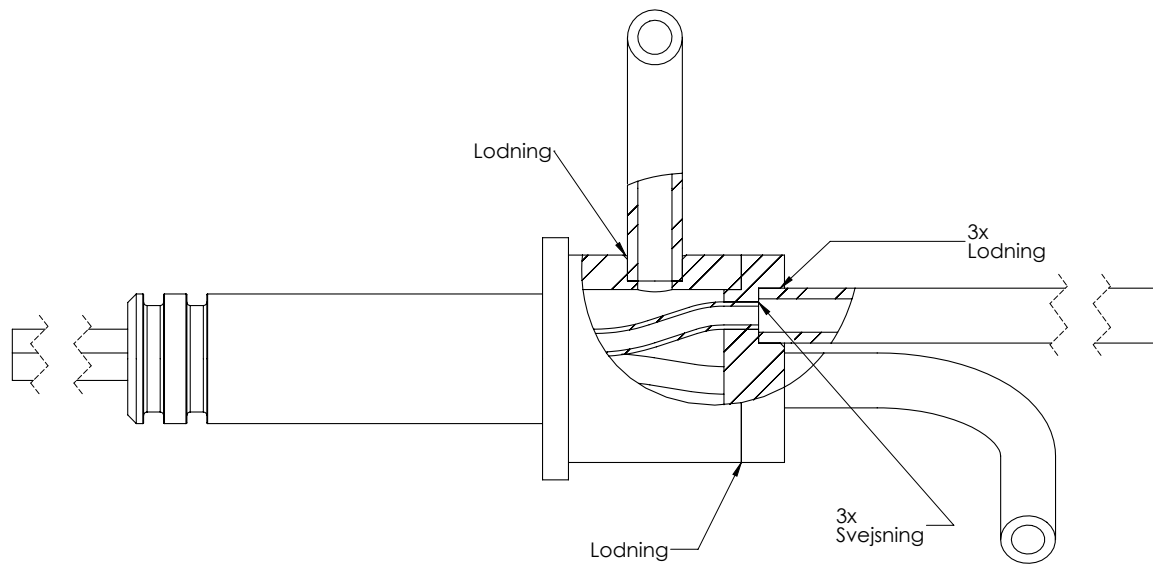
Contact Alexandre Voute alpavo@kemi.dtu.dk 50 21 87 37	Scale 1:1	General rugosity √ Ra3,2 (√)	General tolerance class ISO 2768 - mK	Edges - ISO 13715 -0,2 / +0,2
---	--------------	---------------------------------	--	----------------------------------

Paper format: A4	Units: mm	Laboratory: THz lab
Material: Brass		Part name: [Gate valve] Lid - outer side
Surface finishing: -		
Drawn by: A. Voute	Checked by: Ishaq Khaliqdad	
Approved by: R.W. Larsen	Date: 11-04-2019	Mass: N/A

Danmarks Tekniske Universitet Danmarks Tekniske Universitet - DTU Kemi Kemitorvet, bygning 207 2800 Kongens Lyngby	Drawing number: GV_003	Page 2/2
--	----------------------------------	-------------

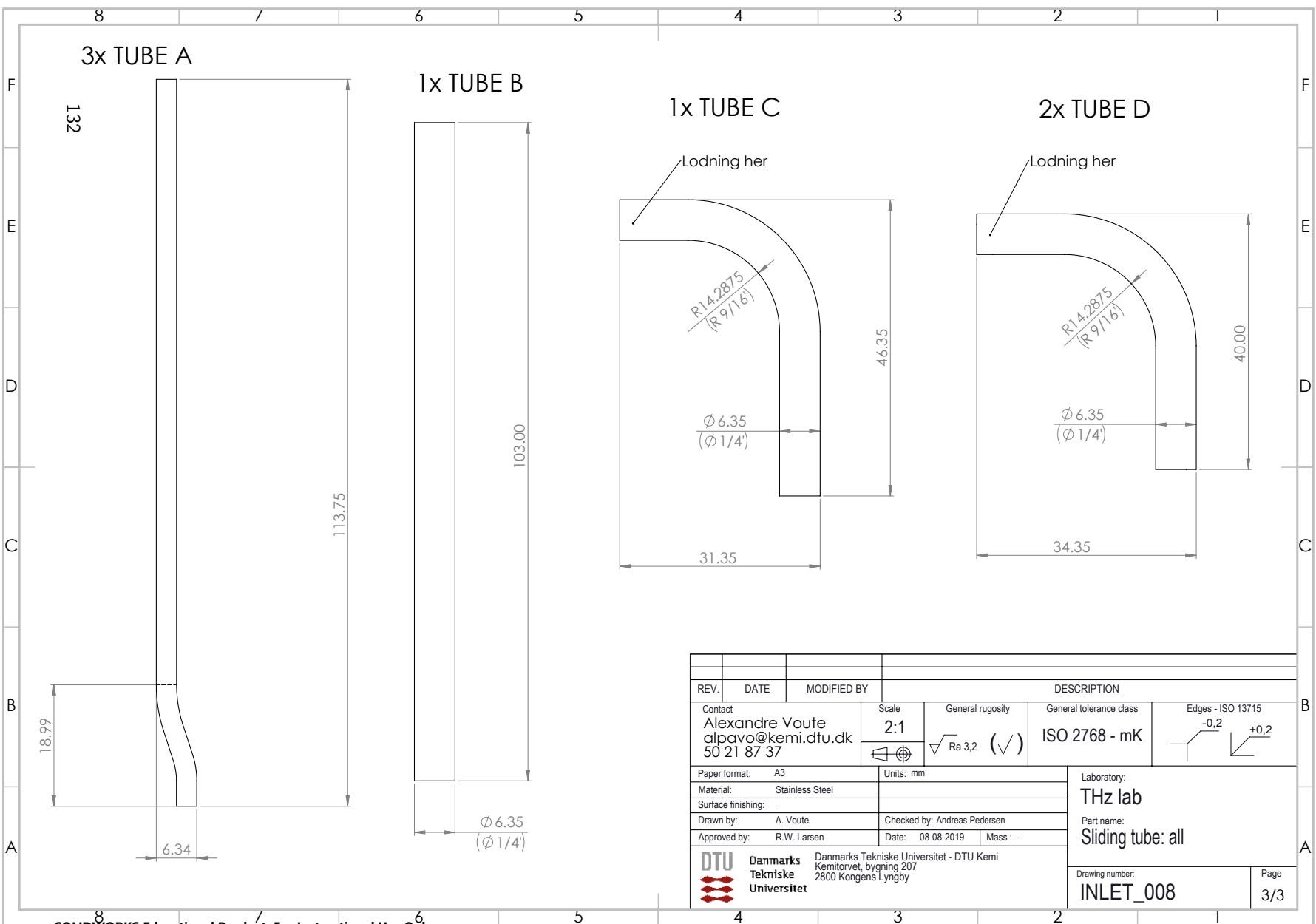


REV.	DATE	MODIFIED BY	DESCRIPTION				
Contact Alexandre Voute alpavo@kemi.dtu.dk 50 21 87 37			Scale 1:1	General roughness $\sqrt{Ra\ 3.2}$ (✓)	General tolerance class ISO 2768 - mK	Edges - ISO 13715 -0.2 +0.2	
Paper format: A3			Units: mm		Laboratory: THz lab		
Material: Stainless Steel					Part name: Sliding tube: all		
Surface finishing: -							
Drawn by: A. Voute			Checked by: Andreas Pedersen				
Approved by: R.W. Larsen			Date: 08-08-2019		Mass: -		
 DTU Danmarks Tekniske Universitet			Danmarks Tekniske Universitet - DTU Kemi Kemitorvet, bygning 207 2800 Kongens Lyngby			Drawing number: INLET_008	
						Page 1/3	

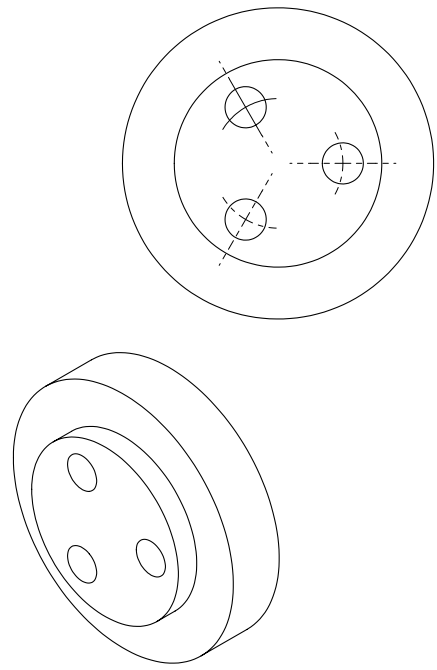
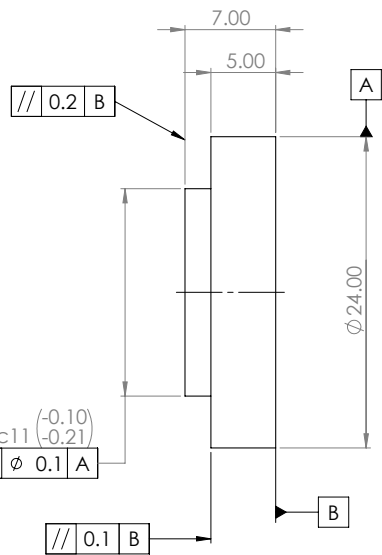
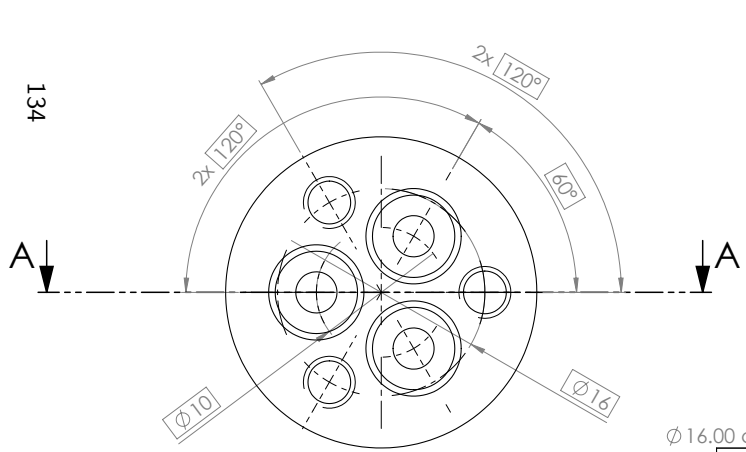


REV.	DATE	MODIFIED BY	DESCRIPTION					
			Contact Alexandre Voute alpavo@kemi.dtu.dk 50 21 87 37	Scale 2:1	General roughness $\sqrt{Ra\ 3.2}$ (✓)	General tolerance class ISO 2768 - mK	Edges - ISO 13715 -0,2 +0,2	
Paper format: A3			Units: mm		Laboratory: THz lab			
Material: Stainless Steel					Part name: Sliding tube: all			
Surface finishing: -								
Drawn by: A. Voute			Checked by: Andreas Pedersen					
Approved by: R.W. Larsen			Date: 08-08-2019		Mass: -			
 Danmarks Tekniske Universitet			Danmarks Tekniske Universitet - DTU Kemi Kemitorvet, bygning 207 2800 Kongens Lyngby			Drawing number: INLET_008		Page 2/3

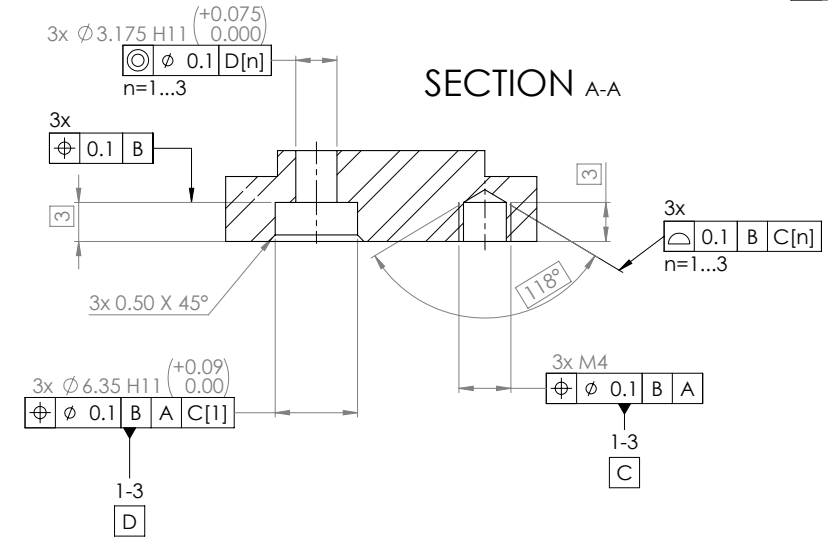
131



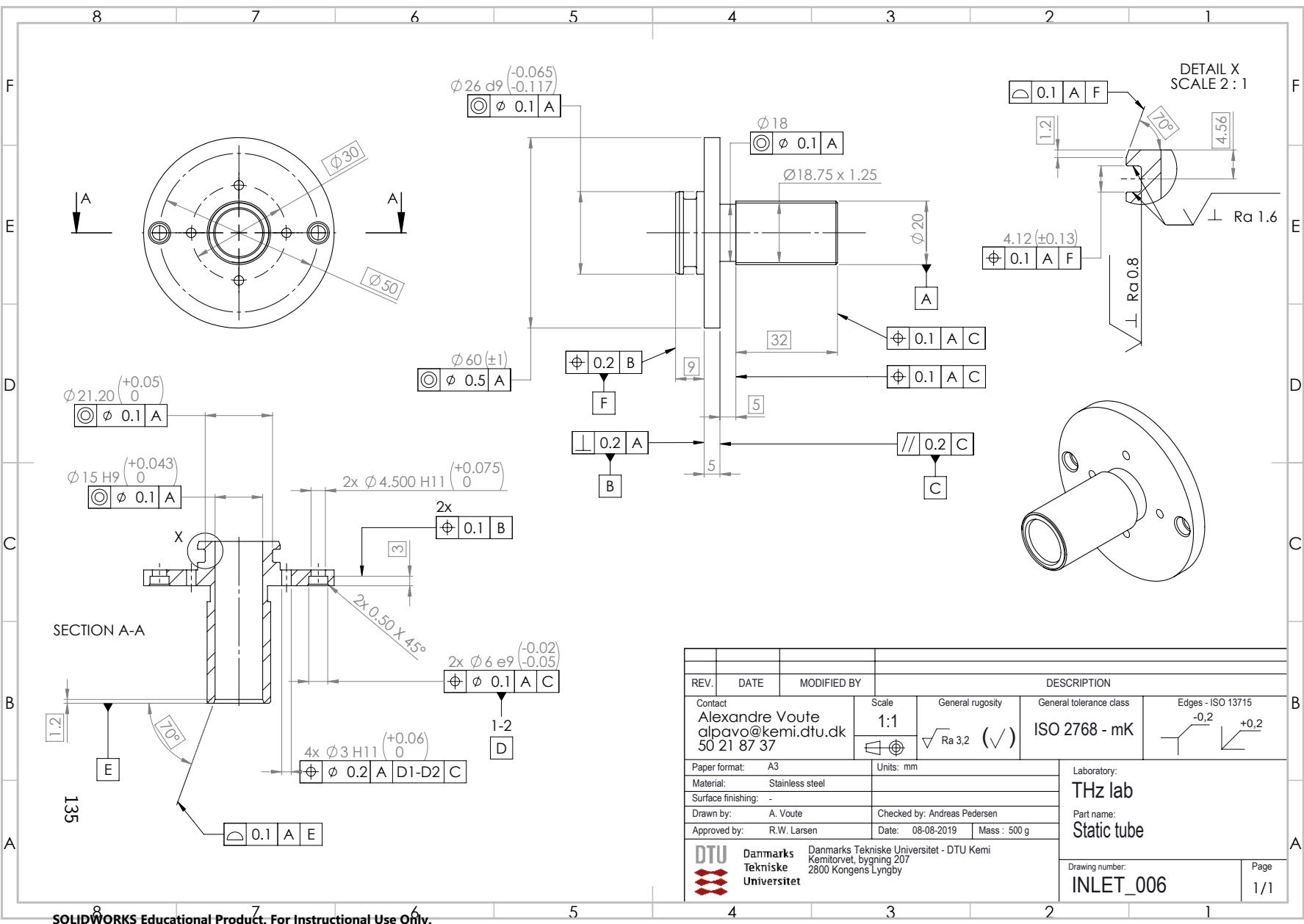
REV.	DATE	MODIFIED BY	DESCRIPTION			
Contact Alexandre Voute alpavo@kemi.dtu.dk 50 21 87 37			Scale 2:1	General rugosity $\sqrt{Ra\ 3.2}$ (✓)	General tolerance class ISO 2768 - mK	Edges - ISO 13715 -0.2 $+0.2$
Paper format: A3			Units: mm		Laboratory: THz lab	
Material: Stainless Steel					Part name: Sliding tube: all	
Surface finishing: -			Checked by: Andreas Pedersen			
Drawn by: A. Voute			Date: 08-08-2019		Mass: -	
Approved by: R.W. Larsen						
DTU Danmarks Tekniske Universitet			Danmarks Tekniske Universitet - DTU Kemi Kemitorvet, bygning 207 2800 Kongens Lyngby			
Drawing number: INLET_008					Page 3/3	



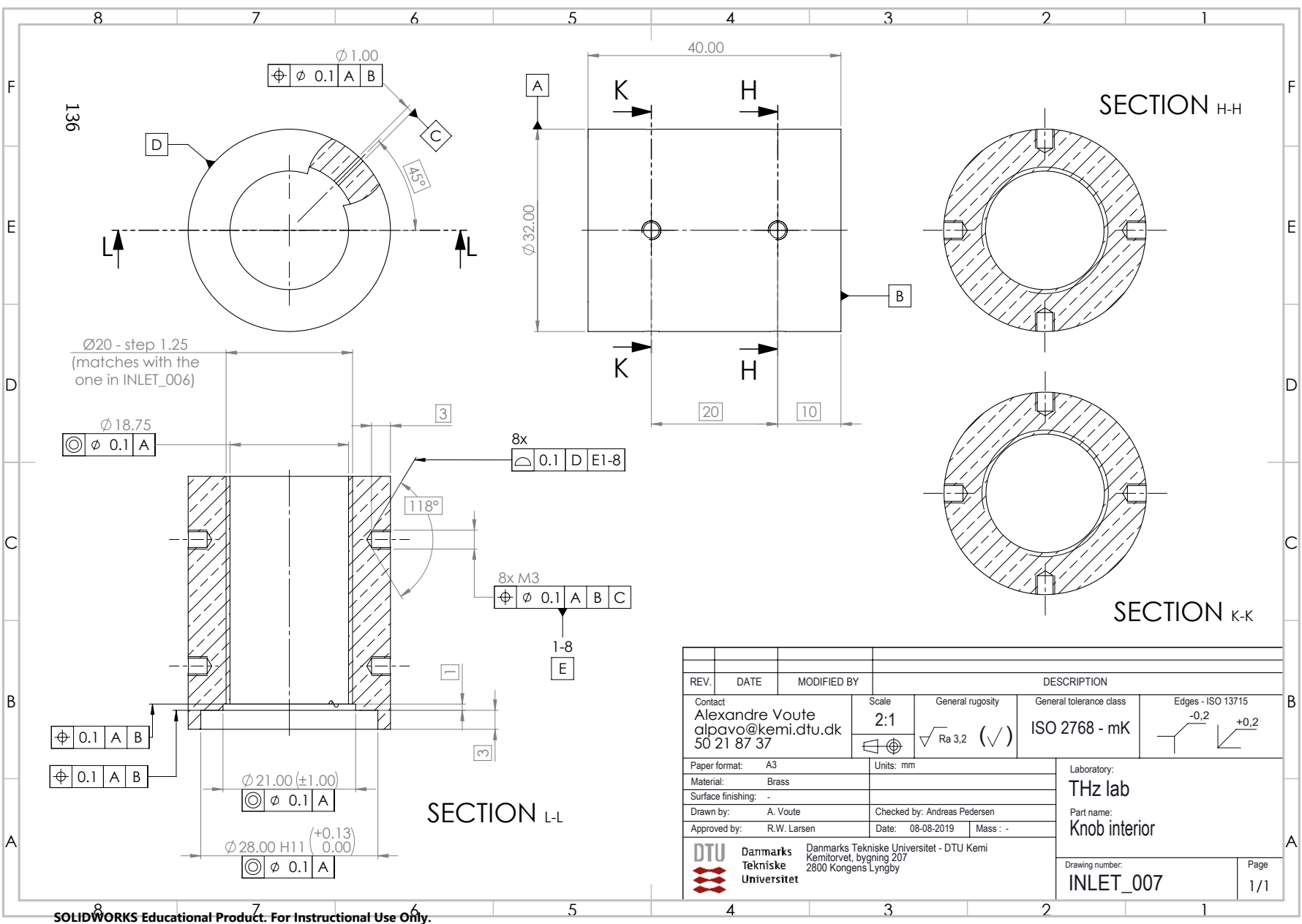
SECTION A-A



REV.	DATE	MODIFIED BY	DESCRIPTION				
			Contact	Scale	General rugosity	General tolerance class	Edges - ISO 13715
			Alexandre Voute	3:1	√ Ra 3.2 (✓)	ISO 2768 - mK	-0.2 / +0.2
			alpavo@kemi.dtu.dk				
			50 21 87 37	Units: mm			
			Paper format: A3				Laboratory:
			Material: Stainless steel				THz lab
			Surface finishing: -				Part name:
			Drawn by: A. Voute	Checked by: Andreas Pedersen			Tubes carrier: cap
			Approved by: R.W. Larsen	Date: 08-08-2019	Mass: -		Drawing number:
							INLET_005
							Page
							1/1

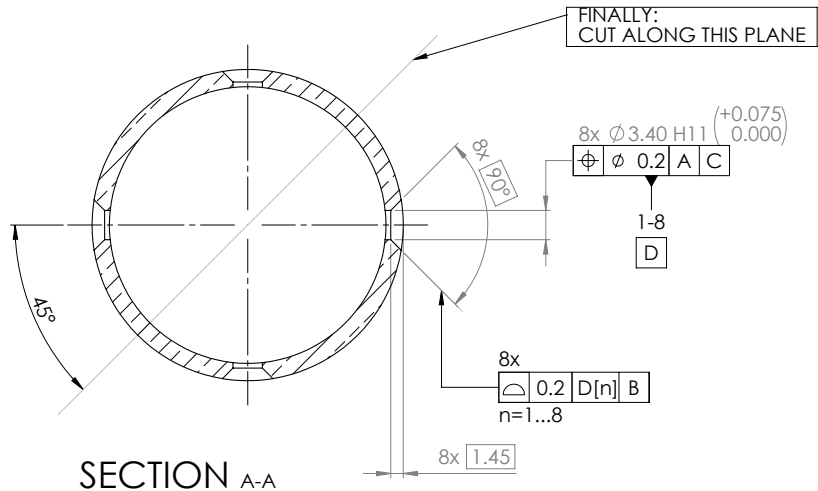
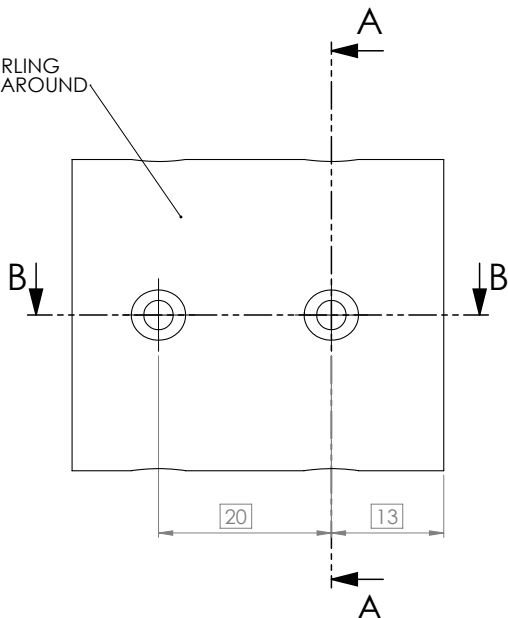


REV.	DATE	MODIFIED BY	DESCRIPTION				
			Contact	Scale	General rugosity	General tolerance class	Edges - ISO 13715
			Alexandre Voute	1:1	$\sqrt{Ra 3.2}$ (✓)	ISO 2768 - mK	-0.2 $+0.2$
			alpavo@kemi.dtu.dk	Units: mm			
			50 21 87 37				
Paper format: A3			Laboratory:		THz lab		
Material: Stainless steel			Surface finishing: -		Part name:		
Drawn by: A. Voute			Checked by: Andreas Pedersen		Static tube		
Approved by: R.W. Larsen			Date: 08-08-2019		Mass: 500 g		
DTU Danmarks Tekniske Universitet			Danmarks Tekniske Universitet - DTU Kemi Kemitorvet, bygning 207 2800 Kongens Lyngby		Drawing number: INLET_006		
						Page 1/1	

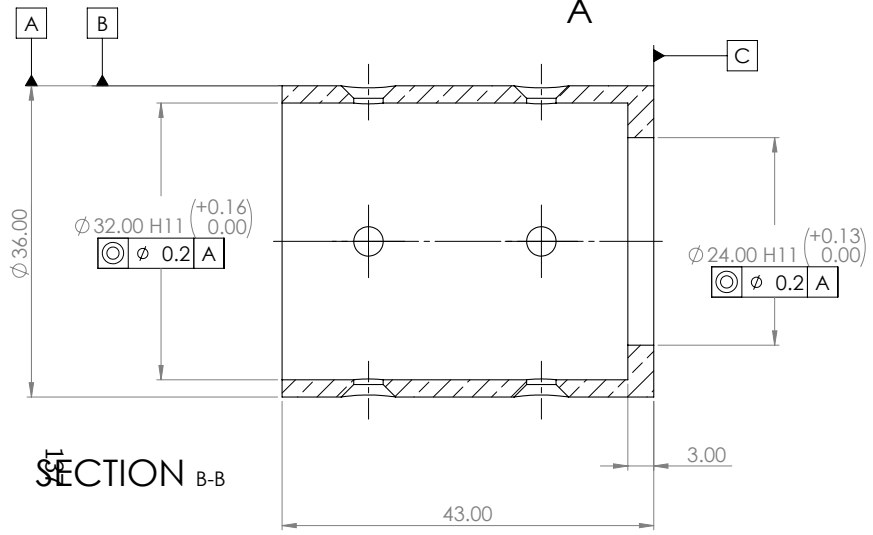


REV.	DATE	MODIFIED BY	DESCRIPTION			
Contact Alexandre Voute alpvavo@kemi.dtu.dk 50 21 87 37			Scale 2:1	General roughness $\sqrt{Ra 3.2}$ (✓)	General tolerance class ISO 2768 - mK	Edges - ISO 13715 -0.2 $+0.2$
Paper format: A3			Units: mm		Laboratory: THz lab	
Material: Brass					Part name: Knob interior	
Surface finishing: -			Checked by: Andreas Pedersen			
Drawn by: A. Voute			Date: 08-08-2019		Mass: -	
Approved by: R.W. Larsen						
DTU Danmarks Tekniske Universitet Kemitorvet, bygning 207 2800 Kongens Lyngby			Danmarks Tekniske Universitet - DTU Kemi		Drawing number: INLET_007	
					Page 1/1	

KNURLING
ALL AROUND



SECTION A-A

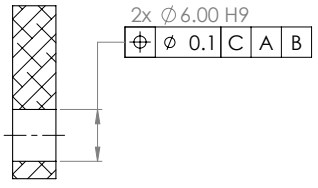
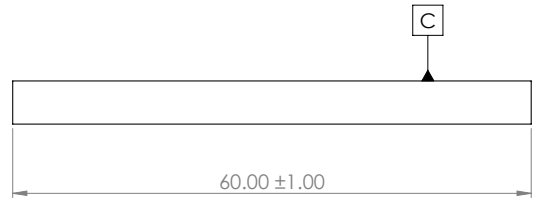
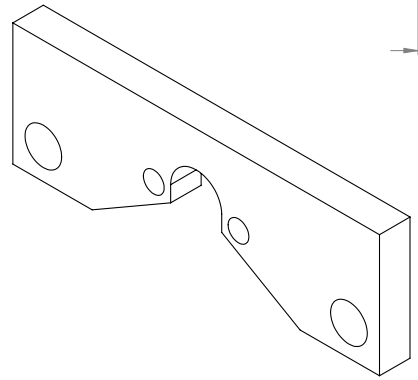
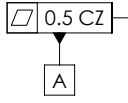
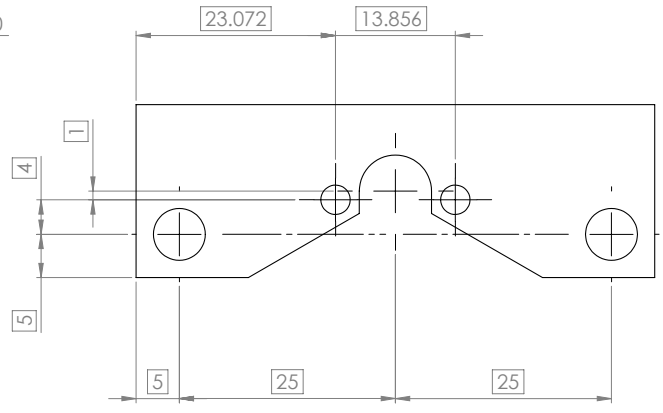
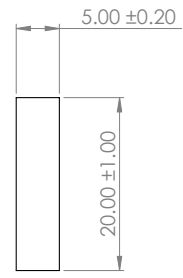
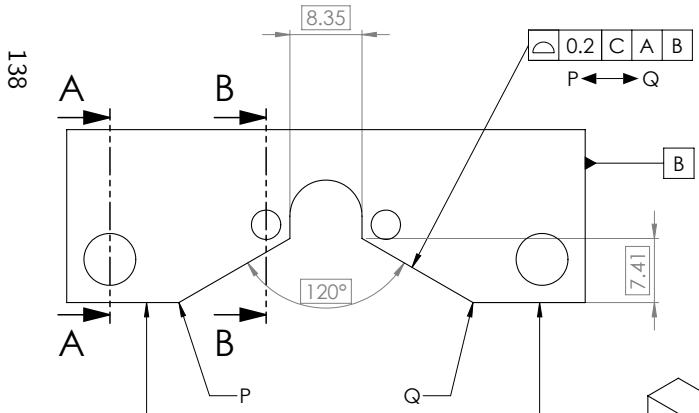


SECTION B-B

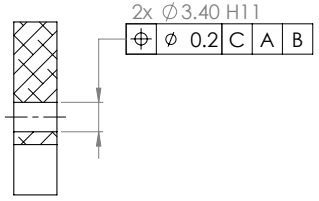
1 copy (cut into 2)

REV.	DATE	MODIFIED BY	DESCRIPTION			
Contact Alexandre Voute alpavo@kemi.dtu.dk 50 21 87 37			Scale 2:1	General rugosity √ Ra 3.2 (✓)	General tolerance class ISO 2768 - mK	Edges - ISO 13715 -0,2 +0,2
Paper format: A3			Units: mm		Laboratory: THz lab	
Material: Brass					Part name: Knob exterior	
Surface finishing: -			Checked by: Andreas Pedersen			
Drawn by: A. Voute			Date: 08-08-2019		Mass: -	
Approved by: R.W. Larsen						
DTU Danmarks Tekniske Universitet Kemitorvet, bygning 207 2800 Kongens Lyngby					Drawing number: INLET_003	
					Page 1/1	

138

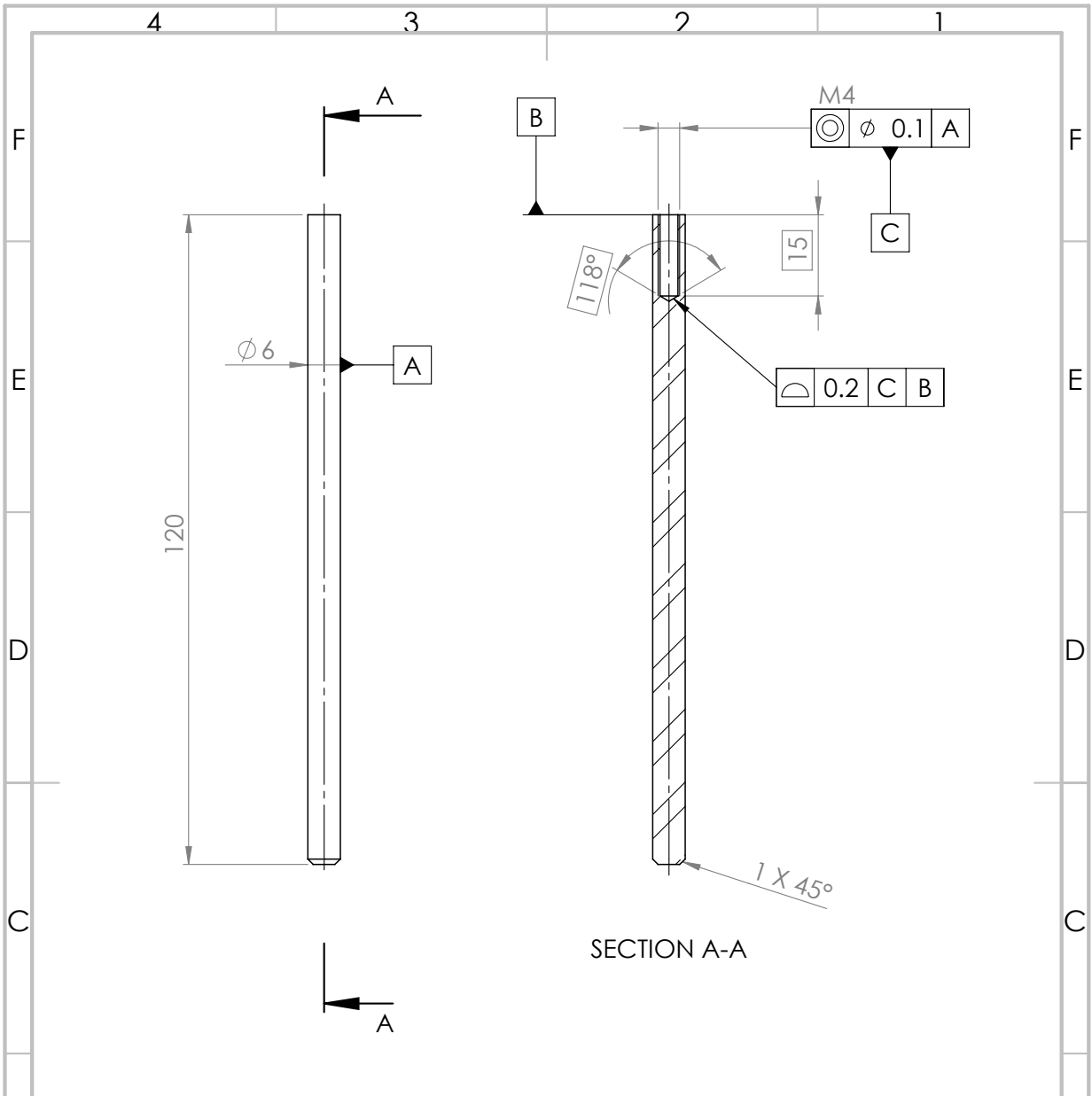


SECTION A-A



SECTION B-B

REV.	DATE	MODIFIED BY	DESCRIPTION				
			Contact Alexandre Voute alpavo@kemi.dtu.dk 50 21 87 37	Scale 2:1	General roughness √ Ra 3.2 (✓)	General tolerance class ISO 2768 - mK	Edges - ISO 13715 -0.2 +0.2
Paper format: A3			Units: mm		Laboratory: THz lab		
Material: Aluminum			Surface finishing: -		Part name: Guide		
Drawn by: A. Voute			Checked by: Andreas Pedersen		Drawing number: INLET_002		
Approved by: R.W. Larsen			Date: 08-08-2019		Mass: -		Page 1/1
DTU Danmarks Tekniske Universitet Danmarks Tekniske Universitet - DTU Kemi Kemitorvet, bygning 207 2800 Kongens Lyngby							



REV.	DATE	MODIFIED BY	DESCRIPTION			
Contact Alexandre Voute alpavo@kemi.dtu.dk 50 21 87 37			Scale 1:1	General rugosity √ Ra 3,2 (√)	General tolerance class ISO 2687 - mK	Edges - ISO 13715 -0,2 +0,2
Paper format: A4			Units: mm		Laboratory: THz lab	
Material: Stainless steel					Part name: Rail	
Surface finishing: -					Drawing number: INLET_001	
Drawn by: A. Voute			Checked by: Andreas Pedersen		139	
Approved by: R.W. Larsen			Date: 08-08-2019	Mass: -	Page 1/1	
Danmarks Tekniske Universitet Danmarks Tekniske Universitet - DTU Kemi Kemitorvet, bygning 207 2800 Kongens Lyngby						

4

3

2

1

F

F

E

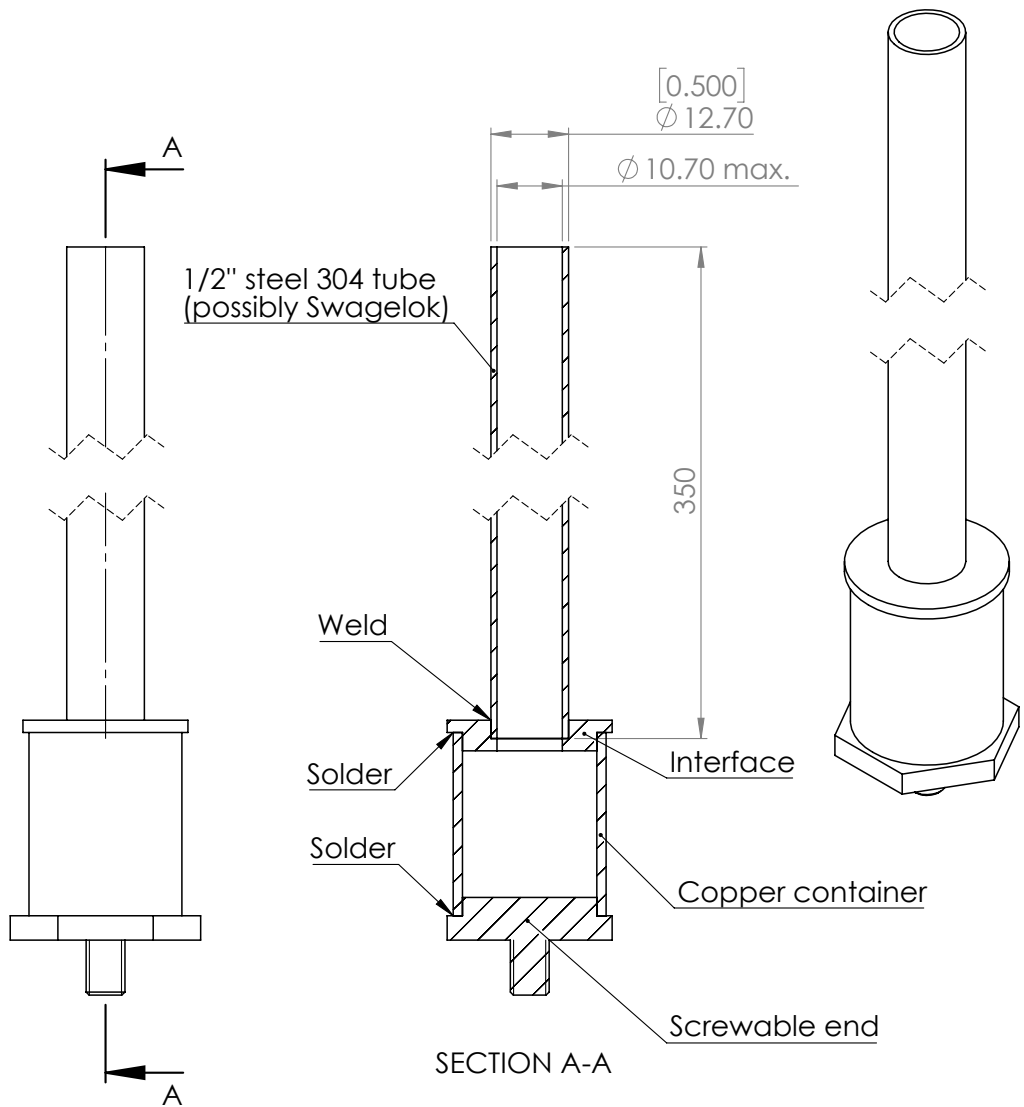
E

D

D

C

C



SECTION A-A

REV.	DATE	MODIFIED BY	DESCRIPTION

Contact
 Alexandre Voute
 alpavo@kemi.dtu.dk
 50 21 87 37

Scale

1:1



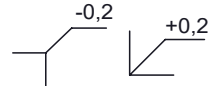
General rugosity

 $\sqrt{Ra\ 3,2}$ (✓)

General tolerance class

ISO 2768 - mK

Edges - ISO 13715



Paper format: A4

Units: mm [in]

Material: -

Surface finishing: -

Drawn by: A. Voute

Checked by: I. Khaliqdad

Approved by: R.W. Larsen

Date: 22-06-2018

Mass: -

Laboratory:

THz lab

Part name:

pH2 tube - Assembly

Drawing number:

THZ-paraH2-004

Page

1/1



**Danmarks
 Tekniske
 Universitet**

Danmarks Tekniske Universitet - DTU Kemi
 Kemitorvet, bygning 207
 2800 Kongens Lyngby

4

3

2

1

F

F

E

E

D

D

C

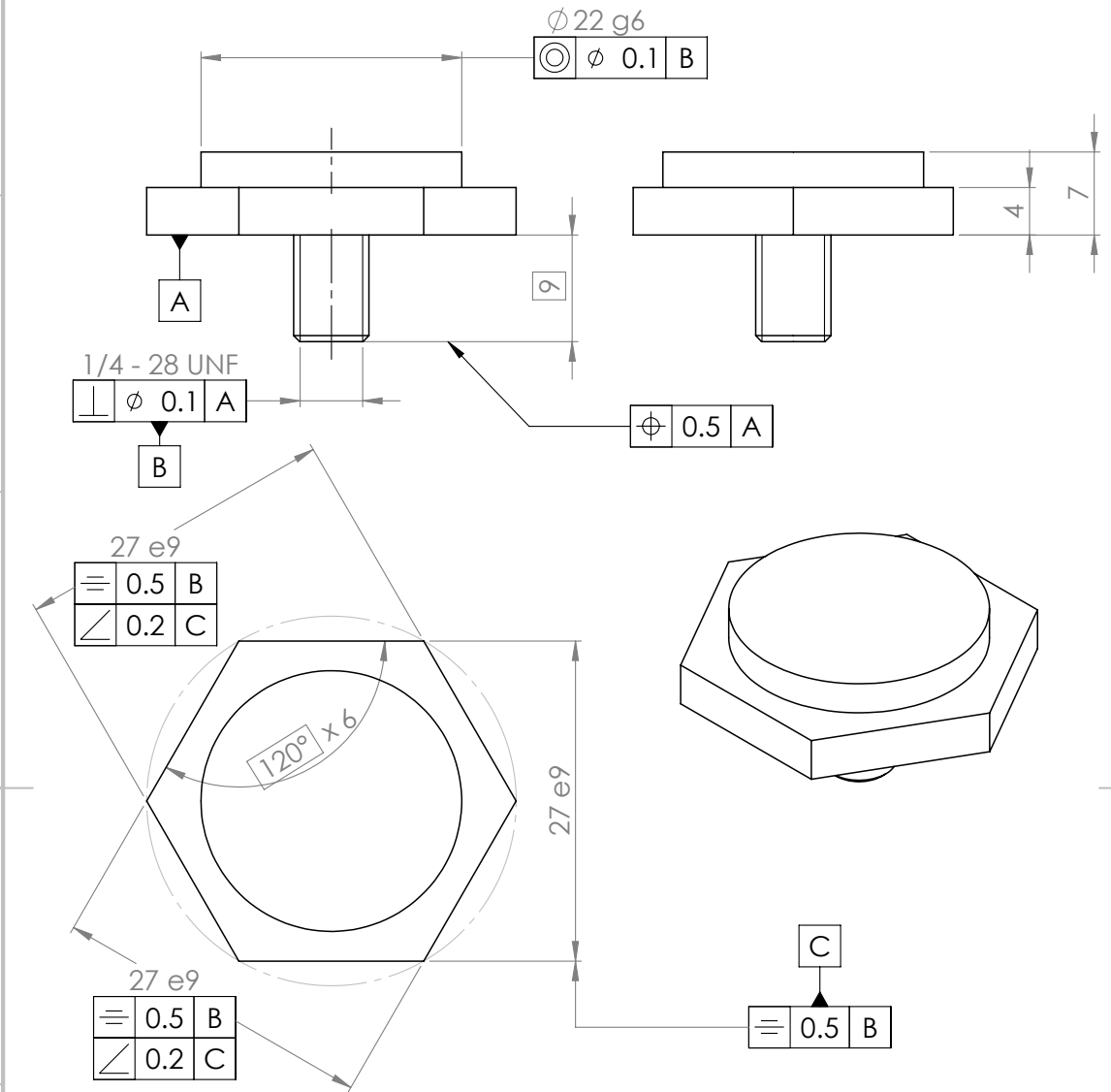
C

B

B

A

A



REV.	DATE	MODIFIED BY	DESCRIPTION

Contact Alexandre Voute alpavo@kemi.dtu.dk 50 21 87 37	Scale 2:1	General rugosity $\sqrt{Ra\ 3,2}$ (✓)	General tolerance class ISO 2687 - mK	Edges - ISO 13715 -0,2 +0,2
---	---------------------	--	---	-----------------------------------

Paper format: A4	Units: mm [in]	Laboratory: THz lab
------------------	----------------	-------------------------------

Material: Copper OFHC	Checked by: I. Khaliqdad	Part name: pH2 tube - Screwable end
-----------------------	--------------------------	---

Surface finishing: -	Date: 22-06-2018	Mass: -	Drawing number: THZ-paraH2-001
----------------------	------------------	---------	--

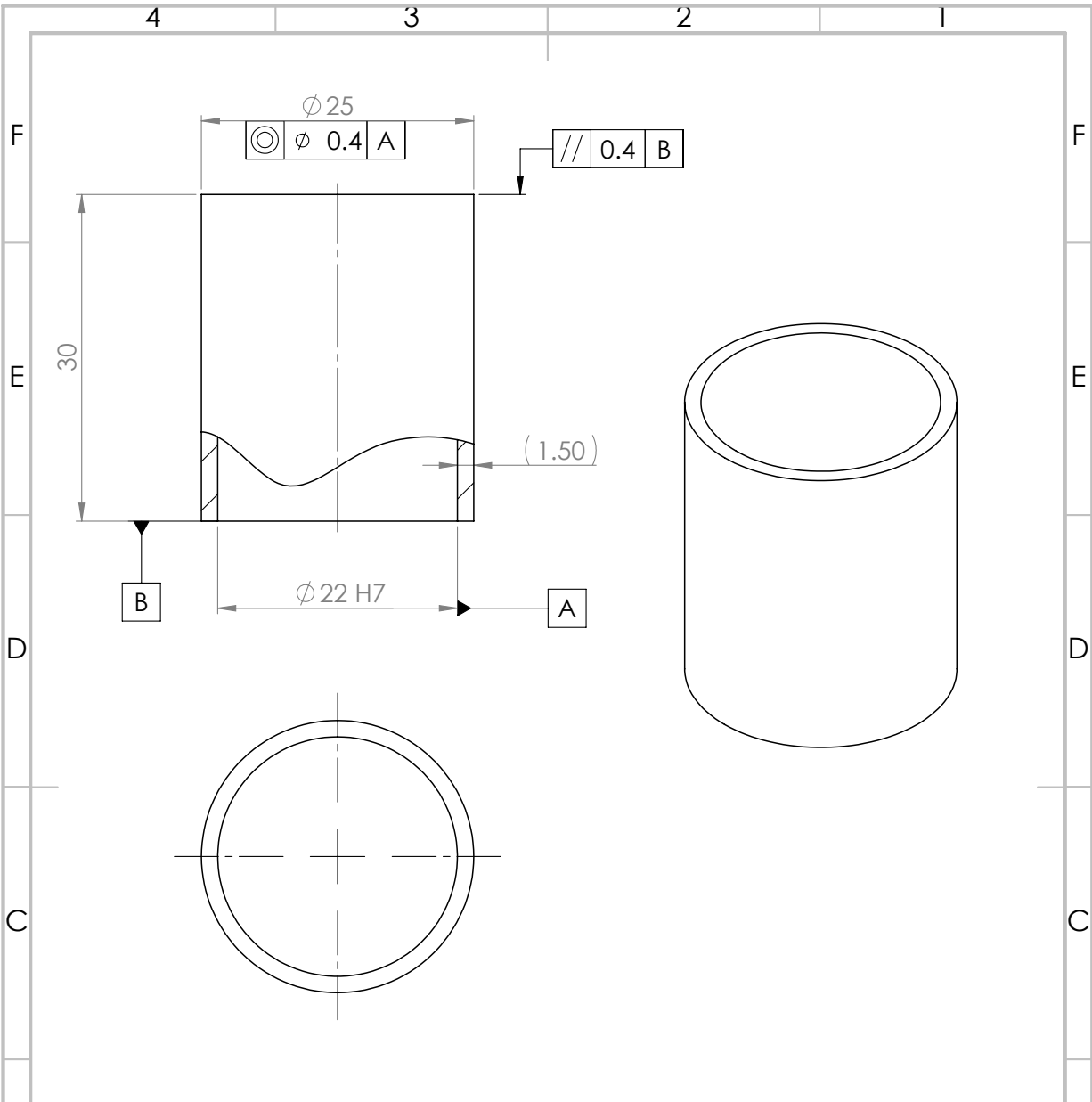
Drawn by: A. Voute	Approved by: R.W. Larsen	Page 1/1
--------------------	--------------------------	-------------

DTU Danmarks Tekniske Universitet	Danmarks Tekniske Universitet - DTU Kemi Kemitorvet, bygning 207 2800 Kongens Lyngby	141
-----------------------------------	--	-----

DTU Danmarks Tekniske Universitet	Page 1/1
-----------------------------------	-------------

DTU Danmarks Tekniske Universitet	Page 1/1
-----------------------------------	-------------

DTU Danmarks Tekniske Universitet	Page 1/1
-----------------------------------	-------------



REV.	DATE	MODIFIED BY	DESCRIPTION			
Contact Alexandre Voute alpavo@kemi.dtu.dk 50 21 87 37			Scale 2:1	General rugosity √ Ra 3,2 (√)	General tolerance class ISO 2687 - mK	Edges - ISO 13715 -0,2 +0,2
Paper format: A4			Units: mm [in]		Laboratory: THz lab	
Material: Copper OFHC					Part name: pH2 tube - Copper container	
Surface finishing: -					Drawing number: THZ-paraH2-002	
Drawn by: A. Voute			Checked by: I. Khaliqdad		Page 1/1	
Approved by: R.W. Larsen			Date: 22-06-2018		Mass: -	
Danmarks Tekniske Universitet			Danmarks Tekniske Universitet - DTU Kemi Kemitorvet, bygning 207 2800 Kongens Lyngby			

4

3

2

1

F

F

E

E

D

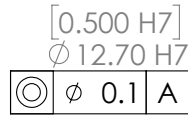
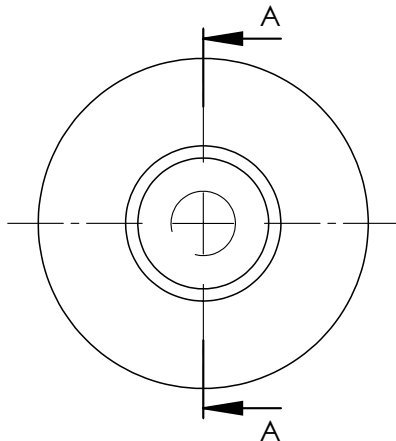
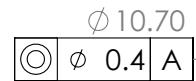
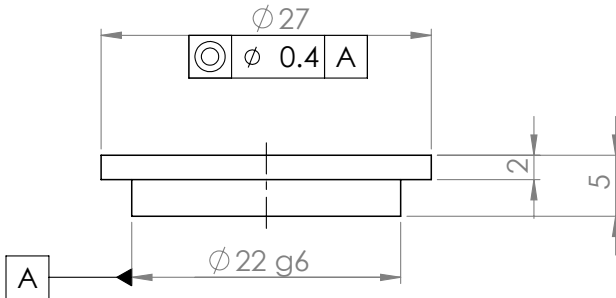
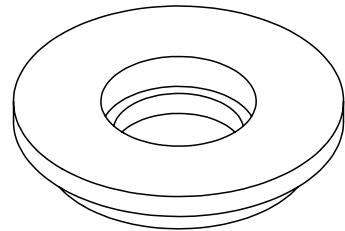
D

C

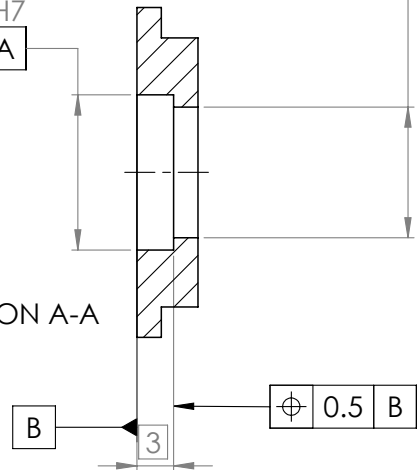
C

A

A



SECTION A-A



REV.	DATE	MODIFIED BY	DESCRIPTION			
Contact Alexandre Voute alpavo@kemi.dtu.dk 50 21 87 37			Scale 2:1	General rugosity $\sqrt{Ra\ 3,2}$ (✓)	General tolerance class ISO 2768 - mK	Edges - ISO 13715 -0,2 / +0,2

Paper format: A4	Units: mm [in]		Laboratory: THz lab			
Material: Stainless steel 304			Part name: pH2 tube - Interface Cu container/Steel tube			
Surface finishing: -			Drawing number: THZ - paraH2 - 003			
Drawn by: A. Voute	Checked by: I. Khaliqdad		Page 1/1			
Approved by: R.W. Larsen	Date: 22-06-2018		Mass: -		143	



**Danmarks
Tekniske
Universitet**

Danmarks Tekniske Universitet - DTU Kemi
Kemitorvet, bygning 207
2800 Kongens Lyngby

4

3

2

1

F

F

E

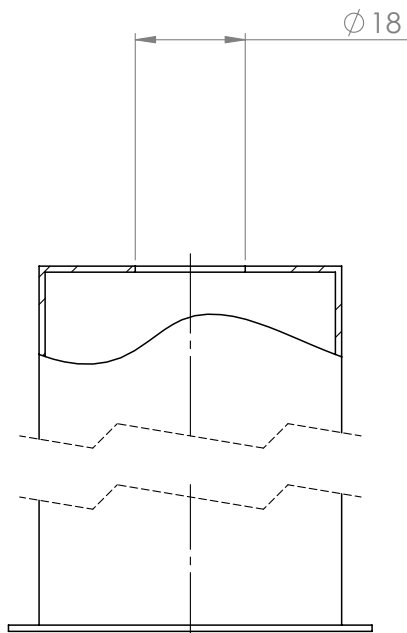
E

D

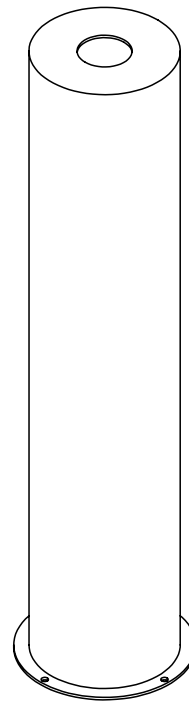
D

C

C



SCALE 1:1



REV.	DATE	MODIFIED BY	DESCRIPTION

Contact Alexandre Voute alpavo@kemi.dtu.dk 50 21 87 37	Scale 1:2	General rugosity √ Ra 3,2 (√)	General tolerance class ISO 2687 - mK	Edges - ISO 13715 -0,2 +0,2
---	--------------	----------------------------------	--	-----------------------------------

Paper format: A4	Units: mm	Laboratory: THz lab
Material: Stainless steel 304		Part name: Radiation shield cryostat
Surface finishing: -		
Drawn by: A. Voute	Checked by: -	
Approved by: R.W. Larsen	Date: 30-07-2018	Mass: -


Danmarks Tekniske Universitet
 Danmarks Tekniske Universitet - DTU Kemi
 Kemitorvet, bygning 207
 2800 Kongens Lyngby

Drawing number: THZ-paraH2-006	Page 1/1
-----------------------------------	-------------

4

3

2

1

A

A

4 3 2 1

F

F

E

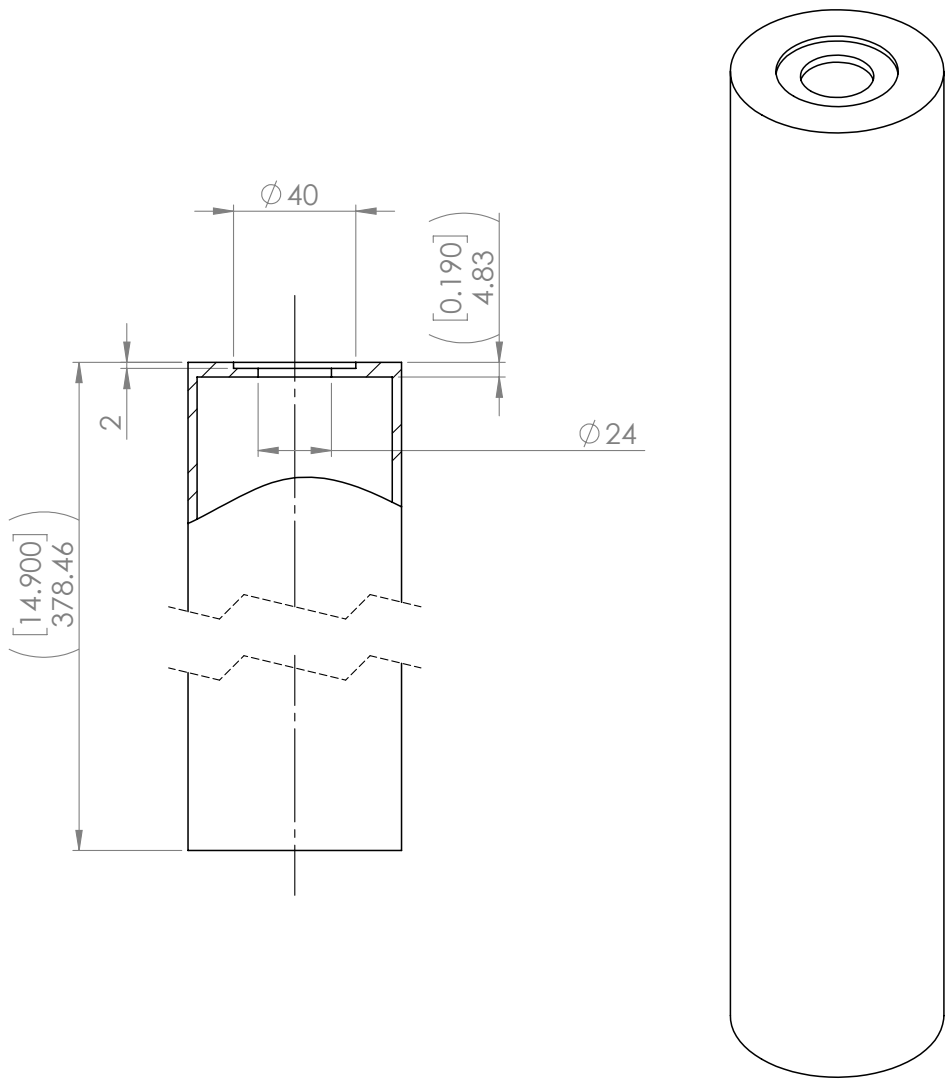
E

D

D

C

C



REV.	DATE	MODIFIED BY	DESCRIPTION

B

B

Contact Alexandre Voute alpavo@kemi.dtu.dk 50 21 87 37	Scale 1:2 	General rugosity Ra 3,2 (✓)	General tolerance class ISO 2687 - mK	Edges - ISO 13715 -0,2 +0,2
---	------------------	--------------------------------	--	---------------------------------------

Paper format: A4	Units: mm [in]	Laboratory: THz lab
------------------	----------------	-------------------------------

Material: Stainless steel 304	Surface finishing: -	Part name: Vacuum shroud cryostat
-------------------------------	----------------------	---

Drawn by: A. Voute	Checked by: -	Drawing number: THZ-paraH2-005
--------------------	---------------	--

Approved by: R.W. Larsen	Date: 30-07-2018	Mass: -	Page 1/1
--------------------------	------------------	---------	-------------

A

A

DTU Danmarks Tekniske Universitet
 Danmarks Tekniske Universitet - DTU Kemi
 Kemitorvet, bygning 207
 2800 Kongens Lyngby

145	Page 1/1
-----	-------------

4 3 2 1

4

3

2

1

F

F

E

E

D

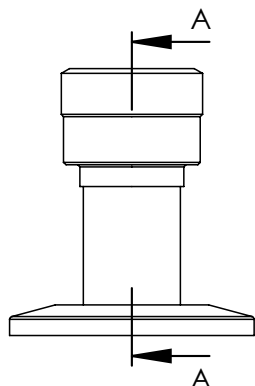
D

C

C

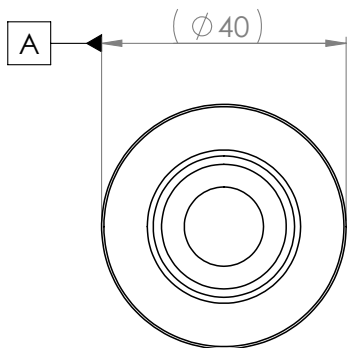
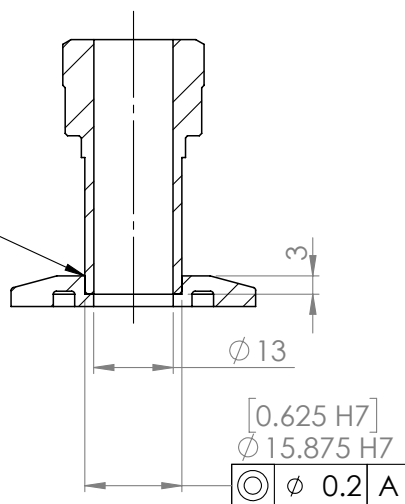
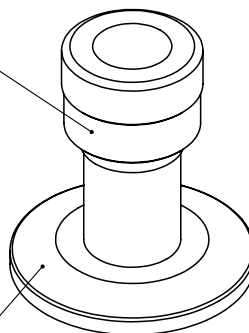
A

A



SECTION A-A

Weld

Swagelok
SS-8-UT-A-10BTKF25 blank flange
(hole to be drilled)

REV.	DATE	MODIFIED BY	DESCRIPTION

Contact Alexandre Voute alpavo@kemi.dtu.dk 50 21 87 37	Scale 1:1	General rugosity $\sqrt{\text{Ra } 3,2}$ (✓)	General tolerance class ISO 2687 - mK	Edges - ISO 13715 -0,2 +0,2
---	--------------	---	--	-----------------------------------

Paper format: A4	Units: mm [in]	Laboratory: THz lab
------------------	----------------	------------------------

Material: Stainless steel 304	Part name: Flange with vacuum fitting
-------------------------------	--

Surface finishing: -	Checked by: I. Khaliqdad	Part number: THZ-paraH2-005
----------------------	--------------------------	--------------------------------

Drawn by: A. Voute	Date: 24-06-2018	Mass: -	Page 1/1
--------------------	------------------	---------	-------------

Approved by: R.W. Larsen		
--------------------------	--	--

Danmarks Tekniske Universitet 146	Danmarks Tekniske Universitet - DTU Kemi Kemitorvet, bygning 207 2800 Kongens Lyngby
---	--

D

Spectroscopy of HCl/water complexes: complementary quantum chemical calculations

Quantum chemical computations have been carried out with Gaussian16 [135] to assist our understanding of the spectra presented in chapter 4, section 4.3. Namely, we performed a series of structure optimizations for a number of complexes such as $(\text{HCl})(\text{H}_2\text{O})$, $(\text{HCl})(\text{H}_2\text{O})_2$, $(\text{HCl})_2(\text{H}_2\text{O})$ and $(\text{HCl})_n$ with $n = 1, \dots, 4$. We used Møller-Plesset second-order perturbation theory (MP2) [136] with the Dunning basis set aug-cc-pVTZ ([137] and following articles). For each optimized structure, harmonic vibrational frequencies and associated IR intensities were computed. Those were also calculated for deuterated analogues. Table D.1 list the positions of the HCl stretching modes in these complexes along with the theoretical shifts with respect to the monomer band.

These computations were used to have a qualitative overview of the shape of the various complexes, visualize their normal modes and compare the positions and IR intensities of the lines. Calculated harmonic frequencies seldom match the position of experimentally observed IR bands (the latter are generally about 90% of the former). However, the differences between these calculated positions can be used as an educated guess for the assignments of spectral features.

The work of Mancini & Bowman (see [61, 86] and section 3.2.1) shows that a correct description of the vibrational ground state of the complex $(\text{HCl})(\text{H}_2\text{O})$ cannot be given by geometry optimization on the PES and the harmonic approximation. Thus we used the planar C_{2v} saddle point, i.e. the stationary point geometry that best reflects the actual ground state, for the computation of the intramolecular normal modes which are supposedly the least affected by the delocalization of the wavefunction over the inversion double-well. Intermolecular modes were not considered here and would anyway necessitate a more advanced model which includes this effect.

Table D.1: Harmonic frequencies of H³⁵Cl and its complexes with water isotopologues in the HCl stretching region at the MP2/aug-cc-pVTZ level of theory. Degeneracy is given parenthetically and intensities account for it. Shifts are given with respect to the calculated HCl monomer band position.

Compound	Position / cm ⁻¹	Shift / cm ⁻¹	Intensity / km·mol ⁻¹	Mode
HCl	3044.3		49.9	
(HCl) ₂	3028.9	-15.3	60.3	Acceptor stretch
(HCl) ₂	2971.2	-73.0	291.5	Donor stretch
(HCl) ₃	2919.9	-124.3	969.5	Coll. asym. stretch (2)
(HCl) ₄	2888.8	-155.5	150.1	Coll. asym. stretch
(HCl) ₂ (D ₂ O)	2875.0	-169.3	496.0	Free HCl stretch
(HCl) ₂ (HOD)	2874.3	-170.0	486.1	Free HCl stretch
(HCl) ₂ (H ₂ O)	2873.9	-170.3	473.9	Free HCl stretch
(HCl) ₄	2866.9	-177.3	1884.4	Pairwise stretches (2)
(HCl)(HOD)	2850.0	-194.3	570.8	HCl stretch
(HCl)(D ₂ O)	2849.3	-195.0	594.0	HCl stretch
(HCl)(H ₂ O)	2849.1	-195.1	617.8	HCl stretch
(HCl) ₂ (H ₂ O)	2595.3	-448.9	870.9	Bound HCl stretch
(HCl) ₂ (HOD)	2592.1	-452.2	830.1	Bound HCl stretch
(HCl) ₂ (D ₂ O)	2589.6	-454.7	823.7	Bound HCl stretch
(HCl)(H ₂ O) ₂	2499.4	-544.9	1172.4	HCl stretch
(HCl)(HOD)(H ₂ O)	2498.5	-545.8	1146.0	HCl stretch
(HCl)(D ₂ O)(H ₂ O)	2498.4	-545.8	1144.4	HCl stretch
(HCl)(H ₂ O)(HOD)	2489.8	-554.4	1047.9	HCl stretch
(HCl)(HOD) ₂	2488.7	-555.5	1017.4	HCl stretch
(HCl)(D ₂ O)(HOD)	2488.6	-555.6	1015.9	HCl stretch
(HCl)(H ₂ O)(D ₂ O)	2486.7	-557.5	1027.7	HCl stretch
(HCl)(HOD)(D ₂ O)	2485.6	-558.6	997.8	HCl stretch
(HCl)(D ₂ O) ₂	2485.5	-558.8	996.4	HCl stretch

The bimolecular reaction $\text{Br} + \text{I}_2$ from the complex $(\text{HBr}) \cdots (\text{I}_2)$

In the course of this Ph.D. project, we carried out some work on the van der Waals complex $(\text{HBr}) \cdots (\text{I}_2)$ and the induced exchange reaction $\text{Br} + \text{I}_2 \longrightarrow \text{BrI} + \text{I}$. This is one of the bimolecular reactions originally studied by the group of Ahmed Zewail [15, 16]. There, it is argued that the formation of IBr is detected as a result of the collision of ground state Br with I_2 , with a rise-time of 53 ps (44 ps when the initial complex is $(\text{DBr}) \cdots (\text{I}_2)$). Despite the simplicity of BrI_2 from the nuclear point of view – there are only three atoms – it is very hard to describe accurately its electronic structure since, as a radical and with the heavy atoms it contains, spin-orbit coupling plays a non-negligible role. No *ab initio* potential energy surface is available for this system. In the above-mentioned articles, a complicated empirical surface was used and adjusted to support the interpretation of the reported results via classical trajectories calculations. However, these experiments were repeated by Wright *et al.* [20, 21] using a different probing mechanism, coming to the conclusion that the interpretations of Zewail were incorrect.

It is worth mentioning that the geometry of the van der Waals complex $(\text{HBr}) \cdots (\text{I}_2)$ is still not known at the time of writing. In fact, in refs. [15, 16], that geometry was deduced from analogous lighter systems. Specifically, they assumed that the three halogen atoms are collinear and that the angle between the $\text{Br}-\text{H}$ bond and the $\text{Br} \cdots \text{I}$ van der Waals bond was either 180° or 125° . We carried out some *ab initio* structure optimization of $(\text{HBr}) \cdots (\text{I}_2)$ with Gaussian16 [135], using the MP2 method [136] and aug-cc-pVQZ basis set [137] with addition of pseudopotentials on the iodine atoms [138] for implicit inclusion of relativistic effects of the core electrons. Harmonic frequencies were computed to check whether the found stationary points corresponded to true minima or saddle points. A L-shaped global minimum geometry was found, with the $\text{H}-\text{Br}$ bond being almost perpendicular to the $\text{Br} \cdots \text{I}-\text{I}$ axis. Instead, the all-collinear geometry was found to be a saddle point. Another local minimum struc-

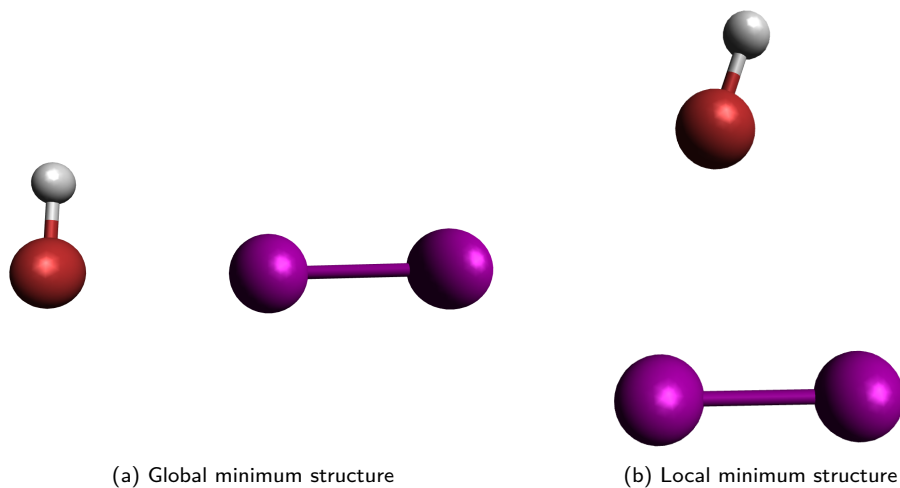


Figure E.1: Optimized true minimum structures of the van der Waals complex $(HBr)\cdots(I_2)$. The local minimum is $6.13 \text{ kJ} \cdot \text{mol}^{-1}$ higher than the global minimum.

ture, $6.13 \text{ kJ} \cdot \text{mol}^{-1}$ higher in energy than the global minimum and whose halogen atoms are not collinear, was also found. These structures are shown in fig. E.1.

We tried to carry out wavepacket propagations using the empirical surface and the initial complex geometries of Zewail et al. In the MATLAB code which was written for this purpose, the triatomic system BrI_2 is described by two Jacobi vectors parametrized with polyspherical coordinates (two distances and one angle). The method of Dateo & Metiu [139] was used for the implementation of the propagator. In particular, the parts containing the radial kinetic energy terms are standard Split-Operator propagators [140, 141]. Their action on the wavepacket is evaluated by passing it in momentum representation via Discrete Fourier Transform along the radial coordinates. Concerning the angular part, a Crank-Nicholson propagator is used [142–144] and its action on the wavefunction is evaluated in a momentum representation obtained by Discrete Cosine Transform [145] along the angular coordinate. However, we never managed to have this wavepacket propagation code to work properly as, except for one-dimensional and some simple two-dimensional problems, we kept obtaining unphysical results (namely, divergence of the wavepacket norm). The angular part of the propagator was the cause of the problem, in spite of the fact that we could reproduce the results in ref. [139] with this method.

Bibliography

1. Zewail, A. H. Femtochemistry: Atomic-Scale Dynamics of the Chemical Bond. *J. Phys. Chem. A* **104**, 5660–5694 (2000).
2. Zewail, A. H. Laser Femtochemistry. *Science* **242**, 1645–1653 (1988).
3. Henriksen, N. E. Femtochemistry – some reflections and perspectives. *Chem. Phys.* **442**, 2–8 (2014).
4. Brooks, P. R. Reactions of Oriented Molecules. *Science* **193**, 11–16 (1976).
5. Jouvét, C. & Soep, B. Photochemistry in van der Waals complexes: Observation of the intermediate state of the Hg^*, Cl_2 reaction. *Chem. Phys. Lett.* **96**, 426–428 (1983).
6. Jouvét, C., Boivineau, M., Duval, M. C. & Soep, B. Photochemistry in excited states of van der Waals complexes. *J. Chem. Phys.* **91**, 5416–5422 (1987).
7. Buelow, S., Radhakrishnan, G., Catanzarite, J. & Wittig, C. The use of van der Waals forces to orient chemical reactants: The $\text{H} + \text{CO}_2$ reaction. *J. Chem. Phys.* **83**, 444–445 (1985).
8. Radhakrishnan, G., Buelow, S. & Wittig, C. Orienting reactants using van der Waals precursors: $\text{OCO} \cdot \text{HBr} + h\nu \longrightarrow \{\text{OCO} \leftarrow \text{H}\} + \text{Br} \longrightarrow \text{CO} + \text{OH} + \text{Br}$. *J. Chem. Phys.* **84**, 727–738 (1986).
9. Rice, J., Hoffmann, G. & Wittig, C. Photoinitiated $\text{H} + \text{CO}_2 \longrightarrow \text{OH} + \text{CO}$ reactions: OH distributions and three-body interactions in $\text{CO}_2\text{H}_2\text{S}$ complexes. *J. Chem. Phys.* **88**, 2841 (1988).
10. Chen, Y., Hoffmann, G., Oh, D. & Wittig, C. $\text{H} + \text{CO}_2 \longrightarrow \text{OH} + \text{CO}$: Yield versus HI photolysis wavelength and OH rotational distributions under single-collision conditions and with CO_2HI complexes. *Chem. Phys. Lett.* **159**, 426–434 (1989).
11. Böhmer, E., Shin, S. K., Chen, Y. & Wittig, C. Photoinitiated H- and D- atom reactions with N_2O in the gas phase and in $\text{N}_2\text{O}-\text{HI}$ and $\text{N}_2\text{O}-\text{DI}$ complexes. *J. Chem. Phys.* **97**, 2536–2547 (1992).

12. Böhmer, E., Mikhaylichenko, K. & Wittig, C. Reactions of hot deuterium atoms with OCS in the gas phase and in OCS–DI complexes. *J. Chem. Phys.* **99**, 6545–6552 (1993).
13. Scherer, N. F., Khundkar, L. R., Bernstein, R. B. & Zewail, A. H. Real-time picosecond clocking of the collision complex in a bimolecular reaction: The birth of OH from H + CO₂. *J. Chem. Phys.* **87**, 1451 (1987).
14. Scherer, N. F., Sipes, C., Bernstein, R. B. & Zewail, A. H. Real-time clocking of bimolecular reactions: Application to H + CO₂. *J. Chem. Phys.* **92**, 5239–5259 (1990).
15. Gruebele, M., Sims, I. R., Potter, E. D. & Zewail, A. H. Femtosecond probing of bimolecular reactions: The collision complex. *J. Chem. Phys.* **95**, 7763–7766 (1991).
16. Sims, I. R., Gruebele, M., Potter, E. D. & Zewail, A. H. Femtosecond real-time probing of reactions. VIII. The bimolecular reaction Br + I₂. *J. Chem. Phys.* **97**, 4127–4148 (1992).
17. Ionov, S. I., Brucker, G. A., Jaques, C., Valachovic, L. & Wittig, C. Subpicosecond OH production from photoexcited CO₂–HI complexes. *J. Chem. Phys.* **97**, 9486 (1992).
18. Ionov, S. I., Ionov, P. I. & Wittig, C. Time-resolved studies of photoinitiated reactions in binary and larger (N₂O)_m(HI)_n ($m \geq 1, n \geq 1$) complexes. *Faraday Discuss. Chem. Soc.* **97**, 391 (1994).
19. Jaques, C. *et al.* Photoinitiated processes in complexes - subpicosecond studies of CO₂–HI and stereospecificity in Ar–HX. *J. Chem. Soc. Faraday. Trans.* **89**, 1419–1425 (1993).
20. Wright, S. A., Tuchler, M. F. & McDonald, J. Picosecond observation of electronic quenching. Br(²P_{1/2}) + I₂($\nu = 0$) → Br(²P_{3/2}) + I₂($\nu > 0$) by geometrically restricted reaction. *Chem. Phys. Lett.* **226**, 570–576 (1994).
21. Tuchler, M. F., Wright, S. & McDonald, J. D. Real time study of bimolecular interactions: Direct detection of internal conversion involving Br(²P_{1/2}) + I₂ initiated from a van der Waals dimer. *J. Chem. Phys.* **106**, 2634–2645 (1997).
22. Wester, R., Bragg, A. E., Davis, A. V. & Neumark, D. M. Time-resolved study of the symmetric S_N2-reaction I[−] + CH₃I. *J. Chem. Phys.* **119**, 10032–10039 (2003).
23. Cheng, P. Y., Zhong, D. & Zewail, A. H. Transition states of charge-transfer reactions: Femtosecond dynamics and the concept of harpooning in the bimolecular reaction of benzene with iodine. *J. Chem. Phys.* **103**, 5153–5156 (1995).
24. Zhong, D., Ahmad, S., Cheng, P. Y. & Zewail, A. H. Femtosecond nucleophilic substitution reaction dynamics. *J. Am. Chem. Soc.* **119**, 2305–2306 (1997).
25. Abou-Zied, O. K. & McDonald, J. D. Picosecond real time study of the bimolecular reaction O(³P) + C₂H₄ and the unimolecular photodissociation of CH₃CHO and H₂CO. *J. Chem. Phys.* **109**, 1293–1301 (1998).

26. Farmanara, P., Stert, V., Radloff, W., Skowronek, S. & Gonzalez-Ureña, A. Ultrafast dynamics and energetics of the intracuster harpooning reaction in Ba \cdots FCH₃. *Chem. Phys. Lett.* **304**, 127–133 (1999).
27. Stert, V. *et al.* Real-time study of the femtosecond harpooning reaction in Ba \cdots FCH₃. *Phys. Rev. A* **59**, R1727–R1730 (1999).
28. Stert, V. *et al.* Femtosecond time-resolved electron spectroscopy of the intracuster reaction in Ba \cdots FCH₃. *Chem. Phys. Lett.* **337**, 299–305 (2001).
29. Havenith, M. *Infrared Spectroscopy of Molecular Clusters* (Springer-Verlag Berlin Heidelberg, 2002).
30. Atkins, P. & de Paula, J. *Physical Chemistry for the Life Sciences* (Oxford University Press, 2010).
31. Israelachvili, J. N. *Intermolecular and Surface Forces* 3rd ed. (Academic Press, 2011).
32. Tannor, D. J. *Introduction to Quantum Mechanics: A Time-Dependent Perspective* (University Science Books, 2007).
33. Henriksen, N. E. & Hansen, F. Y. *Theories of Molecular Reaction Dynamics: The Microscopic Foundation of Chemical Kinetics* 2nd ed. (Oxford University Press, 2018).
34. Aquilanti, V. & Cavalli, S. Coordinates for molecular dynamics: Orthogonal local systems. *J. Chem. Phys.* **85**, 1355–1361 (1986).
35. Podolsky, B. Quantum-Mechanically Correct Form of Hamiltonian Function for Conservative Systems. *Phys. Rev.* **32**, 812–816 (1928).
36. Jacobi, C. G. J. Sur l'élimination des nœuds dans le problème des trois corps. *Journal für die reine und angewandte Mathematik*, 115–131 (1842).
37. Hirschfelder, J. O. & Dahler, J. S. The kinetic energy of relative motion. *Proc. Nat. Acad. Sci.* **42**, 363–365 (1956).
38. Radau, R. Sur une transformation des équations différentielles de la dynamique. *Annales Scientifiques de l'École Normale Supérieure* **5**, 311–375 (1868).
39. Smith, F. T. Modified Heliocentric Coordinates for Particle Dynamics. *Phys. Rev. Lett.* **45**, 1157–1160 (1980).
40. Chapuisat, X. & Iung, C. Vector parametrization of the N-body problem in quantum mechanics: Polyspherical coordinates. *Phys. Rev. A* **45**, 6217–6235 (1992).
41. Gatti, F. *et al.* Vector parametrization of the N-atom problem in quantum mechanics. I. Jacobi vectors. *J. Chem. Phys.* **108**, 8804 (1998).
42. Gatti, F. *et al.* Vector parametrization of the three-atom problem in quantum mechanics. *J. Mol. Struct. (Theochem)* **424**, 181–199 (1998).

43. Gatti, F., Iung, C. & Chapuisat, X. Vector parametrization of the three-atom problem in quantum mechanics II. Valence vectors. *J. Mol. Struct. (Theochem)* **430**, 201–208 (1998).
44. Gatti, F., Iung, C., Menou, M. & Chapuisat, X. Vector parametrization of the N-atom problem in quantum mechanics. II. Coupled-angular-momentum spectral representations for four-atom systems. *J. Chem. Phys.* **108**, 8821 (1998).
45. Gatti, F. Vector parametrization of the N-atom problem in quantum mechanics. III. Separation into two sub-systems. *J. Chem. Phys.* **111**, 7225 (1999).
46. Gatti, F. *Approche vectorielle des hamiltoniens moléculaires : application au spectre rovibrationnel excité de l'ammoniac* Ph.D. thesis (Université des Sciences et Techniques du Languedoc - Montpellier II, 1999).
47. Gatti, F. & Iung, C. Exact and constrained kinetic energy operators for polyatomic molecules: The polyspherical approach. *Phys. Rev.* **484**, 1–69 (2009).
48. Eckart, C. Some studies concerning rotating axes and polyatomic molecules. *Phys. Rev.* **47**, 552–558 (1935).
49. Thompson, W. J. *Angular Momentum. An Illustrated Guide To Rotational Symmetries for Physical Systems* (WILEY-VCH Verlag GmbH & Co. KGaA, 2004).
50. Wilson, E. B. J., Cross, P. C. & Decius, J. C. *Molecular Vibrations: The Theory of Infrared and Raman Vibrational Spectra* (Dover Publications, 1980).
51. Marquardt, R. Theoretical Methods for Ultrafast Spectroscopy. *Chem. Phys. Chem.* **14**, 1350–1361 (2013).
52. Meyer, H.-D., Manthe, U. & Cederbaum, L. S. The multi-configurational time-dependent Hartree approach. *Chem. Phys. Lett.* **165**, 73–78 (1990).
53. Manthe, U., Meyer, H.-D. & Cederbaum, L. S. Wave-Packet Dynamics within the Multiconfiguration Hartree Framework: General Aspects and application to NOCl. *J. Chem. Phys.* **97**, 3199–3213 (1992).
54. Manthe, U., Meyer, H.-D. & Cederbaum, L. S. Multiconfigurational Time-Dependent Hartree Study of Complex Dynamics: Photodissociation of NO₂. *J. Chem. Phys.* **97**, 9062–9071 (1992).
55. Beck, M., Jäckle, A., Worth, G. A. & Meyer, H.-D. The multiconfiguration time-dependent Hartree (MCTDH) method: a highly efficient algorithm for propagating wavepackets. *Phys. Rev.* **324**, 1–105 (2000).
56. Gatti, F., Lasorne, B., Meyer, H.-D. & Nauts, A. *Applications of Quantum Dynamics in Chemistry XIV*, 429 (Springer International Publishing, 2017).
57. Worth, G. A., Beck, M. H., Jäckle, A., Vendrell, O. & Meyer, H.-D. The MCTDH Package, Version 8.2, (2000). H.-D. Meyer, Version 8.3 (2002), Version 8.4 (2007). O. Vendrell and H.-D. Meyer Version 8.5 (2013). Version 8.5 contains the ML-MCTDH algorithm. Used version: 8.5.11 (2019). See <http://mctdh.uni-hd.de/>. University of Heidelberg, Germany.

58. Raab, A. On the Dirac–Frenkel/McLachlan variational principle. *Chem. Phys. Lett.* **319**, 674–678 (2000).
59. Jäckle, A. & Meyer, H.-D. Product representation of potential energy surfaces. *J. Chem. Phys.* **104**, 7974–7984 (1996).
60. Jäckle, A. & Meyer, H.-D. Product representation of potential energy surfaces. II. *J. Chem. Phys.* **109**, 3772–3779 (1998).
61. Mancini, J. S. & Bowman, J. M. Communication: A new ab initio potential energy surface for HCl–H₂O, diffusion Monte Carlo calculations of D_0 and a delocalized zero-point wavefunction. *J. Chem. Phys.* **138**, 121102 (2013).
62. Alikhani, M. E. & Silvi, B. Ab initio study of (H₂O)_{1,2} · HCl: Accurate energetic and frequency shift of HCl. *PCCP* **5**, 2494–2498 (2003).
63. Herzberg, G. *Molecular Spectra and Molecular Structure* (D. Van Nostrand Company Inc., 1950).
64. Schmidt, J. A., Johnson, M. S., Grage, M. M. & Nyman, G. On the origin of the asymmetric shape of the HCl photodissociation cross section. *Chem. Phys. Lett.* **480**, 168–172 (2009).
65. Nauts, A. & Chapuisat, X. Momentum, quasi-momentum and hamiltonian operators in terms of arbitrary curvilinear coordinates, with special emphasis on molecular hamiltonians. *Mol. Phys.* **55**, 1287–1318 (1985).
66. Gatti, F. & Nauts, A. Vector parametrization, partial angular momenta and unusual commutation relations in physics. *Chem. Phys.* **295**, 167–174 (2003).
67. Nauts, A. & Gatti, F. Unusual commutation relations in physics. *Am. J. Phys.* **78**, 1365–1375 (2010).
68. Chen, J., Xu, X., Xu, X. & Zhang, D. H. A global potential energy surface for the H₂ + OH → H₂O + H reaction using neural networks. *J. Chem. Phys.* **138**, 154301 (2013).
69. Fu, B. & Zhang, D. H. Full-Dimensional Quantum Dynamics Study of the H + H₂O and H + HOD Exchange Reactions. *J. Phys. Chem. A* **116**, 820–825 (2012).
70. Mihrin, D. *Investigations of Compositions and Fluid-Fluid Association Mechanisms for Petroleum Fluids. Application of the FT-IR techniques* Ph.D. thesis (Technical University of Denmark, 2020).
71. Andersen, J. *Far-Infrared Spectroscopy of Weakly Bound Hydrated Cluster Molecules* Ph.D. thesis (Technical University of Denmark, 2015).
72. Mihrin, D., Andersen, J., Jakobsen, P. W. & Wugt Larsen, R. Highly localized H₂O librational motion as a far-infrared spectroscopic probe for microsolvation of organic molecules. *PCCP* **21**, 1717–1723 (2019).
73. Mihrin, D., Jakobsen, P. W., Voute, A., Manceron, L. & Wugt Larsen, R. High-resolution synchrotron terahertz investigation of the large-amplitude hydrogen bond librational band of (HCN)₂. *PCCP* **20**, 8241–8246 (2018).

74. Mihin, D., Jakobsen, P. W., Voute, A., Manceron, L. & Wugt Larsen, R. High-Resolution Infrared Synchrotron Investigation of $(\text{HCN})_2$ and a Semi-Experimental Determination of the Dissociation Energy D_0 . *Chem. Phys. Chem.* **20**, 3238–3244 (2019).
75. Bally, T. in *Reactive Intermediate Chemistry* (eds Moss, R. A., Platz, M. S. & Jones, M. J.) 797–845 (John Wiley & Sons, Inc, 2004).
76. Choi, M. Y. *et al.* Infrared spectroscopy of helium nanodroplets: novel methods for physics and chemistry. *International Reviews in Physical Chemistry* **25**, 15–75 (2006).
77. Becker, E. D. & Pimentel, G. C. Spectroscopic Studies of Reactive Molecules by the Matrix Isolation Method. *J. Chem. Phys.* **25**, 224–228 (1956).
78. Wartewig, S. *IR and Raman Spectroscopy* (John Wiley & Sons, Ltd, 2003).
79. Roy, P., Rouzières, M., Qi, Z. & Chubar, O. The AILES Infrared Beamline on the third generation Synchrotron Radiation Facility SOLEIL. *Infrared Physics & Technology* **49**, 139–146 (2006).
80. van der Zande, W. J., Jongma, R. T., van der Meer, L. & Redlich, B. *FELIX Facility: Free electron laser light sources from 0.2 to 75 THz in 38th International Conference on Infrared, Millimeter, and Terahertz Waves (IRMMW-THz)* (2013), 1–2.
81. Forney, D., Jacox, M. E. & Thompson, W. E. The vibrational spectra of molecular ions isolated in solid neon. XII. HCl^+ , $(\text{HCl})_2^+$, ClHCl^- , and $\text{O}_2 \cdot \text{HCl}^+$. *J. Chem. Phys.* **103**, 1755–1766 (1995).
82. Wahl, J. S., Forbes, S. G., Nyer, W. E. & Little, R. N. A New Low Impedance High Vacuum Valve. *Rev. Sci. Instrum.* **23**, 379–379 (1952).
83. Gutberlet, A. *et al.* Aggregation-Induced Dissociation of $\text{HCl}(\text{H}_2\text{O})_4$ Below 1 K: The Smallest Droplet of Acid. *Science* **324**, 1545–1548 (2009).
84. Flynn, S. D. *et al.* Infrared Spectra of $\text{HCl}-\text{H}_2\text{O}$ Clusters in Helium Nanodroplets. *J. Phys. Chem. Lett.* **1**, 2233–2238 (2010).
85. Morrison, A. M., Flynn, S. D., Liang, T. & Douberly, G. E. Infrared Spectroscopy of $(\text{HCl})_m(\text{H}_2\text{O})_n$ Clusters in Helium Nanodroplets: Definitive Assignments in the HCl Stretch Region. *J. Phys. Chem. A* **114**, 8090–8098 (2010).
86. Mancini, J. S. & Bowman, J. M. Effects of Zero-Point Delocalization on the Vibrational Frequencies of Mixed HCl and Water Clusters. *J. Phys. Chem. Lett.* **5**, 2247–2253 (2014).
87. Mancini, J. S. & Bowman, J. M. Isolating the spectral signature of H_3O^+ in the smallest droplet of dissociated HCl acid. *PCCP* **17**, 6222–6226 (2015).
88. Rank, D., Rao, B. & Wiggins, T. Molecular constants of HCl^{35} . *J. Mol. Struct.* **17**, 122–130 (1965).
89. Ault, B. S. & Pimentel, G. C. Infrared spectrum of the water-hydrochloric acid complex in solid nitrogen. *J. Chem. Phys.* **77**, 57–61 (1973).

90. Ayers, G. P. & Pullin, A. D. E. The i.r. spectra of matrix isolated water species – II. The characterisation of non-rotating monomer water species in an argon matrix by xenon doping: The matrix isolated spectra of $\text{H}_2\text{O}\cdot\text{HCl}$ and $(\text{CH}_3)_2\text{O}\cdot\text{H}_2\text{O}$ as model compounds for water dimer spectra. *Spectrochimica Acta part A* **32**, 1641–1650 (1976).
91. Schriver, A., Silvi, B., Maillard, D. & Perchard, J. P. Structure of water-hydrochloric acid complexes in argon and nitrogen matrices from infrared spectra. *J. Chem. Phys.* **81**, 2095–2102 (1977).
92. Barnes, A. J. Molecular complexes of the hydrogen halides studied by matrix isolation infrared spectroscopy. *J. Mol. Struct.* **100**, 259–280 (1983).
93. Engdahl, A. & Nelander, B. Axial motion of water–hydrogen halide and water–halogen complexes in argon matrices. *J. Chem. Phys.* **84**, 1981–1987 (1986).
94. Amirand, C. & Maillard, D. Spectrum and structure of water-rich water-hydracid complexes from matrix isolation spectroscopy: evidence for proton transfer. *J. Mol. Struct.* **176**, 181–201 (1988).
95. Andrews, L. & Bohn, R. B. Infrared spectra of isotopic $(\text{HCl})_3$ clusters in solid neon. *J. Chem. Phys.* **90**, 5205–5207 (1989).
96. Bohn, R. B., Hunt, R. D. & Andrews, L. Infrared spectra of the weak hydrogen, oxygen and nitrogen complexes with hydrochloric acid in solid neon. *J. Phys. Chem.* **93**, 3979–3983 (1989).
97. Engdahl, A. & Nelander, B. The far-infrared spectrum of the hydrogen chloride trimer: a matrix isolation study. *J. Phys. Chem.* **94**, 8777–8780 (1990).
98. Weimann, M., Fárník, M. & Suhm, M. A. A first glimpse at the acidic proton vibrations in HCl -water clusters via supersonic jet FTIR spectroscopy. *PCCP* **4**, 3933–3937 (2002).
99. Fárník, M., Weimann, M. & Suhm, M. A. Acidic protons before take-off: A comparative jet Fourier transform infrared study of small HCl - and HBr -solvent complexes. *J. Chem. Phys.* **118**, 10120–10136 (2003).
100. Huneycutt, A. J., Stickland, R. J., Hellberg, F. & Saykally, R. J. Characterization of gas-phase $\text{HCl}\text{--}\text{H}_2\text{O}$ clusters using pulsed infrared cavity ringdown spectroscopy. *Methods for Ultrasensitive Detection II* **4634**, 70 (2002).
101. Huneycutt, A. J., Stickland, R. J., Hellberg, F. & Saykally, R. J. Infrared cavity ringdown spectroscopy of acid–water clusters: $\text{HCl}\text{--}\text{H}_2\text{O}$, $\text{DCl}\text{--}\text{D}_2\text{O}$, and $\text{DCl}\text{--}(\text{D}_2\text{O})_2$. *J. Chem. Phys.* **118**, 1221–1229 (2003).
102. Ortlieb, M., Birner, Ö., Letzner, M., Schwaab, G. W. & Havenith, M. Observation of Rovibrational Transitions of HCl , $(\text{HCl})_2$, and $\text{H}_2\text{O}\text{--}\text{HCl}$ in Liquid Helium Nanodroplets. *J. Phys. Chem. A* **111**, 12192–12199 (2007).
103. Szcześniak, M. M., Scheiner, S. & Bouteiller, Y. Theoretical study of $\text{H}_2\text{O}\text{--}\text{HF}$ and $\text{H}_2\text{O}\text{--}\text{HCl}$: Comparison with experiment. *J. Chem. Phys.* **81**, 5024–5030 (1984).

104. Latajka, Z. & Scheiner, S. Structure, energetics, and vibrational spectrum of $\text{H}_2\text{O}-\text{HCl}$. *J. Chem. Phys.* **87**, 5928–5936 (1987).
105. Hannachi, Y., Silvi, B. & Bouteiller, Y. Structure and vibrational properties of water hydrogen halide complexes. *J. Chem. Phys.* **94**, 2915–2922 (1991).
106. Packer, M. J. & Clary, D. C. Interaction of HCl with water clusters: $(\text{H}_2\text{O})_n\text{HCl}$, $n = 1 - 3$. *J. Chem. Phys.* **99**, 14323–14333 (1995).
107. Re, S., Osamura, Y., Suzuki, Y. & Schaefer, H. F. Structures and stability of hydrated clusters of hydrogen chloride, $\text{HCl}(\text{H}_2\text{O})_n$, $n = 1 - 5$. *J. Chem. Phys.* **109**, 973–977 (1998).
108. Chaban, G. M., Gerber, R. B. & Janda, K. C. Transition from Hydrogen Bonding to Ionization in $(\text{HCl})_n(\text{NH}_3)_n$ and $(\text{HCl})_n(\text{H}_2\text{O})_n$ Clusters: Consequences for Anharmonic Vibrational Spectroscopy. *J. Phys. Chem. A* **105**, 8323–8332 (2001).
109. Milet, A., Struniewicz, C., Moszynski, R. & Wormer, P. E. Theoretical study of the protolytic dissociation of HCl in water clusters. *J. Chem. Phys.* **115**, 349–356 (2001).
110. Cabaleiro-Lago, E. M., Hermida-Ramón, J. M. & Rodríguez-Otero, J. Computational study of the dissociation of H-X acids ($X = \text{F}, \text{Cl}, \text{Br}, \text{I}$) in water clusters. *J. Chem. Phys.* **117**, 3160–3168 (2002).
111. Odde, S., Mhin, B. J., Lee, S., Lee, H. M. & Kim, K. S. Dissociation chemistry of hydrogen halides in water. *J. Chem. Phys.* **120**, 9524–9535 (2004).
112. Zhang, X., Zeng, Y., Li, X., Meng, L. & Zheng, S. Comparison in the complexes of oxygen-containing σ -electron donor with hydrogen halide and dihalogen molecules. *J. Mol. Struct. (Theochem)* **950**, 27–35 (2010).
113. Liu, H. *et al.* Study on the cooperativity of hydrogen bonds between H_2Y and HX ($X=\text{F}, \text{Cl}, \text{Br}$; $\text{Y}=\text{O}, \text{S}, \text{Se}$). *J. Theo. Comp. Chem.* **13**, 1450037 (2014).
114. Arunan, E. *et al.* Definition of the hydrogen bond (IUPAC Recommendations 2011). *Pure Appl. Chem.* **83**, 1637–1641 (2011).
115. Mancini, J. S. & Bowman, J. M. A New Many-Body Potential Energy Surface for HCl Clusters and Its Application to Anharmonic Spectroscopy and Vibration–Vibration Energy Transfer in the HCl Trimer. *J. Phys. Chem. A* **118**, 7367–7374 (2014).
116. Letzner, M. *et al.* High resolution spectroscopy of HCl-water clusters: IR bands of undissociated and dissociated clusters revisited. *J. Chem. Phys.* **139** (2013).
117. Forney, D., Jacox, M. & Thompson, W. The Mid- and Near-Infrared Spectra of Water and Water Dimer Isolated in Solid Neon. *J. Mol. Spec.* **157**, 479–493 (1993).
118. Duplan, J. C., Mahi, L. & Brunet, J. L. NMR determination of the equilibrium constant for the liquid $\text{H}_2\text{O}-\text{D}_2\text{O}$ mixture. *Chem. Phys. Lett.* **413**, 400–403 (2005).

119. Ceponkus, J., Uvdal, P. & Nelander, B. Rotation of Water in Solid Parahydrogen and Orthodeuterium. *J. Phys. Chem. A* **114**, 12979–12985 (2010).
120. Ceponkus, J., Uvdal, P. & Nelander, B. The coupling between translation and rotation for monomeric water in noble gas matrices. *J. Chem. Phys.* **138**, 244305 (2013).
121. McQuarrie, D. A. *Statistical Mechanics* (University Science Books, 2000).
122. Leachman, J. W., Jacobsen, R. T., Penoncello, S. G. & Lemmon, E. W. Fundamental Equations of State for Parahydrogen, Normal Hydrogen, and Orthohydrogen. *J. Phys. Chem. Ref. Data* **38**, 721–748 (2009).
123. Wagner, S. Conversion rate of para-hydrogen to ortho-hydrogen by oxygen: Implications for PHIP gas storage and utilization. *Magnetic Resonance Materials in Physics, Biology and Medicine* **27**, 195–199 (2014).
124. Silvera, I. F. The solid molecular hydrogens in the condensed phase: Fundamentals and static properties. *Rev. Mod. Phys.* **52**, 393–452 (1980).
125. Friedmann, H. & Kimel, S. Rotation—Translation-Coupling Effect in Noble-Gas Crystals Containing Molecular Impurities. *J. Chem. Phys.* **47**, 3589–3605 (1967).
126. Tsuge, M. & Lee, Y.-P. in *Molecular and Laser Spectroscopy* 167–215 (Elsevier, 2020).
127. Wigner, E. Concerning the paramagnetic conversion of para-ortho hydrogen. III. *Z. Phys. Chem. B* **23**, 28–32 (1933).
128. Harrison, L. G. & McDowell, C. A. The catalysis of the para -hydrogen conversion by the solid free radical $\alpha\alpha$ -diphenyl- β -picryl hydrazyl. *Proceedings of the Royal Society of London. Series A. Mathematical and Physical Sciences* **220**, 77–90 (1953).
129. Taylor, H. S. & Sherman, A. Activated adsorption of hydrogen and the parahydrogen conversion. *Trans. Faraday Soc.* **28**, 247 (1932).
130. Andrews, L. & Wang, X. Simple ortho-para hydrogen and para-ortho deuterium converter for matrix isolation spectroscopy. *Rev. Sci. Instrum.* **75**, 3039–3044 (2004).
131. Tam, S. & Fajardo, M. E. Ortho/para hydrogen converter for rapid deposition matrix isolation spectroscopy. *Rev. Sci. Instrum.* **70**, 1926–1932 (1999).
132. Gush, H. P., Allin, E. J., Welsh, H. L. & Hare, W. F. J. The Infrared Fundamental Band of Liquid and Solid Hydrogen. *Can. J. Phys.* **38**, 176–193 (1960).
133. Tam, S. & Fajardo, M. E. Single and Double Infrared Transitions in Rapid-Vapor-Deposited Parahydrogen Solids: Application to Sample Thickness Determination and Quantitative Infrared Absorption Spectroscopy. *Appl. Spec.* **55**, 1634–1644 (2001).
134. Fajardo, M. E. Solid Parahydrogen Thickness Revisited. *Appl. Spec.* **73**, 1403–1408 (2019).

135. Frisch, M. J. *et al.* *Gaussian 16 Revision C.01* Gaussian Inc. Wallingford CT. 2016.
136. Møller, C. & Plesset, M. S. Note on an approximation treatment for many-electron systems. *Phys. Rev.* **46**, 618–622 (1934).
137. Dunning, T. H. Gaussian basis sets for use in correlated molecular calculations. I. The atoms boron through neon and hydrogen. *J. Chem. Phys.* **90**, 1007–1023 (1989).
138. Peterson, K. A., Figgen, D., Goll, E., Stoll, H. & Dolg, M. Systematically convergent basis sets with relativistic pseudopotentials. II. Small-core pseudopotentials and correlation consistent basis sets for the post-*d* group 16–18 elements. *J. Chem. Phys.* **119**, 11113–11123 (2003).
139. Dateo, C. E. & Metiu, H. Numerical solution of the time-dependent Schrödinger equation in spherical coordinates by Fourier-transform methods. *J. Chem. Phys.* **95**, 7392–7400 (1991).
140. Feit, M., Fleck, J. & Steiger, A. Solution of the Schrödinger equation by a spectral method. *J. Comp. Phys.* **47**, 412–433 (1982).
141. Feit, M. D. & Fleck, J. A. Solution of the Schrödinger equation by a spectral method II: Vibrational energy levels of triatomic molecules. *J. Chem. Phys.* **78**, 301–308 (1983).
142. Ames, W. F. *Numerical Methods for Partial Differential Equations* 2nd ed. (Academic Press, 1977).
143. Press, W. H., Teukolsky, S. A., Vetterling, W. T. & Flannery, B. P. *Numerical Recipes in FORTRAN* 2nd ed. (Cambridge University Press, 1992).
144. Goldberg, A., Schey, H. M. & Schwartz, J. L. Computer-Generated Motion Pictures of One-Dimensional Quantum-Mechanical Transmission and Reflection Phenomena. *Am. J. Phys.* **35**, 177–186 (1967).
145. Broughton, S. & Bryan, K. *Discrete Fourier Analysis and Wavelets: Applications to Signal and Image Processing* 464 (John Wiley & Sons, Inc., 2018).